Electron and X-ray Microanalysis of Planetary Materials: from Comet 81P/Wild2 to the Surface of Mars

Thesis submitted for the degree of

Doctor of Philosophy

at the University of Leicester

by

Hitesh Gunvant Changela BSc Mres

Space Research Centre

Department of Physics and Astronomy

University of Leicester

17th January 2011

Dedication

For mummy and daddy

Electron and X-ray Microanalysis of Planetary Materials: from Comet 81P/Wild2 to the Surface of Mars

Hitesh Gunvant Changela

Abstract

This thesis concerns the electron and X-ray microanalysis of planetary materials: from Comet 81P/Wild2 to the surface of Mars. Advanced techniques in electron microscopy and X-ray spectroscopy have been developed for the microanalysis of the nakhlite martian meteorites and Comet 81P/Wild2 samples from the *Stardust* Mission.

Electron microprobe analysis and a Focussed Ion Beam - Scanning Electron Microscope (FIB-SEM) technique for Transmission Electron Microscopy (TEM) was used to analyse the secondary mineral assemblages in the nakhlites. Fracture-filling assemblages in the nakhlites are found to be dominated by an amorphous, hydrated Fe-silicate - a 'gel.' The gel decreases in $Mg_{at}/Mg_{at}+Fe_{at}$ ratio going up the expected depth profile of the nakhlites. Other phases, especially 2:1 smectites - 1:1 phyllosilicate and carbonate are associated with the gel. Newly discovered 1:1 phyllosilicate, suggested to be serpentine, is also found in the mesostasis of Lafayette. A model is proposed describing the formation of the nakhlites' secondary assemblages by an impact-induced hydrothermal system based on the mineralogical and geochemical differences between different samples.

A suite of *Stardust* cometary samples have also been analysed using FIB-TEM and microfocus X-ray spectroscopy that includes: X-ray Fluorescence Spectroscopy (XRF), X-ray Absorption Near-Edge Structure (XANES) and Extended X-ray Absorption Fine Structure (EXAFS) at the *Diamond* synchrotron. Attempts have been made to distinguish the cometary material from that formed by capture heating in aerogel via the identification of ferric-oxides at track entrances.

Finally, the mineralogy and morphology of a terminal particle from *Stardust* track #154 was studied by analytical TEM. The results show that Comet Wild2 contains a unique Al-diopside-bearing grain, having affinities with the minerals found in refractory objects from the inner Solar System. Upon comparison with different early Solar System materials, the grain's mineral assemblage most closely resembles Al-rich chondrules. This adds to the refractory inventory identified in Comet 81P/Wild2.

Acknowledgements

List of Publications

Some of the results presented in this thesis have been incorporated into the following papers and conference abstracts. The chapters to which these papers and abstracts refer to are given in brackets.

Articles Published in Peer-reviewed Journals

Changela H. G., and Bridges J. C. (2011) Alteration assemblages in the nakhlites: variation with depth on Mars. *Meteoritics and Planetary Science.* doi: 10.1111/j.1945-5100.2010.01123.x *[Chapter 4]*

Bridges J. C., Burchell M. J., Changela H. G., Foster N. J., Creighton J. A., Carpenter J. D., Gurman S. J., Franchi I. A., and Busemann H. (2010) Iron oxides in 81P/Wild-2. *Meteoritics and Planetary Science* 45(1):55–72. *[Chapter 5]*

Abstracts Published in International Conference Proceedings

Changela H. G., and Bridges J. C. (2010) Smectite-serpentine mixtures in the Lafayette meteorite. (Abstract #5300) *Meteoritics and Planetary Science* 45, Supplement. *[Chapter 4]*

Changela H. G., Gurman S. J., and Bridges J. C. (2010) XANES and EXAFS of tracks 41, 134 and 162 from the Stardust mission. (Abstract #5311). *Meteoritics and Planetary Science* 45, Supplement. *[Chapter 5]*

Bridges J. C., and Changela H. G. (2010) Chondrule fragments in Stardust tracks 113 and 154. (Abstract #5280). *Meteoritics and Planetary Science* 45, Supplement. *[Chapter 6]*

Changela H. G., and Bridges J. C. (2010) Secondary minerals in the nakhlites formed at varying depths in an impact hydrothermal cell. (Abstract #1407). *41st Lunar and Planetary Science Conference.* CD-Rom. *[Chapter 4]*

Bridges J. C., and Changela H. G. (2010) Refractory chondrule fragments with carbonaceous chondrite affinities in Comet Wild2/81P. (Abstract #2058). *41st Lunar and Planetary Science Conference.* CD-Rom. *[Chapter 6]*

Changela H. G., and Bridges J. C. (2009) TEM study of alteration assemblages in the nakhlites: variation with burial depth on Mars. (Abstract #2201). *40th Lunar and Planetary Science Conference.* CD-Rom. *[Chapter 4]*

Bridges J. C., Changela H G., Carpenter J. D., and Gurman S. J. (2009) Oxide minerals in Comet Wild 2: TEM and synchrotron characterisation. (Abstract #1889). 40th *Lunar and Planetary Science Conference.* CD-Rom. *[Chapter 5]*

Bridges J. C., Changela H. G., Carpenter J. D., and Franchi I. A. (2008) Iron oxide grains in Starst track 121 grains as evidence of Comet Wild 2 hydrothermal alteration. (Abstract #2193). *39th Lunar and Planetary Science Conference.* CD-Rom. *[Chapter 5]*

Abstracts for UK National Conferences

Changela H. G. (2010) Hydrothermal fluids on Mars: evidence from martian meteorites. *4th Biannual Astrobiology Conference of Britain.* *[Chapter 4]*

Changela H. G. (2009) Alteration assemblages in the nakhlites: variation with depth on Mars. *UK Planetary Forum Meeting 2009.* *[Chapter 4]*

Changela H. G., and Bridges J. C. (2009) Synchrotron characterization of track# 134 from the stardust mission. *Network for Early Solar System Investigation Meeting 2009.* *[Chapter 5]*

.

Changela H. G., and Bridges J. C. (2009) TEM characterization of zoned alteration assemblages in the nakhlites. *Network for Early Solar System Investigation Meeting 2009.* *[Chapter 4]*

Changela H. G. (2008) Focused Ion Beam techniques in TEM sample preparation of planetary materials - application to *Stardust* and SNC Meteorites. *UK Planetary Forum Meeting 2008. [Chapters 4 and 5]*

Changela H. G., Walj S., and Bridges J. C. (2008) Transmission electron microscopy studies of the nakhlite martian meteorites. *Royal Astronomical Society UK Aurora Meeting. [Chapter 4]*

Changela H. G., and Bridges J. C. (2008) TEM, XANES and XAS of comet Wild2 particles. *Network for Early Solar System Investigation Meeting UK 2008. [Chapter 5]*

Electron and X-ray Microanalysis of Planetary Materials: from Comet 81P/Wild2 to the Surface of Mars

Hitesh Gunvant Changela

Contents

Contents

Contents

Contents

Chapter 1
Introduction

1.1 Microanalysis of Planetary Materials

Planetary materials sample different bodies of the Solar System. They are mostly found in the form of meteorites; rocky bodies from the inner Solar System that are seen to fall, or are found on Earth. Other planetary materials from beyond the Earth can be found in the form of Interplanetary Dust Particles (IDPs) or micrometeorites that are collected from the Earth's stratosphere and the surface. Thirdly, there are samples returned from Solar System bodies. The current inventory of samples returned to Earth include lunar samples from the *Apollo* and *Luna* missions, samples of Comet 81P/Wild2 from the *Stardust* Mission and asteroidal samples from 25143Itokawa that were recently returned from the *Hayabusa* mission. In this thesis, I deal with the microanalysis of martian meteorite samples and cometary materials returned from the *Stardust* Mission.

Like geological samples on Earth, planetary materials contain a record of the physical, geochemical and potential biological processes that led to their formation and subsequent geochemical evolution. Meteorites are usually samples of solid bodies from the asteroid belt between the orbits of Mars (1.5 A.U.) and Jupiter (5.2 A.U.). They are derived from amongst the first bodies to have formed during the earliest stages of the Solar System (Hutchison, 2004). Comets are also recorders of the early Solar System but represent bodies that formed at much greater heliocentric distances compared to asteroids (10-10000 A.U.). This means that both these types of planetary bodies record details of the early Solar System that allow us to test theories of planetary formation and evolution. About 50 meteorites are thought to come from Mars (Wood and Ashwal, 1981;Treiman et al., 2001) (see Section 1.3.1). Currently, these types of meteorites represent the only laboratory samples that we have to study of another planet in the Solar System, allowing us to examine the geochemical evolution of minerals on the planet including how water may have affected them.

Heavy elements in the Solar System exist mostly in a solid state. As on Earth, these solids are found as minerals – inorganic solids made up of units that produce a repeated (crystalline) structure. The mineralogy of planetary materials on the micron to the submicron scale is one of the key themes of this thesis. The properties of these

minerals can be described in terms of their chemical compositions, microstructures and the morphologies that they may coexist in. In this thesis, advanced micro-analytical techniques have been used in order to investigate the the mineralogical, elemental and oxidation state properties of cometary and martian samples.

1.1.1 Advances in Microanalysis

As cometary and martian samples are heterogeneous (i.e. composed of varying mineralogies and morphologies) at the micron scale the closer one can analyse a planetary material the more information that can be obtained from it. Microscopy usually involves optical and electron microscopy for physical (i.e. morphological), chemical and mineralogical interpretations. Such techniques typically enable the characterisation of material surfaces towards the micron scale (e.g. polished sections) and bulk unaltered states on larger scales (e.g. optical microscopy). A description of these techniques is found in Chapter 2.

Planetary materials (and any other natural or synthetic materials) can be characterised further by analysing them beyond the resolution limits of these conventional techniques in microscopy (see Chapter 2) or by determining their properties with other X-ray microanalysis techniques e.g. atomic valency information to understand oxidation and reduction (redox) mechanisms – Chapter 3. This can be achieved by selecting specific regions of interest and extracting them for transfer to other instruments for subsequent characterisation. This is an analytical challenge as the dimensions of typical analysis regions are of microns – sub microns in sizes. Some planetary materials can also be analytically too small for conventional microscopy techniques and thus, additional techniques are needed in the laboratory.

A brief description of the advanced microanalytical techniques applied in this thesis will follow with their current application to the field of meteoritics and planetary science. A description of the physical theory behind their application and methods are found in subsequent chapters.

1.1.1.1 Focused Ion Beam Techniques for the Microanalysis of Planetary Materials

Focused Ion Beams (FIBs) can be used for *in situ*/site specific (selected micron-submicron regions) characterisiation of planetary materials. Their use in both planetary and geological studies has been shown (e.g. Stroud et al., 2000; Zega et al., 2007; Graham et al., 2008; Lee et al., 2007; Lee et al., 2008; Lee, 2010). The FIB-Scanning

Electron Microscopy (SEM) extraction technique for Transmission Electron Microscopy (TEM) applied to planetary materials (See Chapter 2) allows for critically important *in situ* micron to submicron characterisation.

The research in this thesis implements the FIB technique in novel ways for the microanalysis of planetary materials. Firstly, it is used to extract soft hydrated phases in micron-sized veins in the nakhlite meteorites (introduced in Section 1.3.1.2) requiring changes to generic FIB extraction methods (Sections 2.9.1.4), for the eventual TEM analysis of phases within them (Section 4.2.4). They have not been characterized and comprehensively studied in this way before. The FIB-TEM technique has also been used on the *Stardust* mission Comet Wild2 samples (Section 5.2.3). This is the first FIB-TEM analysis applied to *Stardust* material in aerogel (introduced in Section 1.2.1.4). Finally, this technique has been briefly shown to be applicable for transfer to the synchrotron for X-ray absorption spectroscopy (Section 3.4.2).

1.1.1.2 Synchrotron Based X-ray Microfocus Spectroscopy of Planetary Materials

Synchrotrons provide a unique opportunity to analyse materials to the highest sensitivity. They can produce highly intense, focused X-rays for probing natural and synthetic materials (see Chapter 3). They have recently been used to characterise *Stardust* samples (a subject of this thesis) in terms of their elemental compositions, redox and mineralogical properties (e.g. Flynn et al., 2008; Westphal et al., 2009; Bridges et al., 2010). Different analytical techniques at synchrotron facilities have been used such as X-ray Fluorescence Spectroscopy (XRF) for elemental analysis and X-ray Absorption Near-Edge Structure (XANES) for redox and mineralogical determination. This thesis also uses these techniques for elemental and mineralogical characterisation of *Stardust* samples but also investigates the use of Extended X-ray Absorption Fine Structure (EXAFS) for a quantitative approach to mineralogical characterisation (Chapter 3 and Chapter 5) of *Stardust* material. These are the first reported EXAFS experiments performed on these planetary materials, where molecular information is determined in the form of bond lengths and co-ordination numbers.

1.2 The Planetary Materials Studied in this Thesis

The planetary materials studied in this thesis sample two very different bodies in the Solar System. They also represent very different analytical challenges. The first set

are cometary samples returned from the *Stardust* Mission. The second is a group of approximately eight martain meteorites (the nakhlites) that have generated much interest for several decades concerning the aqueous processes that may have occured on Mars. The nature of their parent bodies and the scientific motivation for their microanalysis are described below.

1.2.1 Comet 81P/Wild2 & The *Stardust* Mission

The first suite of planetary materials that have been analysed using the micro-analytical techniques previously described are samples of Comet 81P/Wild2 from the *Stardust* Mission.

1.2.1.1 Comets

Comets are the outermost planetesimals of the Solar System. They have been described as a mixture of ices, dust and rock (Whipple, 1950) and this interpretation still holds true for them. Earth-based remote observations have enabled thousands of cometary orbital elements in the Solar System to be catalogued (e.g. NASA's small body orbital element archive). They can have highly eccentric orbits and typically do not lie on the ecliptic plane where the Sun, the planets and the asteroid belt lie on (Weissman, 1999). Two main groups of comets can be found; Short Period (SP) and Long Period (LP) comets. LP comets have high eccentricities. They are commonly attributed to comets found in the spherical shell of the Solar System that lie approximately more than 5000 A.U. from the Sun (Stern, 2003). This region, known as the Oort Cloud is the most distant reservoir of planetary bodies in the Solar System that was first postulated to exist by Oort (1950). However, this is a traditonal view that generally holds for comets, and exceptions to Oort cloud objects being LP comets can arise, such as the famously known Comet 1P/Halley, that is an 'intermediate period Comet' with an orbital period of 75 to 76 yrs (Horner, 2003). Further subdivisions of comets have also been made based on the Tisserand parameter, a dimensionless parameter that measures the orbital motion of one body with respect to another (in this case comets with respect to their largest perturbing object – Jupiter) (Horner et al., 2003). SP comets are defined as having periods of less than 200 years. Most of them have periods between 5 – 20 yrs (Weissman and Campins, 1993). Broadly speaking, they are attributed to comets that would have formed between the orbit of Neptune and

the Oort cloud. A rich source of SPs is the disk of scattered objects within this plane – the Kuiper Belt, first described by Kuiper in 1951 (review in Kuiper, 1974). The Kuiper belt comets is a belt of comets in the ecliptic plane beyond the orbit of Neptune (Weissman, 1999).

The volatile composition of comets leads to dynamical effects when they interact with solar energy. The generic morphology of a comet does not represent its unaltered or 'dormant' state, but typically defines a 'comet.' An illustration of a comet is given Fig 1.1. Cometary nuclei are typically of the order of km's in size (e.g. Stern, 2003). The volatile ices, organics and dust components in the nucleus of a comet are sublimated at perihelion distances to the Sun. A comet is described as 'active' in this state and forms a 'dust tail' by these sublimation processes. The comet's coma, a halo of material derived from the comet nucleus, forms by ejecting gas that drags off dust exisiting in and around the nucleus (Pater and Lissauer, 2001). Interaction with the Solar wind and the bombardment of cosmic rays from the Sun can lead to the ionization of elements within cometary nuclei. They are expelled directly away from the Sun as a plasma that is in alignment with that of the Solar wind (Neugebauer, 1990). This is the 'ion tail' that is typically longer than the dust tail. The dust tail can extend to distances of 10^7 m with ion tails reaching approximately 10^8 m. A complex plasma also forms around the comet as a hydrogen envelope surrounding the comet (Pater and Lissauer, 2001). These features are orders of magnitude larger than the cometary nuclei themselves.
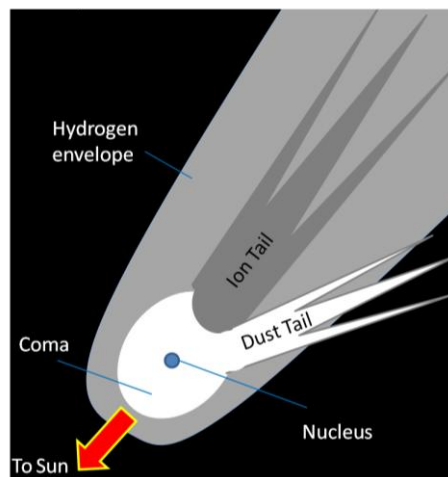
FIG 1.1: Cartoon illustrating the various components of a comet. The dust tail is the mixture of CHONS (Section 1.2.1.1), dust and ice sublimating from the cometary nucleus. The ion tail forms a distinctive tail that is expelled directly away from the Sun after ionization. The coma is the halo of nuclei constituents expelled from the cometary nucleus. The hydrogen envelope is a plasma-induced sheath around the comet.

1.2.1.2 Observations of Cometary Nuclei and Samples

Abundant in primary volatile components, comets are believed to be the most primitive objects in the Solar System. Usually km sized bodies, they have been interpreted as aggregates of materials from the Solar nebula that were not processed like the bodies from the hotter and denser inner Solar System. The composition of comets have been studied in various ways. Astronomical observations, *in-situ* measurements by spacecraft and analyses of indirect cometary fragments in the form of IDPs have enabled us to understand the make-up of cometary nuclei.

Spectroscopic measurements in the infrared region have also enabled compositional information to be determined. Various comets have been shown to contain crystalline and amorphous magnesium-rich silicates (Wooden, 2002). Labotaory analyses of interplanetary dust particles (IDPs) show that amorphous silicates can be found in form of GEMS (Glasses with Embedded Metal Sulphides), high temperature 'exotic' particles with most of them having abnormal oxygen isotopic composition, and are thus believed to be transported into the System from the ISM (Bradley and Dai, 2004). Most presolar grains are refractory oxides (e.g. Al_2O_3 corundum and spinel), solid carbon in the form of graphite and diamond or other ceramic like materials (e.g. Zinner, 1996). Presolar crystalline silicates such as forsterite have also been found in IDPs, although in much rarer abundances (Messenger et al. 2003).

Several cometary flybys have enabled detailed morphological information to be determined about some cometary nuclei. Spectrometers on board these spacecrafts have also provided additional compositional information. Upon Comet 1P/Halley's close approach with Earth in 1986, a suite of spacecraft were sent to study it. In 1986 it was visited by ESA's *Giotto* spacecraft, the Soviet *VEGA* 1 and 2, and the Japanese spacecraft, *Suisei* and *Sakagake* that took optical images and dust measurements. Fig 1.2a shows a reflected optical image of Comet Halley's nucleus. The ion mass spectrometers on the *Giotto* spacecraft and *VEGA* 1 identified 'CHON' (Carbon, Hydrogen, Oxygen and Nitrogen containing compounds) particles, and mixtures of CHON particles (e.g. Clark et al. 1987), amorphous silicates (e.g. Hanner, 1999), and ice (Pater and Lissauer, 2001) with silicate components (Balsiger et al. 1986; Lawler and Brownlee, 1992). The particles displayed a wide range of Mg to Fe ratios, and the silicates were suggested to be predominantly Mg, rather than Fe, dominant silicates (Jessberger et al., 1988). However, it was highlighted by Jessberger (1988) that detailed

chemical analyses of the grains were complicated by the complex impact - ionisation processes in the ion spectrometers on board the spacecrafts. NASA's *Deep Space* Mission flew past comet 19P/Borrelly in 2001 (Fig 1b), showing the unusual dog bone shape of the comet nucleus (Soderblom et al., 2002). In 2005 NASA's *Deep Impact* mission reached Comet 9P/Tempel 1 (Fig 1.2c). An impactor on the comet's nucleus liberated around 10^4 tons of material in the hope that the pristine layers beneath the altered surface would reveal its composition. The results of the mission showed that strong, broad silicate features were dominated by signatures of amorphous pyroxene, amorphous olivine, and magnesium-rich crystalline olivine that had developed by 1 hour after impact (Harker, 2005). Thus it is becoming clear from astronomical observations that comets contain a high proportion of material that formed at high temperature. However, different cometary nuclei can show distinctions by containg low temperature aqueous based mineral assemblages. The Spitzer telescope also obtained infra-red spectra of the the ejecta materials from the *Deep Impact* Mission and indentified ~8% of silicates to be in the form of phyllosilicates more specifically clays, and also Fe-Mg carbonates (Lisse et al., 2006). Thus, remarkably it may be that comets have preserved evidence for liquid water.

IDPs have been collected in the Earth's stratosphere by sampling missions (Reitmeijer, 1988). Chondritic Porous IDPs have a primitive makeup that includes hydrous phyllosilicates and carbonaceous material (e.g. Nier & Shlutter, 1993). In IDPs, chondritic means a composition of (Mg, Al, Si, S, Ca, Ti, Cr, Mn, Fe and Ni) that has abundances less than twice the CI chondrite composition (Reitmiejer, 1998). CI chondrites have a bulk composition of the Sun's photosphere for non gaseous elements (Anders and Grevesse, 1988) and are thus thought to be the most primitive meteorites (least processed). The abundances of sub micron Mg silicates and amorphous Mg silicates in CP IDPs are broadly consistent with the *in situ* spectral analyses and remote observations of comets (Hanner, 1999). In particular, anhydrous CP IDPs are thought to be cometary in origin because "a) they are organically heterogeneous on the submicron scale; b) have very high presolar grain abundances; c) are of relatively high atmospheric entrance velocities, implying that they were released from comets on more eccentric orbits than asteroidal bodies; d) they possess anhydrous silicate mineral grains; f) they are unequilibrated aggregates, i.e., aggregates of mineral species that would not exist as adjacent subgrains if heating had occurred after the grains had aggregated; and g) their refractory mineral subgrains include some of the most primitive

materials known in the solar nebula, including GEMS subgrains (Mg-Fe amorphous silicates called Glasses with Embedded Metal and Sulphides), submicron domains of microcrystalline minerals of similar composition called 'equilibrated aggregates,' single crystal FeS, and single crystal silicate minerals with Mg-contents higher than any other solar nebula materials." (from Wooden et al. 2002). Fig 1.2d provides an SEM micrograph of an IDP particle. These suggested cometary precursors have been the only samples of comets available for laboratory studies, until samples of the Comet Wild2 coma were returned by the *Stardust* Mission.
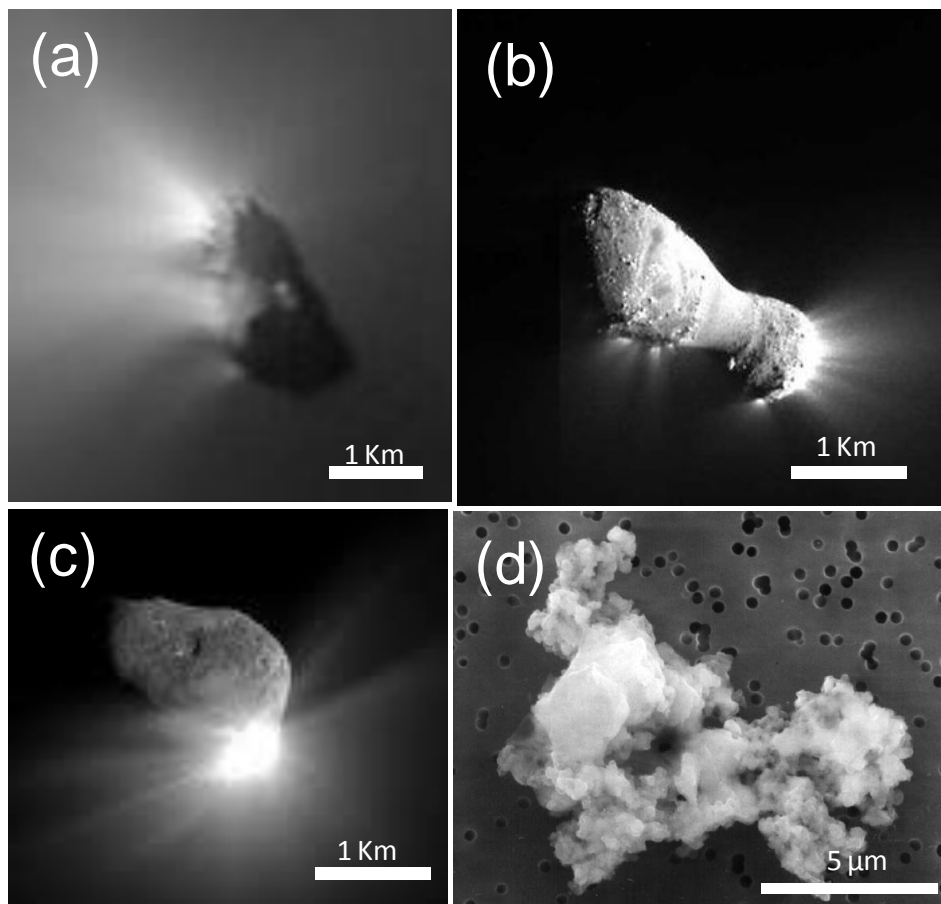
FIG 1.2: (a) Image of Comet Halley nucleus from the *Gioto* Mission. (b) Image of the nucleus of Comet 19P/Comet Borrelly from the *Deep Space* Mission. (c) Comet 9P /Temple 1. (d) An IDP collected in the stratosphere with a U2 aircraft. The IDP is composed of glass, carbon and silicate mineral grains. *Images from www.nasa.gov.*

1.2.1.3 Comet 81P/Wild2

Comet Wild2 is one of the main subjects of this thesis. Comet Wild2 is a Jupiter Family Comet (JFC). This means that it was drawn into the inner Solar System due to the gravitational pull of Jupiter. It is believed to have originated from the Kuiper Belt and was shifted into the inner Solar system in the late 1970s. Thus, the extent of alteration of the comet by solar activity is minimal. The *Stardust* spacecraft (See Section 1.2.1.4) flew by Comet/81PWild2 in 2004 and imaged the cometary nucleus. A review of the results from the flyby is provided by Brownlee et al. (2004) and is summarized here. Comet Wild2 was found to be oblate (Fig 1.3a), unlike the prolate shapes of other comet nuclei (where the polar axis is greater than the equatorial diameter) such as Halley and Borrelly (Fig. 1.2a,b). The nucleus is a rounded body and appromately 4.5 km across. Being rounded, it is suggested not to have been a fragment of a larger body (Brownlee 2004). Like other primitive solar system bodies, Comet Wild2 is dark, most likely due to the carbonaceous nature of the comet. It contains surface depressions – circular pit depressions ('Rahe' in Fig 1.3) that contain halos of excavated material around them (Brownlee, 2004). Flat-floor features are visible that have steep sides of vertical inclination (Left Foot in Fig 1.3). Features such as 'Rahe' are thought to be impact features on the cometary surface. Comet Wild2 also has 'mesas' that were believed to be remnants of ablation where gas emission occurs from ablating cliff faces that retreat with time (Brownlee et al., 2004).
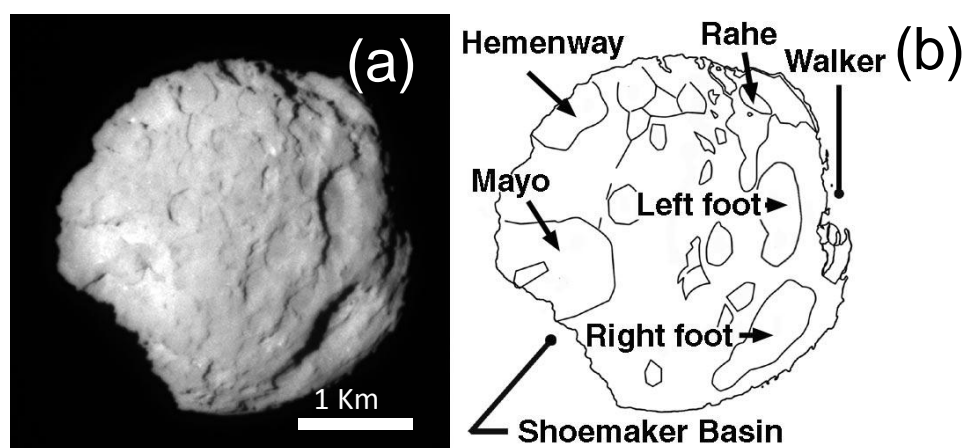
FIG 1.3: (a) Optical Image of Comet Wild2 taken at lose encounter by the *Stardust* spacecraft in 2004 from 230 km distance. (b) The named regions of the comet nucleus with key surface depressions of the rounded comet morphology. *Images from Brownlee et al. (2004).*

1.2.1.4 The *Stardust* Mission

The *Stardust* Mission was the first sample return mission to a comet (Brownlee et al., 2003). It also returned dust particles from interstellar space (Brownlee et al., 2003). Launched in 1999, the *Stardust* spacecraft encountered the coma of Comet Wild2 1.9 A. U. from the Sun, collected material from it and then returned the samples back to Earth. The *Stardust* probe flew through the cometary coma within approximately 230 km of the nucleus (Brownlee et al., 2006). The craft opened its aerogel collector and particles were captured as they impacted the collector surface with a closing velocity of approximately 6.1 kms^{-1} (Brownlee et al., 2003). On it's way to Comet Wild2 its collector tray also opened up to face the Grün flux of interstellar particles (Grün, 1994), a model describing the isotropic distribution and velocities of micrometeoroids in interstellar space. The collected samples were successfully returned to Earth on 15 January 2006.
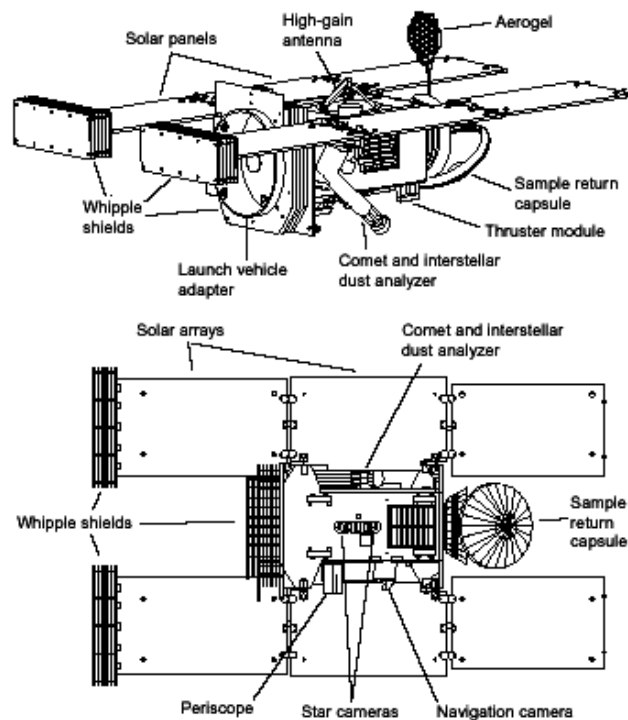
FIG 1.4: Schematic diagram of the *Stardust* Spacecraft. Throughout the encounter other instruments imaged the nucleus, measured the dust flux and size distribution and conducted *in situ* dust compositional analyses (Brownlee et al., 1996). These instruments indicated that the spacecraft was successful in collecting more than 10,000 particles ranging in size from 1 to 300 μm (Brownlee et al., 2004). Burchell et al. (2008) estimated that approximately 1200 particles larger than μm's had struck the cometary collector itself (See section 1.2.1.5).
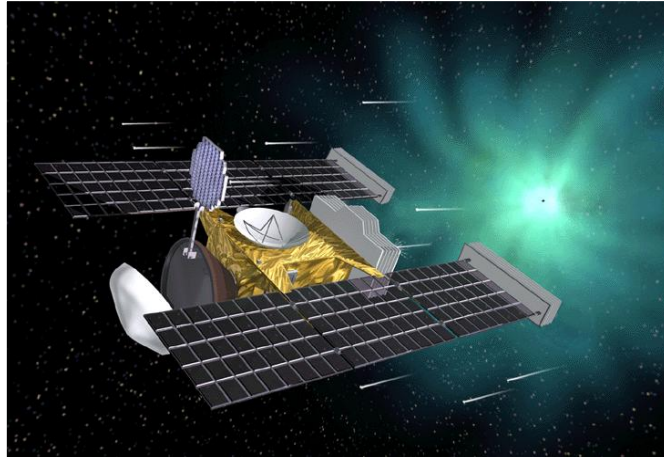
FIG 1.5: Artist Impression of the *Stardust* Space craft encountering the coma of Comet Wild2. *Image Courtesy of www.nasa.gov.*

1.2.1.5 Grain Capture & Cometary Tracks

The colliding dust components with impact speeds of 6 kms^{-1} required a collecting medium that would induce minimal interaction with the bombarding cometary grains. Aerogel was used as this collecting medium. Aerogel is a form of silica. It has a very low density of ~2 mgcm^{-3}. Aerogel tiles with 4 cm thickness were manufactured and configured into a multiple array of tiles for capturing the dust fragments of Comet Wild2 and interstellar particles from the ISM (Fig 1.6). A continuous graded density from 5 mg ml/1 at the surface to 50 mg ml/1 at the base was used to provide gradual deceleration of impacting particles (Tsou et al., 2003). The impacting grains in aerogel created conical-shaped cavities called tracks typically mm's in length. Along the walls of the tracks, ablated material is heterogeneously distributed and a grain or grains are found in terminal position(s) (See Chapter 5). Grains found at the terminal positions are thus, the least altered particles during the track forming process and are the most 'preserved' cometary particles. Since the return of the *Stardust* tracks, three main track types have been classified based on their morphologies: Type A - relatively slender tracks which taper to an end where a "terminal" grain is found, which may however only be an unknown fraction of the originally incident particle, Type B - tracks with an initially bulbous cavity lined with fragments of the impactor and beneath which one or several slender tracks emerge which again often contain terminal grains and Type C - tracks with just a bulbous cavity lined with fragments of the initial particle (Hörz et al., 2006; Burchell et al., 2008).

Cometary tracks have been identified using optical microscopy at NASA-JSC and UC Berkeley. They have then been dissected using precision cutting techniques described in Wesphal et al. (2002). From there, samples have been prepared in different ways for a wide range of analytical techniques. Organic, elemental, chemical, mineralogical and isotopic analyses have all been performed on *Stardust* samples.
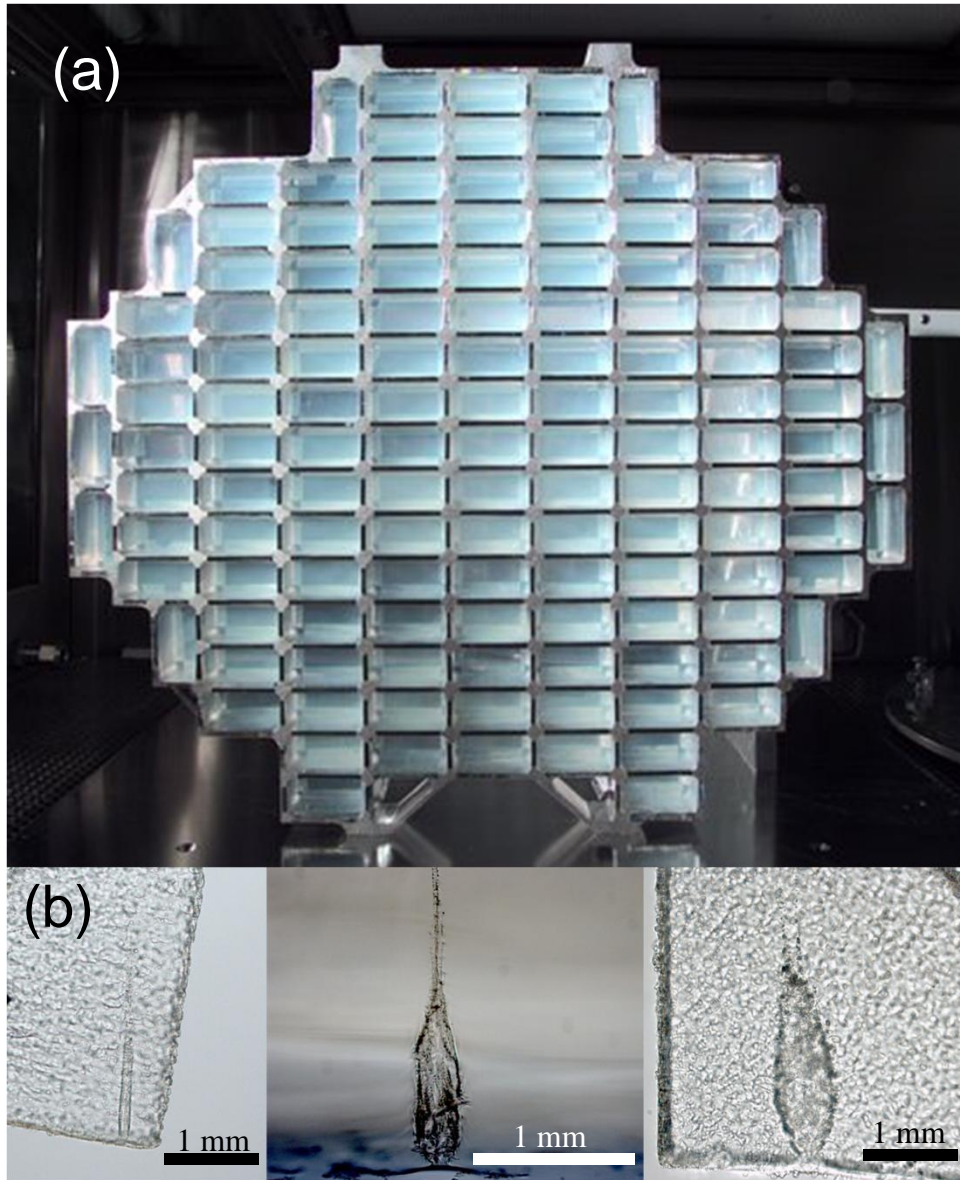
FIG 1.6: (a) Image of the *Stardust* collector tray. The tiles contain the 4 cm wide blocks of aerogel. (b) Optical images of different track types A, B and C (left to right) from track#157, track #159 and track #168 respectively.
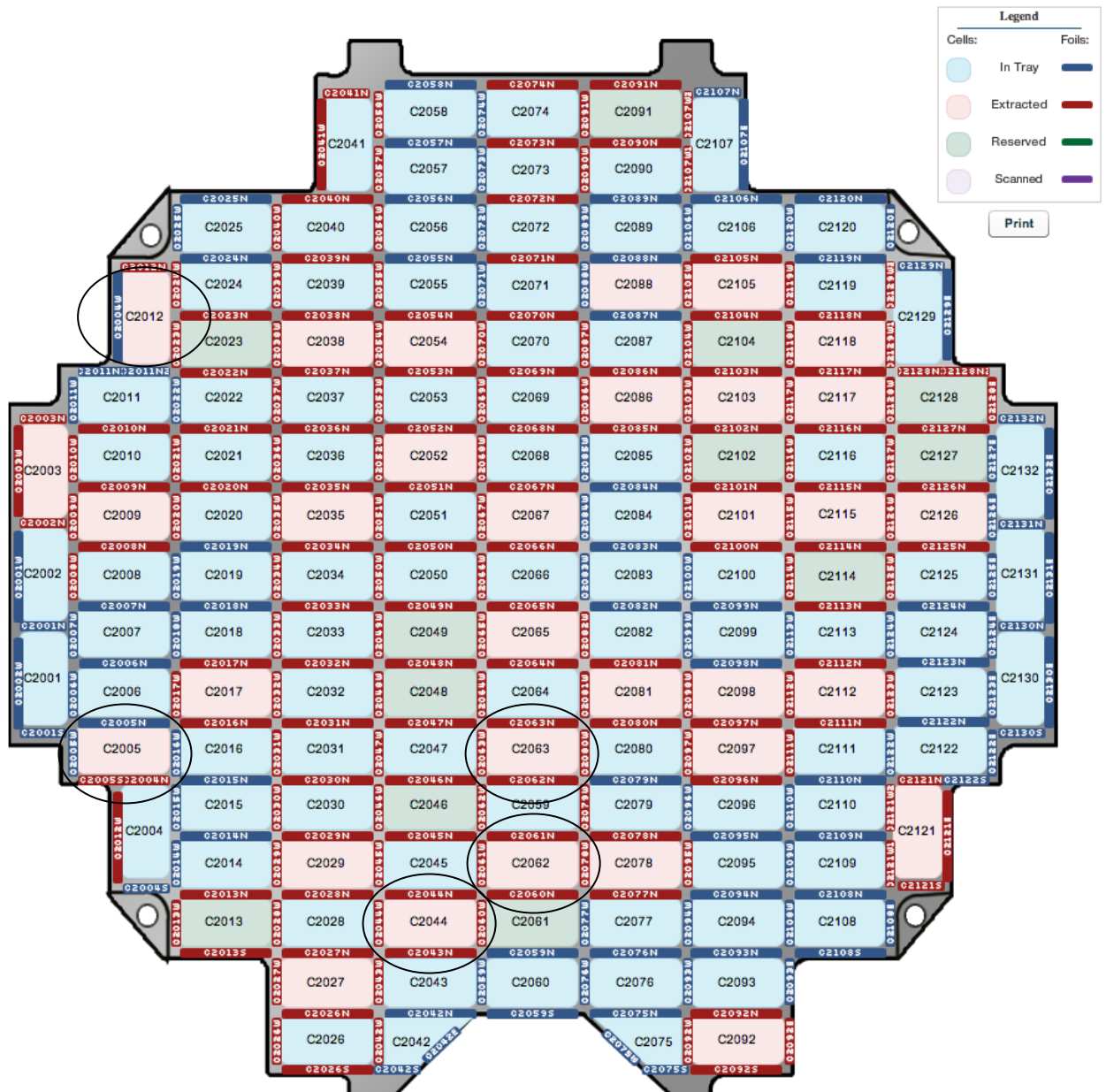
FIG 1.7: Schematic of the aerogel collector tray. The tiles are coded with C followed by the tile number. Tiles that have been extracted (red) were performed at UC Berkeley and NASA-JSC using the methods described by Westphal et al., 2002. The tracks studied in this thesis are from tiles and circled above. The nomenclature for *Stardust* samples begin with the tile number, followed by the track number, followed by the keystone number (a usually triangular-shaped section cut from a track) (See Chapter 5 and 6), followed by section number and finally the grid number as most samples are prepared by microtorme cutting and then placing on copper grids for TEM (see Chapter 6). A list of the samples studied in this thesis can be found in APPENDIX E.

1.2.1.1 Comet 81P/Wild2 and Preliminary Examination

The results of the Preliminary Examination (PE) of Comet Wild2 upon the return of the samples were sumarised by Zolensky et al. (2006) and Brownlee et al (2006). They described terminal particles from the tracks to be an assemblage of ferromagnesian silicates (particularly forsterite and enstatite – $MgSiO_3$), Fe-Ni sulphides and Fe-Ni metal, mainly in nanometre-size grains with relatively few larger, micron-size grains. Al foils that held the aerogel cells in place also contain impact craters filled with cometary material (Hörz et al., 2006; Kearsley et al., 2008). They have shown similar assemblages consisting mainly of Mg-rich silicates and abundant Fe-Ni sulphides in micron-size crater residues.

The presence of refractory material and possibly of grains reminiscent of individual chondrules has been taken to indicate mixing between material formed in the inner Solar System and less refractory material that constitutes the bulk of Comet Wild2 (Brownlee et al., 2006; Nakamura et al., 2008). However, hydrous phases such as serpentine or phases precipitated from hydrothermal fluids are notably absent from the reported Comet Wild2 inventory and this is unexpected because of the *Deep Impact* Mission results (e.g. Lisse et al., 2004) and that IDPs carry widespread evidence for hydrothermal action (e.g. Reitmiejer, 1998).

Ishii et al. (2008) reviewed the mineralogical work carried out on Comet Wild2 to date and suggested that there were stronger similarities to asteroidal meteorites than to IDPs. However, Westphal et al. (2009) have shown that the Fe oxidation state of Comet Wild2 is unique to all other primitive chondrite groups. Oligiore et al. (2010) have also demonstrated a unique Fe-oxidation state of CP-IDPs that potentially lies in a field closer to Comet Wild2 than the chondrite groups. Joswiak et al. (2008) have shown the presence of Na-rich pyroxenes in 15 tracks, also with compositions which are uncommon in known unequilibrated chondrites. GEMS (Glass with Embedded Metal and Sulphide), components that are characteristic of IDPs have also not been firmly identified or distinguished from molten aerogel (Zolensky et al., 2007).

Chondrules are mm-sized melt droplets that are a major constituent of most chondrite stony meteorites. They are thought to have formed at high temperatures within the inner parts of the Solar System and accreted to form planetesimals and eventually the asteroids and larger planets (Hutchison, 2004). Higher temperature inclusions within chondrites such as Calcium Aluminium Inclusions (CAIs) were the first things to crystallise from the cooling Solar nebula (temperatures from ~1500 –

2000 $^{\circ}$C) – Hutchison (2004) and chondrules formed after CAIs (Brearley and Jones, 1998). Short lived radionuclides (e.g. ^{26}Al) suggest they formed ~2 M.a. after CAI (e.g. Hevey. and Sanders, 2006). It is not clear at which stage cometary nuclei formed. However, a study of an anorthite ($CaAl_2Si_2O_8$) terminal particle provided chronological information from *Stardust* samples by using ^{26}Mg abundances to infer the abundances of its parent isotope ^{26}Al and to compare with the earliest CAIs (Matzel et al., 2010). Matzel et al. showed that terminal particle 'Coki' would have formed at least 1.7 million years after the formation of the oldest CAIs. Thus, a question arises as to how these high temperature crystalline silicates found in Comet Wild2 and other cometary nuclei (e.g. Hanner, 1999) form and what the transport mechanisms were that brought them to comet-forming regions if they formed within the inner Solar System (Wooden, 2002). 'Micro' CAI-like terminal particles have been found, an example being a terminal particle named 'Inti'. CAIs and Al-rich chondrules can contain refractory Ca-Al clinopyroxene like that of a terminal particle studied in Chapter 6. Can these particles add new insights into the nature of inner Solar System materials that were transported to comet forming regions?

1.2.1.1 Capture Heating and the Composition of Comet Wild2

The aim of this study of *Stardust* samples is initially to add to our understanding of the mineralogy of Comet 81P/Wild2. This is shown by the characterisation of samples in their aerogel states using synchrotron-based microfocus X-ray Spectroscopy (Chapter 5) and of conventional thin sections for TEM (Chapter 6). From this, it is hoped that a more accurate understanding of the mixing processes of dust and/or larger planetesimals from the inner Solar System that eventually led to the composition of Wild2 is obtained.

Incident cometary particles may break apart during capture and also undergo heating as they traverse through aerogel for reasons described in Section 1.2.1.5 (see also Chapter 5). Hence, any cometary dust grain along an aerogel track should be considered as a fragment of the originally incident dust grain (which generated that aerogel track) and which may have undergone shock and/or heat processing during capture. These mechanisms of flash heating (Burchell et al. 2008) in aerogel have resulted in a host of effects that have challenged our understanding of Comet Wild2's composition prior to capture. Amongst the suite of *Stardust* samples analysed in this thesis are track sections in their original aerogel state, where characterisation close to

track entrances could help us to distinguish between capture-related and cometary material. Particular emphasis is given to the presence of iron oxides that could be the first evidence of hydrothermal alteration on the comet but some grains could be tracers of capture heating (Chapter 5). Distinguishing between indigenous cometary material and capture-related material is vital to understand the composition of Comet Wild2.

The least altered grains are at terminal positions of the tracks. Their mineralogy may provide the best clues to the overall mineralogy of Wild2 and can aid in understanding the processes involved in the accretion of comets. A study of a refractory, Ca-Al rich terminal grain is provided in Chapter 6. It shows unique characteristics compared to the currently known *Stardust* mineral assemblages.

1.3.1 Martian SNC Meteorites & The Nakhlites

1.3.1.1 The SNCs

Amongst the thousands of meteorites that have been catalogued, there are around 50 meteorites that belong to a unique class – the SNC meteorites. They are a group of achondrites, that is stony meteorites lacking chondrules and that are igneous rocks. Martian ones are further subgrouped into three main classes, named after three meteorites – Shergotty, Nakhla and Chassigny (SNC). They have a distinct oxygen isotopic compositions from all other chondrite and achondrite classes, indicating an independent mixing reservoir for their formation (e.g. Romenak et al. 1998). Most of the SNCs are generally accepted to be much younger than chondrites (e.g. the nakhlites 1.3 G.a. - Park et al. (2009) by measuring ^{39}Ar - ^{40}Ar radioisotopes and the shergottites at least 180 M.a. (Jones, 1986) from Rb-Sr and U-Th-Pb chonometers. The oldest is Alan Hills (ALH) 840011 shown to have crystallised at the very early stages of it's parent body – Mars (4.1 G.a. using Lu-Hf measurements – Lapen et al. (2010)). Thus, they are thought to have been derived from a much larger planetary body with an igneous basaltic origin (Bridges and Warren, 2006). The most likely source that has been geologically active over a long period of time is Mars. One of the most compelling indicators, however, of a martian origin is their noble gas compositions. Some of the SNCs contain trapped noble gases (Xe, Kr, Ar, N_2) in impact glass that are a very close match to the martian atmosphere when measured by the mass spectrometer on the *Viking* landers (Bogard et al., 1984).

1.3.1.2 The Nakhlites

The nakhlites group of the SNCs were named after the meteorite, Nakhla that was seen to fall in Egypt, 1911. Currently there are eight other nakhlites that are petrologically very similar to Nakhla and thus classified in that group (see Chapter 4). They all contain very similar cosmic ray exposure ages and are thus assumed to have been ejected from Mars in the same event 11 Ma (McSween and Treiman, 1998). They lack evidence of intense shock compared to the other martian meteorites such as the shergottites (Nyquist et al., 2001). In addition to this, the nakhlites are linked by the presence of similar secondary aqueous alteration phases, which is a focus of this thesis.

Petrological studies of the nakhlites have shown that they are olivine-clinopyroxenites and all represent different parts of an individual lithologic unit on Mars (e.g. Mikouchi et al. 2006; Bridges and Warren 2006; Lentz et al, 1999). Thus, they are likely to be the only currently recognised suite of meteorites that represent a stratigraphy or depth profile on the martian surface or any extraterrestrial parent body. The nakhlite petrologies have drawn much interest about their magmatic origins by comparison with potential terrestrial analogues (Fritz et al. 2005; Lentz, 1999) to constrain their formation in a shallow intrusive or thick lava flow. If they do indeed represent a single litholigic unit on Mars, then they are also unique in that they sample a martian aqueous history along this depth profile (Bridges and Grady, 2000; Bridges et al. 2001). The nakhlites contain preterrestrial secondary mineral assemblages. They have been shown to be truncated by their fusion crusts in the Nakhla and Lafayette nakhlites (Gooding et al. 1991; Treiman 1993) and have K-Ar formation ages pre-dating the arrival of the Nakhla meteorite (Swindle 2002). They have been described to contain 'rust' like material loosely termed as 'iddingsite' – a secondary alteration product collectively describing a mixture of clays, carbonates and soluble salts (Bridges et al. 2001; Treiman, 2005). They have also raised increased astrobiological interest in the past by containing organics (Sephton, 2002) and, more controversially, textures that may be indicative of biofilms within the meteorites (Gibson, 1993; Gibson, 2010).

Water (H_2O) is the fundamental driving force for life and habitability on Earth and thus, would be the first phase to analyse in the search for prebiotic chemical or biotic evidence for life. With exception to the minutely hydrated atmosphere and seasonal ice caps, no evidence of (H_2O) or water has yet to be found on Mars. The surface is, however, rich in mineralogy derived by aqueos activity in the martian past.

FIG 1.8: Photograph of a fragment of the Nakhla meteorite. The green regions are pyroxene minerals. The reddish patches are olivine grains containing veins that are the subject of Chapter 4. The dark glassy area is the fusion crust formed during entry though the Earth's atmosphere. See Chapter 4 for an overview of the mineralogy and petrology of the nakhlites. Image courtesy of *Natural History Museum (NHM).*

A summary of observations with the motivation of understanding Mars' wet past is provided.

3.1.2 Water on Mars and the Context of the Nakhlites

The combination of orbiters, rovers and meteorites has provided clear evidence for the action of water on the Martian surface. Geological networks imaged on the martian surface mimic the geological activity on Earth and are believed to provide evidence of running water that shaped terrains (e.g. Carr, 1983; Baker, 2001) Evidence for water on Mars has been strengthened immensely by the current Mars orbiters – Mars Express and Mars Reconnaissance Orbiter (MRO). Their onboard imagers and infrared spectrometers have also detected mineral deposits that formed by aqueous alteration on the martian surface. Different areas of Mars have been found to contain these minerals such as carbonates, sulphates and phyllosilicates, but their occurrence seems to be rare compared to the landscape and bedrock. Thus, questions regarding the duration of a wet Mars and the extent of water on the Martian surface are still yet to be fully resolved. More recently, however, models have been proposed to account for this such as the potential instability of carbonate precipitation at lower atmospheric partial pressures in a previously wet Mars (Chevrier et al 2007). It has also been suggested that carbonates might be hidden by burial and/or remobilization by episodic changes in temperature, pH

and water volumes (Harvey, 2010). The presence of dust on the martian surface also hinders mineral identification by near IR spectroscopy.

Silicas and amorphous hydrated silicates have been identified by the Compact Reconnaissance Imaging Spectrometer for Mars (CRISM) and the Observatoire pour la Mineralogie, l'Eau, les Glaces et l'Activité (OMEGA) instrument observations (Mustard et al., 2008). Carbonates coupled with the presence of phyllosilicates have recently been discovered by orbiter observations of Noachian (surfaces of Mars between 4.5 and ~3.7 G.a.) or Hesperian terrains (3.7 to ~3.0 G.a.) (e.g. Mustard et al. 2008; Poulet et al., 2005; Bibring et al., 2005). The phyllosilicates that have been recorded in the walls, ejecta and central peaks of the ancient highlands also show a strong association with more localised impact-induced hydrothermal activity (Mustard et al., 2008).

Detection of similar mineral assemblages *in situ* on the martian surface have helped establish the nature of Mars' aqueous history. Weathered basaltic rock and salt components of soil with the enrichments of volatile elements such as S, Cl, Na and K were discovered by the *Viking* landers in 1976, followed by Sojourner of the *Pathfinder* Mission in 1997. They may have been the result of aeolian remobilisation, but have also been shown to have formed by fluids supplied to the surface by hydrothermal processes related to impact craters and volcanism (Newsom et al., 1999). The results of the most recent Mars Exploration Rovers (MER), *Spirit* and *Opportunity* rovers (2004) have probably provided the most substanial evidence for a martian aqueous history. They landed on opposite sides of Mars relatively near the equatorial plane during January 2004. *Opportunity* at Meridiani Planum discovered layered sedimentary rock sequences at the Eagle and Endurance craters that contained salts believed to have formed from precipitation of briny fluid (Soderblom et al., 2004). Minerals indentified include jarosite $KFe^{3+}_3(OH)_6(SO_4)_2$, and hematite (Fe_2O_3) – Klingelhofer et al. (2004). Hematite was found in the form of spherules coined as 'blueberries.' Carbonate rich outcrops have also been recently discovered by the *Spirit* rover in the Gusev crater using the onboard Alpha Particle X-ray Spectrometer (APXS) for elemental abundances, and the Mossbauer Spectrometer for mineral identification and their abundances (Morris et al., 2010). The Mg-Fe carbonate was found to be the same as the average composition of carbonate globules in the martian meteorite AH84001. The APXS also found high abundances of Br (Gellert et al. 2004) highlighting the Gusev crater's aqueous past proposed to have been driven by volcanic hydrothermal alteration in the Noachian period (Morris et al 2010). Hydrated silicates, more specifically

montmorollinite – like phases have also been discovered in the Columbia Hills outcrop of the Gusev crater (Clark et al., 2007), indicating a diverse range of secondary minerals assemblages that are quite similar to those in the nakhlites (see Chapter 4).

Thus far, limited analyses of these secondary veining found in the nakhlites have enabled their nature to be resolved on the sub micron scale and it is hoped that the techniques introduced in Section 1.1.1.1 can provide a more detailed and accurate mineralogical description. An aim in this thesis is to document in more detail how the mineralogy of the nakhlite secondary mineral assemblages within the olivine fractures and mesostasis varies. It will help towards further constraining the nature and origin of hydrothermal fluids on Mars.

1.3 Thesis Outline

This thesis initially describes the theory and methods for the microanalysis of the planetary materials described above (Chapter 2 and Chapter 3). These techniques have been used to investigate and analyse the veining in the nakhlites for a comprehensive FIB-TEM study of the secondary alteration assemblages within them (Chapter 4), and of submicron Fe-oxide grains from the *Stardust* mission (Chapter 5). It also briefly investigates the potential use of FIB preparation for micro-specific *in situ* synchrotron-based X-ray microfocus spectroscopy at *Diamond's* Beamline I-18 (Chapter 3). An in depth study of iron oxides and other minerals in *Stardust* by XANES and EXAFS is provided (Chapter 5) addressing the need to distinguish between capture-related and cometary material. Fianlly, a TEM study of a unique terminal grain from the current *Stardust* inventory in track #154 (Chapter 6) is provided. Conclusions drawn from the microanalysis of these planetary materials are drawn together in Chapter 7 with an evaluation of these studies.

Chapter 2
Methodology I: Theory and Application of Electron Microscopy in the Microanalysis of Planetary Materials

2.1 Introduction

The microanalysis of extra terrestrial materials from meteorites to IDPs, or other materials from sample return missions can provide a wealth of information about the chemical, physical and potentially biological processes associated with the evolution of our Solar System. The use of SEMs, TEMs and Electron Probe Micro Analysers (EPMAs) are well established techniques for the analysis of planetary materials. Spatial resolutions at near atomic scale can be achieved. TEM electron diffraction allows minerals structures to be identified and lattice parameters to be determined. EPMA can routinely detect elemental concentrations down to approximately 0.01 wt%. Meteorites and IDPs can contain submicron-sized grains or inclusions that can only be resolved at the electron scale of imaging (microns to nms). Furthermore, Electron Microscopy (EM) also has the advantage of being non or only partially destructive, and allows a rapid accumulation of data.

In this chapter, the general theory of SEM, TEM, Energy Dispersive Spectroscopy (EDX) and Wavelength Dispersive Spectroscopy (WDS) are described with their associated instruments. Emphasis is given to the preparation of TEM samples using the FIB technique, and TEM calibration for imaging, diffraction and quantitative EDX (also known as Analytical Electron Microscopy AEM) as the micro-analytical research recorded in this thesis has used these methods.

2.2 Scanning Electron Microscopy

SEMs generate digitised images by scanning electrons across a sample (Hillier and Baker, 1944). They require an evacuated environment to avoid the ionisation of air and charging artefacts. This applies to all electron microscopes (EMs). They are usually evacuated with pressures generally ranging from 10^{-4} - 10^{-5} mbar. SEMs usually operate with accelerating voltages ranging from 1-30 kV. A bulk sample and an

electron beam can interact with one another in two fundamental ways. Firstly, an incident electron beam can liberate Secondary Electrons (SEs) existing in the outer orbitals of the atoms in the sample. The low mean free path of electrons (nms) means that they are liberated at the top of the interaction volume of any surface. These secondary electrons can be collected and then be displayed in the form of an image or digital 'micrograph'. A voltage grid can collect the low energy SEs and detect them with a scintillator. At each point of the raster, the light from the scintillator detector is then converted into an electronic signal using a photomultiplier tube and signal processing electronics (Goldstein and Newbury, 2003). SEs are particularly useful for showing textural information from a sample's surface, where surface irregularities can efficiently liberate more SEs towards a detector. They can also be generated by other incident particles such as the FIB (Section 2.9.1).

An incident beam of electrons can also interact by elastic processes. They can be deflected back via coulomb repulsion due to the electrons in the specimen and are thus surface sensitive. These are known as Back Scattered Electrons (BSE). A BSE detector placed perpendicular to the sample will detect a number of BSEs in a material proportional to the Z number(s) of the element(s) in question. BSE imaging can therefore, provide relative compositional information about a specimen.
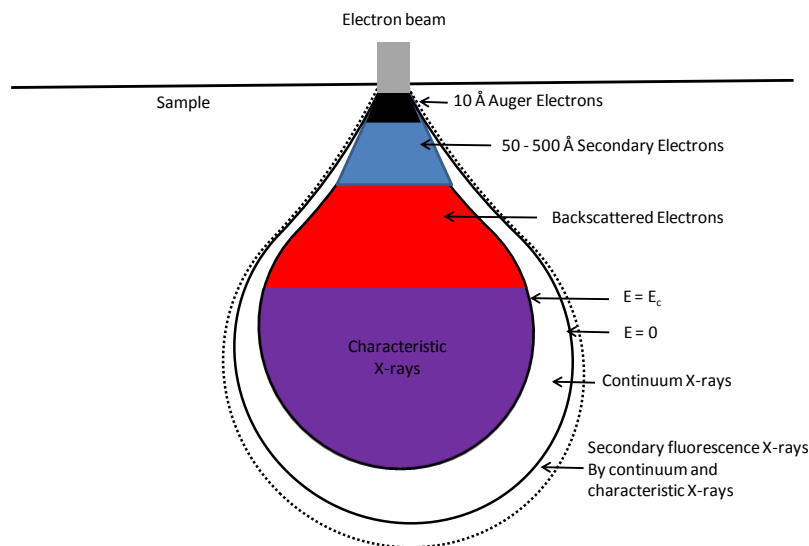
FIG 2.1: Interaction of electrons and a sample. The electrons generate a 'teardrop' interaction volume with its depth and width dependent on the incident energy, Z number and density of the material. The secondary electrons are generated near the top of the interaction volume, backscattered electrons are also generated from deeper in the interaction volume. Other types of radiation such as Auger electrons and characteristic X-rays are used for chemical analysis of a specimen (Section 2.7). Such interaction volumes can be found in bulk samples (micron sizes) in SEM and thin foils (10-100 nm) and TEM

An SEM sample can be a rough specimen but is preferably polished for X-ray analysis, minimising any secondary excitation processes that may occurr. Geological and meteoritical samples are often prepared as thin sections – a thin chip of the material mounted on a glass slide and polished down to approximately 30 μm so that they can also be used for polarised light microscopy. Alternatively they are prepared as polished blocks mounted in resin. In order to avoid the build up of charge on the sample, leading to poor imaging and analysis, the electron beam must be earthed through both the stage and sample. SEMs, therefore work best with conductive samples. Thin sections of meteorites are usually coated with 5-20 nm of conductive material (e.g. carbon or gold). Other attachments to SEMs such as a FIB used for TEM sample preparation (Section 2.9.1) sometimes require additional measures to avoid charging, especially for non conductive planetary samples. The FIB that uses incident Ga^+ ions on a sample (Section 2.9.1) are scattered to a lesser extent than electrons, resulting in much higher fluxes and therefore orders of magnitude more SEs from a sample, improving image signals but also inducing more charge build-up.
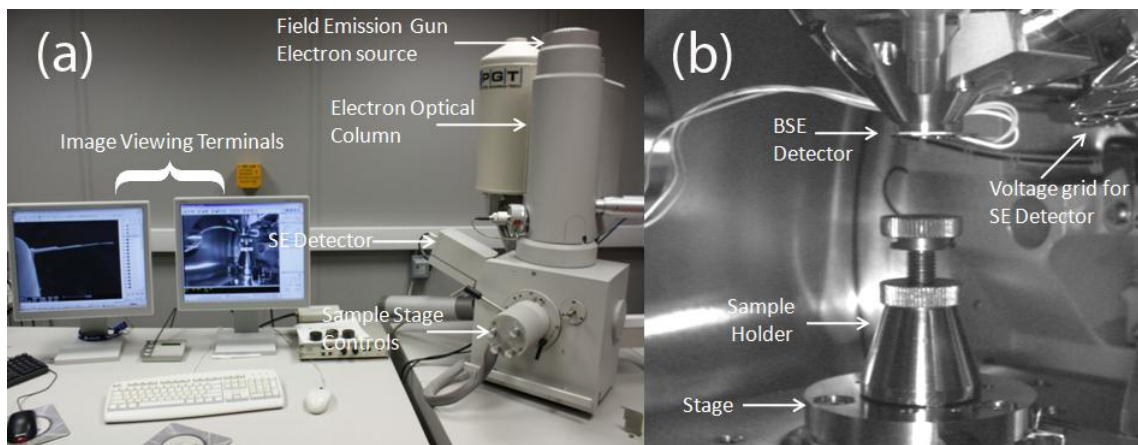
FIG 2.2: (a) The FEI Sirion FEG-SEM used at the Advanced Microscopy Centre (AMC), University of Leicester. (b) Inside the sample chamber. The Sirion's sample chamber is approximately 50 cm × 50 cm × 50 cm.

2.2.1 Scanning Electron Microscopes Versus Optical Microscopes

An optical microscope's (OM) spatial resolution is ultimately limited by the Rayleigh Criterion:

$$\sin \theta = 1.22 \frac{\lambda}{D} \qquad (2.1)$$

Where θ is the angular resolution, λ is the wavelength of the optical light and D is the diameter of the refractive focusing lens. By *Equation (2.1)*, an OM using a high resolution lens such as an oil immersion lens and blue light will have a spatial resolution of approximately 200 nm. SEMs on the other hand have superior resolving power compared to OMs. In an SEM, this is mostly due to an electron beam's small spot size (nm). High spatial resolutions are also complemented by a larger Depth of Field (DOF) given by *Equation (2.2)*:

$$ DOF = \frac{\left(\dfrac{d_1}{M} - d_2\right)}{\alpha} \qquad (2.2) $$

Where d_1 is the required resolving power, d_2 is the electron spot size, M is the required magnification and α is the convergence angle of the beam. The increased DOF is due to the smaller convergence angles and probe sizes of the electron beam in an SEM. This enables a greater variation in depth of a specimen to be examined in focus.

2.3 Transmission Electron Microscopy

The optical design of the TEM is similar to that of an OM. In an OM, a sample is illuminated with a light source, the light from which is focused through a refractive objective lens and then viewed with an eyepiece. The same principle is applied to the TEM. However, instead of visible light a beam of electrons is used as the illuminating source. They are focused on an ultra thin sample (<100 nm) with condenser optics (Fig 2.4). The electrons are transmitted through the thin sample and then projected on a detector after being focused with a set of objective optics (Fig 2.4). The Rayleigh limit (*Equation 2.1*) found in an optical lens is negligible in a TEM with the use of electrons and electromagnetic lenses to focus the electron beam. In a TEM, the spatial resolution r_{min} is governed by the spherical aberration of the objective lens and the wavelength of the electron source for imaging, *Equation (2.3)*:

$$ r_{min} \approx 0.91\left(c_s \lambda^3\right)^{1/4} \qquad (2.3) $$

c_s is the spherical aberration (see Section 2.6.3) of the objective lens (Carter and Williams, 1996). λ for a $100 - 200$ kV TEM is $\sim 10^{-12}$ m. With the electron wavelength being orders of magnitude smaller than optical light, resolutions equivalent to the dimensions of lattice fringes in crystals (angstroms) can be achieved.

Two fundamental types of images can result from the transmission of electrons through a sample. Firstly, when the primary electrons penetrate straight through the specimen close to the optical axis, they generate Bright Field (BF) projections. Secondly, diffracted electrons from for instance a crystal (see Section 2.8) that are at an angle (mrads) to the primary beam are focused to generate Dark Field (DF) images. Apertures can be used to localise either the transmitted beam for BF imaging (the primary beam) or DF imaging (the scattered beam) and projected on a detector such as a fluorescent screen, negative film or digital camera (Fig 2.3). The use of an aperture containing only the BF enhances image contrast. Conversely, localisation of DF will generate an inverse image to the BF where scattering due to phase contrast is imaged. An example of BF and DF images of the same regions can be found in Section 6.3.
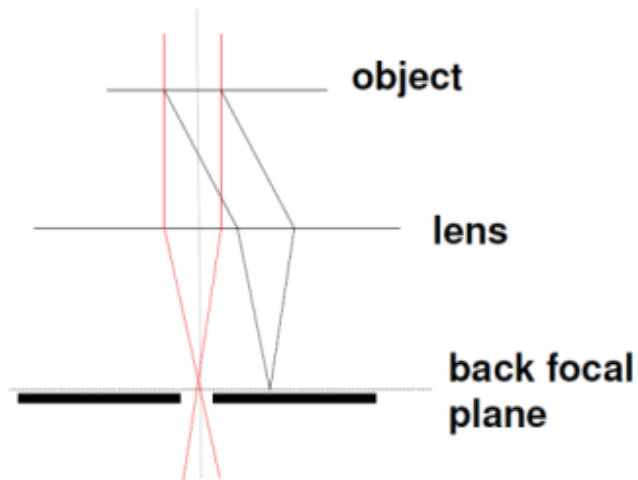
FIG 2.3: Diagram illustrating BF and DF imaging. An aperture inserted in the back focal plane (the objective aperture) can localise the primary beam through the object (Bright Field) shown in red, or the scattered beam for Dark Field imaging (black). A set of intermediate and projector lenses magnify the image further onto a fluorescent screen.

.
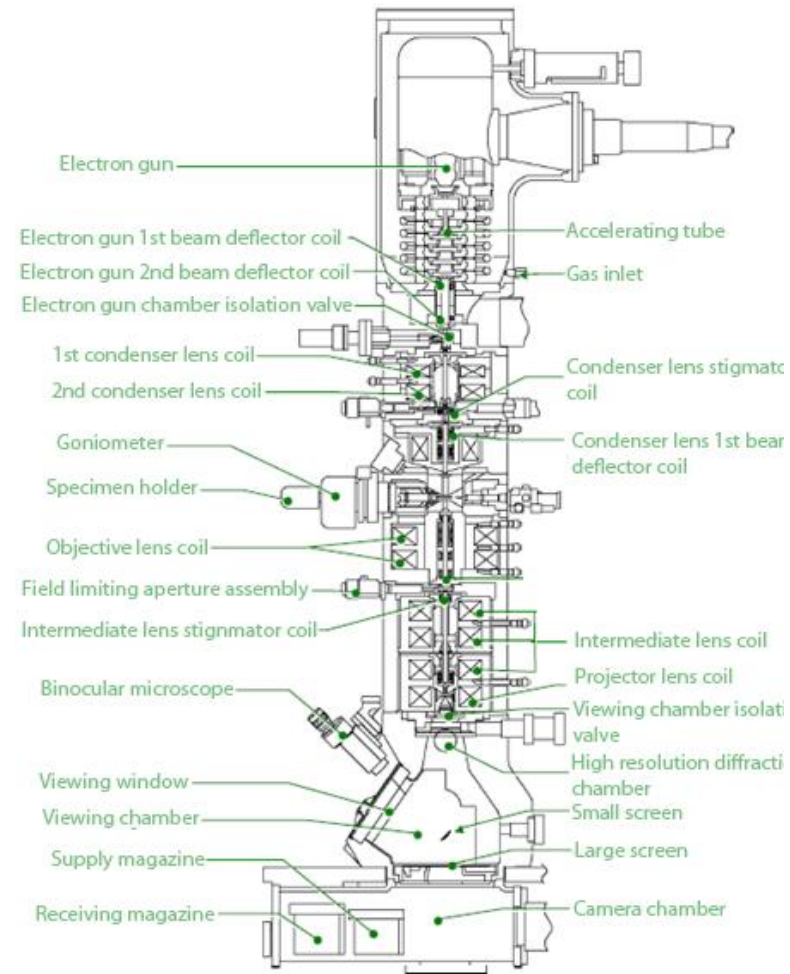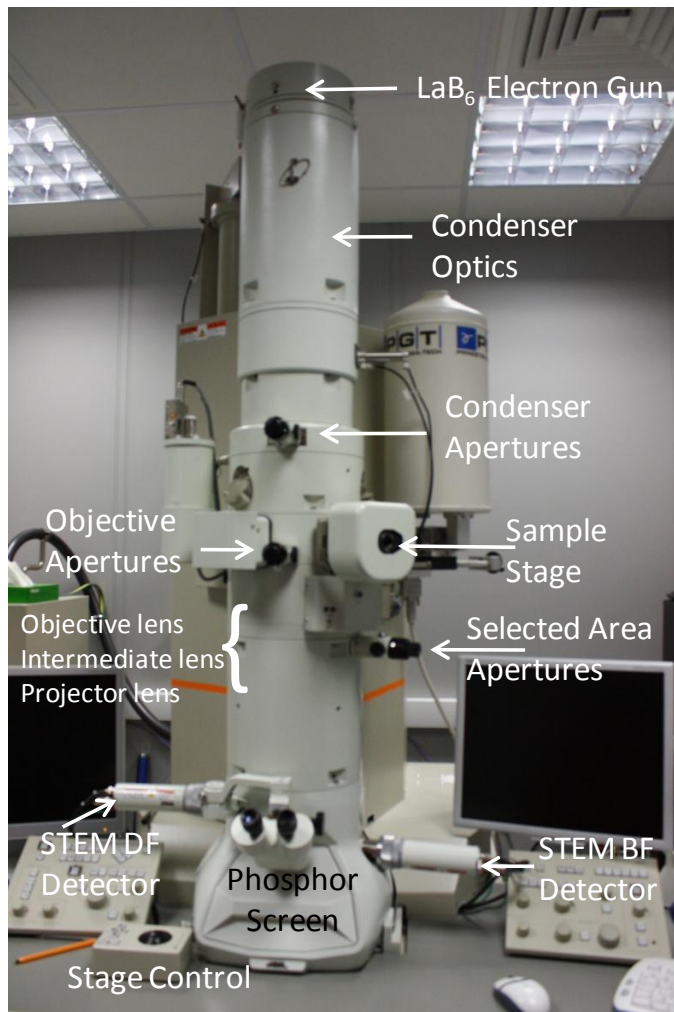
FIG 2.4: Image of the Jeol 2100 at the Advanced Microscopy Centre (AMC), Uuniversity of Leicester (UoL). Mechanical alignment procedures of the beam are carried out with the condenser and objective apertures. Other alignment procedures such as the source tilt, beam alignment along the optical axis are performed electronically with the control panel. A binocular microscope is placed above the phosphor screen improving manual imaging and alignment precision. A *Gatan Ultrascan* 1000 digital camera is located below the phosphor projector unit which can be retracted for subsequent digital imaging. The Schematic of the Jeol 2100 shows the sets of deflector coils and lenses for focussing and alignment of the beam.
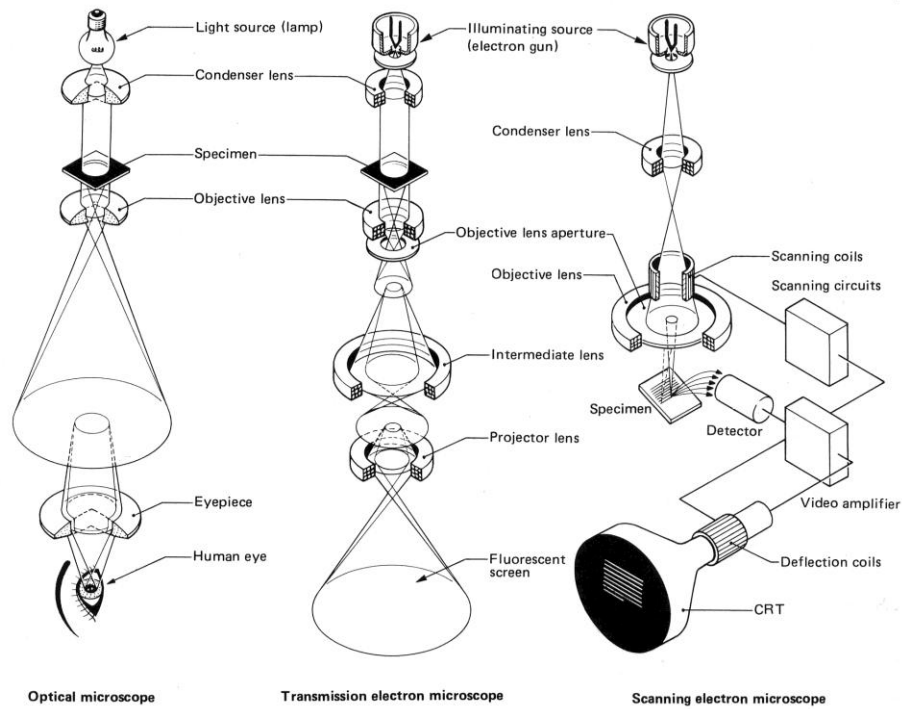
FIG 2.5: General Schematic of OM, TEM and SEM. *Image courtesy of EMATA TEM consultancy*
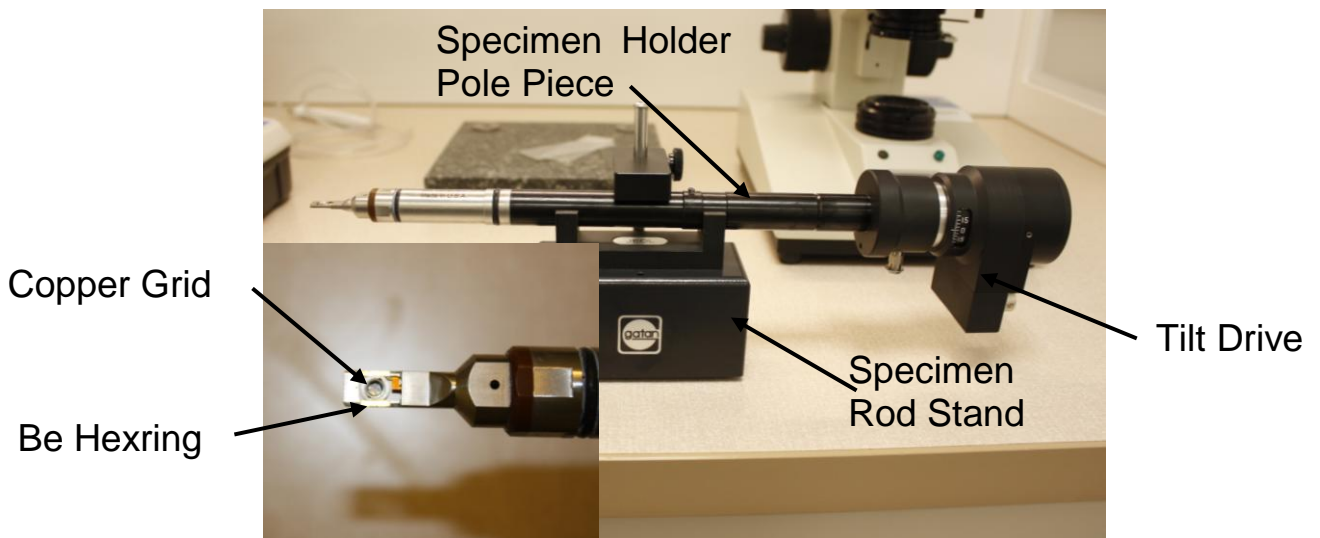
FIG 2.6: Image of the Gatan TEM sample holder that is inserted into the sample air lock. The copper grid containing the sample (see section 2.8 for TEM sample preparation) is fixed at the end with a beryllium screw to avoid the generation of copper X-ray in chemical EDX analyses (Section 2.6). The sample is also on a X-Y goniometer for sample rotation under electron diffraction (Section 2.7).

2.3.1 Scanning Transmission Electron Microscopy (STEM)

In an SEM, a pair of scanning coils is located above the sample position in order to raster the electron beam (Fig 2.4). Scanning coils are also used in a TEM to provide Scanning Transmission Electron Microscopy (STEM) where the beam is rastered over the electron transparent sample. A detector can be placed along the optical axis of the primary beam for STEM BF imaging or around it for detection of the scattered beam by STEM DF imaging (bottom of Fig 2.4).

STEM has numerous advantages over conventional TEM mode. Samples can be chemically mapped with a spectrometer (see Section 2.6.1). In imaging mode, STEM can also provide compositional information based on the scattered electrons being detected. At different angles to the transmitted bright field beam, the electrons that are scattered from the sample are a consequence of both phase and Z number (ADF), or solely the Z number of the material - high annular. An example of this concept is High Angle Annular Dark Field Imaging (HAADF), explained in Fig 2.7, for detection of electrons that diverge greatly from the primary beam based on the Z number. This allows Z contrast information to be determined and has been useful for sub-micron mineral assemblages found in *Stardust* samples.
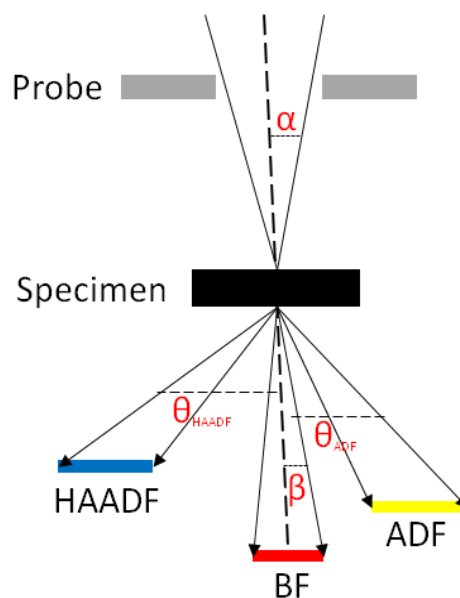
FIG 2.7: Diagram illustrating the different types of electron scattering arising from a transmitted scanning electron beam. HAADF electrons are scattered at the largest angles from the BF Beam and are detected at varying intensities ultimately based on the Z number of the material. Thus HAADF is ideal for imaging compositional heterogeneities in a sample. B ~ <0.5^o, θ_{ADF} ~ $0.5 - 3^o$, , θ_{HAADF} ~ $3 - 10^o$ (Lee, 2010)

2.4 Electron Microprobe Analyser

Electron microprobe analysers are used for spot chemical analysis or mapping of solid materials. It was the first type of instrument used for chemical analysis in EM (McGee and Keil, 2001). Unless EDX analysis is employed (Section 2.7.1), chemical analysis is usually performed with a WDS spectrometer (described in more detail in Section 2.6). The probe operates in broadly the same way as an SEM. Its optical system, however, provides higher and more stable beam currents and hence larger spot sizes to enhance spectral resolutions by increasing peak to background ratios. The theory behind this chemical analysis and the spectrometer used in EPMA is provided in Section 2.6, which describes the crystal spectrometers and geometries that are used in WDS.
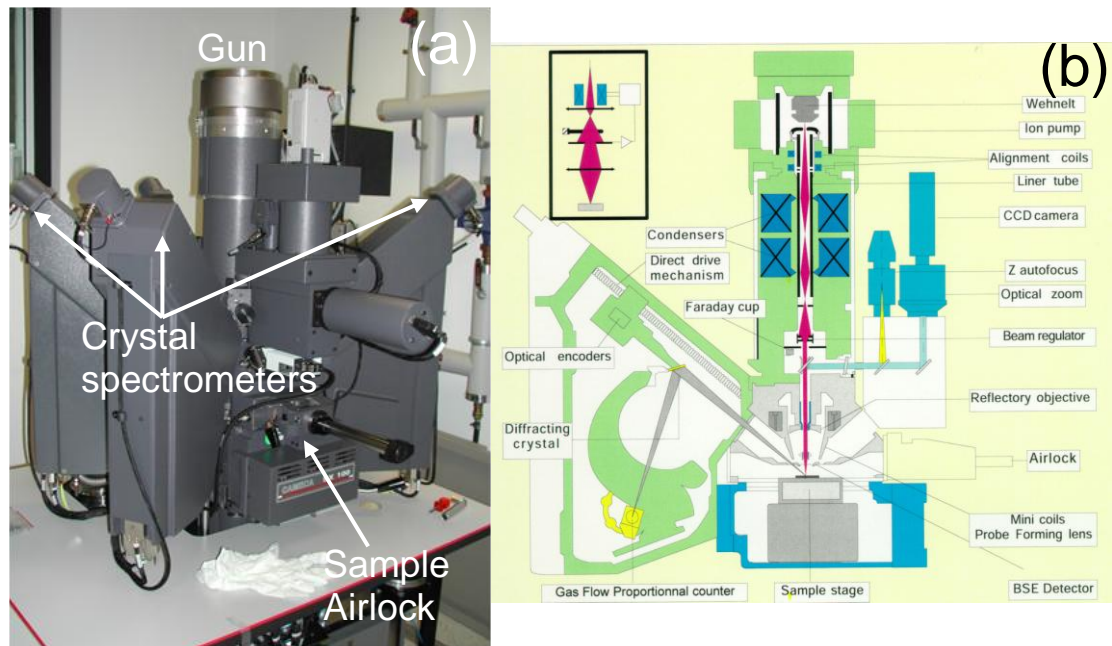
FIG 2.8: EMPA used in this thesis. (a) The Cameca SX100 used at the Department of Mineralogy, Natural History Museum (NHM). This instrument was used for EMPA analysis of the nakhlite SNC meteorites (Chapter 4). The Jeol JXA 8600 at the Dept. of Geology, UoL was also used for analysis of the standards in Section 2.11. (b) Schematic diagram of SX100. A conventional thermionic tungsten filament is used as the electron source. Rather than small spot sizes for increased spatial resolutions, the optics are designed more for beam stability with the beam regulators and alignment coil not found in conventional SEMs. *Image courtesy of http://asimow.com.*

2.5 Electron Optics

The SEM, TEM, EPMA require an electron source for the emission of electrons that are subsequently focused with electron lenses. The underlying physics behind their designs are quite similar. An insight into the theory of electron optical systems follows with a brief discussion concerning their current limitations and limiting resolutions.

2.5.1 Electron Sources

The electron source of an electron microscope is generally one of two forms. The most common source is a thermionic source, usually a tungsten hair line filament. The current density J of electrons emitted from the filament is determined from Richardson's Law (Richardson, 1901):

$$J = AT^2 e^{\frac{-\phi}{kT}} \qquad (2.4)$$

where k is Boltzmann's constant and A is Richardson's constant which depends on the source material. Φ is the work function of the conductor and T is the temperature. The filament current leads to Joule heating of the source material. An increased voltage supply leads to a saturation current that is opposed by a negative bias in the Wehnelt cap (Fig 2.9). Optimum source current for operation is found just below saturation point where beam stability is maintained (Goldstein, 2003). A hairline tungsten filament is usually contained in a Wehnelt cap (Carter and Williams, 1996). Typical filament emission currents and voltages are 100 μA and 1-20 kV respectively.
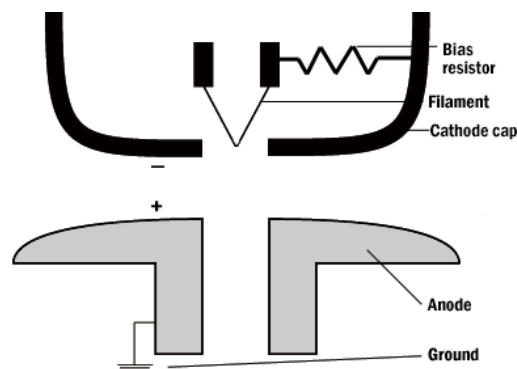
FIG 2.9: Diagram showing the configuration of an electron gun in a Wehnelt. Electrons ejected from the filament are drawn from a bias across the cathode and crossed over in the gap enclosed by the anode.

The other type of source is the Field Emission Gun (FEG) as used in the FEI *Sirion* of the UoL's AMC (Fig 2.2). FEG sources are also made from high temperature metals such as tungsten but are machined to a sharp point (~10 nm tip). This concentrates the electric field when a voltage is applied to them. The enhanced electric field lowers the work function of the material sufficiently for electrons to tunnel out of it (Carter and Williams, 1996). The tunnelling of electrons across a lower potential barrier maintains a more stable beam current. Their relative velocities with respect to one another are more homogenous compared to those in a thermionic emission type. They are therefore, more monochromatic - increasing the signal to noise ratio in the detectors and thus enhancing image resolutions. Other materials for electron sources such as LaB_6 filaments (as used in the Jeol 2100 TEM at the UoL) are also more efficient than hair line filament sources due to their lower work functions.

2.5.2 Electron Lenses

The electron beam after passing the anode requires collimation before being focused onto a specimen. In general, a condenser lens and/or apertures are used for collimating the diverging beam and the objective lens is used for focussing onto a specimen. The charge of the electron enables its deflection by the electromagnetic force. Optical systems can be designed to focus electrons through electrostatic lenses, magnetic lenses or a combination of both (e.g. Tusuno, 1999; Zhan et al., 2009). Commercial microscopes today such as the FEI *Sirion* FEG-SEM and Jeol 2100 TEM at Leicester use magnetic lenses because of the favourable geometries of their optical columns that will minimise spherical aberration (see Section 2.5.3).

2.5.2.1 Magnetic lenses

In a homogenous magnetic field generated by, for example, a magnetic pole piece, a traversing electron will experience an external force when travelling perpendicular to the planes of the field. This is the Lorenz force. The electrons will, thus, follow a circular path which enables deflection of an electron beam to a point. Electrons arriving at a magnetic field at an angle to the optical axis will follow a helical path to a point. Conventional magnetic lenses consist of Cu coils surrounding a soft iron core that concentrate the magnetic field onto the small gap between the inserted pole pieces. The geometry of the conducting coils and the gap of the pole pieces are

engineered such that magnetic field is intensified at the centre of the gap between the pole pieces giving optimal focusing along the optical axis (Williams and Carter, 1996).
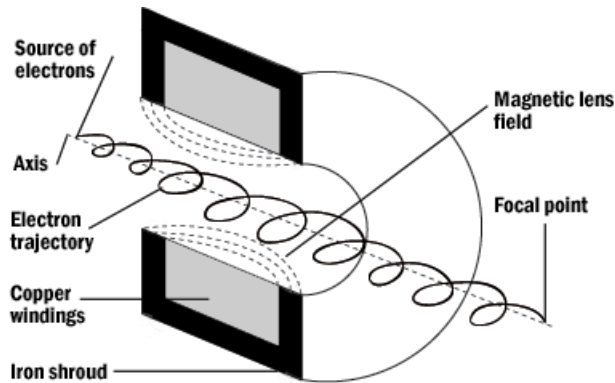
FIG 2.10: Simplified cross section of a magnetic lens. The helical path of the electrons results from the Lorentz force. The copper windings around the soft iron core concentrates the magnetic field at the centre of the lens and along the optical axis.

2.5.3 Aberration effects of Electromagnetic Lenses

The use of electromagnetic lenses can have disadvantages as they are associated with various forms of aberrations. Machining errors, asymmetry in the magnetic windings, inhomogeneous magnetic fields in the iron and buildup of contamination within the electron column are all contributing factors to an asymmetric electron beam (Jeol Applications Manual). These aberration effects ultimately govern the spatial resolution of the EM. They are summarised by the following:

Spherical Aberration

This is a geometric aberration of the electron optical system. It can be lowered by increasing the field intensity of the lens or by placing a suitable-sized circular aperture in the electron beam path to reduce the beam divergence angle α. The radius of the disc of least confusion is:

$$r_s = C_s \alpha^3 \qquad\qquad (2.5)$$

where C_s is the spherical aberration coefficient. A physical treatment of the C_s coefficient and its first derivation in electron optical systems can be found in Mulvey and Willington (1969) and Scherzer (1936) respectively.

Asymmetric Aberration

Machining, poor quality lens material and a dirty beam path can all lead to axial stigmatism. The radius of the least aberration circle is defined as:

$$2r_A = \Delta f_A \, \alpha \qquad (2.6)$$

Where Δf is the spacing of the stigmatic foci. Lenses are used to reduce Δf and correct for the astigmatism.

Wave Optical Aberration

This is the diffraction aberration (i.e. based on the Rayleigh criterion) which arises through diffraction of any lens or slit. The radius of the Airy disk is:

$$2r_D = \frac{1.22\lambda}{\alpha} \qquad (2.7)$$

It can be reduced by making α larger. However, making the beam divergence angle larger will increase spherical aberration. The aperture angle must be optimized and consistent with the spherical and diffraction aberrations.

Chromatic Aberration

This aberration arises because of the variabilitiy in the electron wavelength that are emitted from the source, leading to undesired off axis beam bending. The least aberration circle is,

$$2r_c = C_c \alpha \frac{\Delta E}{E} \qquad (2.8)$$

where C_c is the chromatic aberration coefficient and ΔE is the change in electron energy (Jeol Application Manual). .Lenses are optimized to reduce all of the aberration effects described above in order to enhance resolution of the electron microscopes.

2.6 Vacuum Systems for EM

The size and stability of an electron beam is related to the quality of the vacuum under which the EM is operating. Typical vacuum levels for high vacuum EMs are $<10^{-5}$ mbar. Different types of pumps are used to obtain specific levels of vacuum. Rotary pumps provide low vacuum (10^{-1} mbar) for 'roughing out' the ambient atmospheric pressure. Higher vacuum levels are provided by turbomolecular, diffusion or ion getter pumps. Turbomoloecular pumps (turbo pumps) use a fast spinning rotor within a cylindrical cavity, the stator, with a small gap through which the gas can pass through (Stokes, 2008). Diffusion pumps use heated oil that vaporises and cools the atoms/molecules to force them towards a secondary rotary pump. Ion getter pumps use large adsorbing materials that draw ionised gas through an electric field. The chambers and column in commercial EMs generally use a rotary pump for roughing out from atmospheres after which the turbo pumps are employed. The Jeol 2100 and FEI quanta 3D FIB (see Section 2.9.1) electron and ion sources or 'guns' use ion getter pumps. Vacuum levels are monitored with predominantly two types of gauges. The first is the Pirani gauge that uses a heated wire. The resistance of the wire is dependent on its temperature and by the amount of gas in the vacuum system cooling it. Penning gauges measure the pressure in a vacuum via detection of the amount of ionised gas molecules passing through a cathode by an induced magnetic field.

2.7 Chemical Analysis in Electron Microscopy

The energy of the electrons in an electron microscope beam can be sufficient to eject electrons from the orbital shells of the atoms in a specimen. Quantum mechanics and conservation of energy determines that an electron from an energetically lower orbital shell (e.g. L_1) will replace the ejected electron (e.g. from K shell) and usually release a photon based on the energy difference between them (i.e. Kα line). The wavelength of the X-ray emission λ relates to the atomic number of the element Z by Moseley's Law (Moseley, 1913):

$$\frac{1}{\lambda} = k(Z - \sigma)^2 \qquad (2.9)$$

where k is a constant for a particular series of lines (K, L, M, etc) and σ is the shielding constant for a particular shell (e.g. σ = 1 for the K shell). A photon's energy due to the

transition described in *Equation (2.9)* generally has a wavelength in the X-ray region of the electromagnetic spectrum. It is unique to the Z number of the element. Detection of these photons can thus provide a means for dispersive spectroscopy. One can either identify many different energy photons simultaneously - Energy Dispersive Spectroscopy (EDX) or tune to specific elements' characteristic line emissions individually for higher spectral resolution - Wavelength Dispersive Spectroscopy (WDS). A description of both modes of spectroscopy is provided in this section.

$M_{4,5}$ (3d)
$M_{2,3}$ (3p)
M_1 (3s)

L_2 ($2p_{1/2}$)
L_2 ($2p_{1/2}$)

L_1 (2s)

K_β

$K_{\alpha2}$

$K_{\alpha1}$

K (1s)
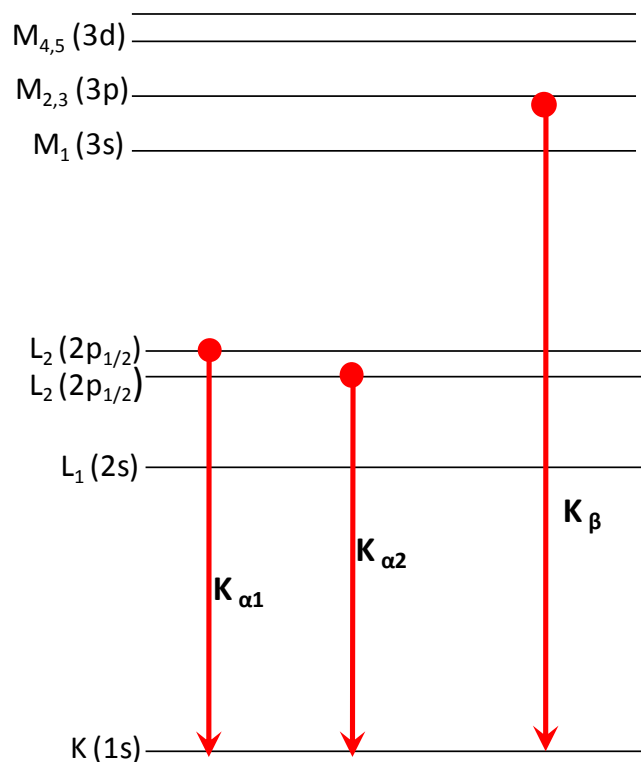
FIG 2.11: Diagram illustrating the different transition lines (KLM) between corresponding core shells of an element. In EM, the efficient production of X-ray photons are generated with an incident overvoltage approximately twice their edge energy. For instance, Fe Kα at 6.93 keV should be measured with an incident beam energy at least 14 keV (Goldstein and Newbury, 2006).

2.7.1 Energy Dispersive Spectroscopy

In an SEM or TEM or electron microprobe, a Si-based solid state X-ray detector such as a Si(Li) diode detector can be positioned at an angle to a sample. X-rays can be collected along the solid angle between the sample and the detector. Li doping is used in the detector material to ensure it has a direct Si band gap. It is also liquid nitrogen cooled to prevent unwanted combinations of electron-hole pairs and hence a large background signal. Characteristic X-rays generated by a sample pass through an

evacuated column sealed by a detector window. This is usually made up of thin low Z material, allowing X-rays to efficiently pass through them e.g. 12 μm thick Be that is found in the *PGT Gamma Tech* and *Oxford Instruments* EDX spectrometer at Leicester. This ensures the transmission of X-rays and the mechanical sealing strength of the window. X-rays pass through the window and impinge on the Si(Li) crystal at the other end of the column. The energy of the incoming X-ray photon is proportional to the number of electrons-hole pairs created in the detector. Fluctuations arise in the number of electron-hole pairs that fundamentally determine the detector resolution (Fraser, 1989). This signal is coverted to a voltage and amplified by a pulse processor. It is then read digitally and allocated to an appropriate energy channel or 'bin' in a MultiChannel Array. Photons of different energies based on the atoms present in the sample arrive at the detector and are allocated to bins. Variations in the number of electron-hole pairs generated in the depletion layer are described by Poisson statistics and result in a Gaussian profile. The peak of Gaussian corresponds to the energy of the transition line. The intensity or integral of the Gaussian peak is proportional to the number of counts processed at that particular energy. A typical energy range for a Si(Li) detector is 20 keV. For 2048 channels which are conventionally used in EDX devices, this results in a display resolution of 10 eV per channel. The overall detector resolution is measured by the width of the Gaussian peaks. Conventionally, the Full Width Half Maximum (FWHM) of the Mn Kα peak is used to determine the energy resolution of a solid state detector and is around 136 eV for the Oxford Instruments EDX spectrometer.

During acquisition, the ratio between the processed counts R_{out} and actual incoming photons R_{in} can give an idea of the performance of the detector at that time. This is known as the deadtime:

$$Dead\ time\ in\ \% = \left(1 - \frac{R_{out}}{R_{in}}\right) \times 100 \qquad (2.10)$$

In the Si(Li) detectors, a deadtime of 20 – 30% is favourable for a good acquisition. From this, a qualitative determination of the composition of the sample being probed can be made.
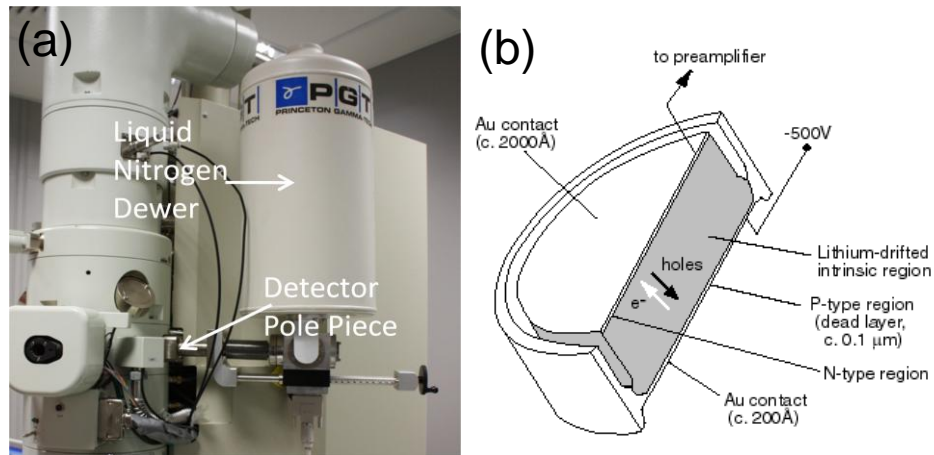
FIG 2.12: (a) EDX spectrometer attached to the Jeol 2100 TEM at the University of Leicester. The liquid nitrogen Dewar is fed to a cold finger attached within the solid state detector. (b) Schematic of a Si(Li) diode EDX detector. When an X-ray photon is absorbed in the intrinsic region, it produces a number of electron-hole pairs proportional to the energy of the absorbed photon. These electrons and holes are attracted to the opposite surfaces and constitute an electrical pulse that is fed to the preamplifier. *Image courtesy of Kevex corporation website.*

As well as characteristic X-rays, a continuum background spectrum is also generated. An electron can be accelerated upon interaction with atomic nuclei in the sample, releasing an X-ray photon. This is Bremsstrahlung radiation. By Poisson statistics, detection of an element is accepted to 99% confidence if the numbers of counts received for a peak is three times the standard deviation of the back ground spectrum.
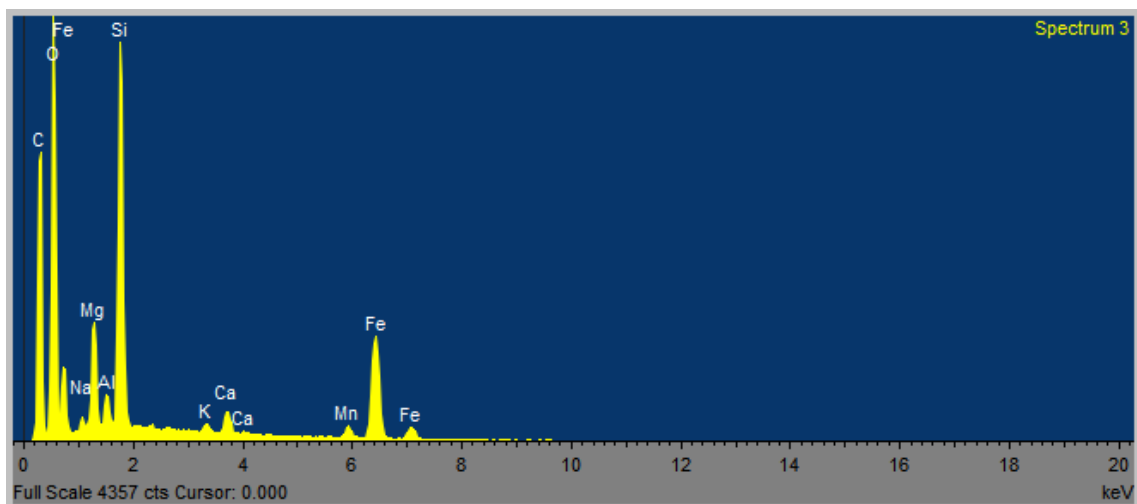
FIG 2.13: An example of a TEM-EDX spectrum obtained with the Oxford Instruments *INCA* software at 20 kV. The software automatically integrates the background and peak Gaussians for quantitative analyses.

2.7.2 Qualitative X-ray Analysis by SEM, TEM and EMPA

An EDX spectrum is composed of the characteristic X-rays and the Bremsstrahlung background as shown in Fig 2.13. For a specific energy range (usually 0-20 keV), an element can be identified with high confidence if peaks corresponding to the transition lines of that particular element are in the spectrum. For instance, a positive identification of Fe would be made if the peaks of Fe $K\alpha_{1,2}$ (6.4 keV), Fe K_{β} (7.06 keV), and Fe $L\alpha_{1,2}$ (0.7048 keV) are all present, unless there are only trace (~ 1 wt% concentration) minor (1-10 wt%) amounts of Fe and therefore, the most efficient transitions ($K\alpha$ and $L\alpha$) peaks may only be detectable. Such observations of peaks can lead to a qualitative determination of the composition of the specimen being analysed. An approach to quantitative analysis is described in the next section.

2.7.3 Quantitative Analysis by SEM and EMPA

The peak intensities of different elements in a sample by EDX and WDS are proportional to their relative abundances. Based on this premise, an empirical measure of the concentration of a particular element can be made. The most straightforward way of producing a quantitative analysis is by comparing an unknown concentration within the sample $C_{unknown}$ to that within a standard $C_{standard}$. This is described by Castaing's first approximation to quantitative analysis (Castaing, 1951):

$$\frac{C_{unknown}}{C_{standard}} = \frac{I_{unknown}}{I_{standard}} \qquad (2.11)$$

where I is the X-ray intensity. In SEMs and microprobes, the interaction between the electron beam and a bulk (e.g. 30 μm thick) sample can be described by various physical effects in the sample, incident electrons and generated X-rays. In EM (an exception being TEM), the main causes of X-ray intensity variation can be attributed to three main factors:

*The Atomic Number **Z** of the Material.*

The atomic number of the atom(s) in the sample can affect the generated X-ray intensity via both backscattering and energy loss. In the former, the extent of elastic scattering of the incident beam increases with Z number (Reed, 2005). A higher

proportion of electrons elastically scattered from a beam consequently results in a higher proportion of electrons that have not been used in X-ray generation. An 'underestimate' of the true number of those higher Z number atoms in the sample would require a correction factor to the intensity peak of that particular element. This is the back scattered correction factor R and is shown in *Equation (2.12)*:

$$R = \frac{1}{1 + \left[0.008Z\left(1 - \frac{E_c}{E_0}\right)\right]} \qquad (2.12)$$

where E_c is the characteristic energy of the element being measured and E_o is the incident energy of the electrons (Reed, 2005). Thus, if the unknown element being measured has a higher Z number than the standard, an upwards correction is made in R. However, a higher Z number also results in a downwards correction in energy loss by inelastic interactions. Lower Z number elements interact more with the incident electrons and therefore, have a higher stopping power S:

$$S = -\frac{1}{\rho}\frac{dE}{dx} \qquad (2.13)$$

where ρ.is the density of the specimen, E is the incident energy and x is the interaction depth. Incorporation of both factors gives the overall Z correction:

$$Z = \frac{R_{std}}{R_{unkwn}} \cdot \frac{S_{unkwn}}{S_{std}} \qquad (2.14)$$

The Absorption of X-rays based on Mass-depth.

The intensity of X-rays across a samples depth or thickness is attenuated by a magnitude described in Beer's Law:

$$\frac{I}{I_0} = e^{-\left(\frac{\mu}{\rho}\right)\rho t} \qquad (2.15)$$

where $\left(\frac{\mu}{\rho}\right)$ is the mass absorption coefficient and ρ is the material density. The path length of X-rays travelling to the spectrometer is determined by the takeoff angle,

$$Path\ length = zcosec\psi \qquad\qquad (2.16)$$

Where z is the interaction depth of the X-rays and ψ is the take off angle. Integration of *Equation (2.15)* over the depth at a given ψ can then provide the ratio between the emergent X-ray intensity and the generated one upon initial excitation by the electron beam. The absorption correction is then defined as:

$$A = \frac{f(\chi)_{std}}{f(\chi)_{unkwn}} \qquad\qquad (2.17)$$

where, $f(\chi) = I_{emergent}/I_{generated.}$

*Secondary X-ray **F**luorescence.*

If the energy of a characteristic X-ray E_C from an element in the specimen is greater than E_C of another element, then secondary fluorescence can occur. This is corrected for with *Equation (2.18)*:

$$F = \frac{1}{1+\Sigma\frac{I_f}{I_p}} \qquad\qquad (2.18)$$

where I_f/I_p is the ratio of the intensity of X-rays from secondary fluorescence to the intensity of X-rays from inner shell photoionisation (i.e. the peak line) of the element in the sample (Goldstein and Newbury, 2003). The combination of all three factors is known as the **ZAF** correction factor - incorporated into *Equation (2.19)*:

$$\frac{C_{unknown}}{C_{standard}} = \frac{I_{unknown}}{I_{standard}} \cdot ZAF \qquad\qquad (2.19)$$

The *ZAF* correction factor is also known as the 'matrix correction'. If the *ZAF* factor is very close to unity, this would indicate a very good resemblance between the 'matrix' of the unknown and standard. Application of *Equation (2.19)* on its own would produce elemental concentrations that could be successively corrected for using *Equation (2.19)* an infinite number of times. A starting parameter must, therefore, be defined to converge to an accepted composition thereafter. This is where automated matrix

correction software is frequently used such as the Oxford Instruments *INCA* and PGT *Spirit* software at the AMC. An initial starting composition is made based on the intensities of the peaks and the automated software's data of standards. The ZAF correction is then made based on standards inputted by the user to generate a new composition. It is then further corrected for using the ZAF factor again. This process is successively iterated until convergence is achieved to a least squares fit. A more comprehensive treatment in the ZAF correction factors can be found in enhancements sections of Goldstein and Newbury (2003). Other Matrix corrections have also been formulated such as binary α-factors (Ziebold and Ogilvie 1963) and multi component systems (Bence and Albee 1968), but ZAF is most commonly used.

2.7.4 TEM Quantitative Analysis

As with SEMs an EDX spectrometer can be installed in the TEM. In a TEM, the working distance of the sample is minimal and the take off angle of X-rays generated from the sample to the detector is lower than in the SEM. The smaller excitation volume with a thin specimen in the TEM lowers the volume for photo-ionisation, resulting in less counts. Longer acquisition times for spectra can rectify this problem to make quantitative analysis with the TEM feasible.

One of the fundamental advantages of TEM-EDX analysis is that the incident X-rays experience far less matrix interactions, if any, than in SEM analysis. A 'purer' quantitative analysis can be made due to minimal 'matrix' effects in the TEM. In TEM-EDX analysis, an empirical description of atomic concentrations in a sample is also governed by the relative intensities of different characterisitic X-rays due to the different atoms in the sample. Unlike in the SEM and electron microprobe, however, the relative intensity of the peaks are primarily governed by the Z number of the elements and thickness of the sample. If the sample is thin enough to produce negligable absorption effects (an ideal thickness for a TEM sample at ~ 80 nm), the concentration of an element in a sample with respect to another element is,

$$\frac{C_A}{C_B} = \frac{I_A}{I_B} \cdot K_{AB}$$

(2.20)

where K_{AB} is known as the *K*-factor (Cliff and Lorimer, 1975) of A with respect to B. The experimental conditions of the microscope, such as the accelerating voltage and

detector take off angle will efeect the value of the *K*-factor (Sheriden, 1989). *K*-factors can be both experimentally and theoretically determined, but with less precision if a theoretical treatment is used (Lorimer, 1984; Horita, 2001). An experimental approach in the calculation of *K*-factors for the Jeol 2100 200 kV TEM is in Section 2.10.

If the sample is not ultra thin and significantly absorbs X-rays, the generated X-ray intensity can be corrected for by using Beer's Law in *Equation (2.15)*. An experimental treatment of thickness correction is also discussed in more detail in section 2.10.3.

A major analytical constraint in TEM lies in the ability to preserve the nature of thin samples (Section 2.8). Also, the most accurate quantitative EDX analysis can only be performed by selection of standards with known compositions. Quantitative TEM-EDX analysis is generally reffered to as a component Analytical Electron Microscopy (AEM) that will be used to refer to it in this thesis.

2.7.5 Wavelength Dispersive X-ray Spectroscopy (WDS)

Prior to the incorporation of the EDX spectrometer with SEMs and TEMs, WDS was the conventional means for chemical analysis and today, remains the most accurate commercial spectrometer with an electron probe in being able to determine concentrations down to ~0.01 wt%. This type of spectrometer is synchronised with the EMPA and is therefore, a separate instrument solely dedicated to compositional analysis of solid materials, although lower resolution imaging can also be performed. Thus, disadvantages lie in it being more expensive, time consuming and difficult to use compared to the EDX attachment on SEMs and TEMs. It does, however, provide superior spectral resolutions – up to 10 times higher than EDX (Goldstein and Newbury, 2003). They can be attached to SEMs as well but currently not as frequently.

Unlike EDX, WDS tunes individually to an element's transition line. This is achieved with the use of a crystal spectrometer. It works on the principle of Bragg diffraction (described in Section 2.7). Each crystal is tuned to a specific energy range based on its d-spacing. The more crystal spectrometers attached to the microprobe, the more elements that can be analysed simultaneously. The X-rays generated by the microprobe will be diffracted at a particular Bragg angle to the crystal and detected by a gas filled proportional counter, and then digitised to a CRT display containing information of the standard pulse size and thus the X-ray intensity (Goldstein and

Newbury, 2003). The Cameca SX100 at the NHM (Fig 2.4) and the Jeol JXA8600 at the Dept. of Geology, UoL used in this thesis have 4 and 3 different crystal spectrometers working simultaneously respectively. Different manufactured crystals have different d-spacings for tuning to specific elements. Thallium acid phthalate (001) TAP crystals are used for 8 – 15 Z number Kα X-rays, pentaerythritol (001) PET crystals are used for 13 – 26 Z number Kα and lithium fluoride (200) LIF are used for 19 – 38 Z number Kα (Wittry and Barbi, 2002). The probe beam size of an EMPA is much larger (μm's) than that of an SEM. Much larger and stable beam currents provide far greater count rates (up to ~50,000 cps compared to ~4000 in EDX). WDS therefore, provides a much higher peak to background ratios P/B, increasing its minimum detection limits and spectral resolution.
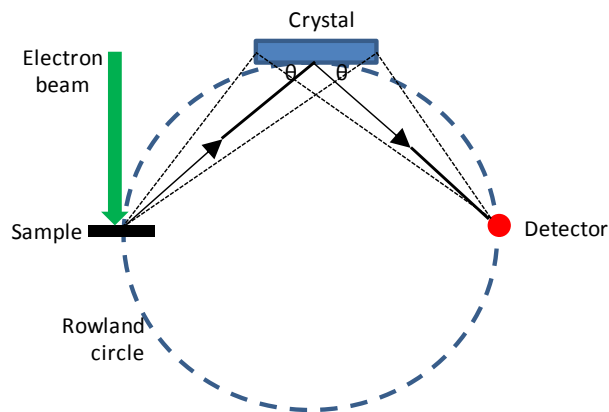
FIG 2.14: Simplified schematic showing the path of X-rays in WDS. The detector is placed at the Bragg angle to the sample based on the energy line being detected on a Rowland circle.

2.8 Electron Diffraction

The wave nature of the electron results in the diffraction of electrons through regular planes. A set of periodic planes will reflect electron wavefronts in phase if the path difference between successive wavefronts is equal to *n* integers of wavelength. This is the Bragg law (Bragg and Bragg, 1913):

$$n\lambda = 2d \sin \theta \qquad (2.21)$$

where *d* is the spacing between the regular planes and θ is the angle of the incident waves to them. As an incident electron beam generally has a fixed path direction,

orientation of a crystalline sample is changed to satisfy the Bragg condition. Under electron transmission, the resultant will be a diffraction pattern. The spacing between peak electron intensities in the pattern (i.e. spots by constructive interference) in one direction, correspond to the lattice spacing of the diffracting crystal along one plane. This enables us to identify the crystal's lattice parameters and hence, its structure. The orientation between different minerals or other phases present in a heterogeneous sample can also be identified, with spatial resolutions restricted by the size of the transmitting beam (e.g. down to 1 nm in the Jeol 2100).

The momentum transfer between electrons is described by the inverse wavelength (de Broglie, 1913) and is thus treated in inverse or reciprocal space. The constructive interference between transmitting electrons at successive planes, leads to diffraction spots that lie on a reflecting sphere – the Ewald sphere (Hirsh, 1965). In crystallography, it is useful to describe the Bragg Law via construction of the Ewald sphere and expressing it in vector notation:

$$\mathbf{g} = \mathbf{k} - \mathbf{k_0} \qquad\qquad (2.22)$$

Fig 2.15 provides a diagrammatic representation of the $\mathbf{g}$ vector. The direction perpendicular to two lattice vectors is known as a zone axis of the crystal. The plane of reciprocal spots that travel through the origin 0 as in Fig 2.15 represent the zero-order Laue zone. It generally represents the smallest dimensions of periodic planes in reciprocal space (Champess, 2001) and therefore the largest in real space. A zone axis is, therefore, the most useful direction of the electron beam for High Resolution TEM (HRTEM) contrast imaging of the rows and columns of atoms in real space (largest d-spacings). If the crystal is tilted slightly off the zone axis, the Ewald sphere can also intersect the first order Laue zone. These are the spots from the reciprocal lattice layer above the zero order. When searching for a zone axis in the TEM, it is thus useful to know when we are observing the lattice spots from a higher order Laue zone to re-orientate the crystal onto the zone axis. Sample holders in the TEM can rotate in all directions to achieve this. Further treatment of indexing of electron diffractions is provided in the TEM calibration Section 2.10.2.
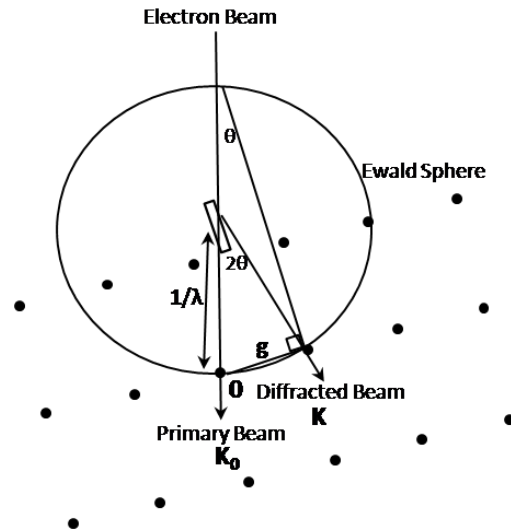
FIG 2.15: The Ewald sphere has a radius of $1/\lambda$. The Bragg condition is satisfied when a point lies on the surface of the sphere. Hence, the **g** vector from the origin (primary beam) to the next successive spot (diffracted beam) on the reflecting sphere is **k-k₀** as in *Equation (22)*. As the radius of the sphere is so large, we perceive the reciprocal lattice on a 2-D plane. *Figure Modified from Champess (2001).*

2.9 TEM Sample Preparation

For a sample to be electron transparent it generally needs to be around 100 nm thick. A sample thicker than this will transmit some electrons to generate an image, but diffraction patterns would be too difficult to interpret due to the multiple scattering effects and absorption by the sample. AEM would also be complicated by the sample's absorption characteristics which would have to be considered in interpreting the X-ray spectra (Section 2.11.2). HRTEM imaging of crystal lattice planes would also be problematic or even impossible. When the sample is less than 100 nm (<80 nm) this is known as the ultra thin criterion (Carter and Williams, 1996) - where negligable absorption effects of X-rays occur. The thinner the sample, the less dynamical effects there are that inhibit electron diffraction and effective High Resolution TEM (HRTEM) are reduced to a minimum. Effective TEM sample preparation is paramount for successful TEM analysis as great care and precision are required to maintain the integrity of a specimen when it is less than 100 nm thick.

2.9.1 Focused Ion Beam

The SEM-FIB instrument can be used to prepare TEM samples of preserved planetary materials. This novel approach to sample preparation is arguably the most effective technique for site specific (*in situ*) TEM sample preparation whilst also

preserving the mineralogical and petrologic characteristics of the specimen. FIB-based TEM thin sections can be applied to other microanalytical techniques such as nano-Secondary Ion Mass spectroscopy (e.g. Zega et al. 2007) enabling isotopic studies to be integrated with detailed mineralogical work.

The UoL's Dept. of Physics and Astronomy has an FEI dual beam *Quanta 3D* FIB-SEM. It contains an ion beam column plus the conventional high vacuum SEM. The electron beam is perpendicular to the sample stage whilst completely flat (i.e. 0° tilt) and the ion beam at 52°. The ion beam consists of a beam of Ga^+ ions. The greater force imposed by the heavier Ga^+ ions (Z = 31) compared to electrons bombarding a sample has the consequence of exceeding the surface binding energy of many substrates, leading to the ejection or sputtering of the material in question. Sputtering of material by milling with the ion beam can be close to the size of the beam depending on factors such as the redeposition. The number of atoms in the sample sputtered per incident Ga^+ ion, known as the sputtering yield *Y* is given by *Equation (2.23)*:

$$Y(E_0) \propto \frac{NS(E)\Delta x_0}{E_0} \qquad (2.23)$$

where E_0 is an arbitrary minimum energy of the ion beam based on the surface binding energy of the material, *N* is the number density of atoms, *S* is the stopping power and x_0 is the depth interval for which the atoms ejected have an energy $>E_0$ (Giannuzi and Stevie, 2005).

The area for milling can be controlled by the allocation of designated areas and patterns displayed on the SE image of the sample. Milling depths *z* can be controlled by incorporation of *Equation (2.23),* with known accelerating voltages, beam currents and dwell time etc. Precise alignment of the beam is required with a good conducting path for beam stability.

The ion beam can be utilised for depositing materials on a substrate. The use of a Gas Injection System (GIS) attached to the microscope injects a hydrocarbon also composed of an element desired for deposition (e.g. C, W or Pt). Contact between the gas and ion beam eliminates the volatile component of the hydrocarbon, leaving the deposited material behind at the location where the ion beam is incident. The FEI *Quanta 3D* contains a GIS for carbon and platinum deposition.

2.9.1.1 FIB Milling Sequence

Controlled μm to nm milling and deposition can provide an extremely powerful tool for 'top down' materials manipulation at the submicron and nanoscale. FIBs were initially used in the electronics industry (Stevie & Giannuzzi., 2005; Orloff et al. 2002) for repairing submicron circuitry. More recently, this instrument has been applied to sample preparation of geological materials, especially for TEM analysis (e.g. Lee et al. 2003; Lee et al. 2007). This can enable the preparation of well preserved samples, maintaining the original mineralogical properties of the specimen in the process.

An automated FEI TEM run script in the microscope software can be used for preparation of a TEM sample. This involves the milling of material to leave a desired thin 'wafer' or 'lamina' remaining at the end of the process. Sample contamination by Ga^+ dosage must be minimised to preserve the integrity of the sample. Thus, the TEM sample must be initially protected with a cap, usually a high Z material such as platinum deposited by the GIS.
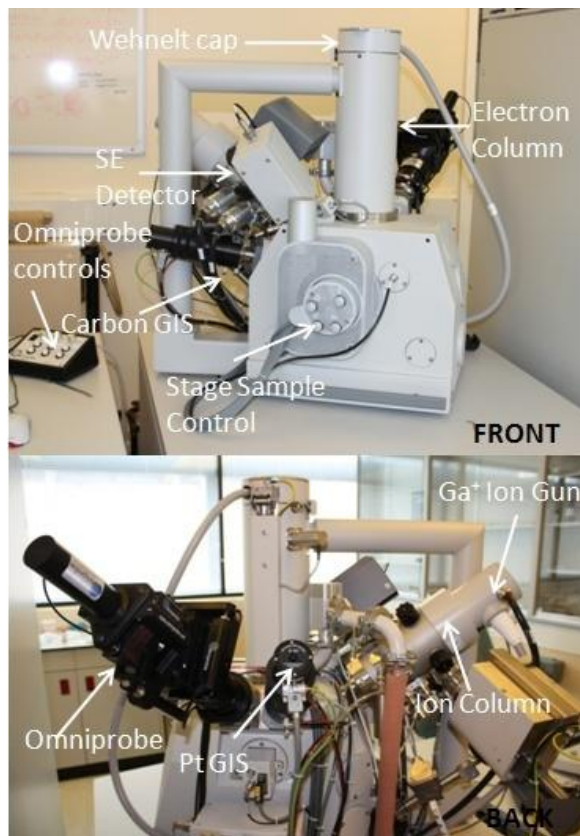
FIG 2.16: The FEI *Quanta* 3D at the UoL Condensed Matter Physics Group, Dept. Physics and Astronomy. *Top.* The front side of the FIB-SEM. A conventional tungsten hairline filament SEM is attached to the Ga^+ FIB at 52° to the sample. *Bottom.* Back side of the FIB-SEM where additional attachments including the *Omniprobe* (Section 2.9.1.3) and Pt GIS are located.

The runscript allows key parameters to be controlled in the process i.e. the wafer dimensions, the thickness of the protective cap and the currents used for the milling or thinning process. The following generalised steps of the runscript are described:
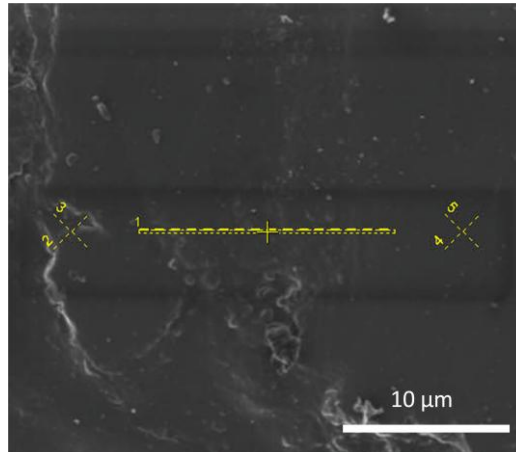
a) A frame is allocated (grabbed) in the secondary ion beam image over which the TEM sample is produced.
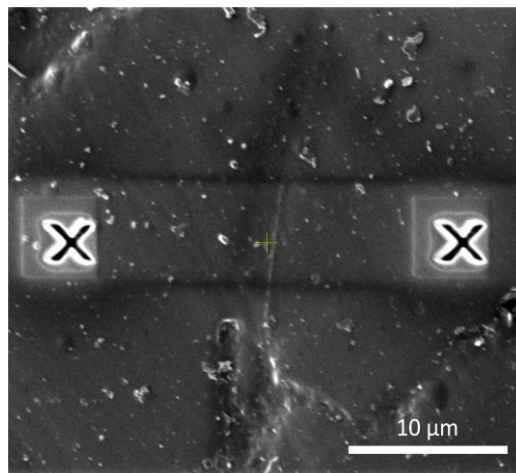
b) Two markers called fiducial points are milled on either side of the location of the wafer for alignment of the ion beam during subsequent milling steps and capping.
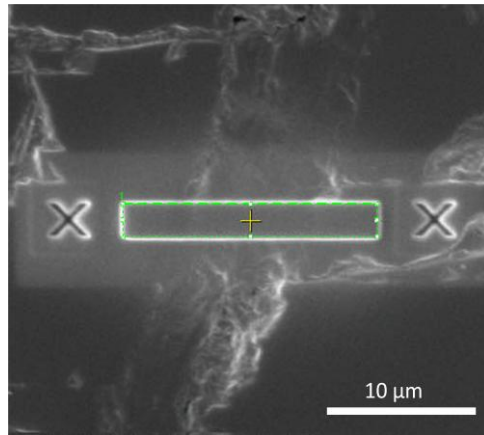
c) A platinum strip of designated thickness (e.g. 2 μm) is deposited with the GIS over the wafer area for protection of the underlying sample from the ion beam, between the two fiducial points.
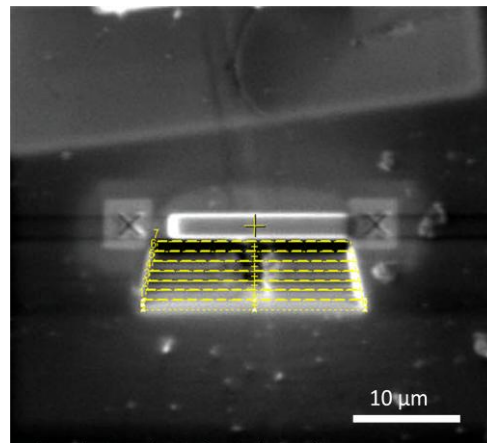
d) Beam currents of high ampere (3-5 nA) are selected for milling above and below the sample. Beam currents are decreased for final thinning of the TEM lamina (e.g. 50-30 pA).
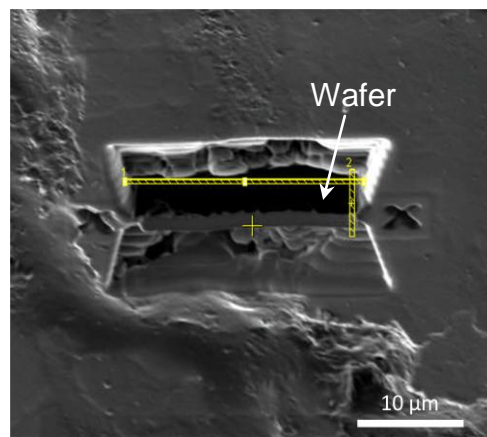
e) The sample is tilted to 7°. An undercut and two side cuts are made of the remaining TEM wafer. The side cuts are made halfway up the side from the bottom of the wafer.

2.9.1.2 Simultaneous use of Electron and Ion Beams

Prolonged dosage of Ga^+ ions can lead to substantial sputtering of material and sample penetration, incurring unwanted sample damage, even with a Pt cap over the sample. Imaging with the electron beam is possible and the ion beam can be used in snap shot mode at very low currents to produce an SE image. In a dual beam system, both beams require focussing at the same point of the sample. Upon operation of the dual beam system, the location of the sample needs to be where both beams are focused at the same spot and at any orientation. This is known as the Eucentric Height (EH). The EH can be obtained from the electron beam image, where the beam is focused at a recognised point on the sample at around $\times$ 2000 magnification. The focal working distance (distance of focused sample to end of the electron column) is set at initially 0° tilt, and with small incremental changes in tilt, the position change of the sample is amended through adjustment of the sample height (z control), and the focussing steps are repeated for ascending tilt angle. Once 52° tilt has been achieved, the EH can be finally checked by sending the stage back to 0° and checking that the sample is focused in the image at the same position for both the ion and electron beam.

2.9.1.3 *Omniprobe* Extraction

The TEM sample requires placement on a holder for subsequent TEM analysis. The wafer is extracted from the milled trench and onto to a FIB holder containing a copper grid. The FEI *Quanta* 3D at Leicester consists of the *Omniprobe*, a mechanical extraction device. This is essentially a tungsten needle which is controlled with a piezo electric motor. The tip of the needle can be guided to the sample and 'welded' with the GIS. After attachment to the copper grid, the end of the sample attached to the needle can be milled off.

2.9.1.4 FIB TEM sample preparation

Preparation of a complete TEM sample by FIB methods are done with the following general steps that have been modified from the FEI company instructions:

(a) An area of interest for TEM extraction is established and brought to EH.

(b) A strip of platinum is deposited to protect the sample through the milling process using the electron beam. A low accelerating voltage (3 kV) and a large current (1.5 nA) is used with a long dwell time (20 μs) and pitch overlap 50% for a maximum cross section interaction between the electron beam and GIS. A layer of approximately 150 nm is deposited.

(c) The platinum strip is centralised to the field of view and brought back to EH, preferably at slightly higher magnification.

(d) The TEM run script is deployed. Parameters relating to the thickness of the TEM wafer and the amount of platinum deposition can be varied in the runscript. A thick cap (2 µm) is preferable in order to ensure the continued presence of capping material after all manual thinning processes have been completed.

(e) Upon completion of the runscript, checks have to be made on the under and side cuts of the wafer. If they were unsuccessfully made, they can be re-done manually at 7° tilt, with the side and undercut being milled in parallel. This will ensure that no sputtered material is deposited back on either cut.

(f) The side which has been released through the cutting is brought to EH again, preferably at high magnification (e.g. x5000 magnification).

(g) With the sample placed perpendicular to the e$^-$ beam (0°), the stage is brought down through the z control.

(h) The GIS needle is inserted, followed by the *Omniprobe*.

(i) The *Omniprobe* is brought to EH i.e. the middle of electron beam and ion beam image. The *Omniprobe* is then brought up above EH by a known amount.

(j) The stage is slowly brought up through the z control up to EH again, ensuring that the *Omniprobe* needle is still above the sample.

(k) The *Omniprobe* is guided down to the side of the released wafer until contact is made on its edge.

(l) A small area of carbon is deposited with the ion beam around the end of the needle, ensuring that the needle is welded to the wafer at low current (e.g. 50 pA).
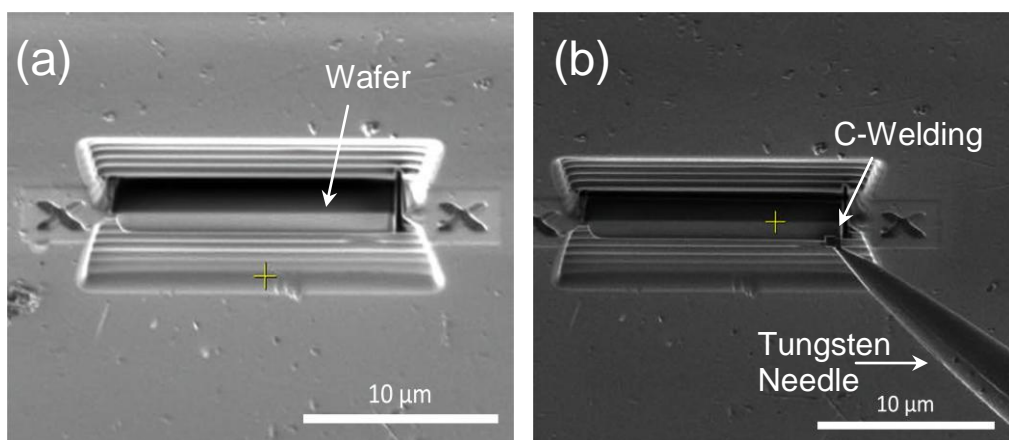
FIG 2.17: SE images of Barwell (L6 meteorite) olivine. (a) Wafer left at the end of the wizard runscript. (b) Attachment of the *Omniprobe* needle to the wafer having used the carbon GIS.

(m) The other side of the wafer is cut, freeing the lamina attached to the *Omniprobe* needle.

(n) The stage is brought back down; separating the wafer attached to the needle. The wafer is then brought to EH and then raised again. The GIS needle is retracted.

(o) The chamber is vented and the FIB-TEM holder is inserted containing the Omniprobe grid copper grid.

(p) The area of the holder for which the wafer is to be attached is placed at EH. The GIS needle is reinserted. The flat side of the *Omniprobe* copper grid is the most favourable side for attachment as its flat face can ensure maximum contact with the lamina upon welding.

(q) The wafer is brought down to the holder through careful guiding of the *Omniprobe* until contact is made.

(r) The end of the wafer is welded to the holder using the carbon GIS as in Fig 2.17b.

(s) The end of the wafer attached to the needle is milled off or the end of the needle itself milled. The *Omniprobe* is released, followed by the GIS needle.

(t) The stage is rotated and tilted such that the wafer is parallel to the ion beam. Any final polishing can be performed with the ion beam at low currents (<100 pA).
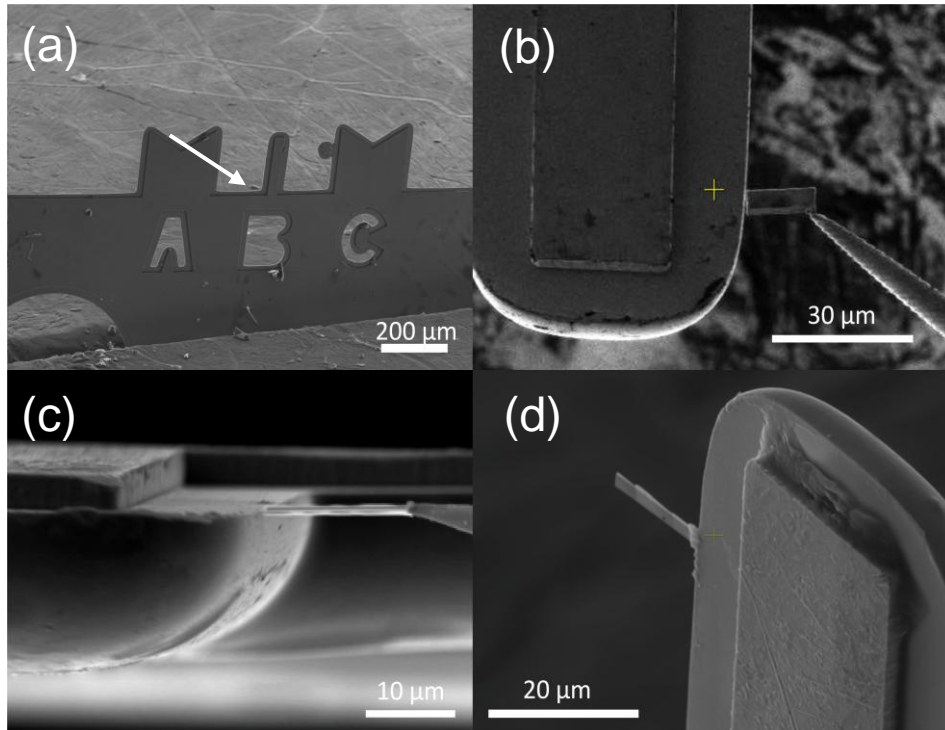
FIG 2.18: Wafer attachment to the *Omniprobe* copper grid. (a) The copper grid used for wafer attachment. Arrow indicates typical location used for TEM lamina. (b) Wafer guided towards grid with the *Omniprobe* as viewed by the ion beam. (c) View from electron beam. (d) Completed, polished wafer viewed at an arbitrary angle.

(u) The sample is now ready for TEM analysis. If the wafer is attached to the flat side of the grid, this side should be facing up against the incident beam to ensure that no obstruction of X-rays from the other side of the grid occurs during subsequent EDX analysis.

Samples that are produced *in situ* by the FIB-SEM method can exist in many different forms and environments. The desired TEM sample might, for instance, be multiple phases with very different sputtering rates along a section, or a particle on a substrate, or potentially monomineralic. The generic recipe described here would have to be adjusted based on the nature of the samples being prepared. This extraction method must be therefore modified and is not the same for every type of planetary material being investigated. For example, extraction of a particle on a substrate would require modification to this generic recipe in the type of capping and wafer size used to preserve surrounding material (see Section 4.3). A monomineralic material, however, may be prepared in a similar way to that described above. Where applied, modifications to this recipe are described for the specific planetary materials analysed in the subsequent chapters of this thesis. Examples of FIB-based analysis of other planetary materials can be found by Zega et al. (2007) and Graham et al. (2008). They also show that coordinated isotope analyses can also be performed on FIB-extracted samples, enhancing the capabilities for *in situ* nano characterisation of planetary materials.

2.10 TEM Calibration

Prior to any TEM analysis, the instrument requires calibration. Calibration steps are performed for all TEM modes of analysis i.e. imaging, spectroscopy and electron diffraction. They are described in the following sections.

2.10.1 HRTEM Scale Bar calibration

Images projected on the phosphor screen can also be generated on a digital camera below the screen. The Gatan *Ultra1000* is attached to the Jeol 2100 TEM at the University of Leicester. Calibration of the scale bar is required at low, intermediate and high magnifications prior to sample analysis. Silicon gratings of varying spacings can be used for the low and intermediate magnifications. Lattice spacing measurements at dimensions of order 10^{-9} - 10^{-10} m require the use of standards with well known lattice

spacings that can be readily imaged and interpreted. Graphitised carbon from *Agar Scientific* has been used for this (Fig 2.19). It has a cubic structure with 0.34 nm lattice spacings and crossing planes can be readily identified in one field of view. The scale bar can then be calibrated directly from these lattice spacing measurements. In HRTEM, the micrograph can be filtered to localise only the lattice information by localising only the lattice information from the Fourier Transform (FT) with the *Digital Micrograph* software and producing in inverse FT to render a filtered HRTEM image for more precise lattice measurements (Fig 2.20).
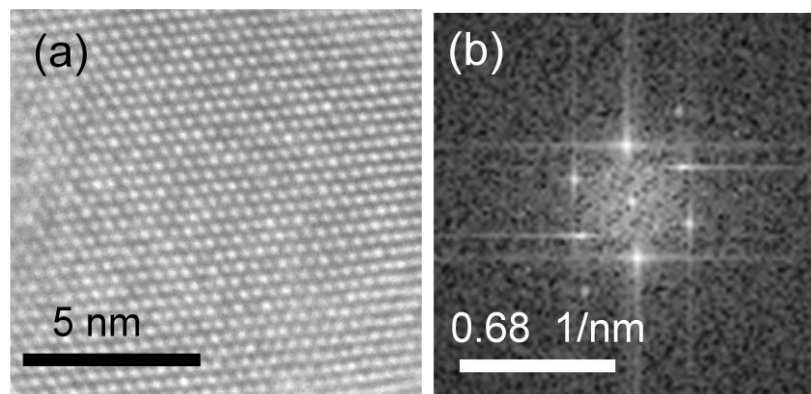
FIG 2.19: *Agar Scientific* graphitised carbon standard used for HRTEM calibration (A) Bright Field HRTEM of the graphitised carbon sample in the Jeol 2100. The spots represent the rows of carbon atoms co-ordinated in a Face Centred Cubic (FCC) structure. (B) Fast Fourier Transform (FFT) of real image in (a). Using the diffractogram, more pixels between two symmetrical spots can be measured for a more accurate measurement of the distance between two adjacent planes using the *Gatan* digital micrograph software.
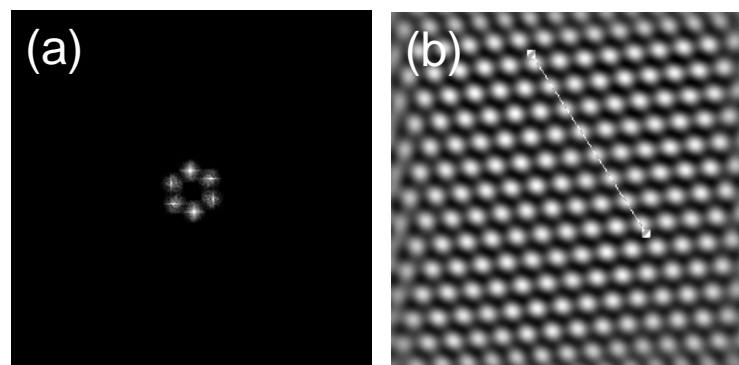
FIG 2.20: (a) FT of selected region from Fig 2.19a that has been masked to only contain the reciprocal lattice of the carbon standard. (b) Inverse FT of (a) to produce a FT filtered HRTEM image from Fig 2.19a.

Calibration has been made for the camera using The Gatan *Digital Micrograph* software. The software enables effective measurement of lattice pixel measurements with the use of histograms to graphically display the spacings as intense peaks. They can then be measured to the nearest pixel and put into the automated scale bar calibration software tool. For an increased number of pixels in the measurement, a Fast Fourier Transform (FFT) of the real HRTEM image will give the reciprocal lattice. (Fig 2.19b). The simulated FFT or 'diffractogram' marks the fringe separation between successive spots as in a Selected Area Electron Diffraction (SAED).
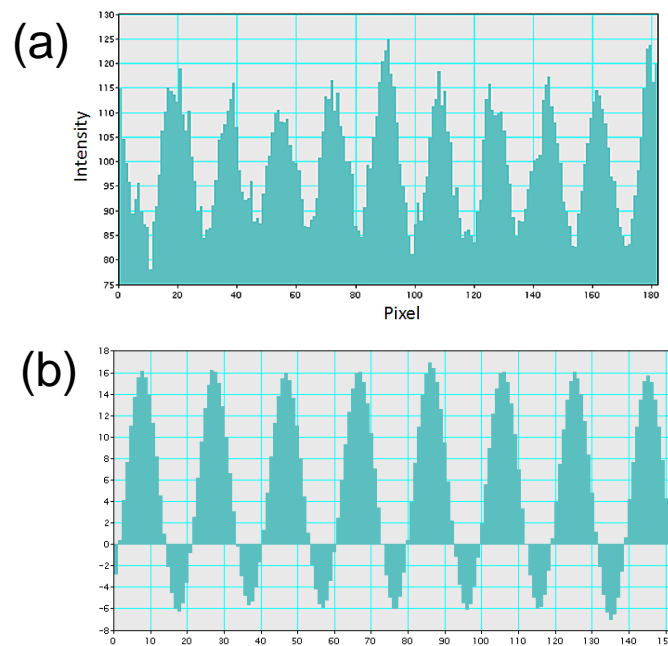
FIG 2.21: (a) Histogram generated with the digital micrograph software across a plane of spots in HRTEM of Fig 2.19a. Measurement in the number of pixels between successive peak intensities can provide an average real space d-spacing. (b) Histogram generated from FT filtered HRTEM in Fig 2.20b.

2.10.2 Diffraction Calibration

Interpretation of the structural details of a mineral by electron diffraction requires calibration with diffraction standards of known lattice spacings. Typical calibration steps for diffraction analysis are described. The interpretation and indexing of cubic and more complicated non cubic crystals are also described here.

2.10.2.1 D-spacing Calibration with Evaporated Aluminium Oxide

A sample positioned at a distance *L* from the projection of its focused diffracting pattern has a lattice spacing *d* inversely proportional to the distance between the diffracting lattice plane's diffraction spots *R*,

$$Rd = L\lambda \qquad\qquad (2.24)$$

where λ is the electron wavelength in the microscope. Using *Equation (2.24), d* can be determined with experimental calculation of $L\lambda$, known as the 'camera constant' of the microscope at a particular magnification or 'camera length' of the imaged diffraction pattern. Conventionally, a polycrystalline standard is used to calibrate this. Multiple measurements of the same *d*-spacings can be easily made from the ring patterns such as evaporated Al_2O_3.
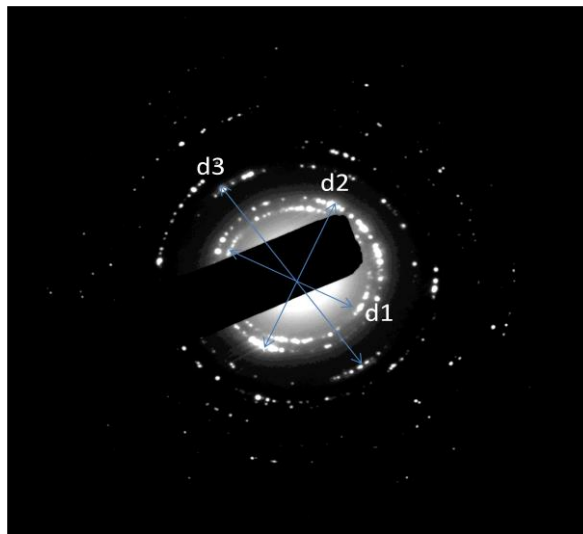
FIG 2.22: SAED diffraction pattern of *Agar Scientific* evaporated Al_2O_3 standard. *d1*, *d2* and *d3* correspond to the 1st, 2nd and 3rd order diffraction rings respectively (Table 2.1). Calculation of the camera constant has been made from multiple measurements of all three rings and generating an average value for the camera constant.

The measured ring spacings shown in Fig 2.22 and Table 2.1 (APPENDIX A) are for the first three diffraction rings of the *Agar* Al_2O_3 standard. Al_2O_3 has an FCC structure. Due to extinction rules, only all odd and all even *h*, *k* and *l* indices provide suitable orders of reflection N *($h^2 + k^2 + l^2$)*.

2.10.2.3 Indexing of Cubic and non Cubic Structures

As the three primitive lattice vectors of a unit cell in a cubic crystal are all orthogonal to one another and the same length, the angle Ø between any two planes can be readily defined with *Equation (2.25)*:

$$\cos \emptyset = \frac{h_1 h_2 + k_1 k_2 + l_1 l_2}{\sqrt{h_1^2 + k_1^2 + l_1^2} \sqrt{h_2^2 + k_2^2 + l_2^2}} \qquad (2.25)$$

Where a is the lattice constant h, k and l are the Miller indices of the plane (Champess, 2001). The spacing d of a plane is:

$$d = \frac{a}{\sqrt{h^2 + k^2 + l^2}} \qquad (2.26)$$

The ratio of two sets of d-spacings of particular Miller planes are independent of the lattice constant a by *Equation (2.26)* and is therefore constant for all cubic minerals. Measurement of the distance R between two sets of spots in reciprocal space expressed as a ratio can then be matched to the ratio of two potential planes. The indexed planes can then be verified by measuring the angle between them and checking if the planes satisfy *Equation (2.25)*.

This process cannot, however, be applied to non-cubic structures. In a non cubic crystal the lattice vectors can be at variable angles and relative lengths based on one of many permutations between the 7 crystals classes for minerals. The lattice spacing for a triclinic crystal – with all lattice dimensions a, b, c and angles α, β, γ of varying magnitude is given by *Equation (2.27)*:

$$d^{*}_{hkl}{}^2 = h^2 a^{*2} + k^2 b^{*2} + l^2 c^{*2} + 2klb^* c^* \cos \alpha^* + 2lhc^* a^* \cos \beta^* + 2hka^* b^* \cos \gamma^* \ (2.27)$$

where * donates the dimensions and angles in reciprocal space (McKie & McKie, 1974). A different method for indexing unknown non cubic crystal classes is, therefore required. Potential zone axes can be proposed based on assumptions of the unknown mineral's crystal class and the shape of its reciprocal lattice. This may be assisted by chemical information by EDX. The proposed zone axis of the assumed mineral can then be simulated by using diffraction simulation software such as W*eb EMAPS* (Zuo and Mobon, 2004).

2.11 Calibration for TEM-EDX Quantitative Analysis

Equation (2.20) that is used to calculate the concentration of an element in the TEM requires determination of a sensitivity *K*-factor. To determine K_{AB}, C_A and C_B are

derived from a standard. An element is used (usually Si or Fe as they are found in many minerals and alloys) to which all other *K*-factors are normalised (Cliff and Lorimer, 1975). This allows other *K*-factors (e.g. K_{CB}) to be calculated ($K_{CB} = K_{AB}/K_{AC}$) if they entirely make up the sample's composition (i.e. $C_A + C_B + C_C = 100\%$). The PGT *Gamma Tech Spirit* software contains default *K*-factors for the microscope that are normalised to Si (i.e. K_{XSi}). They are provided in Fig 2.23.
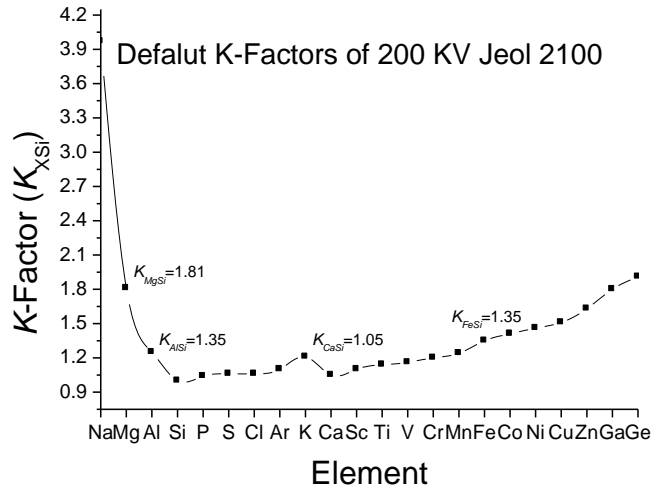
FIG 2.23: Default K-factors provided with the *Spirit* software for the Jeol 2100.

These 'nominal' *K*-factors values act as a starting point for generating a quantitative analysis with the *Spirit* software, which measures peak/background ratios and uses *Equation (2.20)* on the desired elements in an EDX spectrum. By trial and error, modification of the K_{XSi} values for an element *X* have been made to fit the composition of a standard. These trial *K*-factors have then been tested on other secondary standards of similar and known compositions. This can be seen by substituting C_A, and C_B with C_x and C_{Si} respectively in *Equation (2.20)* to give:

$$\frac{C_X}{C_{Si}} = \frac{K_X}{K_{Si}} \cdot \frac{I_x}{I_{Si}} \qquad (2.28)$$

Where I_x and I_{Si} are the intensities of element *x* and Si respectively. This procedure is described in more detail in the following sections and proved to be a valid method for calculating experimental *K*-factors on standards using O-based stoichiometry with *Spirit* and the Cliff-Lorimer method. Peak intensities are integrated automatically by the

software and Net peak counts are also calculated with background subtraction around the peaks selected. The *K*-factor to use is inputted manually.

2.11.1 Mineral Standards

Mineral standards of known composition have been used to determine the experimental *K*-factors. Igneous minerals in Type 6 chondrites are equilibrated (contain an homogenous chemical composition) and thus ideal for this. Barwell is an L6 ordinary chondrite. Its Fo_{75} olivine has been used in this thesis to determine the *K*-factors for Fe and Mg. These values were then tested against an olivine of a different Mg# - $Mg_{at}/(Mg_{at}+Fe_{at})$ ratio. San Carlos olivine, a terrestrial sample from New Mexico is equilibrated, with Fo_{91} (i.e. $Mg_{at}/(Mg_{at}+Fe_{at}) \times 100 = 91$) composition and was used for this test (Kohlstedt and Mackwell, 1987). Oxygen-based stoichiometry can be verified with a calcium-poor pyroxene of known composition. Ca *K*-factors have been chosen to be determined with a diopside mineral of known composition ($En_{50}Wo_{45}Fs_5$) and tested on Barwell Ca-rich pyroxene ($En_{47}Wo_{44}Fs_8$). $En_x = Mg_{at}/(Mg_{at}+Fe_{at}+ Ca_{at}) \times 100$; $Wo_x = Ca_{at}/(Mg_{at}+Fe_{at}+ Ca_{at}) \times 100$ and $Fs_x = Fe_{at}/(Mg_{at}+Fe_{at}+ Ca_{at}) \times 100$.

For the Al *K*-factor, a pure Al-silicate mineral has been used − kyanite (Al_2SiO_5). These major elements were selected for calibration in order to perform AEM analyses of the Wild2 samples in Chapter 6.

2.11.2 Elemental *K*-factors

Barwell Olivine

Barwell olivine was extracted and manually thinned to ensure the ultra thin foil criterion. An EDX spectrum was taken for 600 s in the TEM with a 25 nm spot size. deadtimes below 15% were measured. *K*-factors of Fe and Mg were generated to produce a stoichiometric olivine of 75% at. Mg/Mg + Fe composition using the Cliff Lorimer method. The following *K*-factors were determined that provided closest to this compositon:

$$K_{MgSi} = 1.25 \qquad K_{FeSi} = 1.36$$

San Carlos Olivine

The Mg and Fe *K*-factors were tested on an extracted wafer of San Carlos olivine. Multiple spectra were obtained for approximately 200 s. Table 2.2 in

APPENDIX A shows the representative and average compositions that were obtained. We see an average Mg# of 91% consistent with the accepted composition of San Carlos olivine (Kohlstedt and Mackwell, 1987). The experimental K-factors derived for Mg and Fe therefore provide us with acceptable quantitative analyses for other olivine compositions.

Frontier Mountain Chondrite

Frontier Mountain FRO90045.001 is an L4 ordinary chondrite. The experimental K-factors were tested against an Fe-Mg pyroxene to check for consistency in this oxygen based stoichiometry by AEM. A calcium-poor pyroxene was identified and its composition measured by SEM-EDX. The pyroxene was then extracted under the same conditions and analysed by AEM. The respective compositions that were obtained are found in Table 2.3 (APPENDIX A).

To the nearest tenth of a percentile concentration, the composition measured by AEM of this enstatite is consistent with that by SEM-EDX (i.e. Si/O and (Mg+Fe)/Si ratios). Table 2.3 shows that the deviation of Fe at% (absolute error) is slightly higher when compared with the SEM-EDX composition and Mg at% (absolute error) lower concentration marginally that has compounded the error in Mg# by 2% compared to the SEM-EDX composition. At first glance, one may suggest that an increased thickness could have cause these results. However, in Section 2.11.3, we also see how initially notable thickness changes should not have this much of an effect if there was some deviation from ultra thin criterion. Compounded errors can lead to a 2% absolute error when cation ratios are taken for Fo and En numbers etc. The current accuracy does verify the use of these K-factors for TEM quantitative analysis for at least Fe and Mg based olivines and pyroxenes that are studied by AEM in Chapter 6.

Diopside

Mg-Ca-Fe pyroxene (diopside $En_{50}Wo_{45}Fs_5$) was extracted and manually thinned to achieve ultra thin foil criterion. This was used to derive an experimental K-factor for Ca by using the established Mg and Fe K-factors. SEM-EDX was used to determine its composition prior to extraction. TEM-EDX was performed in the same way as the other standards (200 - 600 s acquisition with a 25 nm spot size. Deadtimes of 20-30% were used and the Ca K-factor was amended to fit the pyroxene composition, and using the already calibrated Mg K-factor. Table 2.4 (APPENDIX A) shows the

SEM-EDX composition and the TEM-EDX composition before and after calibration of the Ca K-factor. A K-factor for Ca was obtained that then brought the diopside Ca concentration equal to the SEM-EDX composition to the nearest 0.1 wt%.

$$K_{CaSi} = 1.1$$

Kyanite-Al$_2$SiO$_4$

A kyanite (Al$_2$SiO$_5$) standard was provided by the Dept. of Geology, UoL. Being a pure Al silicate, the Al K-factor was set to fit the ~25 at% of Al and Si/O ratio of 1:5 as shown by its SEM composition (Table 2.5 APPENDIX A). An ultra thin TEM sample was made and a TEM-EDX spectrum were obtained using the same acquisition settings as for the other standards to give the following K-factor:

$$K_{AlSi} = 1.0$$

Secondary Test Barwell Pyroxene

Barwell pyroxene, measured as En$_{47}$Wo$_{45}$Fs$_8$ by WDS was used to test the accuracy of the calibrated K-factors. Table 2.6 in APPENDIX A shows the TEM-EDX measurements in comparison to the obtained WDS data prior to extraction for TEM (See Fig 2.20 for HRTEM image of the pyroxene). The table shows the Mg/(Mg+Fe+Ca) − En#), Fe/(Fe+Mg+Ca) − Fs# and Ca/(Ca+Mg+Fe) - Wo# ratios to be consistent within 1% of one another. In atomic proportions, the greatest absolute error seems to be in the Si concentration between the two measurements (average 19.5 at% for WDS compared to 20.4 at% for TEM-EDX. The greatest error found in the Si concentration could be attributed to Si being unstandardised and normalised with respect to the other elements. However, the measured cation ratios and consistent stoichiometry with pyroxene suggest that the described experimental calibration steps have been successful for AEM of silicates containing Fe, Mg, Al and Ca to an absolute error of approximately 1% (assuming that the WDS measurements are exact values).
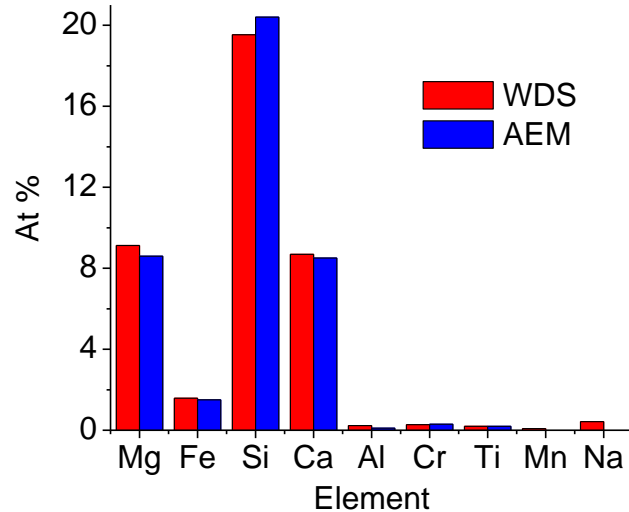
FIG 2.24: Average composition of Barwell augite by WDS compared to AEM composition. Relative error for the major elements atomic concentrations are: Si 4.4%, Mg 5.8%, Fe 5.1% and 2.2% for Ca. Note the largest changes in the experimental k-factors from default settings are for the lowest Z numbers i.e. Mg and Al. Thus, the largest uncertainty in experimental K-factors are for the lower Z numbers. Relative errors for trace concentrations have not been considered.
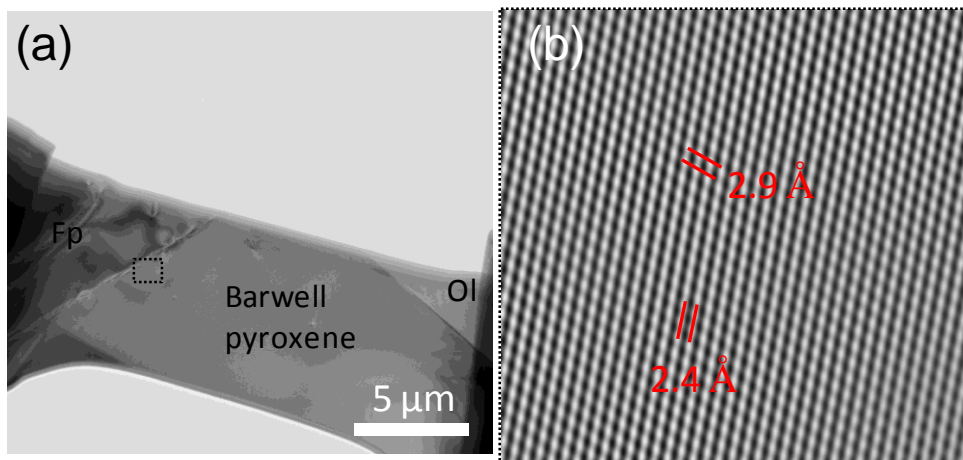
Fig 2.25: Secondary test Barwell pyroxene standard for Mg, Fe and Ca *K*-factors. (a) Low magnification BF image of extracted sample. The pyroxene is surrounded by feldspar (left and olivine (top right). (b) FT filtered HRTEM of the augite grain close to the boundary of the feldspar, where one of the TEM-EDX spot analyses was also taken. Note that the protective cap has been lost from the final thinning process. However, HRTEM imagaing shows that the mineral structure was presevered and not amorphised by the milling and extraction process. Feldspar, Fp; Olivine, Ol.

TABLE 2.7: *Summary of calibrated K-factors for the PGT Gamma Tech on Jeol 2100*

Element	Default K-factor	Calibrated K-factor	Relative Error in AEM (%)
Mg	1.81	1.25	5.8
Fe	1.25	1.36	5.1
Ca	1.05	1.10	2.2
Al	1.25	1.00	–

Table 2.7 summarises the values of the K-factors that were determined and the relative errors found upon comparison with the Barwell pyroxene standard. The largest changes in the experimental *K*-factors from default settings are for the lowest Z numbers i.e. Mg and Al. Thus, the largest uncertainty in experimental K-factors is for the lower Z numbers. Relative errors for trace concentrations in the Barwell augite have not been considered.

2.11.3 Thickness correction for AEM

A correction can be applied to the Cliff Lorimer *Equation (2.20)* by use of the thickness attenuation coefficient in *Equation (2.15)* and the path length based on the take off angle of the detector in *Equation (2.16)* to provide an Absorption Correction Function (ACF) (Goldstein and Newbury, 2003). To test this with the *Spirit PGT Gamma-Tech* software, a wafer of Barwell olivine was produced initially with a thickness of 500-600 nm. The wafer was then sectioned into the four different thicknesses; the first being ultra thin and measured at ~80 nm, the next at ~130 nm, the third section at ~290 nm and the final section at ~600 nm (Fig 2.26). The thicknesses were measured directly from the FIB-SEM SE images. Difficulty in accurately measuring these thicknesses is due to the relative unevenness of the wafer and human error in the measuring tool. These measurements are therefore only approximations.

TABLE 2.8: *AEM compositions of Barwell olivine at different thicknesses, with and without thickness corrections.*

	Ultra Thin		130 nm (No correction t = 0)		290 nm (No correction t = 0)		600 nm (No correction t = 0)
Wt %	Representative	Average (N = 8) Representative		Average (N = 5) Representative		Average (N = 3)	(N = 1)
MgO	38.7	39.2	37.4	37.3	35.2	35.9	25
MnO	0.2	0.1	0.5	0.3	0.5	0.4	0.5
FeO	22.8	22.5	24.6	23.6	27	26.7	41.6
SiO2	38.2	38.2	37.5	38.8	37.4	37	32.9
Total	100	100	100	100	100	100	100
At %							
Mg	21.5	21.7	21	20.8	19.9	20.1	15.3
Mn	0	0.9	0.2	0.1	0.2	0.1	0.2
Fe	7.1	7	7.7	7.4	8.6	8.7	14.3
Si	14.2	14.2	14.1	14.5	14.2	14.1	13.5
O	57.1	57.1	57.1	57.3	57.1	57	56.8
Total	100	100	100	100	100	100	100
Mg#	**0.75**	**0.76**	**0.73**	**0.74**	**0.70**	**0.70**	**0.52**
Wt %			$(t = 130\ nm, \rho = 3.2\ gm^{-3})$		$(t = 290\ nm, \rho = 3.2\ gm^{-3})$		$(t = 600\ nm, \rho = 3.2)$
MgO	-	-	38.7	38.5	38.2	38.4	32.1
MnO	-	-	0.4	0.3	0.3	0.3	0.3
FeO	-	-	23.2	22.3	23.2	23.8	32.5
SiO_2	-	-	37.7	39	38.3	37.6	35.1
Total	-	-	100	100	100	100	100
At %							
Mg	-	-	21.5	21.3	21.2	21.4	18.7
Mn	-	-	0.1	0.1	0.1	0.1	0.1
Fe	-	-	7.3	6.9	7.2	7.4	10.6
Si	-	-	14.1	14.5	14.3	14	13.7
O	-	-	57	57.2	57.2	57	56.9
Total	-	-	100	100	100	100	100
Mg#	**-**	**-**	**0.75**	**0.76**	**0.75**	**0.74**	**0.64**
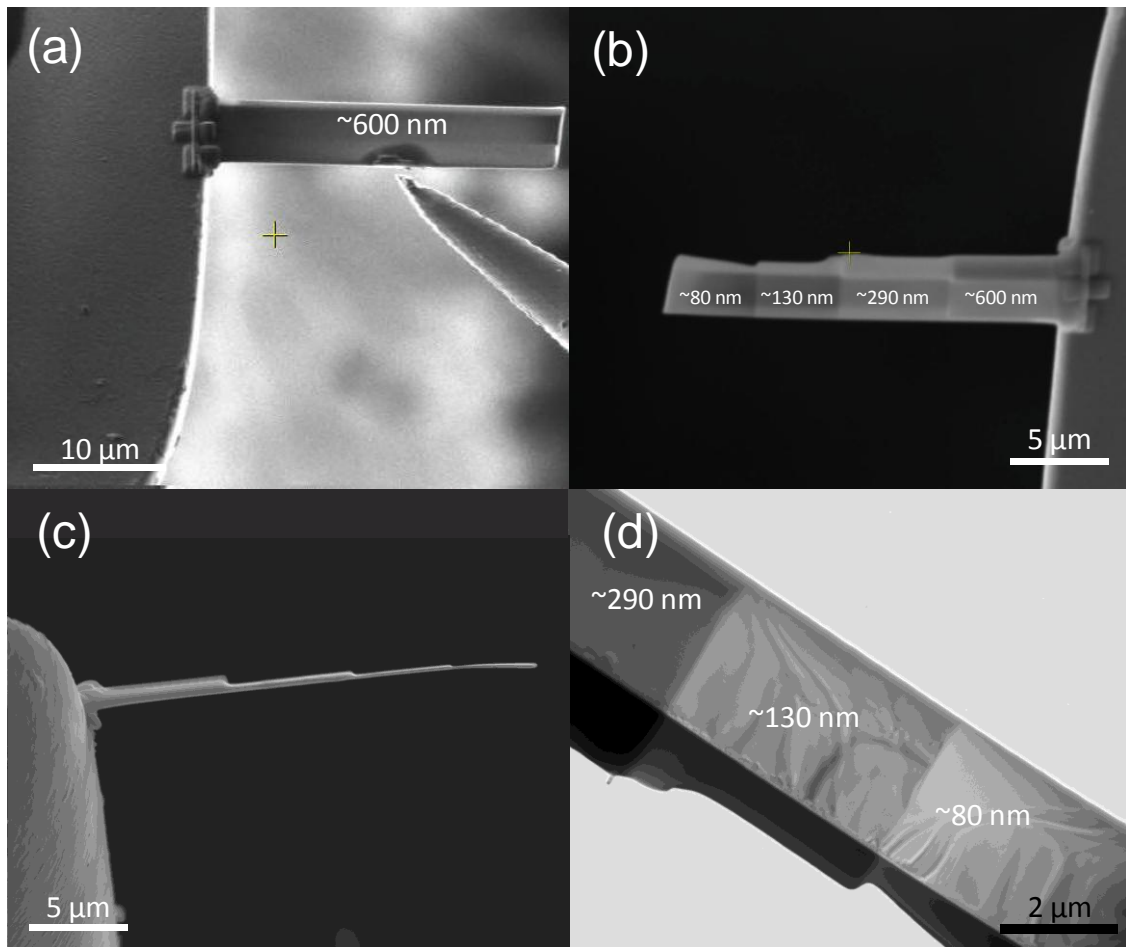
FIG 2.26: Extended wafer (20 μm length) of Barwell Olivine. (a) A 400-500 nm thick wafer was extracted onto an *Omniprobe* grid. (b) The wafer was divided into 4 segments of different thicknesses. (c) They were also measured with the SEM measuring tool, post thinning. (d) Low magnification BF TEM image showing the first three segments of the variable thickness Barwell olivine wafer.

Application of the calibrated *K*-factors to thicker samples will underestimate the cations' intensities (with the proviso that fluorescence effects do not play a role and low energy K-lines are not re-excited); especially the lower energy X-rays such as Mg Kα, as they are attenuated by the increased absorption. By applying the thickness measurement to the quantitative analysis routine, with an assumed density of olivine (3.2 gm^{-3}), effective corrections can be made for the absorbed low energy X-rays such as Mg Kα. In Table. 2.8, we see the Mg# diminishing with increased thicknesses. However, corrections made for 130 nm and 290 nm brings the composition back to stoichiometric Barwell olivine. At 600 nm with no correction, the Mg# is decreased by 23% from its accepted value. After application of the thickness correction, this still leaves it 11% from Fo$_{75}$. At such high thicknesses, the Cliff Lorimer technique with this absorption correction clearly breaks down. Therefore, at very large thicknesses (i.e.

~600 nm), matrix effects come in to play and a thickness correction using Beer's Law will not suffice.
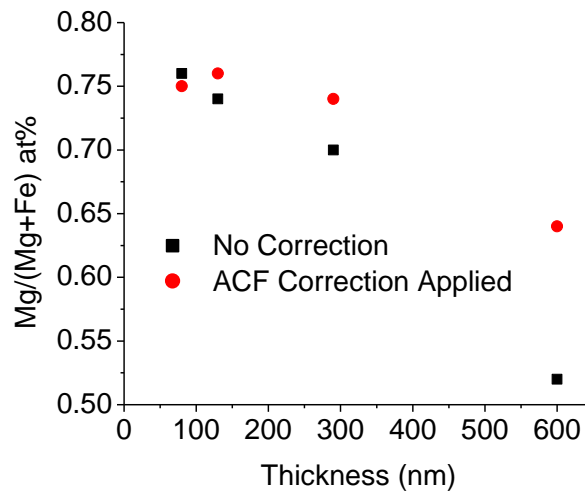
FIG 2.25: Average Mg# of Barwell olivine at four different thicknesses with and without the ACF factors applied by the software. Applying the ACF up to 290 nm brings the Mg# consistent to its accepted value within 1 at% absolute error. Accepted value is 0.75. Thus, sample thicknesses from 100-300 nm, when used with a thickness correction prior to the Cliff-Lorimer quantitative analysis, can provide a reasonably accurate TEM-EDX analysis, at least of Mg-rich olivine.

2.12 Summary and Conclusions

The theory behind electron microscopy has been provided, with details of specific instruments that have been used for the microanalysis of planetary materials in this thesis.

A FIB-TEM sample preparation technique has been devised and adopted for subsequent studies described in this thesis. Calibration steps for TEM, electron diffraction and AEM analyses in subsequent chapters have also been described.

Experimental K-factors using the Cliff Lorimer method and thickness corrections have been successfully determined for some major elements, justifying the AEM results to follow in this thesis. *K*-factors for Mg, Fe, Ca and Al (normalised to Si) were found to be 1.25, 1.36, 1.1 and 1.0 respectively. Relative errors in major element concentrations have been shown to range from ~ 2 – 5% for these k-factors by comparison with the secondary Barwell pyroxene standard. Thickness corrections for TEM wafers from 100-300 nm have been shown to provide acceptable EDX measurements of Barwell olivine. At 600 nm, the ACF function does not suffice.

Chapter 3
Methodology II: Synchrotron-based X-ray Microfocus X-ray Spectroscopy

3.1 Introduction

Synchrotron beamlines are extremely powerful diagnostic tools in micro analytical studies. They are the brightest and most coherent sources of X-rays used in sample analysis. Their intensities can provide elemental detection limits approaching parts per billion that are coupled with sub micron to nanometre spatial resolutions. Their energies can be tuned around the transition edge energies of an element, providing atomic and molecular structural information. Samples can also be analysed in their bulk state and in atmosphere, enabling sample preservation and ease of sample containment prior to potential analysis by other micro analytical techniques. X-ray microfocus spectroscopy has therefore been a vital tool for the analysis of *Stardust* tracks. The application of this technique within this thesis has been used on *Stardust* Comet Wild2 samples.

This chapter introduces the synchrotron beamline used in this research. The key theory of synchrotron-based microfocus X-ray spectroscopy is also described here. The analytical techniques of X-ray Absorption Spectroscopy; XRF, XANES analysis and EXAFS are covered. They were first established at synchrotrons in the early 70s (Sayers et al., 1971; Lytle, 1999). Compositional-based imaging (mapping and point spectra), can help us to understand the elemental distributions concentrations (XRF). By using X-ray Absorption Fine Structure (XAFS) techniques (i.e. XANES and EXAFS) we can determine mineral identifications with their structural and co-ordination environment(s).

This chapter is followed by a brief investigation into the use of FIB-based samples for XAFS inorder to enhance the capabilities of *in situ* synchrotron based characterisation of planetary materials.

3.2 The *Diamond* Light Source

The *Diamond* Light Source at Didcot, Oxfordshire is a 3 GeV synchrotron that was first commissioned in 2006. At *Diamond*, bending magnets accelerate electrons with relativistic speeds around a storage ring with currents of typically 200 mA. Various types of microprobes and nanoprobes can be eventually available at the 40 proposed beamlines at *Diamond*. Currently, there are 7 beamlines in operation. Individual beamlines are tailored for either broadband X-rays in the form of bending magnetic or wriggler radiation, or tuned (at generally lower energies) using undulator radiation (see section 3.2.1). Diamond is therefore termed as a third generation synchrotron. At *Diamond*, electrons are initially accelerated with a small linear accelerator that then leads to a smaller booster ring to finally enter the main synchrotron.

3.2.1 Beamline I-18

The beamline used at *Diamond* in this thesis is Insertion Device I-18. I18 is the Microfocus Spectroscopy Beamline. The Insertion Device for I18 is an in-vacuum undulator with magnetic period 27 mm (Mosselmans et al., 2000). Oscillating electrons from the main ring are fed into the undulator that produce coherent (e.g. uniform plane waves) and canonical dipole X-ray radiation (Attwood, 2000). They are further narrowed with an aperture. A set of double Si [1 1 1] and [3 1 1] monochromators are used for energy selection using the principle of Bragg reflection through the correctly oriented monochromator(s), as described in *Equation (2.7)*. The beam can be tuned from 2-20 keV, with an energy resolution $\Delta E/E$ of each Si [1 1 1] and [3 1 1] crystal being 10^{-4} and 10^{-5} respectively. Focusing optics are used based on a Kirk-Baez optical design (Kirkpatrick and Baez, 1948). Detailed theory of synchrotron radiation and X-ray optics are not provided here but can be found in sources such as Attwood (1999) and Michette (1986).

A 9 element germanium solid state detector is used at the beamline, capable of detecting fluorescence X-rays above 5 keV and a 4 element Si drift fluorescence detector is used for energies from 2-5 keV. Helium-based ion chambers are located at positions before and after transmission through the sample for intensity measurements. A live video microscope is used for viewing the sample and alignment of the sample with the focus of the X-ray beam (Fig 3.1). The OM is typically aligned using gold

cross hairs that block transmission of the beam and energy calibration is made with an Fe foil standard. An Image of the Diamond synchrotron and a schematic of Beamline I-18 is in Fig 3.2.
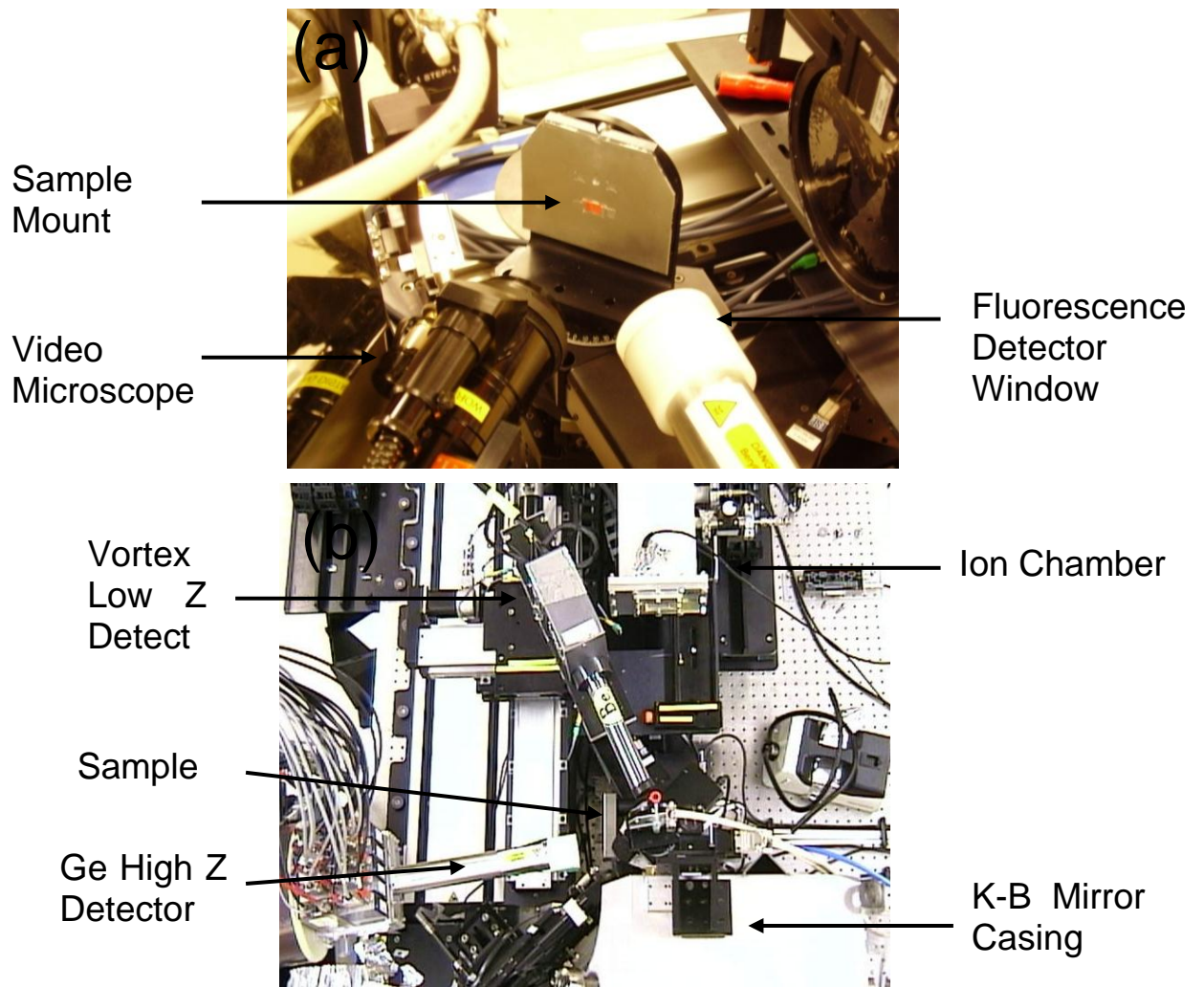
FIG 3.1: (a) Photograph of sampling area. The sample is attached in the centre of the mount (orange Kapton tape) that is fastened with magnets at the corners of the mount. (b) Plain view of experimental hutch showing the end of the beamline with the positioned detectors.

(a)

(b)

(c)
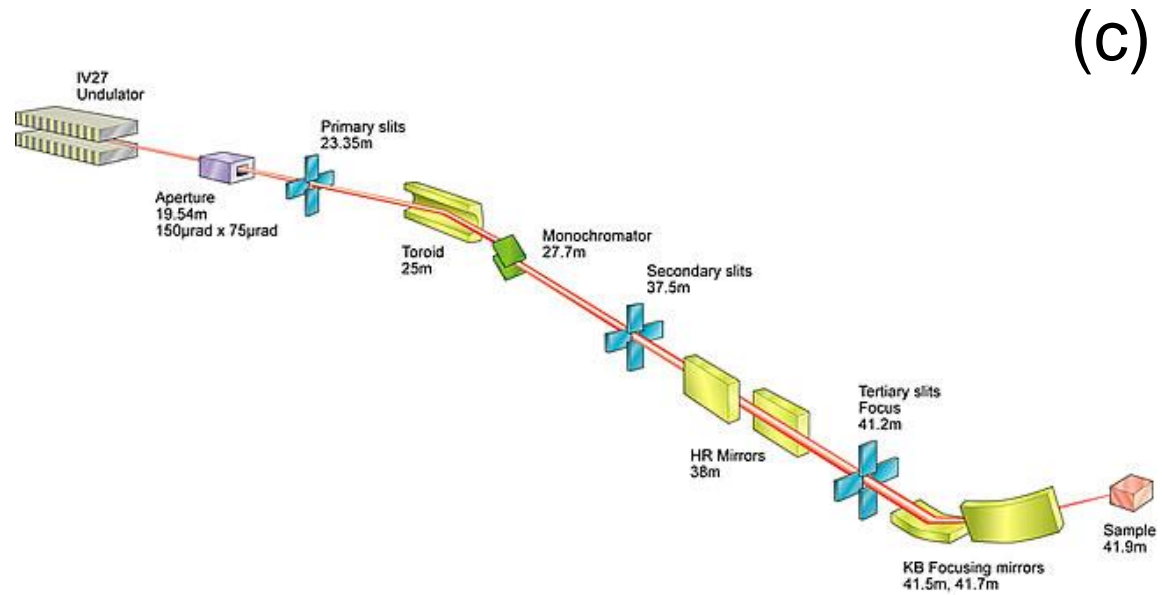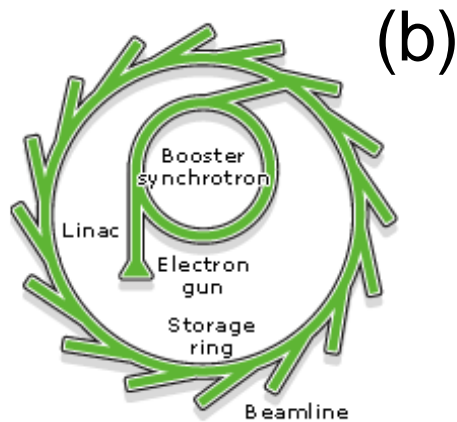
FIG 3.2: The *Diamond* Light Source. (a) Aerial photograph of the *Diamond* facility. ~80 m Storage ring diameter (b) Cartoon illustrating the entire synchrotrons 3rd generation set-up. (c) The design of Beamline I-18. Image from *Diamond.ac.uk*.

3.3 X-ray Microfocus Spectroscopy

The design requirements of I18 are specified for XRF, XANES and EXAFS. The theories behind these techniques are described here, together with an introduction to the key software tools used at *Diamond* for data acquisition.

3.3.1 X-Ray Fluorescence Spectroscopy (XRF)

The release of X-ray photons by the liberation of core shell electrons (as described in Section 2.6) can also be the consequence of incident X-ray photons. The liberated free electron is the photoelectron as first described by the photoelectric effect in metals by Einstein (1905). Similar to EDX and WDS analyses, these fluorescence X-rays are detected with a solid state detector based on similar physical principles as described in Section 2.2.1.

Movement of the sample under the focused X-ray beam of I-18 allows an area of the sample to be analysed for fluorescent X-rays within an approximate 2×2 μm beam and an approximate flux density of 10^{11} photons $s^{-1}m^{-2}$. Tuning of the incident beam energy just above the absorption edge energy (binding energy of a core shell electron) of an element of interest will maximise the probability of X-ray generation at that particular edge-energy. Positioning the solid state detector at 45° to the sample prevents saturation in the detector by the elastically scattered X-ray photons. Under fluorescence detection, the probability of absorption of X-rays as a function of energy $\mu(E)$ is related to the beam intensity by *Equation (3.1)*:

$$\mu(E) \approx \frac{I}{I_0} \qquad (3.1)$$

Where I is the measured X-ray intensity and I_0 is the incident beam intensity incident on the sample at a particular energy (Newville, 2004). With the use of an ion chamber, the transmitted beam intensity through the sample can be measured. Application of Beer's Law in *Equation (2.14)* can provide the absorption coefficient as:

$$\mu(E) = \log\frac{I}{I_0} \qquad (3.2)$$

The detection of fluorescent X-rays from a sample in a similar manner to EDX allows an energy dispersive spectrum to be generated, a main difference being the large peak of the elastically scattered X-rays. Fig 3 shows how the scattering peak for 10 keV X-rays, for instance, can overlap with Cu Kα and Zn Kα peaks. Movement of the sample with a piezo electric stage can allow mapping or point spectra to be generated in at least ~2μm steps to allow elemental characterisation of the sample. In this study, fluorescence spectra and maps have been analysed using the European Synchrotron Radiation Facilities's (ESRF) *PyMCA* software. Calibration files of the detector made by I-18 are loaded in *PyMCA* in order to link the detector display channels to their respective fluorescent energies. An example of a fluorescent spectrum from Beamline I-18 using PyMCA is in Fig 3.3. Energy windows can be displayed from any region of interest from the spectrum to show elemental distributions. Spectral fits can also be acquired for peak overlaps and X-ray background subtraction.
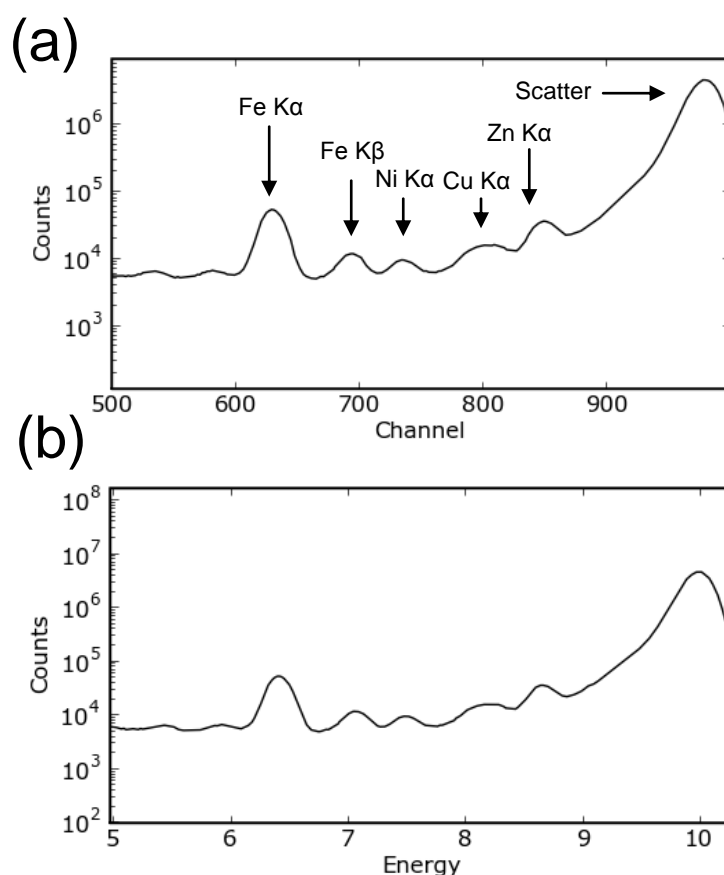
FIG 3.3: (a) A representative uncalibrated characterisitic X-ray fluorescence spectrum at I-18 using the *PyMCA* software. The incident X-ray energy is 10 keV, represented by the elastically scattered peak and inelastically scattered (Compton scattered) peak that is indistinguishable from the elastic peak. (b) The channels are allocated to their corresponding energies via a calibration file of the desired detectors.

3.3.2 X-ray Absorption Fine Structure

The probability of X-ray absorption maximises at the binding energy of the core shell electron. An absorption profile at the edge energy specific to each element is known as the 'white line' (Fig 3.4). Around this energy, quantum mechanical selection rules of orbitals and the interaction of the free electron wavefunction with its immediate chemical environment would determine addition transitions around the edge energy (e.g. Kronig, 1931). The transition between two quantum states leading to photo absorption can be summarised by Fermi's Golden Rule:

$$\mu(E) \propto |\langle i|H|f\rangle|^2 \qquad\qquad (3.3)$$

where $\langle i|$ is the initial state (an X-ray, a core electron, and no photo-electron), $|f\rangle$ is the final state (no X-ray, a core-hole, and a photo-electron), and H is the Hamiltonian operator. (Newville, 2004). The absorption spectrum around 50 eV above and below the edge energy is due to the near-edge structure and is thus classified as XANES (Koningsberger and Prins, 1988). Changes in the charge distribution of a given atom in different chemical environments can alter the core binding energies of the atom. The combination of orbital transitions around the edge, the amplitude of the white line with respect to the rest of the XANES region and the peak energy shift due to the extent of electro-negativity can be used to 'fingerprint' the charge state and chemical environment of a given material, and hence enable us to identify minerals. A relative absorbance profile along the edge structure shows these absorption features as 'bumps' around the white line and oscillations at higher energies that decay. They can be presented minus the background spectrum via subtraction of the pre and background and normalisation to the post edge region. At *Diamond*, *Pyspline* software (Tenderholt et al., 2007) has been used for this. As the pre-edge background usually linearly diminishes towards the white line, a linear subtraction will usually suffice. A normalisation constant is derived by normalising past the white line in the EXAFS region. This study has concentrated on the Fe-K edge for XANES and EXAFS (Section 3.4). Any other element edges can be analysed by their fine structure if the energy capabilities of the beam line meet the edge energy of a particular element.
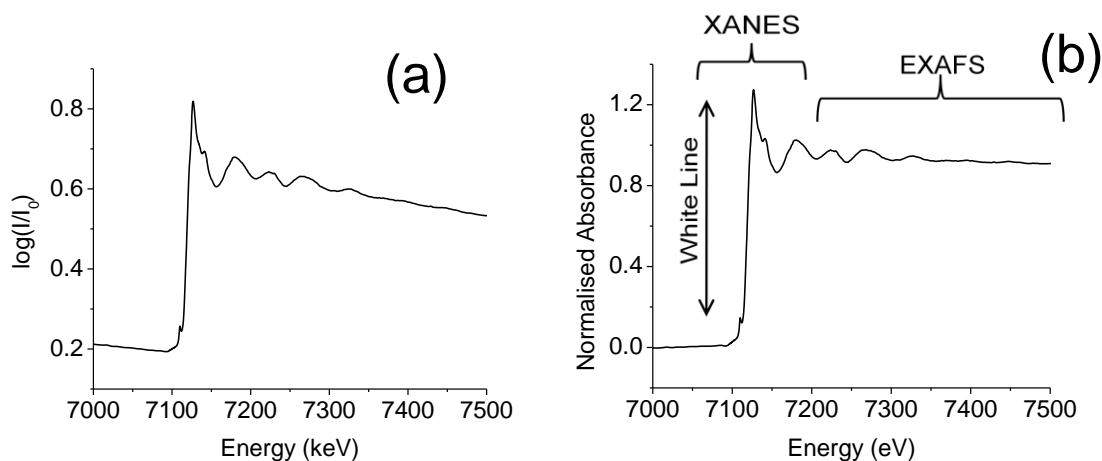
FIG 3.4: Fe K-edge XANES relative absorbance spectrum of a magnetite Fe_3O_4 NHM standard at I-18 (See Appendix). (a) Raw absorbance profile (b) Pre-edge background subtracted and normalised spectrum of (a) using *Pyspline.* The pre-edge bump is due to a transition to the unoccupied d-orbitals in Fe.

3.3.3 Extended X-ray Absorption Fine Structure

The interaction between the photo electron and its nearest neighbours is best described by spherical wave theory and is therefore treated in reciprocal or *k*-space (Lee and Pendry, 1975). The difference in energy between the absorption edge energy E_0 and an arbitrary energy E along the fine structure is the transition energy, and is re arranged for *k* using in *Equation (3.4)*:

$$k = \sqrt{\frac{2m(E-E_0)}{h^2}} \qquad\qquad (3.4)$$

The EXAFS fine structure is defined by absorption features past the edge, whose oscillations are defined as:

$$x(E) = \frac{\mu(E)-\mu_0(E)}{\Delta\mu_0(E)} \qquad\qquad (3.5)$$

where $\mu(E)$ is the measured absorption coefficient, $\mu_0(E)$ is a smooth background function representing the absorption of an isolated atom, and $\Delta\mu_0$ is the measured jump in the absorption $\mu(E)$ at the threshold energy E_0.

The post edge background is generally described by a higher order polynomial than the pre-edge background (i.e. 3rd order). A post-edge background can be allocated to an EXAFS spectrum using *Pyspline* that has been used for the calculation of *x(k)* in

this thesis. The best background $\mu_0(E)$ is selected that intersects the EXAFS regions half way across the oscillations.

Using *Equation (3.4)*, *Equation (3.5)* can be interpreted as the EXAFS function as a function of $k - x(k)$. The different frequencies in the oscillations correspond to different near-neighbour coordination shells which can be described and modelled according to the EXAFS equation:

$$x(k) = \sum_j \frac{N_j e^{-2k^2\sigma_j^2} e^{-2R_j/\lambda(k)} f_j(k)}{kR_j^2} \sin\left[2kR_j + \delta_j(k)\right] \qquad (3.6)$$

where $f(k)$ and $\delta(k)$ are scattering amplitudes and phase shifts respectively of the atoms neighbouring the excited atom. N is the number of neighbouring atoms, R is the distance to the neighbouring atom, and σ^2 is the Debye-Waller factor describing the disorder in the neighbour distance (Lee and Pendry, 1975). This calculation can be modelled to fit the experimental EXAFS and enable one to derive values for R, N and the Debye Waller-factor. They are fitted to the experimental EXAFS by a fitting EXAFS package called *DL_EXCURV* (Gurman et al., 1984). An example of a fitted EXAFS spectra using *DL_EXCURV* on an NHM hematite standard is shown in Fig 3.5. Typical experimental conditions used for EXAFS i.e. one second integration at every each 0.2-0.4 eV energy step from 6962-7090 eV, followed by 5 s onwards up to and beyond the up to 7500 eV for Fe K-edge EXAFS will take approximately 40 minutes for one spectra.

DL_EXCURV is based on rapid curved waved theory (Gurman et al., 1984) rapid curved wave theory takes parameters describing the radial shells of atoms surrounding the central atom. Using *Equation (3.6)*, *R*, *N* and σ^2 are fitted using a least squares regression fit method to the experimental EXAFS. A fit parameter is used to define a minimal difference between the calculated theoretical EXAFS function and experiment.

An elemental or chemical environment is introduced by setting the central atom and backscattering atoms for subsequent atomic potential and phase shifts that are calculated by the program. The rapidly decaying EXAFS function can be amplified by weighting $x(k)$ by a factor of k^n. The fit procedure is then initiated by setting values of *R* and *N* from which the iteration steps begin and the fit paramter is minimised with each iteration and a satisfied variance is established between the theoretical and

experimental EXAFS functions. The best optimisation minimum is achieved when each core shell is consecutively refined i.e. optimising with the first shell and then adding the second shell to repeat the fitting procedure etc. Transfer from k-space to real space is then made with a Fourier transform of *x(k)*.
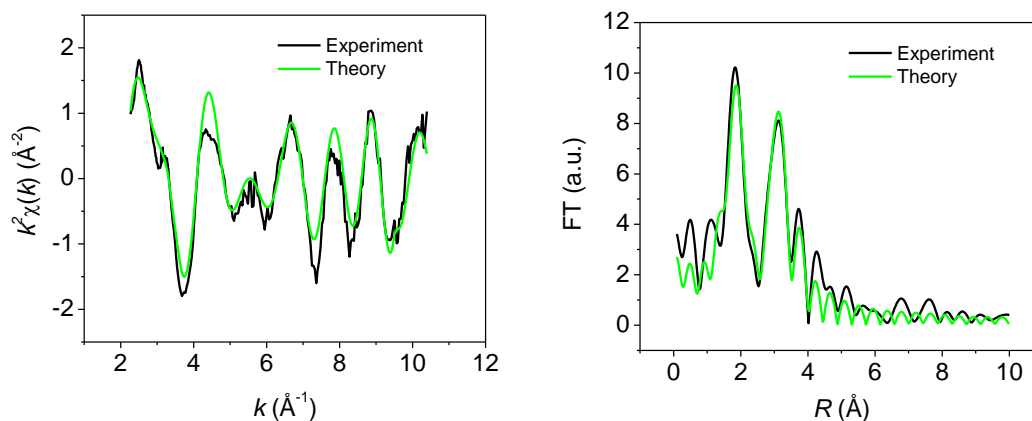
FIG 3.5: EXAFS of the NHM hematite Fe_2O_3 standard at I-18. The FT of simulated EXAFS function results in a Fe-O first shell with R = 2.03 Å $\pm$ 0.01 Å. The Fe-Fe coordination is fitted to a split shell with Fe-Fe distances of 3.00 Å $\pm$ 0.02 Å and 3.34 Å $\pm$ 0.01 Å . See APPENDIX B for other mineral standards. The EXAFS of these standard minerals have been used to idenitify mineral types in Stardust samples (Chapter 5). They have also been compared to molecular bond lengths determined by X-ray and neutron diffraction techniques, published in the Daresbury Chemical Database (APPENDIX BII.).

Elemental and chemical compositional information (by XRF), redox information and mineralogical fingerprinting (XANES) and molecular and chemical co-ordination information (EXAFS) can be obtained from these microfocus X-ray spectroscopy techniques. XRF has been a key technique used for initial characterisation of complete tracks for elemental distributions of along them and the identification of key localities of materials or 'hotspots,' as well as terminal areas (i.e. Flynn et al., 2008). Westphal et al. (2010) have also used XANES at the Berkeley Advanced Light Source (ALS) in order to assess the Fe - oxidation state of Comet Wild2 from the *Stardust* Mission. The use of EXAFS, however, has not been reported on any of the *Stardust* samples. This may be due to the limited capability the other beamlines for maintaining beamline or monochromator stability during EXAFS analyses, or a result of the analytical challenge faced by identifying unknown molecular and chemical environments of phases smaller than the beam spot size. The use of EXAFS is, therefore ideal on relatively large grains e.g. ~ 10 μm in size with thicknesses far smaller than their absorptions lengths.

3.4 Sample Preparation for X-ray Microfocus Spectroscopy

The *Stardust* track samples studied in this thesis have been directly analysed in their keystone and sliced aerogel states. The low density and molecular mass of aerogel does not pose any significant absorption constraints on the high energy X-rays such as Fe Kα, allowing XRF and XAFS to be performed via the detection of fluorescent X-rays.

Identified track features or hotspots analysed by XANES and EXAFS require comparison to standards for mineralogical identification. The procedure used to prepare these samples is introduced here together with a brief investigation into the novel use of FIB-prepared samples for XAFS and potentially other microfocus spectroscopy techniques.

3.4.1 Mineral Standard Sample Preparation

Our range of silicate and oxide mineral standards provided by the NHM (APPENDIX B) have been prepared as pellets for detection under transmission. The absorption length of these crystals i.e. the distance over which the X-ray intensity decreases by a factor of e^{-1} permits the use of ~10 μm grain size powders, 5 mg of which are diluted in 95 mg of boron nitride and compressed into pellets. The powders were manually produced using a mortar and pestle and then attached to *Kapton* tape for minimal absorption (see also Section 5.3). This technique is proved to be an effective method for obtaining XAFS data. However, inhomogeneity in grain size and pellet thicknesses can lead to unwanted errors in XAFS because the absorbance of the sample will vary at different parts under the same X-ray beam. Also, a powdered sample is required, making the use of specific *in situ* analysis of a meteoritic sample, for instance, almost impossible.

3.4.2 FIB Extraction of a Mineral Standard for XAFS

Section 2.10.1 demonstrated the use of mineral standards to determine experimental K-factors. Could such standards also be used for XAFS and quantitative XRF? Also, can mineral standards be extracted using a modified FIB TEM sample preparation technique described in section (2.8.2) and transferred to the synchrotron? In order to demonstrate the potential use of the FIB in X-ray microfocus spectroscopy, a sample of nickel sulphide was extracted from a powder standard. The sample was an

old pentlandtite (Fe,Ni_9S_8) sample but initial SEM surveys showed sample inhomogeneity with only some grains containing Ni. All of the supposedly pentlandite grains from SEM also seemed heavily oxidised. A list of standards used for AEM *K*-factors in Section 2.10 and XANES can be found in APPENDIX B.

3.4.2.1. Extraction Method

The FIB technique used for the preparation of TEM samples was amended in order to produce a wafer with appropriate dimensions. In terms of the nickel sulphide standard, a nominal thickness of 1 µm was selected that would be plausible for extraction purposes (although higher thickness are possible) whilst accommodating for detectable fluorescence and/or absorption of the standard. Stages of the FIB extraction process are shown in Fig 3.6. To allow for the large XAFS beam size relative to the TEM electron beam, a much larger wafer was produced, at 6 × 20 µm in size. The powered standard was dabbed onto an *Agar* carbon sticky pad and analysed by SEM-EDX. An approximately 100 µm sized grain containing Ni, S and O by qualitative EDX was selected for extraction. In this entire sample, it was one of the only grains containing Ni and all of the other surrounding grains were Fe-S grains. The assumed pentlandite sample (but with anomalous O) was transferred to the FIB for extraction, where the method described in Section 2.8.1 was used to generate the wafer. The run-script, however, was aborted after the initial trenching with the high 5 nA - 1 nA beam currents, to leave a standing wafer of approximately 1.2 µm thickness (Fig 3.6b). The wafer was extracted by the method described in Section 2.8.2. However, additional welds were placed between the needle and wafer using the carbon GIS to ensure stability of the much larger than usual wafer and larger currents were used for cutting the wafer free (0.3 nA).
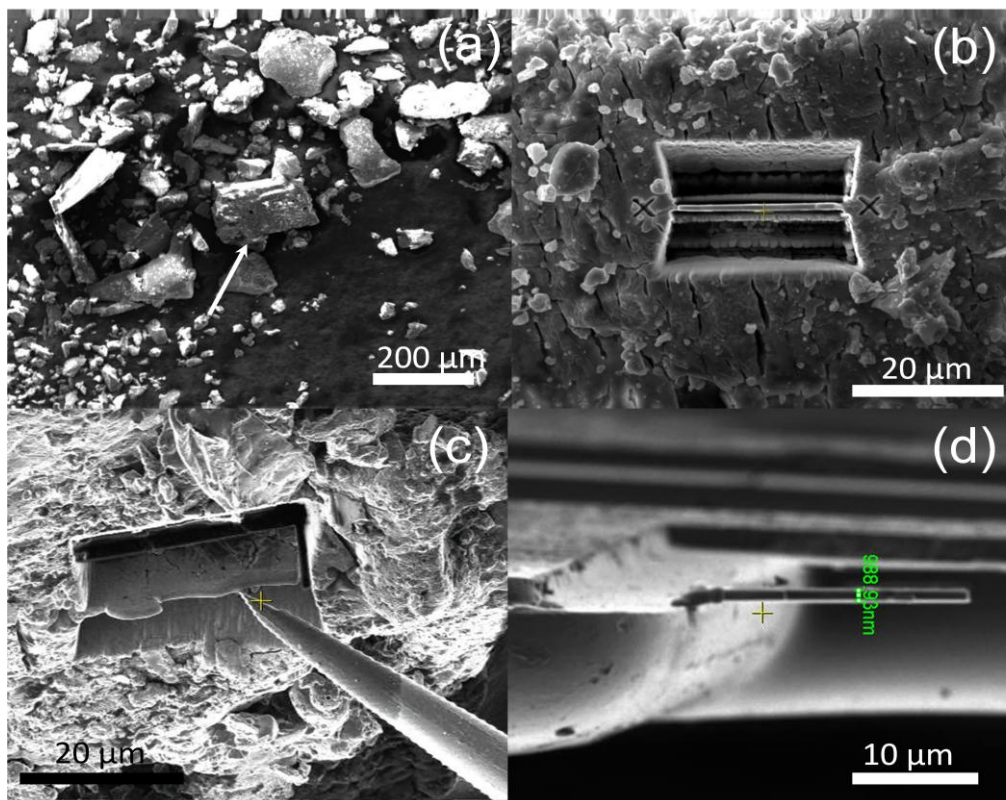
FIG 3.6: FIB extraction process for Ni-S-O grain. The powder standard was pentlandtite but SEM analyses showed the grains to be oxidised. (a) Low magnification SEM image of grain in the centre of field to field of view. The grain is mixed in with Fe-sulphides and positioned on a carbon sticky pad. (b) Milling of the wafer to ~120 μm thickness(c) Wafer extraction. (d) Attached to *Omniprobe* grid and final polishing to 1 μm.

3.4.2.2 Method for XANES Analysis

The copper grid was placed flat on *Kapton* tape and then attached to the sample mount in Beamline I-18 (as in Fig 3.1a). The beam was aligned to a video microscope image where the wafer was visible. The stage was moved to centralise the wafer in the video microscope image. Due to time constraints, the sample was not mapped by XRF. As soon as a Ni peak was detected by quick XRF point spectra XANES was then performed.

Ni K-edge XANES was performed on the wafer. Approximately 120 data points were integrated across the XANES for pre and post Ni edge. Two second integration was performed at each 6.04- 1.02-eV energy step from 8181 - 8364 eV, followed by 1 s onwards up to and beyond 8363 eV – 8425 eV.

3.4.2.3 Results

Absorption was achieved at the Ni K-edge. A Ni XANES profile was also obtained successfully on the wafer (Fig 3.8).
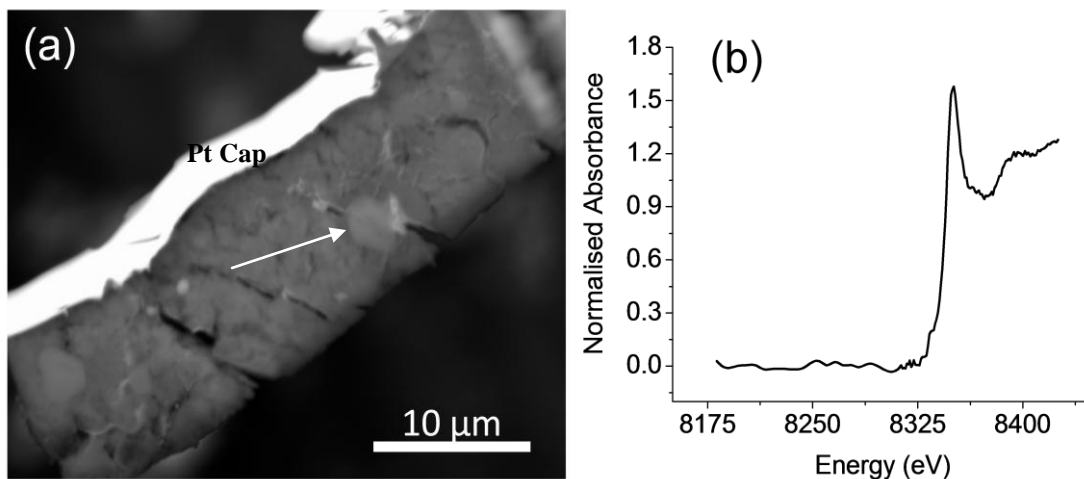
FIG 3.8: SE imaging and Ni-XANES of Ni-S-O wafer. (a) Wafer under the SEM. Note the heterogeneity of the assumed pentlandite grain itself, which contains rounded or mottled Ni-S-O grains identified by qualitative SEM-EDX (b) Ni K edge XANES profile obtained from the wafer.

3.4.2.4 FIB sample versus Conventional Diluted Powder Samples.

The actual sample selected in this study may not have been ideal as it seems to be heavily oxidised, with individual modified nickel sulphide grains within the wafer, demonstrated by the heterogeneity of the FIB sample. This makes any XAFS non ideal by the potential overlap of different phases. Due to the time constraints at Beamline I-18, the wafer was unable to be mapped prior to XAFS. Thus, it was not clear that the sample was completely enclosed by the beam. However, a XANES profile was successfully obtained for this standard with a distinctive white line at the Ni K edge. This initial pilot study demonstrates the ability to extract samples *in situ* by FIB-SEM for XANES. Measurements of fluorescent X-rays from the sample were not performed but could also have been investigated. The true absorption length for these types of minerals would be closer to the nominal 10 μm used for the powdered pellets, although Ni-XANES were still obtained. It is not clear from this study whether *in situ* FIB preparation of samples are more suitable under fluorescence or transmission.

The problems faced with diluted samples such as sample grain size and pellet thickness heterogeneity could theoretically be overcome with the FIB as long as the sample being extracted is larger than the beamline spot size and is aligned directly under

the beam. By potential XRF mapping, the true co-ordinates of the centre of the sample could have been known, ensuring complete overlap between the sample and beamspot. Note that in this trial study, an assumption was made that the grain extracted from was representative of an homogenous standard, but was, however, heavily altered by suspected natural oxidation being a very old standard. Careful selection of appropriate standards is required.

3.5 Summary and Conclusions

The theory behind microfocus X-ray spectroscopy has been provided, with details of the *Diamond* synchrotron Beamline I-18 used for *Stardust* analyses in Chapter 5. These techniques can provide compositional based imaging (mapping and point spectra), providing elemental distribution concentrations by XRF, mineral identifications and redox information using XANES, and local co-ordination environment(s) of these mineral(s) by EXAFS.

The clear advantages of *in situ* microanalysis using the FIB technique has been demonstrated in a novel way. A FIB-synchrotron sample preparation technique has been investigated by XANES in order to assess its feasibility for future work. We have seen that successful XANES spectra can be obtained from FIB based samples, demonstrating a successful preparation and extraction procedure for such samples, but further work is required using more homogeneous standards and different samples thicknesses under both fluorescence and transmission modes to assess whether they would be better than conventional powder standards, standing alone. The clear potential of *in situ* XAFS has been demonstrated.

Chapter 4
Low Temperature Mineralogy of the Nakhlites: A Model For the Nakhlite Hydrothermal Cell

4.1 Introduction

The nakhlites are clinopyroxenites thought to have crystallised as cumulates within a thick basic-ultrabasic lava flow or shallow (~100 m) intrusion on Mars 1.3 G.a. (e.g. Treiman, 1993; Bridges and Warren, 2006; Lentz et al., 1999). Fe-rich olivine grains make up approximately 10% volume of all but one of them (MIL03346, which has no cumulus olivine). They all have similar cosmic ray exposure ages (~ 11 M.a.) and are hence, thought have been liberated from the same ejection event on Mars (Nyquist et al., 2001).

4.1.1 Secondary Alteration Mineralogy of the Nakhlites

Within the seven known nakhlites: Nakhla; Governador Valadares (GV); Lafayette; North West Africa NWA998; NWA817; Yamato Y000593/Y000749 (paired) and Miller Range MIL03346 there are secondary mineral assemblages (e.g. Ashworth and Hutchison, 1975; Gooding et al., 1991; Bridges et al., 2001; Gillet et al., 2002; Treiman, 2005). These are present in fractures within olivine and also within the mesostasis (Bridges and Grady, 2000). The pre-terrestrial, martian origin of the veins has been established because Nakhla and Lafayette veins are seen to be truncated by the fusion crust (Gooding et al., 1991; Treiman et al., 1993). The secondary mineral assemblages vary in abundance and composition between the nakhlites but include siderite, clay-like phases and salts. They have been dated by K-Ar within the time range ≤670 Ma (Swindle et al., 2000) and so this constrains the timing of the hydrothermal alteration to a relatively recent time in Mars history.

The secondary mineral assemblages may have been derived from an evaporating brine percolating through the nakhlite parent body (Bridges and Grady, 2000; Bridges et al., 2001). This is, for instance, consistent with the varying Ca content of the siderite between Lafayette and the other nakhlites (Bridges and Grady, 2000). They formed at

low temperature ($<150\ ^{\circ}$C) and rapidly, to form metastable mineral compositions. Some secondary minerals within the nakhlites may however be terrestrial e.g. sulphates within the Antarctic finds, Y000593/Y000749 (Kuebler et al., 2004).

4.1.2 Nakhlite Petrology

The nakhlites contain 80-90% of subhedral augite $(Ca,Na)(Mg,Fe,Al)(Si,Al)_2O_6$. The cumulus clinopyroxene compositions (shown in Fig 4.1) are consistent with the crystallisation of a silica saturated basaltic liquid (Berkeley et al., 1980). Olivine making up approximately 10% volume is fayalitic. The olivine composition in its respective nakhlite is also given in Fig 4.1. The interstitial material between these igneous minerals is plagioclase rich. Based on comparison of textures (Berkeley et al., 1980), major and minor element and mineral compositions and redox conditions (Burns, 1981), the nakhlites are confidently believed to have been derived from the same parent magma and lithologic unit (Lentz et al., 1999). A terrestrial analogue to the nakhlite pyroxenites is Theo's Flow in Ontario, Canada (Treiman et al., 1996; Lentz et al., 1999). Theo's flow has a subsurface 60 m pyroxenite layer strikingly similar to the nakhlites in size and spatial distributions of its cumulus grains (lentz et al., 1999). Thus, the ultra basic parent magma that crystallised into the nakhlites was most likely a sub surface intrusion approximately10-100 m thick.
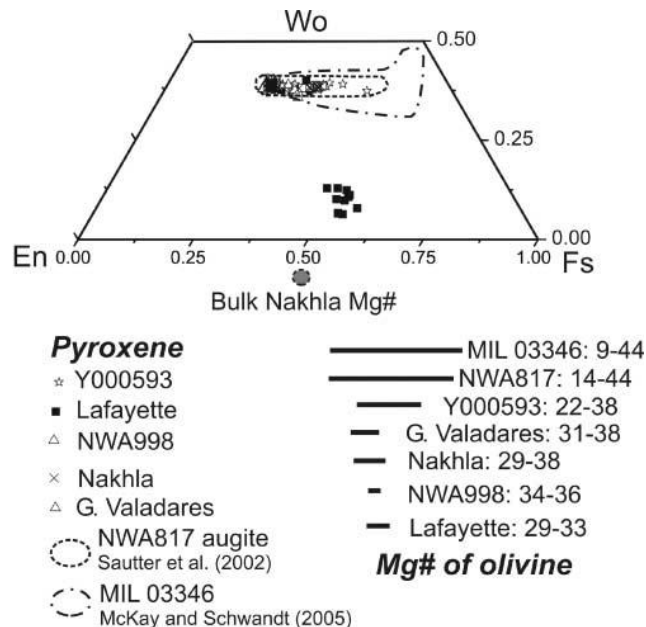
FIG 4.1: Pyroxene and olivine compositions of the nakhlites extracted from Bridges and Warren (2006). The pyroxene composition is $En_{0.37-0.62}Wo_{0.37-0.43}Fs_{0.24-0.41}$ and is therefore an Fe-rich augite. The olivine composition ranges from $Fo_{0.09-0.44}Fa_{0.91-0.56}$ and is hence fayalitic olivine.

4.1.3 Variation with depth on Mars

Mikouchi et al. (2003, 2006) suggested the probable relative original depths of the nakhlites on Mars by comparing their mineralogy and groundmass textures. Bridges and Warren (2006) added to this model using the composition of secondary assemblages. In these models, MIL03346 is nearest the surface, the Yamato meteorites close to the top surface, followed by Nakhla, then GV with Lafayette at the bottom. Treiman et al., (1993) suggested that in Lafayette the water to rock ratio and the temperatures upon alteration could have been higher compared to the rest of the nakhlites.
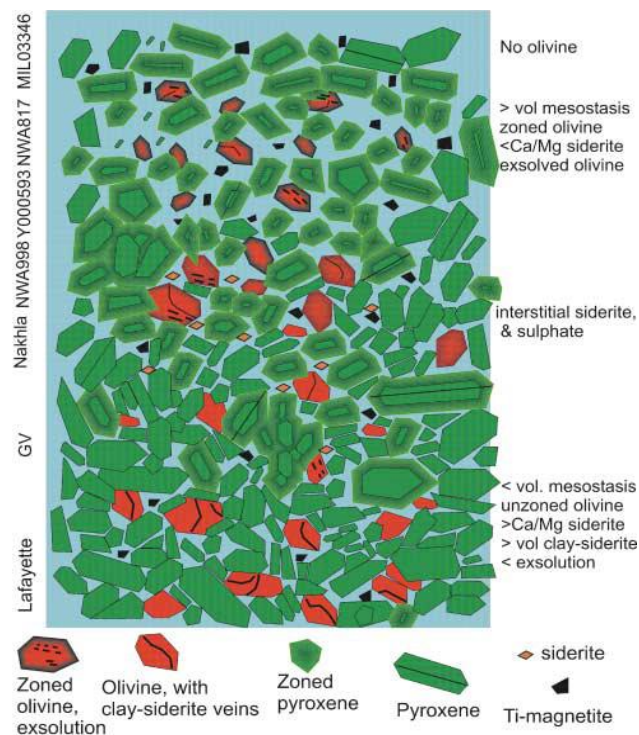
FIG 3.2: Diagram illustrating the relative depths of the nakhlites and the types of secondary assemblages associated with them, extracted from Bridges and Warren (2006). This model was derived by Mikouchi et al. (2003;2006). However, NWA998 has been suggested to be further up the pile due to the similar secondary assemblages found to those within Nakhla and GV closer towards the middle of the pile by Bridges and Warren, 2006.

The results in this section are considered in the light of likely relative depths of the nakhlites and position within a hydrothermal system, perhaps associated with an impact event. From this a model has been derived to help explain the formation of some recently identified phyllosilicate and carbonate on the martian surface (e.g. Morris, 2010 Ehlmann et al., 2008; Mustard et al., 2008).

4.2 Methods and Samples

4.2.1 Samples

Polished thin sections of Y000749 and Y000593 have been provided by the Japanese National Institute of Polar Research. A thin section of Nakhla (BM 1911, 369) and polished resin blocks of GV (BM 1975, M16) and Lafayette (BM 1958,775) were prepared at the Natural History Museum (NHM). Resin blocks of GV and Lafayette were polished in oil in an attempt to initially preserve soluble phases (Bridges and Grady, 2000). A nontronite clay standard (Urgeirica Beira Alta, Portugal-MB 1972, 142) was also provided by the NHM.

4.2.2 SEM and SEM-EDX

All five nakhlite samples were initially analysed with Scanning Electron Microscopy (SEM). The Phillips XL30 ESEM and FEI Sirion Field Emission Gun (FEG)-SEM of UoL's AMC were used for this. Alteration products within the olivine were imaged in more detail and further analysed by Energy Dispersive X-ray Spectroscopy (EDX). The FEG-SEM and ESEM are equipped with a PGT EDX system and Oxford Instruments INCA spectrometer. EDX spectra and X-ray maps were made at 15 kV and 20 kV accelerating voltage respectively.

4.2.2.1 Vein Width Measurements

Five veins within 5 olivine grains in each of the sampled nakhlites were measured to record vein sizes. As veins can be found to be irregular in size, the maximum width of each vein was measured. The measuring tool in the microscope software of the PhillipsXL30 was used for this. The scale bar was checked with an *Agar* Planotet silicon test specimen calibration standard.

4.2.2.2 Volume Fraction of Secondary Minerals

Montages of 5 olivine grains from each of the nakhlites were produced and loaded in *Image Pro Plus* software to calculate volume fractions of the secondary assemblages within each of the thin sections. A suitable magnification was selected allowing the veins to be resolved from an image and distinguished between empty fractures. This turned out to be 350 times magnification in the microscope terminal. A montaged olivine grain was rendered using Adobe *Photoshop*.
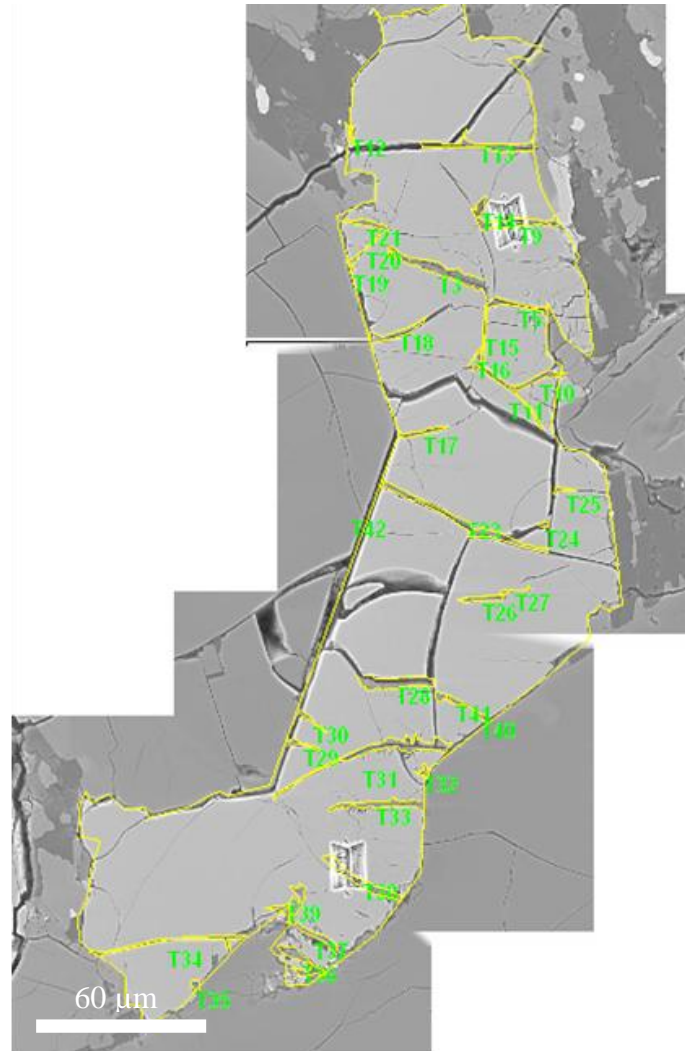
FIG 4.3: BSE montage of an olivine grain from Nakhla used for volume fraction measurements of the secondary veining using *Image Pro Plus* software. The scale bar was calibrated to the image and areas of veining were selected to produce an area measurement relative to the total area of the olivine grain.

4.2.3 EMPA

EPMA was also performed on the samples. The Cameca SX100 was used in the Department of Mineralogy, NHM. The microprobe was operated at 20 kV accelerating voltage with a beam current of 20 nA. Alteration products within the olivine veins were analysed in phases with width ~5 μm or more, in an attempt to constrain interaction volumes within individual phases. The detection limits were approximately 0.01 wt% oxide for all elements but was based on the calculated statistical requirement of net peak counts being 3 times greater than the standard deviation of the background that was calcukated from the software in the raw data. A description of the crystal spectrometers used for different elements can be found in section 2.7.5.
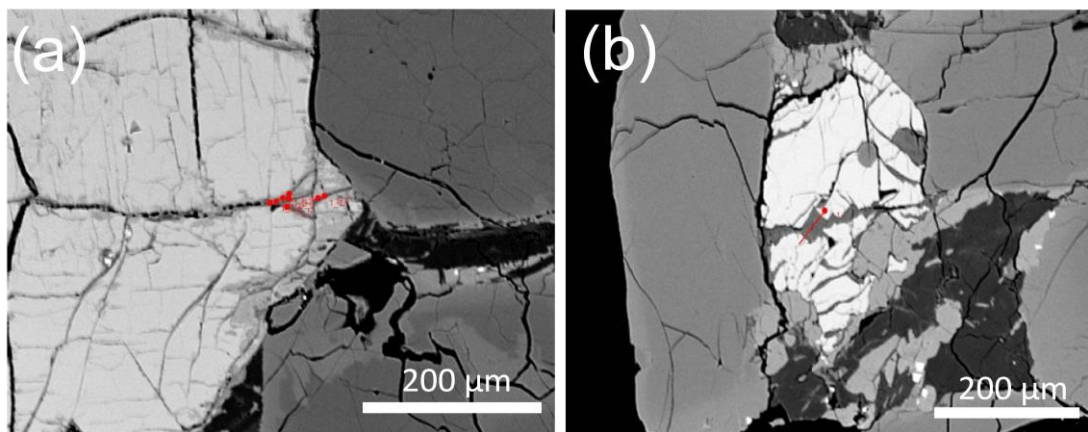
FIG 4.4: Examples of sampled veins for EMPA. The electron microprobe uses a BSE detector for allocation of areas for analysis. Either individual spots were chosen along a vein as in (a) or for much wider veins, a line scan was generated with 10 adjacent spots (b). The raw microprobe data was then manually filtered for any suspected overlapping signatures from surrounding phases such as the olivine or other secondary minerals such as siderite or iron oxide.

4.2.4 FIB-SEM TEM Sample Preparation

After SEM-EDX and EPMA based characterisation, cross-sections of selected veins were prepared for TEM. The dual FIB-SEM technique was used for TEM sample preparation. The FEI Quanta 200 3D with a Ga^+ ion beam was used at UoL; milling an approximately 70-110 nm thick wafer containing a section of the secondary assemblage(s). For precise milling of the sections, the automated TEM runscript was used with the Ga^+ beam at 30 kV to generate a 0.1-0.2 μm thick wafer. The runscript steps down milling currents from 5 nA to <100 pA. Vein regions chosen for extraction frequently contain some void space between the olivine and veining assemblages.

Electron transparent wafers of these regions are therefore very fragile. In order to maintain their stability, the produced sections were imaged with snap shots at sequential stages of the milling sequence and the runscript was aborted before the final milling currents were employed. Some Y000593/000749 wafers were sectioned at 20 kV in an attempt to help preserve the secondary features with lower voltages and currents. Prior to application of the runscript, the selected areas in this study were capped with a 30 x 5 µm Pt layer of approximately 150 nm thickness using the electron beam. An additional 2 µm thick cap was placed on top of this during application of the wizard script using the Ga^+ beam. Both layers were deposited by the Pt hydrocarbon in the Gas Injection System (GIS). These capping layers protected the sample area from the Ga^+ ions during the milling and deposition processes. Wafers of length 15 µm and 4.5 µm width were produced. They were extracted and attached to an *Omniprobe* copper grid. Welding of the micro-needle to the wafer and the wafer to the copper grid was performed with the FIB-SEM carbon GIS. Final 'polishing' currents were employed manually after attachment to the grid for optimal electron transparency. The NHM nontronite standard was prepared by taking flakes scraped onto a carbon sticky pad, coated with 15 nm carbon and then inserted directly into the FIB-SEM for extraction and subsequent attachment to an *Omniprobe* grid.

The Jeol 2100 TEM with a PGT EDS system was used for analyses of the extracted veins and standards. Its LaB_6 source was operated at 200 kV and 109-111 µA emission current. Bright field (BF) imaging, High Resolution TEM (HRTEM), TEM-EDS, and Selected Area Electron Diffraction (SAED) were performed on the TEM samples. D-spacing calibration was performed with an *Agar* graphitized standard with 0.23 nm lattice planes. Due to contortion and irregularities of fringes, HRTEM measurements were made directly from the HRTEM BF images, using a histogram intensity profile tool with the *Gatan Digital Micrograph* Camera software. Errors based on the *Agar* standard were all less than 5% and this conservative upper limit is taken for this analysis. The d-spacing measurements were also calibrated with an evaporated Al-oxide diffraction standard at desired camera lengths. Nanobeam diffraction was also generated on phases too small for SAED (less than approximately 50 nm). Qualitative EDX was typically performed for 200 s using a 25 nm spot size. Some spectra were acquired for longer times on smaller phases, with spot sizes such as 15 and 10 nm.
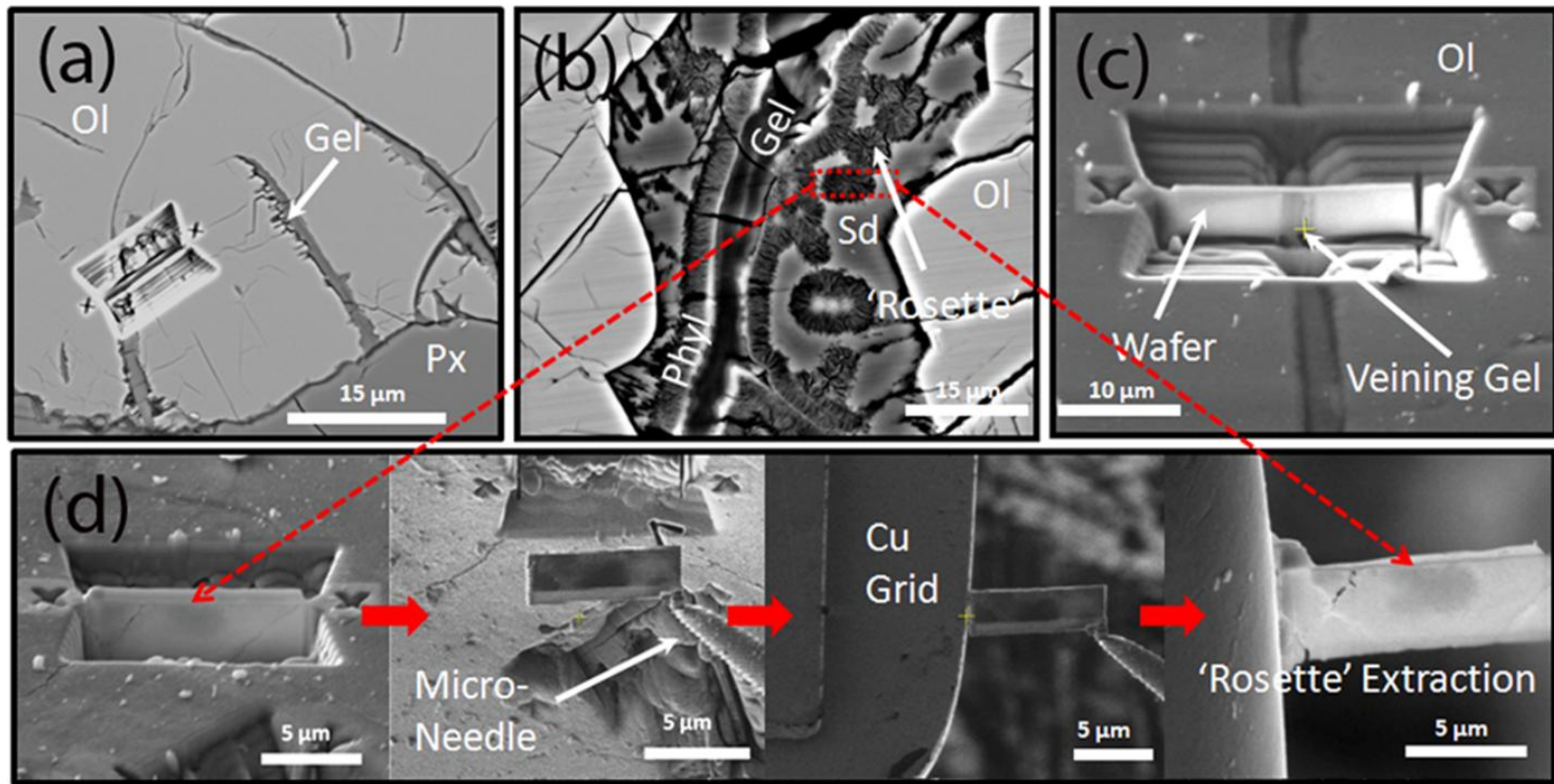
FIG 4.5: FIB extraction technique of nakhlite secondary alteration assemblages. (a) Nakhla. Remaining milling trench across the veining assemblages after the FIB extraction process. Gel = amorphous hydrated Fe-silicate (See results section 4.3) (b) Lafayette. The most diverse array of alteration phases were found in the olivine veining of Lafayette at the base of the nakhlite pile (Section 4.3). As well as the core veining following along the margins of the fracture walls, circular phases or rosettes were extracted as shown in (d). (c) Yamato000593. A representative 52° stage rotation SEM view of one of the wafers containing the veining assemblages after FIB milling (d) Extraction process of 'rosettes' in Lafayette (b) showing the FIB extraction processes of these phases (see results Section 4.3). Sd Siderite Phyl Phyllosilicate.

4.3 Results

4.3.1 Vein Mineralogy and Morphology

All of the nakhlites studied - Lafayette, Nakhla, GV, Y000593, Y000749 have fracture-filling veins in the olivine which consist largely of amorphous hydrated silicate – a 'gel'. Phyllosilicate is also present in the veins of Lafayette and siderite is found in varying amounts in Nakhla, GV and Lafayette.

4.3.1.1 Vein Sizes and Densities

The fracture fillings are limited to within the boundaries of the olivine grains and the average vein sizes are shown in Fig 4.6. In Lafayette, veins can be up to 50 μm wide and occupy 9.5 % of the sampled olivines (Fig 4.6). Apart from Lafayette, the vein widths are broadly similar across the nakhlites, with the Yamato meteorites averaging 4 μm, and Nakhla and GV averaging 5-6 μm. However, Nakhla and GV do contain a few large veins of olivine) compared to Nakhla and GV (~3%), and they have a larger volume of the gel compared to Nakhla and GV (Fig 4.6b).
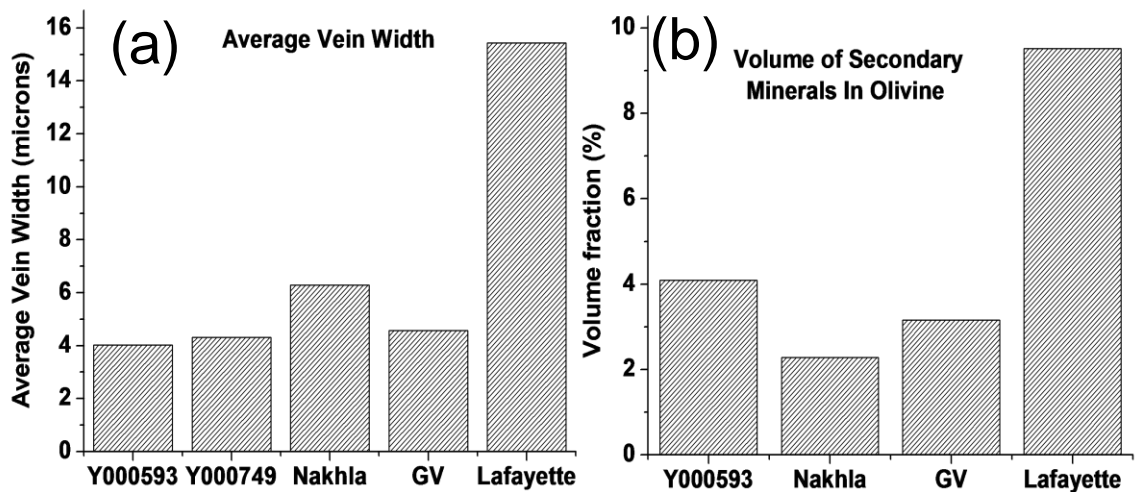
FIG 4.6: (a) Average maximum width of 25 veins in each of the studied nakhlite thin sections. (b) Total volume fraction of secondary minerals (i.e. veining volume) from the sum of 5 olivine grains in each of the nakhlites.

4.3.1.2. Vein Mineralogy

Lafayette

Ca-Mn-Mg siderite ($FeCO_3$) is present at the outer margins of sawtooth-shaped, fracture-controlled veins in Lafayette (Figs. 4.7, 4.8). This siderite is partially corroded and replaced by phyllosilicate, which in turn has an Fe-oxide phase (possibly ferrihydrite, see bottom of this section) at its inner edge (Fig 4.7). Phyllosilicate has only been found in Lafayette. One to two µm diameter rosettes of the same phyllosilicate (see below) are also present within the surrounding Ca-siderite. The gel occupies the centre of the Lafayette veins. Thus the crystallisation sequence was: olivine fracturing, siderite crystallisation, siderite corrosion and the formation of phyllosilicate as zones within the veins and within spherical rosettes. This crystallisation seems to have been terminated by the formation of the Fe-oxide phase. Lastly silicate gel was precipitated in the centre of the veins. The phyllosilicate has a fibrous texture with the mineral grains arranged perpendicular to the fracture sides. This may be a result of the direction of mineral growth from the vein walls inwards. The BSE image in Fig 4.7 shows that the rosettes of radial phyllosilicate grains have Fe-oxide rich central regions like the inner margins of the vein phyllosilicate. The contact between the Lafayette phyllosilicate and the gel is a complex intermixed zone of phyllosilicate and fine and ultra fine-grained Fe-oxides from < 5 to 10 nm size (Fig 4.8a). In the carbonate regions surrounding the gel core and phyllosilicate, TEM shows precipitates of Mn-rich siderite – identified by qualitative EDS – that are from 50-100 nm in diameter (Fig 4.8b) which are enclosed within domains of more Ca-rich siderite. Trace amounts of Na are also found within all of the siderite grains. Bright field TEM images show the phyllosilicate textures to vary from coarse 100-200 nm width fibers to gradually finer grained ≤5 nm and then the amorphous gel in the centre of the veins (Fig 4.8c). The coarsely crystalline areas are found as fibrous crystals. The lattice fringe spacings of the phyllosilicate vary for different regions of the sample (Table 1, 2 APPENDIX C). Fringes from 0.7 – 0.9 nm were found in the veining phyllosilicate (Fig 4.8d). The veining phyllosilicate from which EPMA analyses were made (Section 4.3.3) contained 0.9 nm fringes that were in 2 separate domains. The phyllosilicate in the rosettes also have 0.9 nm basal fringes that are 'sandwiched' between minor 0.7 nm fringes (Fig 4.9a). Another rosette was also extracted and found to have lattice fringes from 0.9 - 1.1 nm (Fig 4.9b).

The spherical morphology of the rosettes was confirmed by its extraction and subsequent imaging (Fig 4.10). They are embedded in the calcic siderite with the large (~ 50 μm) grains of carbonate sitting in an Mn poorer carbonate matrix. The phyllosilicate crystals follow along the lathes or platelets that radiate from an amorphous Fe-richer core.

Regular rings are also observed within the coarse grained areas by both SAED and nanobeam diffraction, indicating multiple crystallographic orientations within the phyllosilicate. Comparison with the nontronite standard prepared in the same way for TEM yielded fairly similar 3-ring polycrystalline SAED patterns (Fig 4.11a, b). The co-existence of the polycrystalline patterns may reflect a natural variation in grain size within the samples, including nanoscale in addition to the relatively coarse (100-200 nm width) grains. The nontronite standard d-spacing measurements (Table 2) are generally larger than the Lafayette phyllosilicate ring patterns. Nanobeam diffraction of a fine grained iron oxide shows d-spacings of symmetrical diffraction spots at 1.56 ± 0.05 Å with an hexagonal symmetry (Fig 4.11c). The symmetry suggests that this nanoscale mineral might be ferrihydrite (Michel et al., 2007).
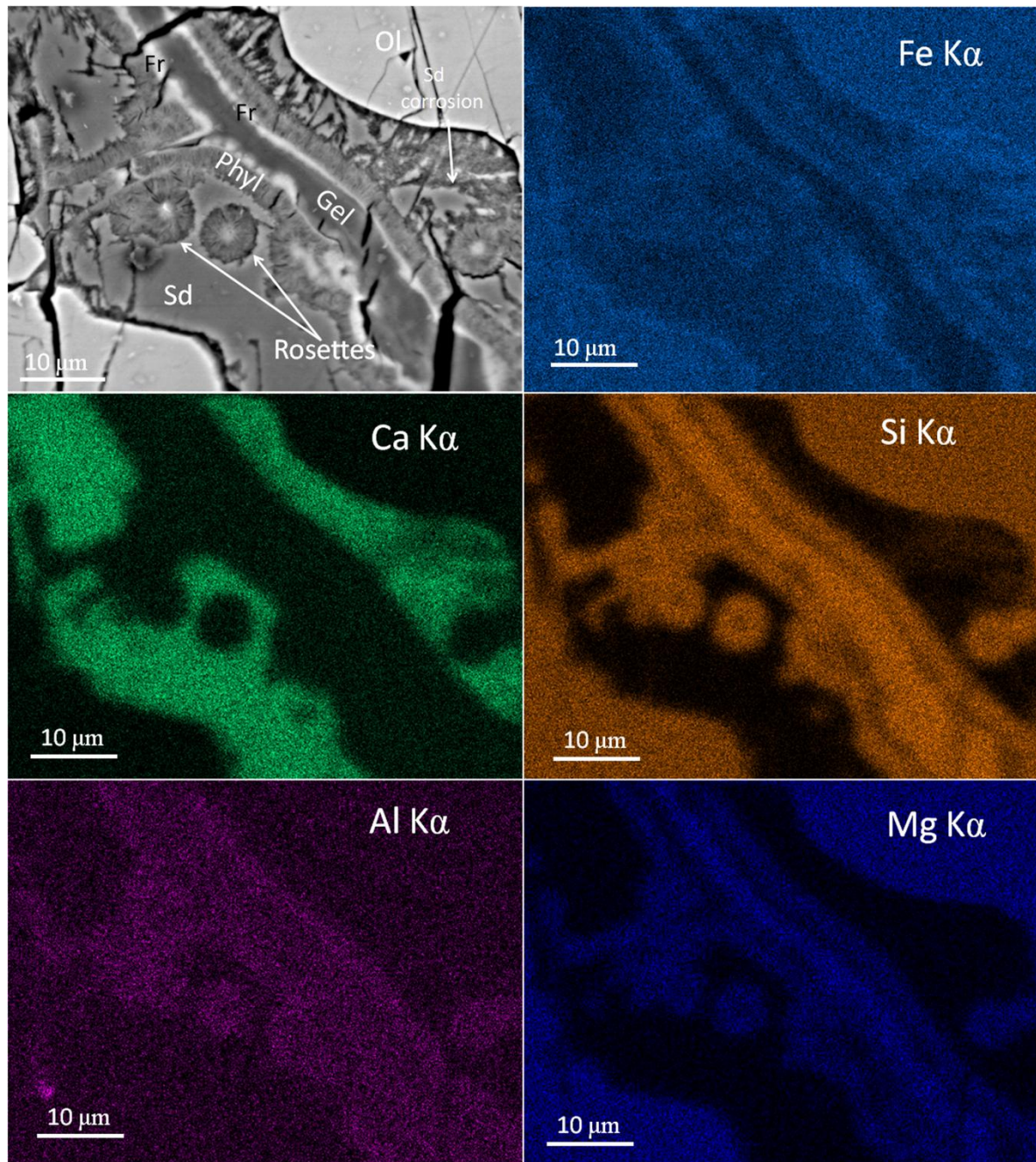
FIG 4.7: SEM-EDX mapping of siderite-phyllosilicate-gel and 'rosette' assemblage in Lafayette vein. Fe is concentrated in the zone between the gel and phyllosilicate, and also in the core of the rosettes. Si is concentrated in the gel. Al is richer in the phyllosilicate regions and Ca is concentrated within the carbonate. Textures show corroded siderite being replaced by the phyllosilicate. Scale bar is 10 μm. Top left is BSE image that was mapped Annotations in BSE image are: Fr Fe oxide (ferrihydrite?), Phyl phyllosilicate, Ol olivine, Sd siderite.
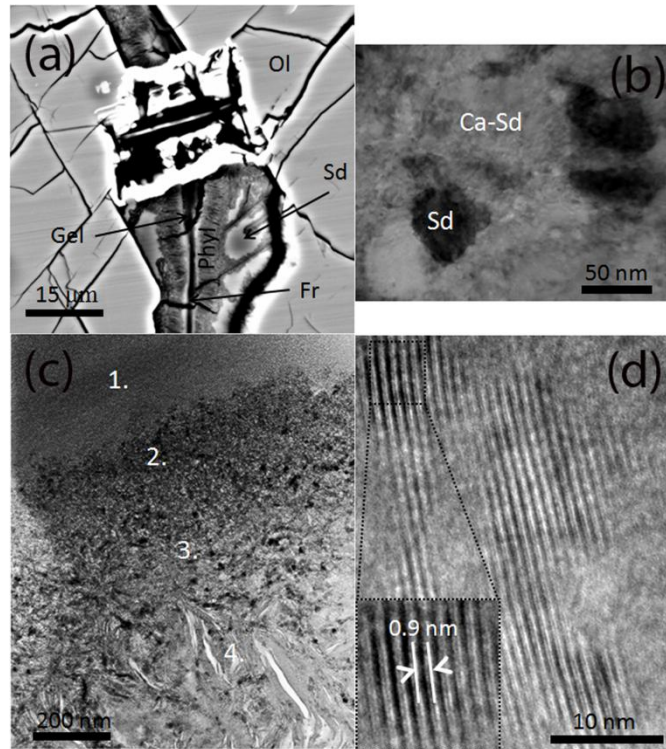
FIG 4.8: Lafayette. (a) BSE image of extracted region from Lafayette vein. (b) Bright field image of Ca-Mn-siderite region surrounding the phyllosilicate and gel (i.e. region of intense Ca Kα from X-ray map in Fig 4.7). Grains of Fe-Mn rich siderite show high scattering (they are dark grains) indicating a different crystallographic orientation to the Ca-siderite. (c) Phyllosilicate - gel transition in (a). Transition zones in Lafayette veins start from a coarse phyllosilicate (4), becoming fine grained (3), then finer grained (2) and leading to the amorphous silicate gel (1) in the centre of the veins. (d) HRTEM image of veining phyllosilicate from which EMPA analyses were made, showing the presence of 0.9 nm lattice fringes suggested to be Fe-smectite. Phyl phyllosilicate, Ol olivine, Sd siderite (Fe-Mn rich), Ca-Sd calcium-rich siderite.
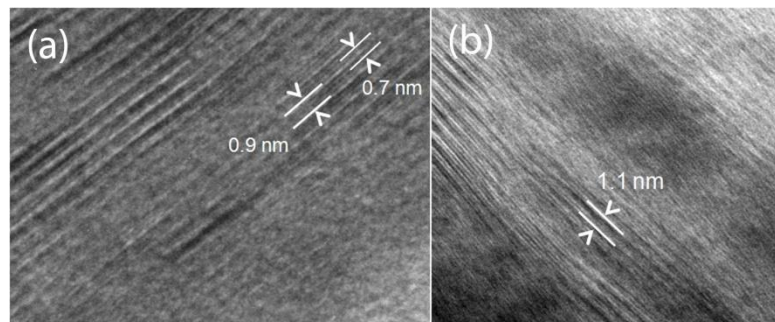
FIG 4.9: HRTEM bright image of the phyllosilicate found in the rosettes. (a) The main fringes at ~0.9 nm spacing are sandwiched by 0.7 nm fringes. (b) Lattice fringes from another rosette containing similar fringes but also including 1.1 nm spacing.
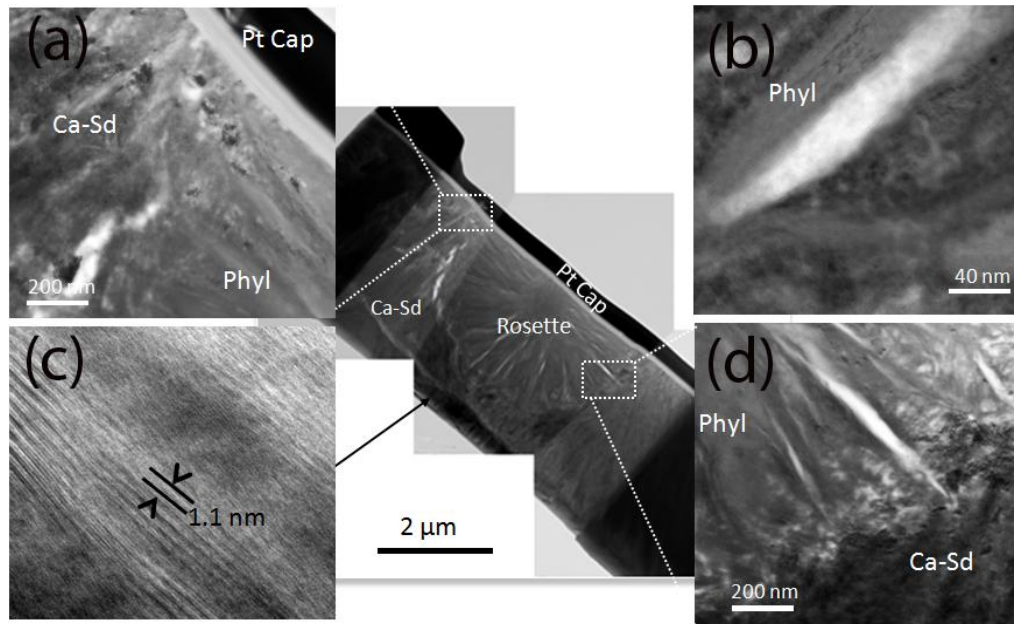
FIG 4.10: TEM of phyllosilicate rosette in Fig 4.5b and d. Low magnification Bright Field image of extracted rosette in centre. (a) Contact between rosette embedded within the carbonate. Dark grains of carbonate are enriched in Mn. (b) Intermediate magnification of the lathes or 'sprays' radiating from the centre of the phyllosilicate rosette. (c) HRTEM along one of the lathes of phyllosilicate shown the presence of 0.9 nm - 1.1 nm fringes. (d) Contact between radiating sprays and surrounding Calcium-Fe carbonate - Ca-Sd.
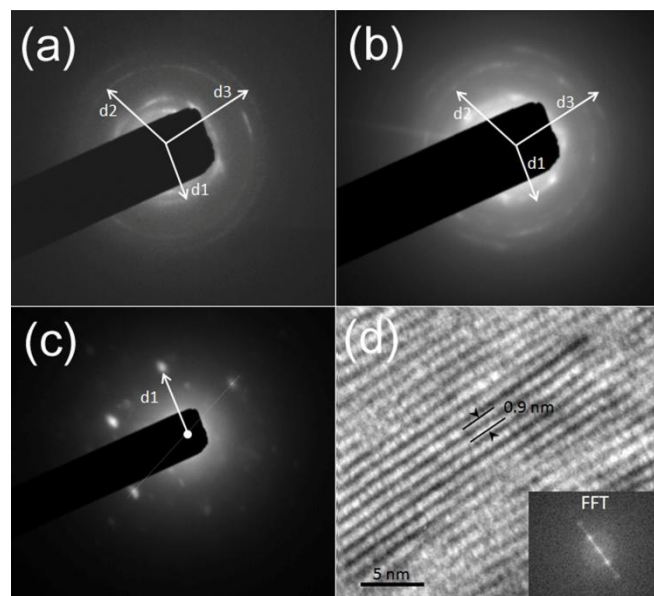
FIG 4.11: Lafayette (a) SAED of Lafayette phyllosilicate. d1 = 2.60 Å, d2 = 1.55 Å, d3 = 0.131 Å. (b) SAED of nontronite standard. d1 = 2.62 Å, d2 = 1.62 Å, d3 = 1.40 Å. (c) 5 nm nanobeam diffraction of weakly crystalline dark grains (Fe oxide, ferrihydrite?) in the phyllosilicate. d1 = 1.56 Å. Errors ≤5%. (d) HRTEM bright field of nontronite (smectite) standard.

Nakhla and Governador Valadares (GV)

In Nakhla and GV many veins contain crystalline siderite along their margins with the silicate gel in the centres of the veins. No phyllosilicates have been identified. The siderite-bearing zones have an irregular texture on the submicron scale compared to the more regular vein textures seen in Lafayette. The crystalline siderite regions are commonly found along one of the margins and do not follow the whole length of the vein across the olivine. They do however span across the entire depth of the FIB sections ~ 4 μm (Fig 4.12a). Bright field TEM micrographs show that the siderite-bearing zones consist of grains less than approximately 50 nm in size (Fig 4.12b). These zones have complex fine grained textures but TEM-EDX of many grains across entire zones yield qualitative identification of Mg-Ca-Mn siderite. Siderite compositions can, however, vary within Nakhla, with qualitative analyses showing some zones to be rich in Ca and Mn, whilst others are Mg-rich with trace amounts of Ca and Mn, as shown in Fig 4.12c. The textures are finer grained than the siderite in Lafayette e.g. grains of 10-25 nm diameter. The Lafayette siderite also differs in having low $MgCO_3$ compositions and traces of Na. Previous, quantitative EPMA analyses of Lafayette siderite have shown it to contain 22-37 mol% $CaCO_3$, 4-35 mol% $MnCO_3$, 0-2 mol% $MgCO_3$ with Nakhla having 0-6 mol% $CaCO_3$, 1-40 mol% $MnCO_3$, 2-41 mol% $MgCO_3$ (Bridges and Grady, 2000). SAED of the Ca-Mn-siderite zone in Nakhla is shown in Fig 6d. The carbonate zones in Nakhla and GV frequently exist only on one side of the veins (Fig 4.13b) though zones on both sides of veins in Nakhla have occasionally been identified.
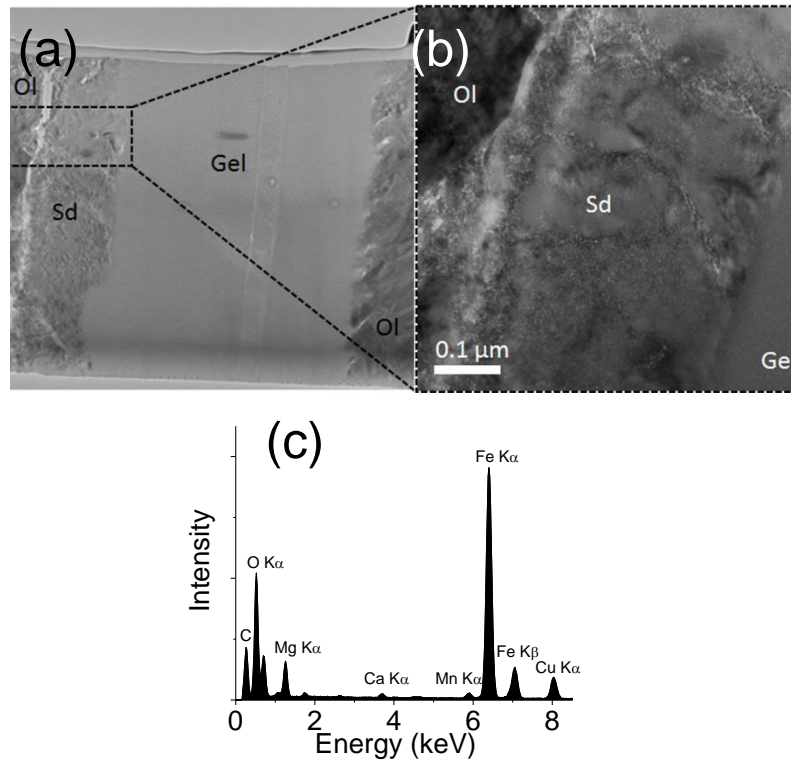
FIG 4.12: (a) Low magnification bright field TEM of vein section from Nakhla. (b) Higher magnification of siderite zone with grain sizes typically 5-10 nm. Large rarer grains (~50 nm) can also be found. (c) Characteristic TEM-EDX signature from Sd zone in (b).
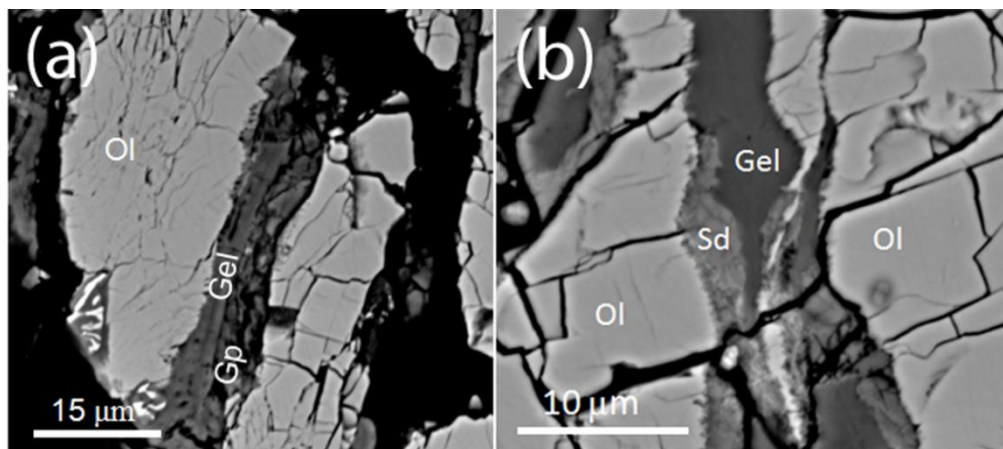
FIG 4.13. Veins identified in Nakhla and GV. (a) BSE image of large gel vein in Nakhla. A zone of gypsum is associated with the gel. (b) BSE image of GV vein similar to Nakhla vein but with an outer zone of siderite. Typical veins in Nakhla also have the same siderite-gel assemblage. Ol olivine, Sd siderite, Gp gypsum.

Veins in Nakhla have also been found to contain zones of calcium sulphate, identified as gypsum from SAED (Fig 4.14). Finer grains of gypsum (which co-exist with the coarser gypsum) are approximately 5 nm in diameter and have multiple crystallographic orientations, shown by their ring diffraction patterns (Fig 4.14b).
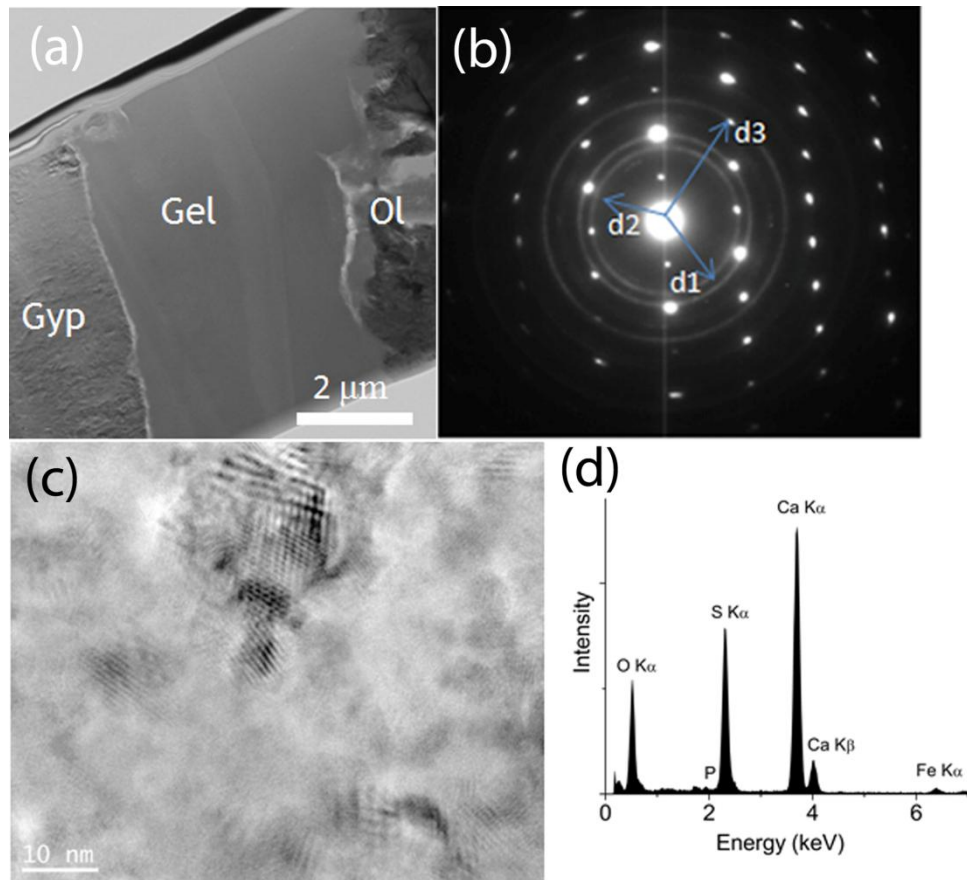
FIG 4.14: Gypsum vein found in Nakhla (SEM image of other part of vein is shown in Fig 6A. (a) Low magnification bright field image of wafer. (b) SAED of gypsum region. Monocrystalline pattern from an assumed large grain is superimposed by a ring pattern due to the majority fine grained material with multiple orientations. d1 = 0.247 nm, d2 = 0.214 nm and d3 = 0.135 nm. The d-spacings have been matched to Schofield et al., (1996) to verify gypsum. Mono diffraction is suggested [0 -1 0] monoclinic (c) HRTEM bright field in gypsum zone. (d) TEM-EDX of gypsum zone. Ol olivine, Sd siderite, Gyp gypsum.

Y000593 and Y000749

Y000593 and Y000749 alteration veins within olivine are dominated by silicate gel (Fig 4.15). This amorphous signature is characteristic of the hydrated silicate found across all of the nakhlites, with the exception of the coarse phyllosilicate in Lafayette.

In Y000593 and Y000749 traces of S are concentrated along the edges of silicate gel veins, sometimes with minor Cl and K. These are regions where it seems that the olivine has been altered to a partially crystalline silicate. This partially broken down olivine is also present as patches within the gel (Fig 4.15a). Recent studies have suggested this type of phase to be laihunite $Fe^{2+}Fe^{3+}_2(SiO_4)_2$ - a non stoichiometric olivine-type mineral (Noguchi et al. 2009). Laihunite is an oxidation product of olivine that has a distorted olivine structure with Fe^{3+} charge balanced by vacancies e.g. Kondoh et al., (1985); Bandfield et al. (1990). In Y000593, more irregular veins have been found, lacking any zonation but they include amorphous islands distinguished by having larger amounts of S and K (Fig 4.15c). No carbonates have yet been identified through TEM in the Yamato meteorites. Both Y000593 and Y000749 seem therefore to have a much lower proportion of crystalline secondary martian minerals than the other nakhlites in this study. Carbonate EDX signatures have been tentatively identified in previous studies of other thin sections (e.g. Spencer et al., 2008) but the mineralogical evidence for this has not yet been established. Iron oxides (grains approximately 100 nm in size) are also occasionally found in Y000593 (Fig 4.15c). The paired meteorite Y000749 contains some veins entirely composed of the sulphate jarosite $KFe^{3+}_3(OH)_6(SO_4)_2$ (Fig 10a). Jarosite veins have been identified which cross cut part of the fusion crust and are, therefore terrestrial in origin (Fig 4.16d). Much of the sulphate veining was found in close proximity to this region of the thin section and cross cutting the gel. Jarosite has not been identified in the less terrestrially altered meteorite pair Y000593.
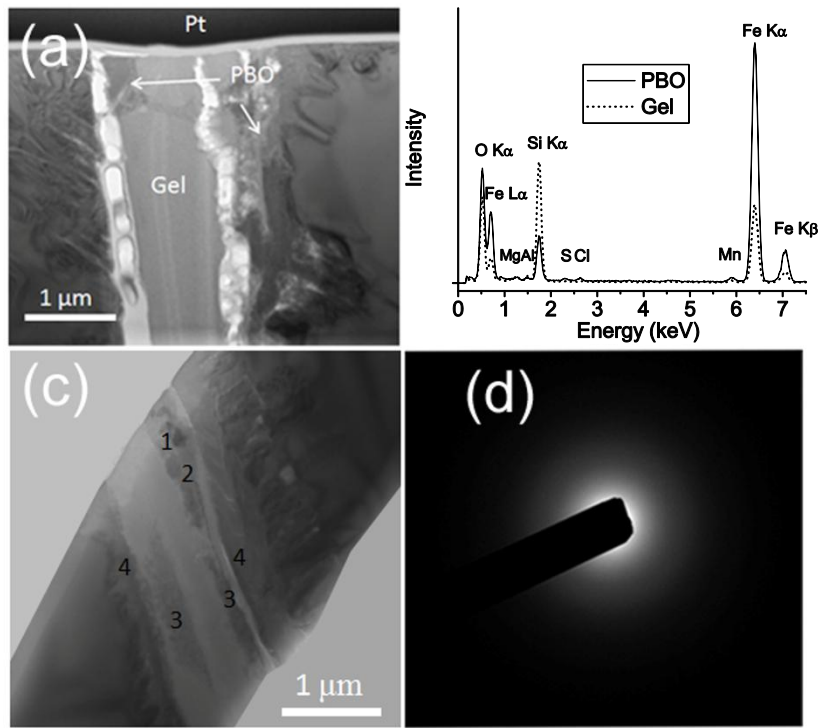
Fig 4.15: Y000593. (a) Low magnification bright field of Y000593 wafer. Partially Broken Down Olivine (PBO) is associated with the gel. (b) TEM-EDX of the gel (dotted line) and the Si-poor PBO region. (c) Low magnification bright field image of an irregular vein in Y000593. 1 = Fe-oxide grain, 2 = 'island' of amorphous Fe-Mg-K-Na sulphate/silicate, 3 = amorphous Fe-Mg-K-Al-Cl sulphate/silicate, 4 = PBO region as in (a). (d) SAED of gel phase showing the amorphous structure of the gel. Ol olivine. Pt is the protective Pt bar deposited during the FIB-SEM extraction process.
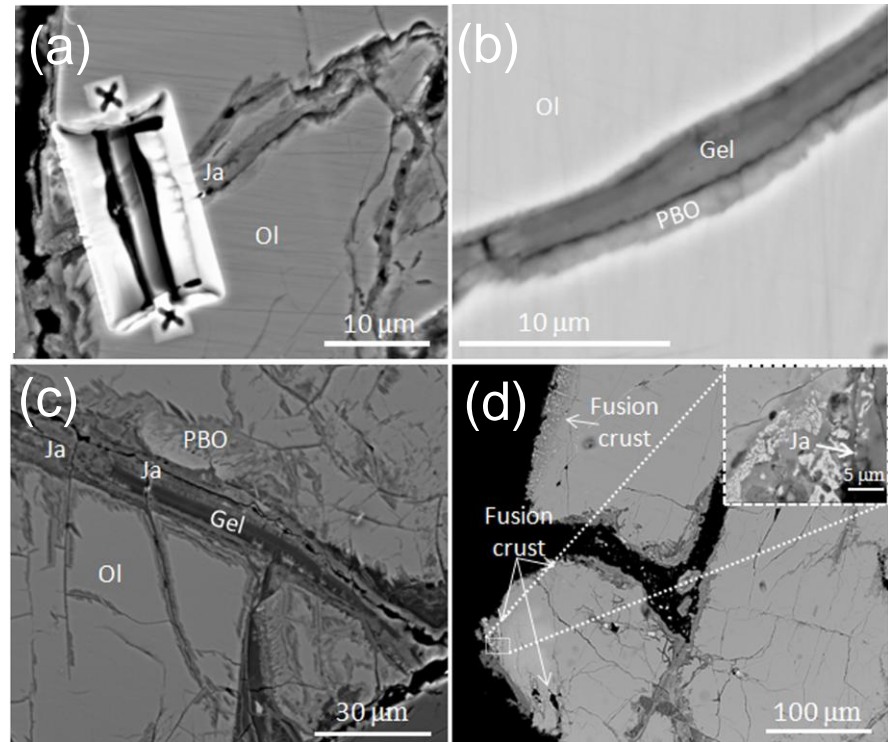
Fig 4.16: BSE images of a variety of veins found in Y000593 and Y000749. (a) Jarosite vein. Jarosite veins are only found in Y000749. A milled trench for a TEM section is shown across the vein. (b) Typical alteration vein found in Y000593. Areas of PBO are less well defined than the PBO in the veins of Y000749. (c) Y000749 vein containing a large PBO zone along its margin which is adjacent to terrestrial jarosite. (d) Y000749 fusion crust with adjacent fracture partially filled by jarosite in Y000749. Inset shows jarosite veining cross cutting the fusion crust. Ja jarosite, Ol olivine, PBO partially broken down olivine.

4.3.2 Mesostasis Phyllosilicate

Some of the mesostasis of Lafayette has been replaced by phyllosilicate. It has a more irregular fibrous texture than the vein phyllosilicate where the fibres have crystallised perpendicular to the fracture walls. Small patches of gel (Fig 4.17) were also found within one region of mesostasis phyllosilicate making up approximately 10 vol. % of it. Qualitative EDX suggests that other regions of mesostasis contain the same phyllosilicate. The mesostasis phyllosilicate and gel occupies approximately 2% of the polished section that were studied. As well as this alteration phase, this region, shown in Fig 4.17a contains mainly plagioclase feldspar with Fe-Ti-oxides, Ca-Cl phosphate and Fe-sulphide. HRTEM shows most of the basal fringes to be ~0.7 nm that is characteristic of a 1:1 phyllosilicate e.g. serpentine. However, some parts of this mesostasis phyllosilicate have fringes of 1.1 nm representing a 2:1 structure. HRTEM (e.g. Fig 4.17b) shows its lattice fringe spacing to vary from ~0.7 nm to 1.1 nm which is inconsistent with a pure smectite identity which is characterised by basal spacings of ~1 nm (Table 1, 2). Representative EDX and average compositions of this phyllosilicate and gel are given in Tables 4.3 and 4.4. of APPENDIX C.
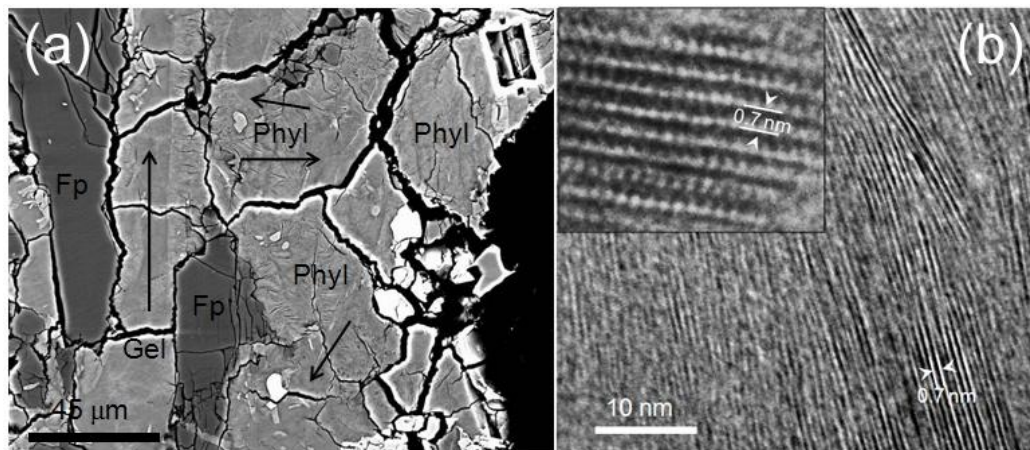
FIG 4.17: Phyllosilicate found in the mesostasis of Lafayette. a)BSE image of phyllosilicate region. Small patches of assumedgel are also found (arrowed). b) HRTEM Bright Field of thewafer extracted on the top right of the image in (a). d-Spacings (0.67 nm) that we have found are mostly smaller than those of the smectite in olivine and our nontronitestandard and suggest the presence of serpentine. Fp, feldspar;Phyl, phyllosilicate; Gel, amorphous silicate gel.

4.3.3 Gel and Phyllosilicate Compositions

The composition of the gel is that of a hydrated Fe-Mg-Al silicate. Microprobe data of the gel and phyllosilicate in the nakhlite samples are plotted in Fig 4.18 and also shown in Tables 4.3 and 4.4. For both the gel and phyllosilicate, Fe against Si abundance defines distinct lines, with negative slopes, for each nakhlite (Fig 4.18a). This has already been established in previous studies of Nakhla and Lafayette (Gooding et al., 1991; Treiman et al., 1993). However, the Fe v. Si lines plot with different y-intercepts in the order of Lafayette phyllosilicate (lowest) Lafayette gel - GV gel - Nakhla gel - Y000593 gel (highest). The normalised Fe v. Si wt% ratios are broadly similar across the nakhlites with the gradient of their slopes being -1.2 with only the Y000593 gel (gradient -1.6) being different. Previously reported terrestrial Fe-rich smectite compositions such as saponite and nontronite (e.g. Brigatti, 1983) plot within the same field of the gel and phyllosilicate analyses. Mg/(Mg +Fe) atomic ratios decrease in the order of assumed decreasing depth (Fig 4.18b), ranging from a consistent average of 0.37-0.39 (in the Lafayette gel veining, mesostasis clay and the clay veining), 0.32 in the gel of GV, 0.24 in Nakhla to 0.15 in Y000593. The highest alkali elements Na + K concentration are within GV gel (0.74 wt %), then Nakhla gel (average 0.59 wt%), followed by Lafayette gel (average 0.34 wt%) with the lowest amount in Y000593 gel (see also Fig 4.18c). The Lafayette gel, however, is quite variable in Na + K content, ranging from 0.13 - 0.75 wt%. Thus there is a tentative indication of some alkali enrichment within the Nakhla and GV gel compared to the gel and phyllosilicate within Lafayette. The olivine veining phyllosilicate has a higher alkali content than the mesostasis phyllosilicate with the phases averaging Na + K = 0.74 and 0.36 wt% respectively. Calcium contents are highest in Lafayette (gel average 0.90 wt%), closely followed by Nakhla (average 0.88 wt%) and then Y000593 (average 0.22 wt%) suggesting this element shows a fractionation trend in the gel previously identified by siderite analyses between Lafayette, Nakhla, GV (Bridges and Grady, 2000). Aluminium is most abundant in Lafayette gel and phyllosilicate, followed by Y000593 (Fig 4.18 d). Nakhla and GV have very low abundances (0.05-0.22 wt%) of Al_2O_3. The phyllosilicate in Lafayette olivine (Table 4.3) has Al_2O_3 contents lower by 3-5 wt% than that in the mesostasis. Sulphur is most abundant in the gel of Yamato meteorites, especially in Y000749, averaging 5.6 wt% SO_3 (Table 4.3) compared to approximately 1.3 wt% or less

in the other nakhlites (Fig 4.18f). Due to the suspected terrestrial alteration of Y000749, the other gel elemental wt% abundances in Y000749 have not been plotted in Fig 4.18.

Large regions of coarse phyllosilicate in Lafayette − within olivine fractures and in the mesostasis − were also analysed by EPMA in Table 4.3. The ternary diagram in Fig 4.19 shows that Lafayette phyllosilicate plots from the serpentine to saponite and nontronite composition solid solution lines. These lines are defined by the atomic ratios of Si, Al: Fe, Mg (8:4) for nontronite $(CaO_{0.5},Na)_{0.3}Fe^{3+}_2(Si,Al)_4O_{10}(OH)_2 \cdot nH_2O$, Si,Al:Fe,Mg (8:6) for saponite $(\frac{1}{2}Ca,Na)_{0.33}(Mg,Fe^{+2})_3(Si,Al)_4O_{10}(OH)_2 \cdot 4H_2O$ and Si,Al:Fe,Mg (3:2) for serpentine. Previous studies have suggested an Fe-rich smectite identity in both Nakhla and Lafayette (e.g. Burns and Martinez 1991; Gooding et al. 1991; Treiman et al. 1993). Treiman et al.'s coarse smectite in Lafayette identified chemically as saponite also matches this composition. The ferric iron rich smectite - nontronite, has higher Si + Al abundances than the Lafayette phyllosilicate. The closest smectite to the Lafayette phyllosilicate composition is the Fe-rich saponite, griffithite, which has an unusually high abundance of Fe^{3+} in its octahedral sites (Komadel et al., 2000). However, site allocations of cations based on 22 oxygens for a smectite structure (Table 4.4) indicate a slight excess of octahedral cations (average 6.2) in the vein phyllosilicate. Due to even higher calculated excesses in octahedral sites for some phyllosilicate (6.7 based on 22 oxygens) and the presence of low basal fringe measurements i.e. ~0.7 nm, which are inconsistent with pure 2:1, smectite phyllosilicate, Table 4 also presents the stoichiometry based on 7 oxygens for a serpentine area within the mesostasis. Thus, d-spacing and chemical analyses show the Lafayette vein and mesostasis phyllosilicate has a range of compositions consistent with a mixture of serpentine and smectite (saponite to serpentine-type) phyllosilicates. The data so far raises the possibility that there is a higher proportion of serpentine in the mesostasis phyllosilicate. The phyllosilicate identities are considered further in Section 4.4.3.
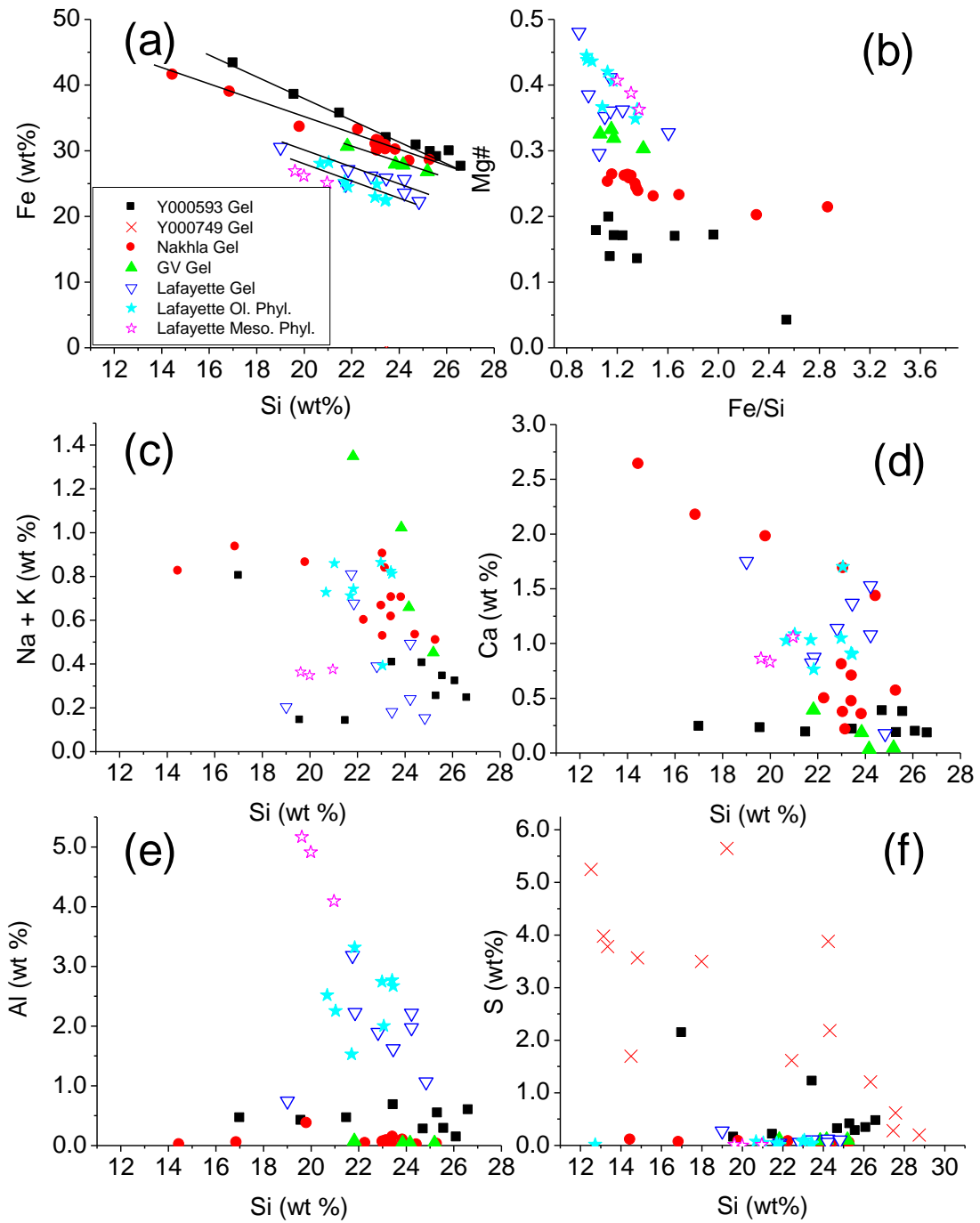
FIG 4.18: EPMA Microprobe analysis of the gel in the nakhlites and Lafayette phyllosilicate. The Lafayette mesostasis gel analysis is SEM-EDX. (a) Fe wt% v. Si wt%. Y000593 gel slope = -1.6, Nakhla gel slope = -1.2, GV gel slope = -1.2, Lafayette gel slope = -1.2 and Lafayette phyllosilicate slope = -1.2. (b) Mg number (Mg#) v. Fe/Si (wt). (c) Volatiles (Na + K) v. Si wt%. (d) Ca v. Si wt%. (e) Al v. Si wt%. (f) S v. Si wt%. Compositions in (a-f) were normalised to anhydrous 100%. The difference between the Y000593 gel slope and that of the other nakhlites suggest that Y000593 was not on exactly the same fluid fractionation path.
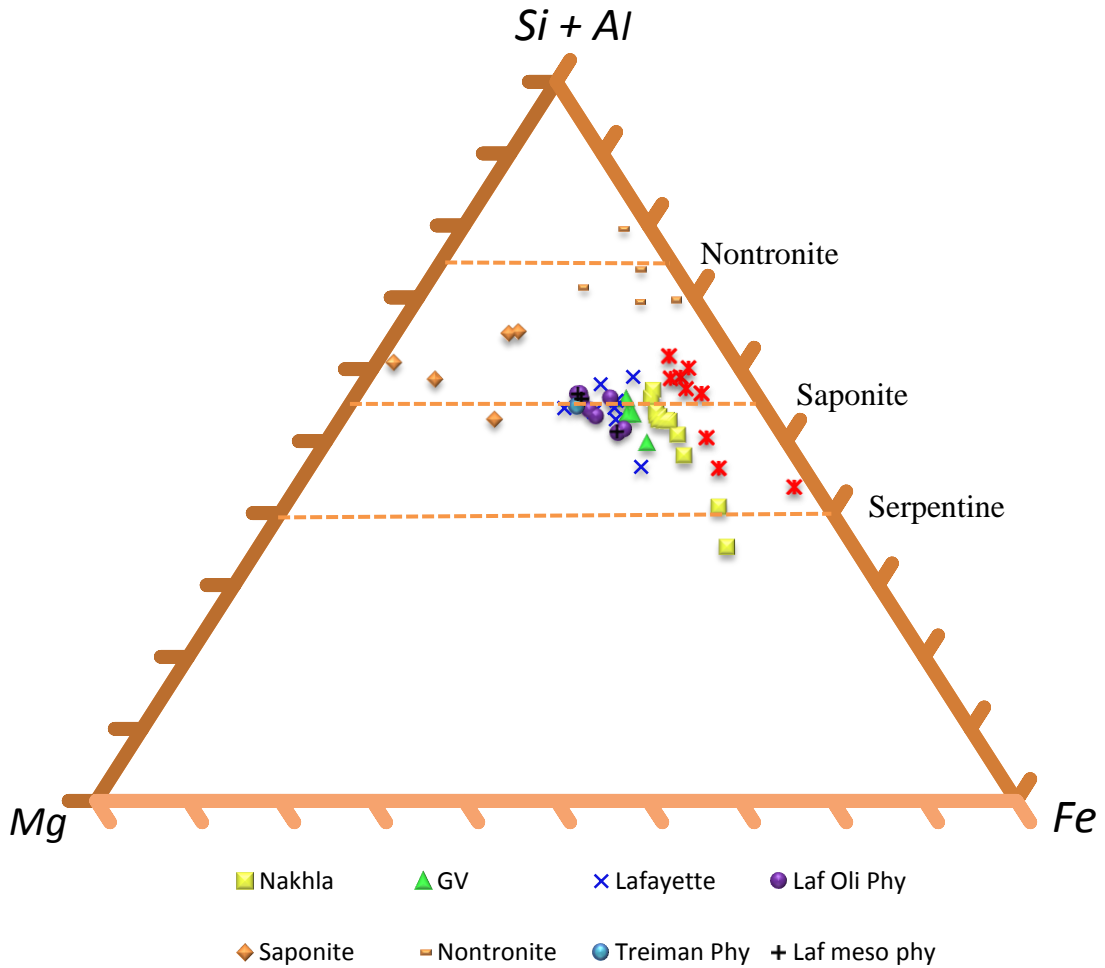
FIG 4.19: Atomic ratios of the nakhlites' gel and Lafayette phyllosilicate. Iron is total Fe^{2+} and Fe^{3+}. Clay analysis of Lafayette from Treiman et al., (1993) is also included. Similar terrestrial saponites are from: Kodama et al., (1998); Komodel et al., (2000); Brigatti et al., (1999); Deer et al., (1966). Terrestrial nontronites are from: Brigatti et al., (1983); Köster et al., (1999); Gates et al., (2002). Horizontal lines represent stoichiometric compositions of nontronite, saponite and serpentine.

Table 4.3: *Gel Compositions (wt %)*

	Y593 gel	Y593 gel av. n = 9	Y749 gel	Y749 gel av. n = 17	Nakhla gel	Nakhla gel av. n = 13	GV gel	GV gel av. n = 4	Laf. gel	Laf. gel av. n = 8	Laf. meso. gel	Laf. meso. gel av. n=8	Y593[a]	Y749[b]	Nakhla[c]	Laf.[d]
Na_2O	0.12	0.15	0.14	0.28	0.16	0.24	0.43	0.37	0.29	0.11	0.3	0.3	n.d.	0.13	1.16	0.3
MgO	3.84	3.77	4.12	4.84	6.56	6.2	8.14	8.23	10.8	9.29	8.5	10.8	3.8	7.49	6.82	13.9
Al_2O_3	0.9	0.72	1.58	1.42	0.15	0.12	0.06	0.07	5.2	3.02	6.7	4.8	0.56	3.49	0.74	4.77
SiO_2	47.1	44.8	39.9	37.4	43.5	39.5	43.9	43.5	40.2	41	40.7	41.6	51.4	49.1	40.2	49.1
CaO	0.22	0.31	0.46	0.54	0.42	1.24	0.22	0.2	1.00	1.26	1.7	1.1	0.08	0.45	1.14	0.7
K_2O	0.16	0.24	1.12	1.55	0.58	0.49	0.68	0.57	0.58	0.3	0.4	0.3	0.52	0.55	0.6	0.41
$TiO2$	0.06	0.04	0.06	0.04	0.04	0.02	0.03	0.03	0.02	0.06	b.d.	b.d.	n.d.	0.02	0.2	0.01
Cr_2O_3	0.05	0.03	0.02	0.03	0.02	b.d.	b.d.	b.d.	b.d.	b.d.	b.d.	b.d.	n.d.	n.d.	n.d.	n.d.
MnO	0.5	0.61	0.22	0.44	0.46	0.79	0.54	0.52	0.53	0.91	0.5	0.5	0.22	0.15	0.63	0.48
FeO	33.4	37.8	32.7	33.9	33.1	34.5	31	31.2	27.7	27.7	26.9	24.2	25.7	28.8	34.1	29.00
SO_3	0.7	1.08	3.34	5.63	0.05	0.05	0.15	0.16	b.d.	0.15	0.4	0.09	2.79	n.d.	n.d.	n.d.
Cl	0.03	0.07	0.06	0.08	0.24	0.25	0.94	0.74	0.02	0.13	b.d.	b.d.	n.d.	n.d.	n.d.	n.d.
Total	87.1	89.6	83.7	86.2	85.3	83.4	86.1	85.6	86.3	83.9	86	83.6	79.1	90.1	85.6	97.9

[a]Iddingsite Y000593, Nogushi et al. (2009), [b]Iddingsite Y000749, Treiman and Goodrich (2002), [c]Iddingsite Nakhla, Gooding et al. (1991), [d]Iddingsite Lafayette, Treiman et al. (1993). b.d.: below detection limits; n.d.: no data

Table 4.4: *Composition of Lafayette olivine and mesostais phyllosilicate.*

	Olivine (smectite)	Olivine (smect. av)	Meso. (serp.)	Meso. (serp. av)
Na_2O	0.3	0.2	0.1	0.1
MgO	11.4	10.5	10.6	10.4
Al_2O_3	4.5	4.1	8.3	7.9
SiO_2	45.1	42.6	38.1	38.1
CaO	1.13	1.4	1.0	1.1
K_2O	0.6	0.6	0.3	0.3
TiO2	b.d.	b.d.	b.d.	b.d.
Cr_2O_3	b.d.	b.d.	b.d.	b.d.
MnO	0.6	0.7	0.6	0.6
FeO	26.1	27.6	30.0	29.6
SO_3	0.05	0.08	b.d.	b.d.
Cl	0.02	0.05	b.d.	b.d.
Total	89.8	87.8	89.0	88.3

		[*]22 Oxygens		[*]7 Oxygens	
tetrahedral	Si	7.10	7.02	2	2.01
	Al	0.88	0.82	-	-
	Fe^{3+}	0.03	0.16	-	-
	Sum	**8**	**8**	**2**	**2.01**
octahedral	Fe^{tot}	3.41	3.51	1.31	1.31
	Mg	2.74	2.59	0.83	0.82
	Mn	0.06	0.09	0.02	0.03
	Al	-	-	0.51	0.49
	Sum	**6.21**	**6.19**	**2.67**	**2.65**
interlayer	Ca	0.19	0.24	0.06	0.02
	K	0.15	0.12	b.d.	0.01
	Na	0.05	0.06	b.d.	b.d.
	S	0.007	b.d.	b.d.	b.d.
	Cl	0.007	b.d.	b.d.	b.d.
	Sum	**0.41**	**0.42**	**0.06**	**0.03**

[*]Site allocations are given for average compositions of olivine phyllosilicate and mesostrasis phyllosilicate based on 22 oxygens and 7 oxygens respectively.

4.4 Discussion

In the following sections the nakhlite parent fluid and the formation conditions of the secondary assemblages are described. The relative depths of these nakhlites have already been proposed with the Yamato meteorites at the top, followed by Nakhla, then GV and Lafayette at the bottom (Mikouchi et al., 2003, 2006; Bridges and Warren, 2006). The nakhlites' petrologies are similar to some terrestrial PreCambrian ultrabasic lava flows which formed at depths of approximately 10-100 m (e.g. Lentz et al., 1999). The results have been interpreted to suggest that the fluid moved from deep (Lafayette) towards the other, shallower nakhlites. It is proposed that the fluid was derived from a subsurface source such as the melting of a buried ice reservoir e.g. permafrost (Demidov and Gilichinsky, 2009) rather than formation at the martian surface followed by migration of the fluid to deeper levels.

4.4.1 Fluid pH, Temperature and Redox Conditions

The analyses show a change from the coarse phyllosilicate and siderite at the margins of the Lafayette veins to the amorphous gel in the centre of the veins. This may be because the amorphous gel in the nakhlite veins cooled more rapidly than the coarse Lafayette assemblages which formed at an earlier stage in the alteration sequence. Corrosion of the Ca-siderite in Lafayette prior to the Fe-smectite/serpentine crystallisation suggests that during the hydrothermal event the fluid stopped being in equilibrium with carbonate, presumably due to exhaustion of HCO_3^- and a lack of CO_2 being dissolved and recharged into the fluid. Furthermore, the Fe oxide (ferrihydrite?) rims to the phyllosilicate are evidence that the fluid became progressively more oxidising.

Chevrier et al. (2007) described a thermodynamic model to explain the stability of smectite-carbonate assemblages on Mars. Even though their model addressed conditions on early Mars, it maybe also applicable to the mineral assemblages in the Amazonian nakhlites. They demonstrated how smectite can be precipitated at a lower pCO$_2$ than previously thought (e.g. at ≤1-10 mbar). Their phase equilibrium calculations for the carbonate and smectite are expressed as a function of Mg/(Mg+Fe) atomic ratio (Fig 4.20). Based on suggested partial pressures in the Amazonian (Manning et al. 2006), ranging from 10-100 mbar which we take to be equivalent to the amount of CO_2 in a suggested ice

reservoir, and the average Mg number of 0.4 for the phyllosilicate in Lafayette, the pH of the nakhlite parent fluid would have been close to neutral/weakly acidic (Fig 4.20). Reduction in pCO_2 due to carbonate precipitation would then have led to the formation of phyllosilicate. If a higher proportion of CO_2 was stored in the ice from which the hydrothermal fluid was derived, pH conditions would be shifted to more alkaline values.

Temperatures for the formation of Fe-smectite can vary from up to 250 ^{o}C (Tosca et al., 2008), and would have been less than or equal to the temperatures governing the precipitation of the Ca-siderite, unless an additional heat source had emerged (Vicenzi & Heaney, 2000). However, the order of phase formation from siderite to clay followed by amorphous gel identified here does not show any evidence of a second thermal event. In terms of carbonate, this is consistent with crystallisation of metastable carbonate occurring rapidly at low temperature ≤150 ^{o}C (e.g. Golden et al., 2000, Baker et al., 2000). Isotopic measurements of $\delta^{18}O$ show heavy enrichment in the Nakhla carbonate (Saxton et al., 2000) and also imply low temperatures for siderite deposition (80-170 ^{o}C). Chevrier et al. (2007) also showed the stability fields for nontronite, Fe^{3+} and ferrihydrite as a function of dissolved silica activity and pH. At neutral pH, silica saturation leads to the formation of amorphous silica and Fe oxide (ferrihydrite) stability. This is consistent with the assemblage of Fe-oxides (although there is not any conclusive identification of ferrihydrite), followed by the precipitation of gel that has been described. Treiman et al. (1994) identified the presence of ferri iron oxide phases that could be the same identified Fe-oxide phases. Reducing conditions leading to the formation of saponite or a trioctahedral phyllosilicate from a pre-existing nontronite phase (Manceau et al., 2000) or other dioctahedral phyllosilicate seems unlikely in the nakhlites with late stage precipitation of ferric iron oxides. Fe oxide grains within smectite have also been suggested to crystallise as the weathering of silicate minerals progresses (Sherman et al., 1962) and this is consistent with the Lafayette phyllosilicate assemblage.

By this model, sub surface phyllosilicate formed without thermodynamic equilibrium with the hydrosphere. An assumption in the model of Chevrier et al. is thermodynamic equilibrium between the atmosphere and subsequent stable minerals. However, the mineral sequences found in Lafayette (e.g. phyllosilicate after carbonate and amorphous silica with Fe oxide after phyllosilicate oxidation) are very similar to the

sequence described by Chevrier et al., (2007). Replacement of carbonate by phyllosilicate in a progressively cooling fluid implies an upper limit ~150 °C for phyllosilicate formation. In order to produce this hydrothermal activity, a thermal event must have occurred: The association with sawtooth fractures that have been subsequently filled with secondary phases and Mars' heavily cratered past could imply that impact was the heat source. Saw-toothed fracturing within other nakhlites have been demonstrated by previous authors (Treiman et al., 1993; Gillet et al., 2002). Bridges et al. (2001) also suggested short lived pulses of fluid in the parent rocks of the SNCs and the formation of metastable phases over a period of days to months rather than the extended timeframes over thousands of years such as those in long-lived hydrothermal systems.
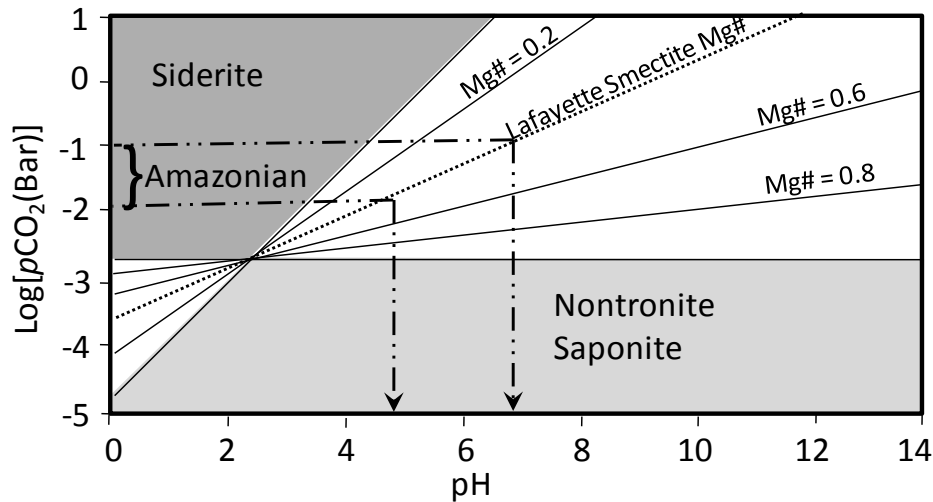
FIG 4.20: Thermodynamic model showing the stability of phyllosilicates on Mars (Chevrier et al., 2007). The phase equilibrium diagram for the carbonate and nontronite/saponite is expressed as a function of Mg/(Mg+Fe) atomic ratio. The dotted line represents the Mg# of Lafayette phyllosilicate (~0.4). The Amazonian log$p$CO$_2$ ranging from -1 to -2 corresponds to weakly acidic to neutral pH condition for nontronite/saponite stability.

4.4.2 Hydrous Silicate Gel

It is suggested on the basis of the SAED results (Fig 4.15d) that the 'gel' parts of the veins are amorphous. The softness of this phase does raise the possibility of crystallographic structure having been destroyed during sample preparation with the FIB.

This phase common to all of the nakhlites studied is clearly distinct from the phyllosilicates and Fe-oxides found in Lafayette. Its composition also crosses smectite and serpentine solid solution lines.

The amorphous nature of some material within the veins has also been suggested by previous authors (e.g. Ashworth and Hutchison, 1973; Vicenzi & Heaney, 1999). Ashworth and Hutchison's (1975) preliminary study of Nakhla using microtome sections indicated the presence of a colloidal gel. Weakly crystalline minerals with compositions similar to the gel, can form from the weathering of iron-rich saponites (Kohyama & Sudo, 1974; Romero et al., 1992). The amorphous gel in the nakhlites has a variable composition but closely resembles the range of phyllosilicate composition that has been determined. However, textural evidence of late stage precipitation of the gel from the hydrothermal fluid could suggest that the gel is not the result of phyllosilicate alteration.

Fiore et al. (1995) demonstrated that gels can also act as an intermediate stage or a precursor for the formation of spherical phyllosilicate particles. In an experimental synthesis of saponite/nontronite by Grauby et al., (1994), gel precursors were made which were then formed into clay via mixing with distilled water and gradual heating (30 days) at 200°C under alkaline conditions (pH 9-10). Treiman and Lindstrom (1997) also proposed that the Lafayette 'iddingsite' formed from a precursor gel similar to smectite composition. Given that the Lafayette gel is chemically close to the composition of the Lafayette phyllosilicate (Fig 4.19), but has a lower Mg number than the phyllosilicate (see next section) a final pulse of fluid may have cooled too quickly to crystallise into phyllosilicate and instead precipitated as a metastable gel. Cooling may have been enhanced by the decreasing volumes that were available to be filled within the fractures during the last fluid pulse. The progressively finer grained textures identified at the inner margins of some Lafayette phyllosilicate veins are also consistent with this cooling.

4.4.2.1 Compositional Fractionation of Gel

It has been shown that Fe + Si in the gel increases and Mg/(Mg+Fe) decreases up the nakhlite pile. The gel in the nakhlites from near the surface has a greater Si content than the coarser crystalline secondary silicates at the base of the known nakhlite pile. The variation in Fe + Si abundances between the different nakhlites studied here, together with

the phyllosilicate to gel precipitation order may be the result of SiO_4^{4-} enrichment and Fe fractionation during the lifetime of the fluid. The fluid precipitated much of its less soluble cations (e.g. Ca) in Lafayette, followed by decreasing proportions in GV then Nakhla and also Y000593. This process could have led to silica enrichment in the fluid and hence facilitated precipitation of the gel phase.

Neither the Mg number of the nakhlites' olivines, pyroxenes (Bridges and Warren, 2006) nor the meteorites' bulk Mg numbers (Meyer, 2006) follow the Mg/(Mg+Fe) fractionation trend identified in the alteration phases. This suggests that the fluid passing through these fractures brought in the majority of its ionic constituents through dissolution of surrounding rock before encountering the nakhlite parent rocks that have been available for study, although the hydrothermal cell as a whole, may have been solely within a nakhlite lithology. A similar conclusion was reached by Gillet et al., (2002) in their study of the NWA817 nakhlite. Evidence that some localised dissolution and remobilisation into the fluid also took place is shown by the mesostasis phyllosilicate of Lafayette because it is enriched in Al. The low Al abundances in the gel of Nakhla and GV imply that the local dissolution of Al-rich mesostasis did not, however, contribute to the gel composition in the nakhlite olivine veins (Fig 4.18e).

4.4.3 Phyllosilicate

Chemical analyses show the Lafayette phyllosilicate lie between the serpentine, saponite and nontronite solution lines (Fig 4.19) but with unusually high total Fe concentrations compared to terrestrial samples. Table 4 shows the atomic proportions of the cations and their respective sites based on 22 oxygen atoms and 8 cations in the tetrahedral sites for the veining phyllosilicate. The deficit of tetrahedral cations (Si, Al) indicates that there is some Fe^{3+} substitution into the tetrahedral sites and Fe^{3+} with Fe^{2+} in the octahedral sites. This feature is relatively common in natural trioctahedral saponites (Nimis et al., 2004), where all octahedral sites are filled compared to every third site being empty in dioctahedral structures such as nontronite. Fe-rich saponites are also frequently found in many terrestrial soils (Brigatti et al., 1999). However, they do not contain as much Fe as in the clay of Lafayette. Octahedral site substitutions of Fe^{2+} and Fe^{3+} in saponite to nontronite solid solutions have been experimentally demonstrated by Grauby et

al., (1994). In a previous study of Nakhla, Burns et al. (1991) reported the presence of ferric iron in veining 'iddingsite'. Based on this study, it would have most likely been the veins' amorphous gel. Gooding et al.'s (1991) Nakhla 'rust' classified as a ferric smectite also underlines the ferric nature of the hydrous silicates in the nakhlites.

The 1.1 nm d-spacings also identified are consistent with an Fe-smectite identity for some of the phyllosilicate. Fully collapsed smectites have fringes of 1 nm and can be a result of electron beam exposure and containment under high vacuum conditions (Klimentidis and Mackinnon, 1986). The 0.9 nm fringes of similar stacking sequence are slightly low for smectites but it is believed to also be a fully collapsed Fe-smectite phase based on the 0.9 nm fringes also identified in the nontronite standard. Previous TEM studies of the Lafayette phyllosilicate (Treiman et al., 1993) by ultra microtomy also identified 1 nm d-spacings. However, the low basal spacings 0.7 nm which have been found are also present, particularly in the mesostasis, are not consistent with smectites but rather of kaolins and serpentines. The stoichiometry and d-spacing of the phyllosilicate in the mesostasis of Lafayette is consistent with the presence of a berthierine-type serpentine composition $(Fe^{2+},Fe^{3+},Mg,Al)_{2-3}(Si,Al)_2(OH)_4$ with vacancies in the octahedral sheet - Table 4.4 (APPENDIX C). Thus the phyllosilicate is a fairly complex mixture of Fe-smectite and serpentine. In the light of this complexity it is possible that future work will identify further phyllosilicates within the nakhlites.

The presence of ferric iron within the smectite component (as also suggested by Gooding, 1991), the serpentine and also potentially the gel indicate a more oxidising environment than would be associated with a ferroan trioctahedral end member such as a pure saponite or ferroan serpentine. The oxidising nature of the martian near surface is well known. Progressive oxidation of the fluid associated with the enrichment of ferric iron is suggested by the crystallisation of some iron oxide at the inner margins of the vein phyllosilicate. The oxidising nature of the fluid is also consistent with the presence of laihunite e.g. Bandfield et al., (1990).

In this study, phyllosilicates have only been identified in Lafayette and not the other nakhlites. In contrast, Gooding et al., (1991) suggested that there were also occasional flakes of ferric smectite in Nakhla. The TEM results of Gillet et al. (2002) for NWA817 also suggest that some poorly crystalline smectite with d-spacing ~1 nm did form in that

meteorite. The abundance of phyllosilicate amongst the hydrous silicate phases in the nakhlites is uncertain but, apart from in Lafayette, the gel is clearly the dominant nakhlite secondary silicate phase.

4.4.4 Saline Zones (Siderite and Gypsum)

The soluble salts e.g. sulphates found in Nakhla and GV in this study and previously (e.g. Bridges and Grady, 2000) are further up the hydrothermal cell and hence closer to the martian surface than the Lafayette assemblage. Their presence suggests that evaporation occurred in the nakhlites' parent rocks, with the most soluble sulphates and chlorides precipitating from the final portions of the hydrothermal fluid.

The lack of any identified zones of pre-terrestrial crystalline sulphates or carbonate in Y000593/Y000749 implies that soluble salts were not precipitated from an evaporating fluid in the part of the nakhlite parent rocks sampled by the Y000593/Y000749 meteorites. Alternatively, some soluble salts (e.g. chlorides, sulphates) might have been lost during their terrestrial residence or had leached out from the inner parts to regions closer to the fusion crust (Wentworth and Gooding, 1994). The fluid passing upwards through the nakhlites on Mars could have been exhausted in sulphate and carbonate once it reached the Yamato nakhlites. This suggests that Y000593/Y000749 was on a similar (i.e. parallel) but not identical fluid pathway to that which the other nakhlites studied here were linked by. Although the Yamato meteorites would have been even closer to the cold martian surface than the other nakhlites (Mikouchi et al., 2003, 2006), they may have experienced a slightly higher water to rock ratio than Nakhla or GV due to the marginally higher volume of veins in Y000593. The difference between the Y000593 Fe v. Si gradient (Fig 4.19) and that shown by the other nakhlites in this study supports this slightly different fluid history. Similarly NWA817 may have experienced a similar but not identical fluid fractionation and cooling history.

Terrestrial overprints have also occurred in the Antarctic finds such as the sulphur rich islands within the gel of some Y000593 veins (Fig 4.15c) and jarosite in Y000749 (Fig 4.16).

4.4.5 MIL03346, NWA998 and NWA817

Secondary assemblages have also been reported in the other nakhlites MIL03346, NWA998, NWA817 that have not been included in this study (e.g. Imae and Ikeda, 2007; Treiman and Irving, 2008; Gillet et al., 2002). Imae and Ikeda (2007) tentatively identified serpentine and saponite within olivine fractures of MIL03346. However, in the absence of structural information this could have been the identified 'gel' as shown by the gel analyses of nakhlites in this study on the ternary diagram of Fig 4.19, which can lie between the serpentine and saponite solid solution lines. MIL03346 vein analyses record low Mg numbers similar to those of the Yamato meteorites (Imae and Ikeda 2007). Treiman and Irving's (2008) study of the gel or phyllosilicate in NWA998 also reported a saponite composition. The Mg numbers of their quantitative analyses are similar to those of Nakhla. Ferroan carbonate and Ca-sulphates, thought to be of martian origin, have also been identified. This resembles the types of assemblages identified in Nakhla and GV. However, structural information about the hydrous silicate phases in NWA998 is missing and thus it is not clear whether they are crystalline or the amorphous gel phase. The similarity between the secondary assemblages in NWA998 and Nakhla and GV is consistent with an origin for NWA998 in the upper parts of nakhlite pile (Bridges and Warren 2006). This is however, in contrast to Mikouchi et al.'s (2006) model where based on inferred cooling rates and ground mass textures, NWA998 is at the bottom of the nakhlite pile.

Gillet et al.'s (2002) study of NWA817 did report crystalline Fe-smectite in some of that meteorite's olivine veining. The Mg number of that alteration material is closest to that of GV in this study. However, Mikouchi et al (2006) proposed that NWA817 lay at one of the shallowest depths of the nakhlites along with MIL03346. Thus although these results suggest that phyllosilicate is concentrated in the lower parts of the nakhlite pile, where the W/R was highest and cooling rate slowest there is evidence from other workers that occasionally some crystalline smectite formed in higher parts, perhaps as a results of localised variations in W/R (see below) and cooling rate along parallel fluid pathways.

4.4.6 Nakhlite Hydrothermal Cell

The fracturing seen in the nakhlites suggest a shock event pre-dating the formation of secondary assemblages that filled them. One can hypothesise that impact was the source of opened and sawtooth fractures and heat in the hydrothermal system. Hoffman (2000) showed that H_2O-dominated subsurface ice extended to depths from 5 to 10 km in Amazonian terrains, far below the maximum ~100 m depth of the nakhlites. Impact-induced melt sheets have been shown to sustain large temperatures (>100 ^{o}C) for long periods of time, 10^4-10^5 years, in 100 km sized craters (Daubar and Kring, 2001; Abramov and Kring, 2005). Neighbouring rocks to such large craters should experience higher degrees of shock compared to the relatively small amounts experienced by the nakhlites (Fritz et al., 2005). However, we do not know what radial distance the nakhlites were from the assumed impact source of the hydrothermal cell. We start with the assumption of a relatively small crater impact (<10 km) inducing a hydrothermal system. The Amazonian age of the nakhlites (1.3 Ga) shows that they were derived from a relatively young martian surface. Areas of the northern lowlands that have similar ages to the nakhlites, show 10^{-3} - 10^{-4} craters/km^2 for crater diameters ranging from 1-10 km (Hartmann and Neukum 2001). Large craters (>100 km) are much rarer (densities approximately 10^{-7} craters/km^2) and are therefore less likely to be the impact heat source of this hydrothermal cell.

The Lonar crater, India (diameter 1.8 km) contains evidence of extensive hydrothermal alteration in the form of phyllosilicates due to the impact event and has been suggested to represent a lower limit for a crater size associated with an impact-induced hydrothermal system (Hagerty and Newsom, 2003). Based on this, the lower limit for the nakhlite impact crater associated with the hydrothermal fluid is approximately 2 km. Schwenzer and Kring (2009) modelled the mineral abundances for smectites and other low temperature minerals in impact-derived hydrothermal cells. They have shown that the secondary assemblages are largely controlled by W/R ratios and temperature. Experimental simulations by Baker et al., (2000) with CO_2-H_2O fluids interacting with basaltic rock show siderite to form at 200 ^{o}C with W/R ratios of 1 to 10 and they proposed that this was consistent with the nakhlites' hydrothermal system. Taking Lafayette as our most altered rock and the volume of secondary assemblages as approximately 10% of the olivine, which is 10% of the bulk rock (Treiman, 2005), the volume of water equivalent to the total

volume of secondary assemblages is 1 %. With conversion to a mass ratio W/R, based on a nakhlite having a specific gravity of approximately 3.5 (Lange and Carmichael, 1987), our W/R to produce this volume of secondary assemblages at one instant in time would be 0.003. Naumov (2005) suggested that relatively high flow rates of fluid (10^{-4} to 10^{-3} m/s) are likely in impact-induced hydrothermal systems. Assuming a pure deposition process through the volume of veining, the flow rate of Naumov (2005) and the length of the Lafayette mass to be 1 m, W/R ratios from 1-10 (Baker et al., 2000) imply a short-lived hydrothermal system of 1-10 months. The W/R value, within this range, would have been highest in Lafayette and decreased towards the margins of the hydrothermal cell. A combination of more rapid cooling and lower W/R may therefore have generally prohibited the formation of phyllosilicates in the other meteorites. This is consistent with the impact model of Schwenzer and Kring (2008) in which smectites are favourably precipitated when the W/R ratio increases, although their W/R ratios were much higher (~1000) and modelled for larger hydrothermal systems. Some variation in cooling rates and W/R may explain the presence of some crystalline smectite in NWA817 at a shallow depth in the nakhlite rocks (Gillet et al., 2002).

4.4.7 A Model of the Nakhlites' Alteration Process

4.4.7.1 Carbonate and Clay Identified on the Martian Surface

Carbonates coupled with the presence of phyllosilicates have recently been discovered through orbiter observations of Noachian or Hesperian terrains on Mars (Ehlmann et al., 2008; Mustard et al., 2008; Poulet et al., 2005; Bibring et al., 2005). Carbonates and hydrated silicate deposits have also been identified in the Gusev crater by the integration of hydrothermal fluids (Morris, 2010). These secondary minerals are similar to those found in the nakhlites (i.e. siderite and Fe-smectite, serpentine). The formation conditions for smectites identified in this way have been suggested to require significant water reservoirs with moderate to alkaline pHs and warm temperatures, either maintained on the surface or in the shallow crust of Mars (Mustard et al., 2008; Poulet et al., 2005). Similar conditions would also favour carbonates on the martian surface such as those found in the Nili Fossae region where surface fluvial activity and possibly shallow lake deposits could have been the setting for carbonate formation (Ehlmann et al., 2008).

The phyllosilicates which have been recorded in the walls, ejecta and central peaks of the ancient highlands, however, also show a strong association with more localised impact-induced hydrothermal activity (Mustard et al., 2008). On the basis of the evidence from this nakhlite study, even though of different age to the minerals identified from orbit, it is suggested that impact is a likely origin for many of the martian phyllosilicate and carbonates.

4.4.7.2 Impact Driven Hydrothermal Alteration of the Nakhlites

In a hydrothermal cell initiated by an impact on the martian surface, the possible stages of fluid activity recorded in the nakhlites were as follows:

1. An impact (assumed to be 1-10 km D_c) created fracturing in the nakhlites (as most clearly shown by the sawtooth fractures in Lafayette, Nakhla and GV) and melted H_2O-CO_2 ice within approximately 100 m of the surface. The icy fluid source had a stored CO_2 depository equivalent to ~10-100 mbar pCO_2. This CO_2 dissolved in the fluid to form HCO_3^-.

2. The fluid, with a W/R ratio of 1-10 in Lafayette, dissolved olivine and mesostasis within the nakhlite parent body and migrated upwards from Lafayette at the deepest level towards Nakhla near the surface. The more insoluble cations Fe, Ca, Mn were the main constituents of the first secondary mineral siderite to precipitate out along the edges of the fracture walls within the olivine. This was followed by the crystallisation of a mixture of serpentine and saponite/nontronite smectite in the veins followed by Fe oxide as the fluid became progressively more oxidising in Lafayette. The fluid at this stage was less than or equal to 150 ^{o}C with near neutral pH.

3. Depletion in Ca, Fe, Mn, Mg and CO_2 exhaustion led to silica enrichment in the fluid. Amorphous or very weakly crystalline silica-rich hydrous gel was then deposited in the centre of veins as the fluid cooled. The fluid also dissolved parts of the mesostasis in Lafayette and precipitated some intermixed serpentine and smectite with gel there as well. Weakly crystalline, partially broken down olivine is also found at the margins of many veins in the Yamato meteorites.

4. The nakhlite parent fluid seeped upwards from Lafayette towards GV, Nakhla and the Yamato meteorites - depositing the gel together with some siderite in GV and Nakhla

veins and mesostasis. Only a little smectite-serpentine (e.g. other workers have mentioned some in Nakhla and NWA817) was precipitated beyond that in Lafayette because of the faster cooling rate in the hydrothermal system once the gel precipitation had commenced and also because of the decreasing W/R in the latter stages. As the fluid migrated, its composition fractionated with a decrease in siderite Ca/Mg ratio, and the gel's Mg/(Mg+Fe) ratio and an increase in Fe + Si contents. Some incorporation of Al from dissolved mesostasis in Lafayette into the phyllosilicate that replaced it also occurred in addition to this fluid fractionation between the nakhlites.

5. The Yamato meteorites (and NWA817) may have encountered separate fluid paths, due to their slightly higher W/R ratio than Nakhla and GV, different Fe/Si ratio and higher Al contents in the Y000593 gel. The Yamato meteorites would have, however, experienced a similar fluid fractionation sequence as Lafayette to Nakhla except the fluid in Y000593 had been exhausted of HCO_3^-.

6. Once the fluid reached the near surface, e.g. in Nakhla, progressive evaporation of the fluid led to the formation of soluble salts such as gypsum and halite. There is some evidence the most soluble cations were also adsorbed into the gel (e.g. Na^+ and K^+) in higher abundances at this point. The deposition process of the secondary assemblages in the hydrothermal cell lasted approximately 1-10 months following the impact.
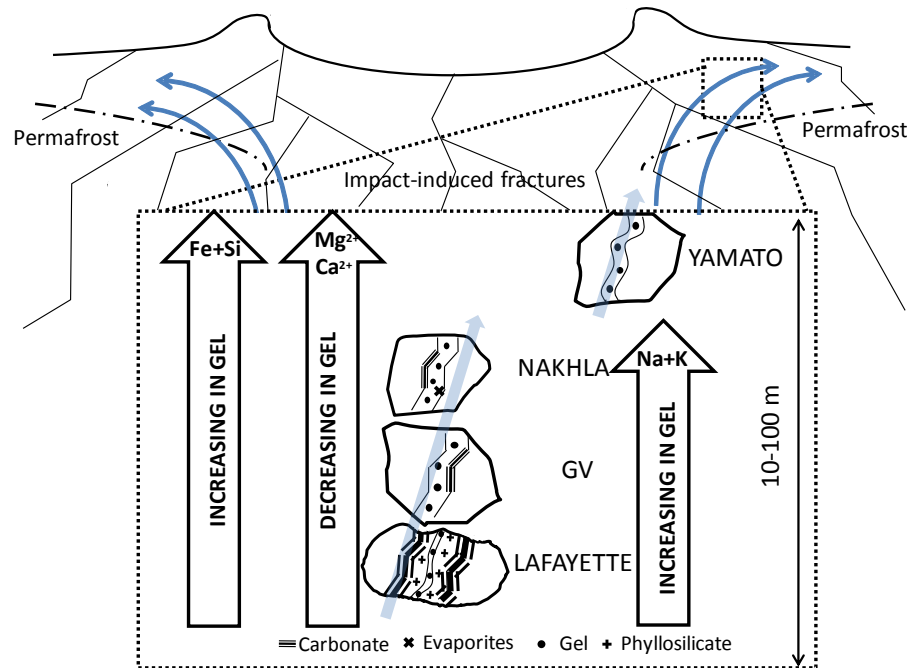
FIG 4.21: Diagram illustrating the variation in the types of veining found between the Lafayette, GV, Nakhla and Yamato nakhlites in an impact-induced hydrothermal system. An impact on the martian surface initiated the melting of buried H_2O-CO_2 ice (permafrost). The fluid (indicated by curved arrows) flows in the direction from Lafayette to Nakhla through impact-induced fractures. The enlarged region shows the different assemblages associated with the olivine grains of the different nakhlites. The Yamato meteorites experienced a parallel pathway of fluid but still experienced the same fluid fractionation sequence in Mg# and Ca. Other nakhlites not studied here e.g. NWA817 may also have been on parallel fluid pathways.

4.5 Conclusions

A variation in the mineralogy of the Lafayette, Governador Valadares (GV), Nakhla, Y000593 nakhlite secondary assemblages is found that follows a trend associated with their relative formation depths ~10-100 m under the surface of Mars. The secondary assemblages consist of siderite, Fe smectite-serpentine, minor Fe oxide, an amorphous hydrated silicate phase 'gel' of smectite-serpentine like composition and soluble salts such as gypsum. These minerals are mainly present in olivine fractures but also within the mesostasis. All of the nakhlites studied are dominated by the amorphous gel phase. Note that both structural (TEM-SAED) and chemical analysis is required in order to distinguish between the phyllosilicates and the gel phase, rather than solely quantitative chemical analysis.

Textural observations suggest that within the olivine fractures of Lafayette the crystallisation sequence was Ca-rich siderite that was corroded and partially replaced by phyllosilicate followed by Fe oxide crystallisation. Then amorphous silicate gel was precipitated in the fractures. Finally, soluble salts crystallised from the fluid. Partially broken down olivine (probably laihunite) is also present at the margins of some olivine fractures within Y000593. All of the secondary minerals apart from the final soluble salts precipitated in Lafayette. The other, shallower depth nakhlites that have been studied contain the gel, siderite and salts (apart from Y000593/Y000749 which contains only the gel). Other workers have shown that occasionally phyllosilicate crystallised in other nakhlites, which is suggested to be the result of variations in W/R and/or temperature.

The phyllosilicate in Lafayette is a complex mixture of 1:1 and 2:1 phyllosilicate, suggested to be Fe-serpentine and Fe-smectite, although the relative complexity of phyllosilicate means that the possibility of other phyllosilicates being identified in future should not be ruled out. There is a higher proportion of serpentine within the mesostasis phyllosilicate, based on most commonly observed ~7 Å fringes and a serpentine type chemical composition by EMPA.

A model has been proposed describing the nakhlite hydrothermal setting. It is suggested that the aqueous fluid was near neutral pH, less than or equal to 150 $^{\circ}$C and became progressively more oxidised, silica-rich, and, ultimately, when near the surface, evaporite-salt rich. An association with sawtooth fracturing and upwards fluid migration has led to the proposal that the fluid was initiated by melting of buried H_2O-CO_2 ice after a local impact. The fluid migrated through the nakhlites towards the surface. On the basis of likely W/R ratios (1-10; experimental work of Baker et al., 2000) and fracture-filling times based on fluid velocities (Naumov, 2005), the hydrothermal system lasted months/years rather than thousands of years, cooling relatively rapidly. The fluid fractionation is most clearly shown by variation in the Mg/(Mg+Fe) ratio and Fe + Si abundances between the gel of the nakhlites and ultimately precipitation of soluble salts.

Veining in Y000749 contains a terrestrial overprint of jarosite and other sulphates. More information on the nakhlite hydrothermal cell may be obtained by further analysis of the other nakhlites (MIL03346 and, NWA817 and NWA998) in the light of this study and more thin sections with those of the other nakhlites.

Chapter 5
Iron Oxides In Comet Wild2/81P: Distinction Between Cometary and Capture-Related Material

5.1 Introduction

Since the recovery of the *Stardust* capsule in January 2006, samples from the coma of Comet 81P/Wild 2 have started to reveal what this Jupiter family comet is made of (Brownlee et al., 2006). Burchell et al., (2008) estimated that approximately 1200 particles larger than 1 μm had struck the cometary collector at 6.1 km s^{-1}. The high speed of the impact events causes some processing of the particles during capture. The types of cometary track that form are summarised in Section 1.2.1.5. The incident particle may thus break apart during capture and also undergo heating as it hits and passes through the aerogel. Hence any cometary dust grain along an aerogel track should be considered as a fragment of the originally incident dust grain (which generated that aerogel track) and that may have undergone shock and/or heat processing during capture. The most extreme cases of alteration are mostly likely to occur upon impact, where high temperatures are obtained via flash heating and the largest impulse is received by the cometary grain.

5.1.1 Capture Heating

Detailed mineralogical studies of the cometary grains distributed along the aerogel tracks (as distinct from terminal grains at the ends of tracks) have shown the importance of understanding the effects of collection such as heating and oxidation or reduction within the aerogel at 6.1 kms^{-1}. This is discussed in more detail in Grossemy et al. (2008) and Burchell and Kearsley (2008) and Burchell et al. (2006a). Rietmeijer et al. (2008) and Leroux et al. (2008) used analytical TEM analyses of samples from along cometary tracks to show that the most frequent microstructure consists of a silica-rich glassy matrix containing a large number of vesicles and abundant Fe-Ni-S inclusions. This suggests that a large proportion of incoming dust particles were fully melted and mixed with molten

aerogel. The larger particles towards the terminal ends of the aerogel tracks have preserved more of the pristine cometary material. This is in agreement with studies of laboratory analogue samples where mineral projectiles grains of known composition were captured in aerogel using light gas gun experiments (e.g. Noguchi et al., 2007; Hörz et al., 2008; Burchell et al., 2009).

This chapter reports on the analyses of grains found from four *Stardust* tracks; a transverse slice from the entrance of track #41 (extracted from *Stardust* cell C2044), the entire track #134 (cell C2012), and a longitudinal cut from the entrance of track #162 (cell C2062). Particles from the terminal area of track #121 (cell C2005) have also been studied. A variety of complementary analytical techniques have been used i.e. optical microscopy, SEM, TEM, micro XRF fluorescence and Fe-XANES, EXAFS. The focus of this chapter has been the identification of oxide phases in the samples and consideration of their possible origins. Distinction between cometary material, capture heating products and terrestrial contamination will help to further constrain the true mineralogy of Wild2.

5.2 Samples and Methods

5.2.1 Samples

The track #41 keystone (from C2044,0,41,0,0) was cut and prepared at the University of California (Berkeley) (using the method described in Westphal et al., 2002;). In the nomenclature of Hörz et al. (2006) and Burchell et al. (2008), track #41 is a Type B, "turnip" shaped track, where the particle has broken up during impact, producing a large cavity (lined with fine fragments of the impactor) in the upper half of the track. This cavity is accompanied by two styli, which emerge beneath the cavity, aligned with the incident impact direction; terminal grains can be found at the end of these styli. The sample used here was a 4 x 2.5 mm transverse slice through the track, close (0.8 mm) to the track entrance (Fig 5.1) and as such was a sample of cometary grains distributed along a track. The aerogel slice was placed between two glass slides with a depression within which the aerogel slice was laid. An optical image of part of the aerogel slice, showing one of the several captured grains, is shown in Fig 5.1.

FIG 5.1: Track #41. This is a Type B track of length ~4 mm and the impact was from the left of the image moving right. It was removed from the cometary collector cell 44. Our slice was cut 0.8 mm in (grey vertical rectangle) from the track entrance. Track image courtesy of NASA-JSC.

Track #121 is shown in Fig 5.2 and is a Type A, "carrot" shaped track. Track #121 was recovered from a chip that fell off C2005 during the tile removal process. There appears to have been relatively little initial disaggregation of the incident particle during capture in the coma and terminal grains are present at the end of the track. Au mounts for the samples from track #121 were prepared at the Open University, UK. These were sent to NASA-JSC and microtomed sections of terminal areas from track #121 samples (C2005,2,121,1,0 and C2005,2,121,2,0) placed onto the Au mounts and returned to the UK for analysis.
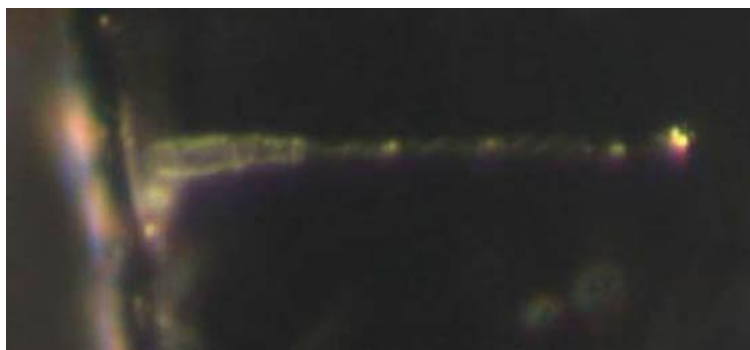
FIG 5.2: Track #121. This is a Type A "carrot" shaped track of length ~0.9 mm and the impact was from the left of the image moving right. It was taken from a chip from the cometary collector cell 5. The terminal grains used here were removed from the end of the track (bright region at right hand side of image). Image courtesy of NASA-JSC.

A complete keystone containing track #134 was also analysed. It most closely resembles a Type A track, is approximately 350 µm long and was curated at UC Berkeley. An optical micrograph of track #134 is in Fig 5.3. The track has a narrow entrance, slightly broadens out mid-track and then tapers off to a main terminal area.
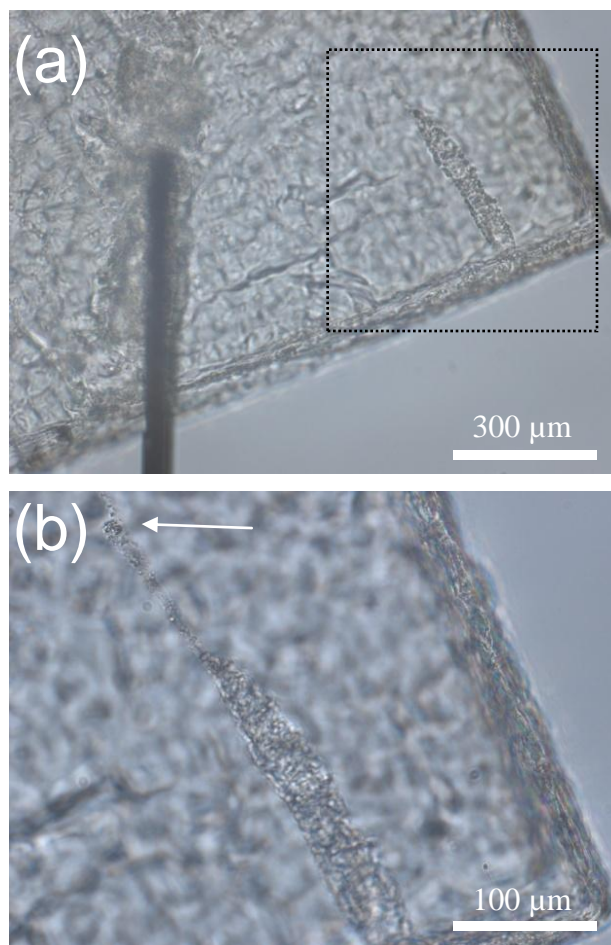
FIG 5.3: Optical micrograph of the keystone containing track #134. (a) The aerogel keystone is held in place with a silicon fork. (b) Higher magnification of the track. The white arrow indicates the main terminal area.

The entrance of track #162 was also curated by UC Berkeley. The sample is an aerogel block approximately 700 µm down the track entrance. Its slender shape represents a carrot shape and thus falls into the Type A category. Tracks #41, #134 and #162 were analysed using the X-ray microfocus spectroscopy techniques at the Diamond synchrotron. The experimental parameters used for these analyses are described in section 5.2.4.
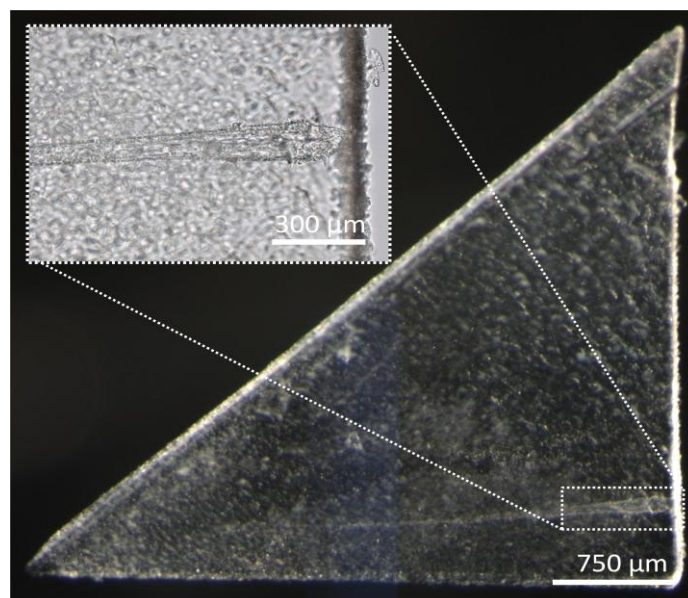
FIG 5.4: Optical micrograph of track #162 keystone and sample C2062,2,162,0,0. The section of #162 is the first ~750 microns of the track. The narrow carrot shaped track bears resemblance to a type A track feature, similar to track #134. Micrographs modified from the *Stardust* Catalogue.

5.2.2 SEM analyses

Following the microRaman analyses with collaborators at the University of Kent and the Open University (See Bridges et al., 2010), the track #121 terminal samples were studied with an FEI Sirion Field Emission Gun SEM (FEG-SEM) and a Philips XL30 Environmental SEM at UL. The FEG-SEM was operated at 4-9 keV and a beam current of 400 pA for imaging. Qualitative EDS point analyses were performed at 12.5-15 keV, ≤650 pA beam current with a PGT EDS system on the FEG-SEM. Beam currents were measured on a Faraday cup. The ESEM (with Link EDS) was used at 1 torr pressure when sample charging on C2005,2,121,2,0 occurred during some analyses using the FEG-SEM. This was found to overcome the majority of charging problems. EDS analysis times ranged from 50-1000s for point analyses depending on our assessment of sample charging, potential damage and elemental concentrations. For C2005,2,121,2,0 individual spectrum X-ray counts from across the sample were added together to produce a representative spectrum.

The analyses were planned to minimise the effects of sample damage on the cometary minerals. Reflected light photography and MicroRaman analyses (University of Kent) were performed by the UK *Stardust* consortium before our SEM analyses and synchrotron

work (Foster et al., 2008). Track #41 was analysed by microRaman and synchrotron radiation, the track #121 terminal samples by microRaman, then SEM followed by FIB-SEM extraction to TEM, the results of which can be found in Bridges et al. (2010).

5.2.3 FIB & TEM analysis

After identification by SEM of iron oxide grains within a terminal area of track #121 (C2005,2,121,2,0) a technique was developed for extraction of one of the grains for TEM analysis. An approximately 120 nm thick wafer containing a cross section of one of the iron oxide grains. The FIB-SEM Ga^+ ion beam used for the milling was operated at 20 kV accelerating voltage. Prior to application of the runscript, the particle was capped with a 10 x 2.5 μm C layer of approximately 150 nm thickness followed by Pt of equivalent dimensions in order to protect the Fe oxide grain from the effects of the ion beam. Both layers were deposited via electron beam deposition using the Gas Injection System (GIS). The conventional 15 x 4 μm TEM runscript was amended to produce a 5 x 4 μm sample, wafer dimensions required miniaturisation in order to preserve the rest of the terminal mass. A 120 nm thick wafer was produced to ensure that the particle cross section would remain intact. The wafers were imaged with secondary electron snap shots at sequential stages of the milling sequence and the runscript was aborted before the final milling currents in order to help preserve the grain. Manual thinning was applied post extraction with low beam currents <100 pA to ensure electron transparency of the grain. The wafer was extracted in situ using the *Omniprobe* lift out mechanism, and attached to a copper grid using carbon welding with the GIS and ion beam at 20 kV.

The Jeol 1200 with a PGT EDS system was used for TEM. Bright field imaging, STEM EDS and Selected Area Electron Diffraction (SAED) were performed on the particle and surrounding gold foil mount. STEM EDS analyses were performed at 14 points in and around the iron oxide grain for 50 s each and X-ray mapping was performed with STEM mode for 2 hours.

In order to check that the Ga+ ions in the FIB did not create amorphous Fe oxides, FIB-SEM analyses of magnetite-bearing symplectites in nakhlite meteorites were conducted (Changela, 2008). The preservation of the magnetite and other phases suggests that FIB-SEM analyses did not change the structure of the FeO studied in the *Stardust* samples.
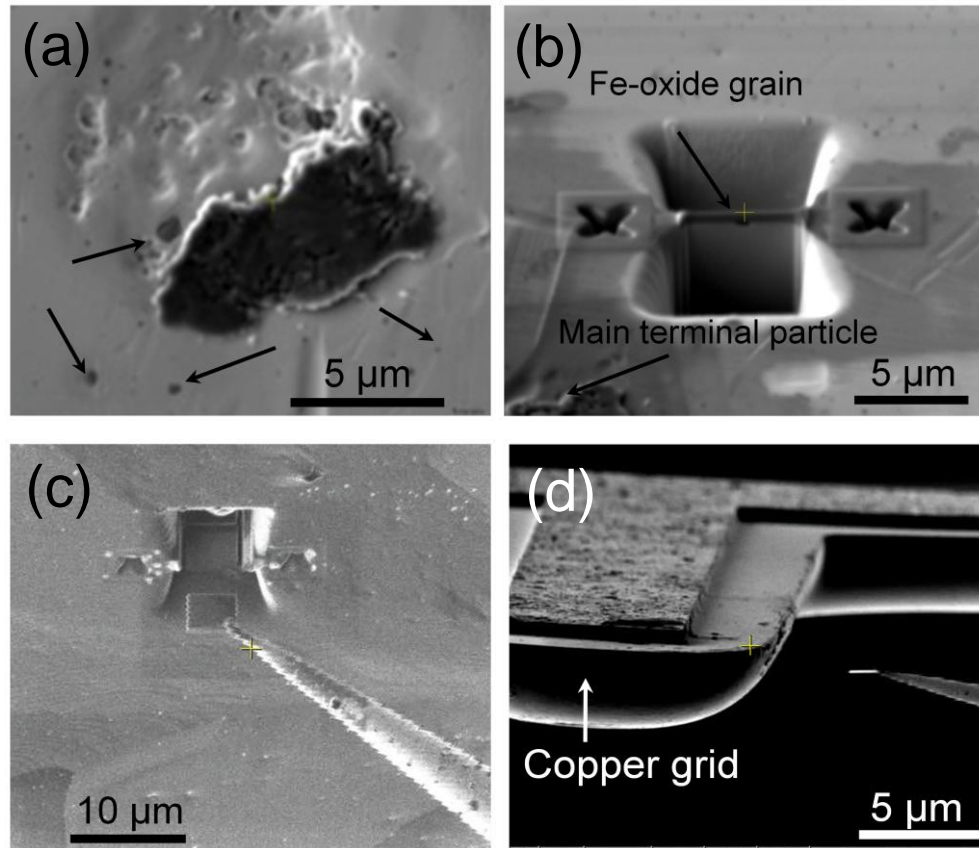
FIG 5.5: Extraction of an oxide grain around the terminal area of track #121. Due to the smaller dimensions of the areas compared to meteoritic extractions, the procedure had to be scaled down in producing a 5 μm width wafer rather than the conventional 15 μm. (a) SE image of C2005,2,#121,1,0 at 5 kV with the FIB electron beam. Iron oxide has been found within and around the terminal area. (b) SE image of an identified iron oxide grain around the terminal area at 5 kV with the FIB electron beam. The particle is capped with 150-200 nm C followed by Pt using electron beam deposition. (c) SE ion beam snapshot at 4 pA and 20 kV. The TEM run script with the ion beam was run at 20 kV. Side and under cuts of the wafer were produced manually at 7° tilt. The wafer is extracted with the Omniprobe needle after attachment of the sample with C welding. (d) Copper grid is inserted within the SEM in order to attach the TEM wafer using C welding.

5.2.4 Microfocus XRF, XANES & EXAFS

Microfocus XRF and XANES spectroscopy was performed at Beamline I-18 (Chapter 3). XRF (fluorescence) maps were generated at 3 areas of the transverse slice of track #41 (C2044, 10, 41, 0, 0). The germanium fluorescence detector was placed 45° to the sample with the beryllium window as close as possible to maximise count rates. 250 x 250 µm maps were produced at 13 keV and a dwell time of 5 seconds. Beam spot sizes were 3-4 µm. Long integration times of 500 s were performed on hotspots identified after mapping. Fe K edge XANES (X-ray Absorption Near Edge Structure) was performed on hotspots. Approximately 120 data points were integrated across the XANES pre and post Fe edge. One second integration was performed at each 0.2-0.4 eV energy step from 6962-7090 eV, followed by 5 s onwards up to and beyond the EXAFS region of 7500 eV.

Initial XRF mapping with subsequent XANES and EXAFS on specific areas of interest were also performed on track #134. The aerogel keystone was directly inserted into the sampling chamber. Elemental mapping was performed over the energy range 2-20 keV with energy steps of approximately 0.2 eV and a spot size of around 4 µm.

A range of mineral standards were also analysed for mineralogical XAFS analyses: magnetite (Fe_2O_3FeO), hematite (Fe_2O_3), Mg-rich olivine from the Admire pallasite meteorite (Mg/Mg+Fe atomic ratio 0.88), chromite $FeCr_2O_4$, Fe-sulphide – pyrrhotite ($Fe_{1-x}S$) and troilite (FeS). They were powdered with an agate mortar and pestle and mixed with boron nitride powder at 5 mg to 95 mg proportions, the pellets were then used for Fe Kα XANES. Samples and standard powders were mounted on *Kapton* tape to preserve their integrity. It's use, together with the low density aerogel within which the cometary tracks lie, means that X-ray absorption effects for elements with Z ≥ Ca were negligible, as employed in previous *Stardust* synchrotron based studies (e.g. Flynn et al., 2008; Lanzirotti et al., 2008). The track #162 sample was mounted between layers of *Ultralean* that was fastened to one of the I-18 sample holders. Fe K-edge XANES spectra were reduced using *Pyspline* software, XRF data with PyMCA software. The resultant XANES spectra were normalised by the software to the Fe K-edge EXAFS region. The Berkeley XANES spectral library was also used to compare with our XANES results, as used in studies by Gainsforth et al. (2008); Westphal et al. (2009) and Oligiore et al. (2010).

5.3 Results

5.3.1 SEM and TEM of terminal areas of track #121

C2005,2,#121,1,0

This sample consists of a 10 x 10 μm mixture of glassy aerogel and a few percent of cometary grains. The relatively smooth surface texture and compositional analyses suggest that this part of track #121 has undergone some melting during capture heating. Spot analyses showed that there were some iron oxide grains (Fig 5.6a), where the oxygen peaks of the spectra were higher than background and lacking Si. These appear to be partially oxidised particles due to their oxygen peaks being lower than that of pure iron oxides (Fig 5.6d). Long acquisition times on numerous spots and grains had no other detectable elements except Fe, O with Au, Al, Si most likely resulting from the substrate and aerogel. As some glassy aerogel was attached to the iron oxides, grain sizes were difficult to measure accurately but ranged up to approximately 200-600 nm. A second element signature for some grains was Mg-Fe-O-Si, characteristic of silica-rich glass in the *Stardust* samples (Zolensky et al., 2006; Leroux et al., 2008; Rietmeijer et al., 2008).

Following SEM characterisation, the Fe oxide grain extracted from this sample by FIB-SEM (section 5.2.3) was analysed by TEM (Fig 5.6e-f) in order to check its composition and determine its structure. Fig 5.6 d shows an EDX spectrum taken from the grain. The Ga peak arises from some implantation during the ion milling process; the Au peak is due to excitation of some X-rays from the underlying mount.

Selected Area Electron Diffraction of the Fe oxide grains showed the absence of any diffraction pattern and thus the oxide is structureless. The surrounding gold foil did however show diffraction demonstrating that it is the amorphous nature of the Fe oxide rather than the thickness of the extracted wafer that caused the lack of a diffraction pattern.

C2005,2,#121,2,0

This sample consists of a 6 x 4 μm aggregate of aerogel and scattered cometary grains. Like the #121,1,0 sample it contains a dominant Fe signature (associated with iron oxide identified by initial Raman analyses – Bridges et al., 2010) in addition to Si which is mainly produced from the aerogel (Fig 5.6b). However, the surrounding aerogel precluded imaging discrete grains. Subtracting the Au background from an X-ray spectra taken from

the sample indicates, qualitatively, that it contains S as well as Fe and Mg. This suggests the presence of minor sulphides, although these have not been detected by microRaman (Bridges et al., 2010), perhaps because of their small total volume. Such sub-micron size grains could be fragments that were stripped off larger grains during capture. Unlike #121,1,0 this sample does not appear to have undergone melting.

Both #121,1,0 and #121,2,0 are samples of the terminal areas and thus iron oxides are present near the end of this track. A large single terminal grain has not been identified in these samples.

5.3.3 XRF and XANES of Track #41

The track 41 slice was found to contain a range of different minerals and oxidation states. Numerous grains or hotspots approximately 10 μm in diameter were identified (Fig 5.7a, c, e). The most commonly found XRF spectra found at the Fe hotspots are shown in Fig 6d. The grains are scattered around the track's bulb margin. Other XRF in Fig 6 showed Fe-Ni, compounds, Fe-Ti, Cr-Fe-V-Ti-Mn, and an unidentified Fe-Zn compound (which may well be an aerogel contaminant, see below). The detectable presence of V and relatively high Ti contents in the chromite are significant because this is characteristic of extraterrestrial (chondritic) chromite rather than terrestrial chromite (Alwmark and Schmitz, 2006). In this sample the suggested chromite and Fe-Ti hotspot were adjacent grains (Fig 5.7e).
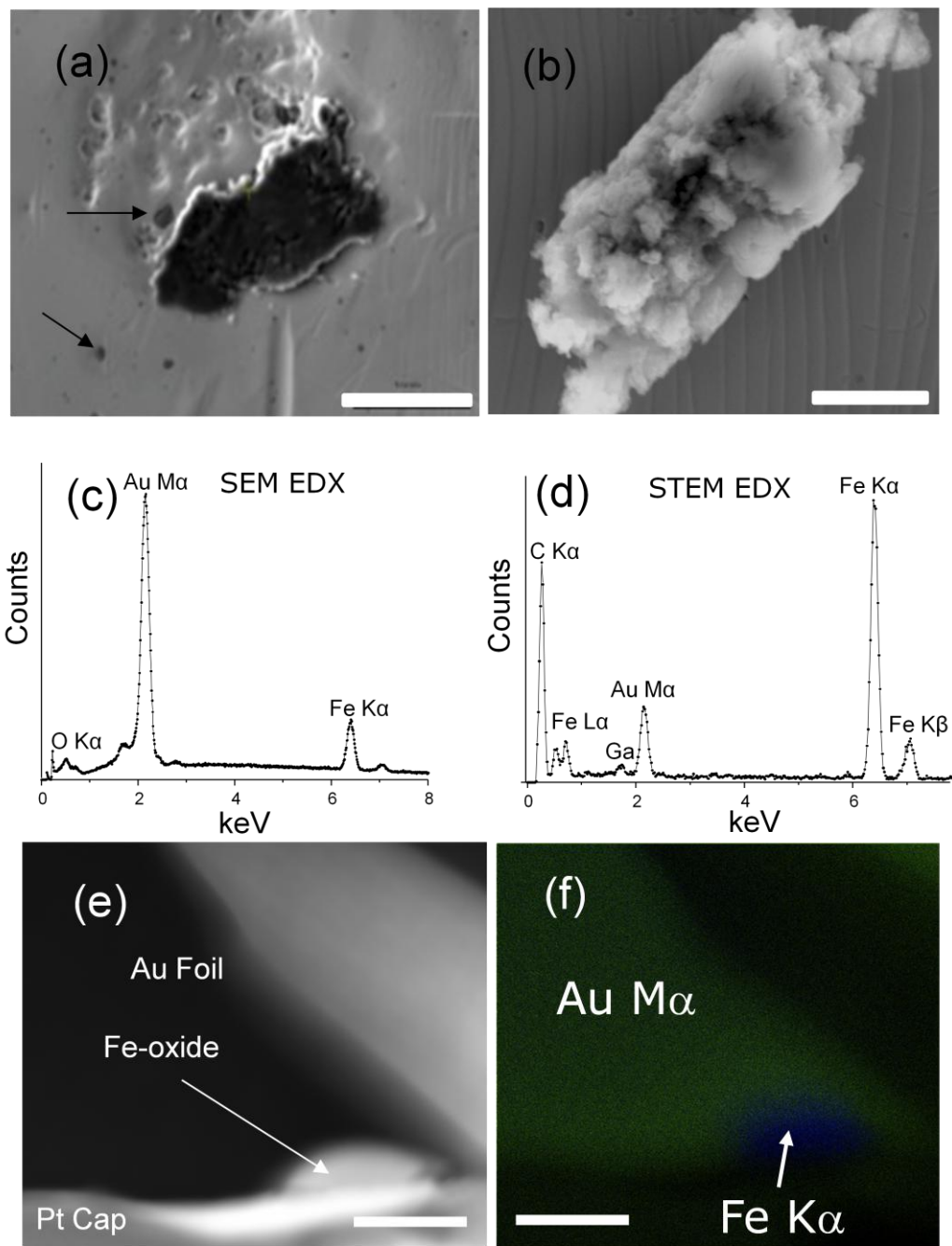
FIG 5.6: (a) SE image of sample C2005,2,121,1,0 at 5 kV. Iron oxide (grains arrowed) has been found within and beside the terminal area of aerogel. Scale bar is 5 μm. (b) SEM image of terminal area of C2005,2,121,2,0 at 9 kV. Scale bar is 5 μm. MicroRaman spectroscopy suggests the presence of magnetite-hematite (c) SEM EDX spectra of iron oxide grain in C2005,2,#121,1,0. The Au peak is from the substrate on which the particle was pressed. (d) 50 s integrated EDS spectra of an iron oxide grain in TEM after FIB extraction from C2005,2,#121,1,0. O Kα peak is to the left of the Fe Lα peak. (e) STEM bright field image of wafer containing Fe oxide. Scale bar is 0.2 μm. (f) EDS map of the wafer. Scale bar is 0.2 μm. Blue indicates Fe Kα intensity and the location of the Fe-oxide, green is Au Mα intensity.
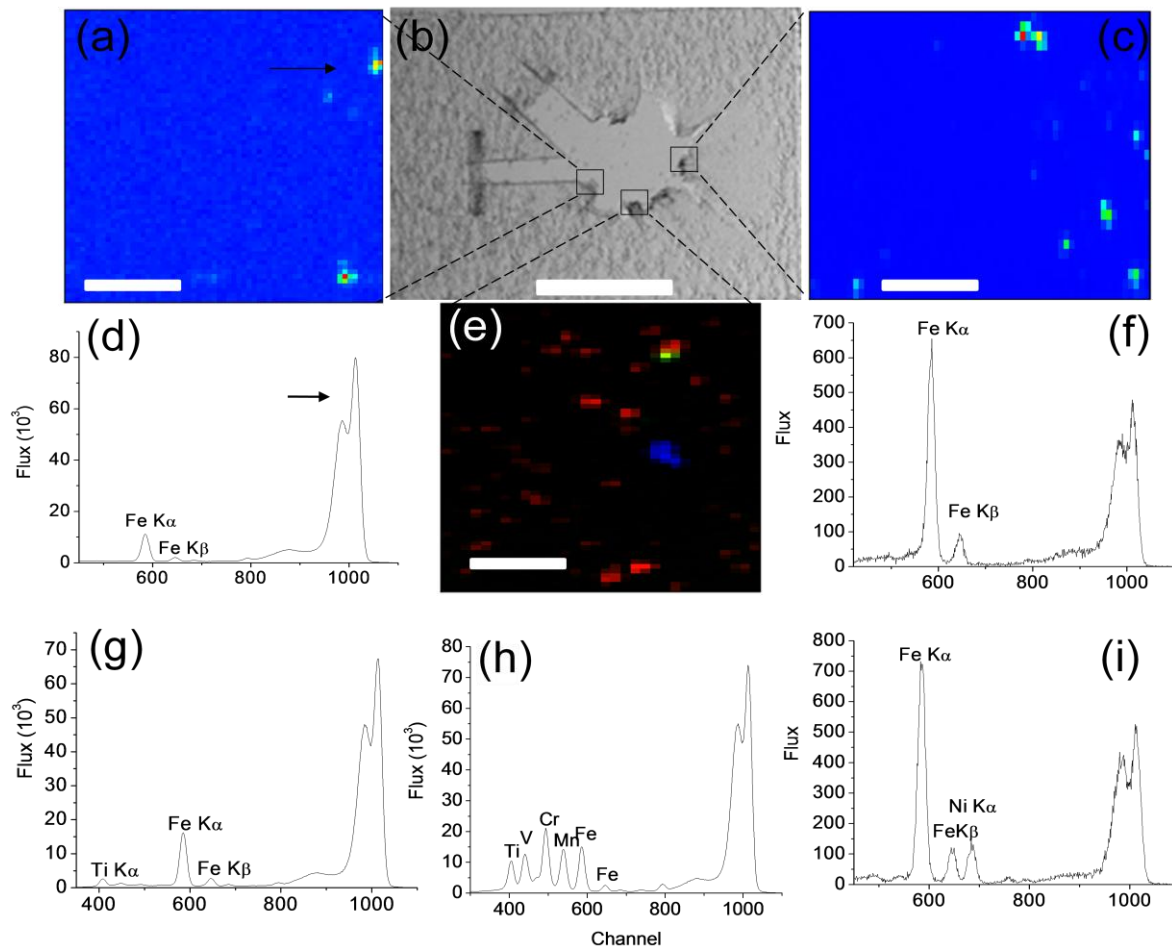
FIG 5.7: XRF mapping of track #41 sample. Note that the horizontal channel scale of the spectra does not correspond exactly to a keV scale although the relative positions of the characteristic peaks are accurate and peak labels were verified sperately via beamline I-18 calibration. (a) - (c) Reflected light microscope image of transverse slice of track #41. The central, roughly circular hole is the track cavity. The rectangular channels are artifacts made by the mounting forks used to hold the sample during extraction from the aerogel tile. Scale bar is 1 mm. (b) Fe Kα map, each pixel measures approximately 4 x 4.5μm marked on the optical image of the transverse slice. numerous grain approximately 10 μm in diameter. Scale 80 μm. (c) Fe Kα map which was also very similar to the Ni window (not shown here). Most hot spots in this area show a Fe-Ni-bearing composition displayed in i. (d) Typical Fe- hotspot spectrum showing Fe Kα peak. The main peaks (arrowed) are the elastic and Compton scattering peaks. (e) RGB intensity map of another position indicating Fe (red), Cr (green) and Zn (blue) hotspots. (f) Concentrated Fe-hotspot in RGB map. (g) Fe-Zn hotspot 500 s integration spectra (blue in RGB). (h) Cr hotspot – V-rich chromite (Green in RGB). The V intensity peak is greater than that of Ti. V enrichment is a characteristic of extraterrestrial chromite (I) Fe-Ti hotspot (ilmenite?) which is adjacent to the Fe-Cr-V-Ti-Mn hotspot. (i) Typical Fe, Ni spectrum from map c.

Fe-XANES analyses (Fig 5.8, 5.9) show that Fe hotspots have a marked absorption peak at 7110 – 7111 eV, before the main K edge representing the transition from the unoccupied d states in Fe. Another peak associated with iron oxide occurs at around 7140 eV (Fig 5.8). Similar effects have been reported elsewhere for ferric oxide-bearing phases e.g. Prietzel et al. (2007). Matching of the hotspots in track #41 with various oxide, silicate and sulphide standards (Fig 5.8) show that they are very close to that of the magnetite (absorption peak at 7110 eV) and hematite standards (absorption peak at 7111 eV) and are consistent with a mixture of these 2 phases.

XANES of the Fe-Ti and the Fe-Cr-C-Ti-Mn phases also show absorption features at the 7140 eV region demonstrating that they are also oxidised Fe. Based on this and the elemental compositions, we can assume that they are spinel-type minerals rather than metal alloys. The notable white line uncharacteristic of a sulphide in the Fe-Ni hotspot also suggests oxidation associated with this hotspot. However, due to the X-ray beam spot size, we cannot know unambiguously whether the oxidation feature is solely associated with the Fe-Ni. The absorption peak consistent with Fe oxidation is, however, present in all of the hotspots including the FeNi hotspot.
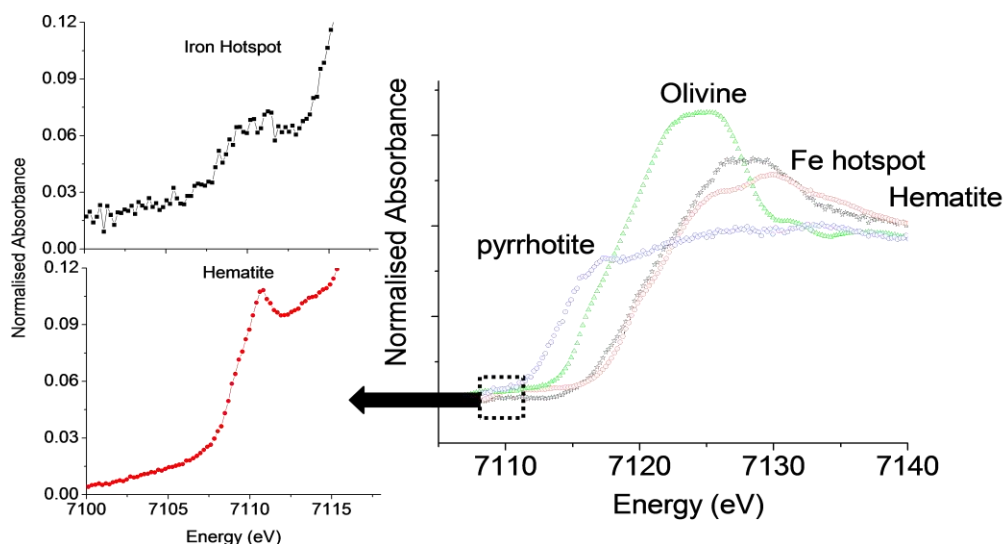
FIG 5.8: Fe XANES of various mineral standards with a representative Fe hotspot from track #41. The Fe hotspot spectra are consistent with a mixture of magnetite and hematite and inconsistent with the Fe-XANES of olivine or Fe sulphide (pyrrhotite). The olivine standard and Fe-sulphide standard both completely lack the peaks associated with ferric iron at 7110 eV and 7111 eV in magnetite, hematite and the Fe hotspots.
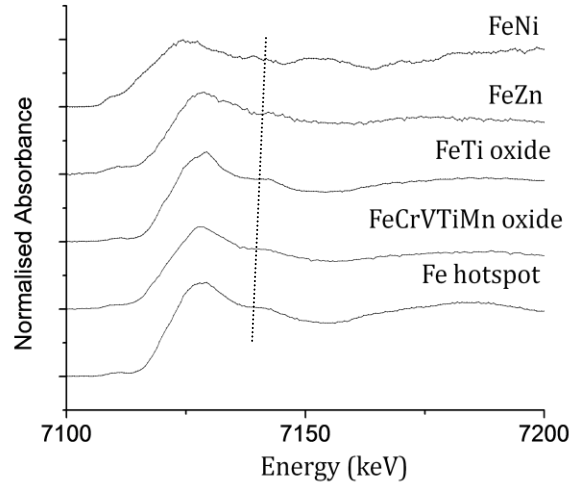
FIG 5.9: Fe-XANES of Fe hotspots co-existing with other elements. A small absorbance feature around 7140-7150 eV is indicated with the dashed line which shows the presence of oxide in all the samples, including the relict FeNi metal and the Fe-Zn contaminant phase. The relict Fe-Ni metal also has an absorption feature around 7160 eV, a feature characteristic of metal (Pingitore et al. 2002).

A simple fit routine was made fitting the standards with the sample's iron hotspots over the Fe-XANES edge (Fig 5.10). A best fit data set was defined by the following formula:

$$FIT = [sam - (a \cdot hem + (1 - a) \cdot mag)]^2 \qquad (5.1)$$

where *sam* are the iron hotspot sample's normalised absorbance at one point over the XANES region, *hem* is the same as above but for the hematite standard, *mag* is that of magnetite and *a* is the proportion factor of the standard data for finding the best fit and varies from 0 (pure magnetite) to 1 (pure hematite). Variation of *a* and evaluating *Equation (5.1)* using a routine with MATLAB (APPENDIX D.I) gives a minimum and hence best *FIT* value suggesting a mixture of 38% magnetite, 62% hematite for this iron hotspot.

Fits to goethite around its Fe Kα edge were poorer due to the increased positive energy shift of the pre-edge feature. However, a ternary *FIT* calculation was derived calculating the best fit for a mixture of hematite and magnetite and goethite using *Equation (5.2)*:

$$FIT = [sam - (a \cdot hem + b \cdot mag + c \cdot goe)]^2 \qquad (5.2)$$

where *a*, *b* and *c* are the proportions of hematite, magnetite and goethite respectively and add up to 1. Evaluating *Equation (2)* with the possible permutations of *a*, *b* and *c* (MATLAB code in APPENDIX D.II) give a least squares *FIT* of 0.019 at its minimum with 0.41 magnetite, 0.44 hematite and 0.15 goethite (Fig 5.10b).
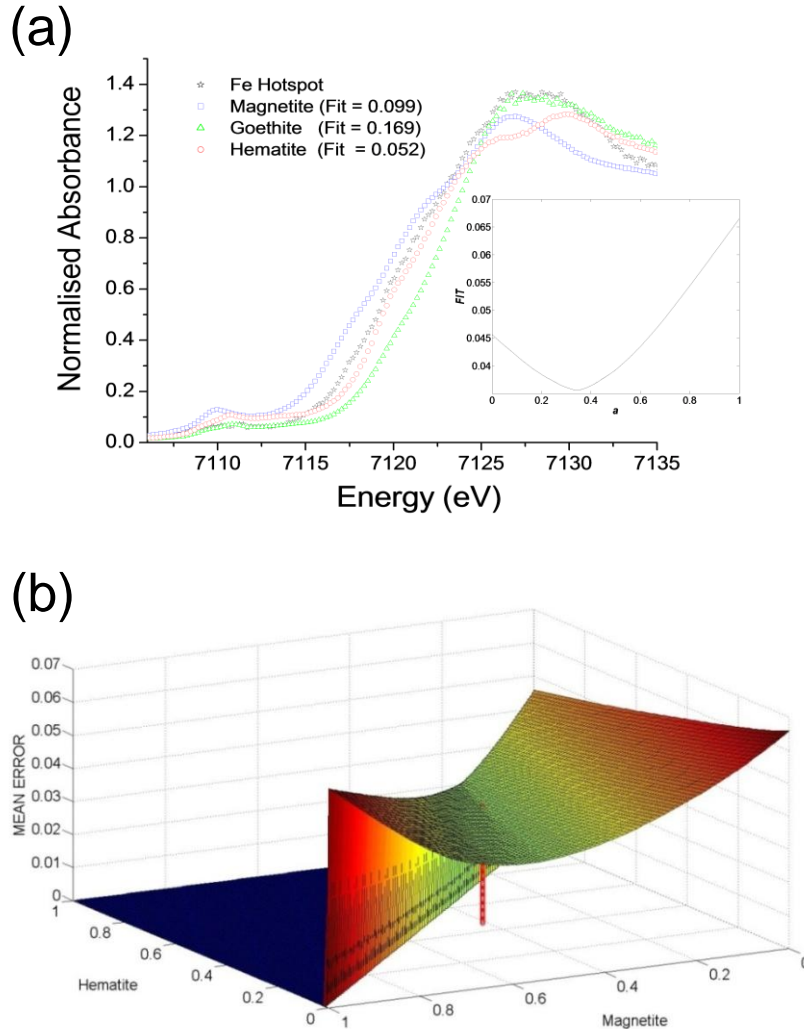
FIG 5.10: Least squared regression fits of Fe-hotspots to pure Fe-oxides. (a) Comparison between goethite FeOOH, hematite Fe_2O_3, magnetite Fe_2O_3 with an Fe hotspot. The main absorption edges (7115-7125 eV) have a similar gradient for all the samples and are consistent with the presence of ferric oxide. The inset diagram shows a best fit calculated between the two spectra – hematite and magnetite – that are most similar to the Fe hotspot spectra and are consistent with the microRaman (Bridges et al. 2010; Foster et al. 2008) The representative Fe hotspot shown is fit as a mixture of 38% magnetite, 62% hematite. (b) 3-D plot showing the best *fit* acquired by the mixture of magnetite, hematite and goethite. The plot shows the location of the minimum *fit* value against hematite and magnetite proportions. The remaining goethite proportion is 1 – a(hematite)-b(magnetite).

Sulphur could not be analysed by XRF with the Ge detectors but, by comparison with other work on *Stardust* samples (e.g. Leroux et al. 2008) it is possible that sulphides could have been present. However none of the XANES-EXAFS spectra in track 41 grains are consistent with an Fe-sulphide identity, sulphides being characterised by the absence of a marked absorption edge e.g. pyrrhotite (Fig 5.8).

5.3.4 XRF and XANES of Track #134

Fe Kα fluorescence maps showed iron distribution in #134 to be scattered at the broad end of the track and more concentrated towards the tapering thin end. The XRF maps are shown in Fig 5.11.
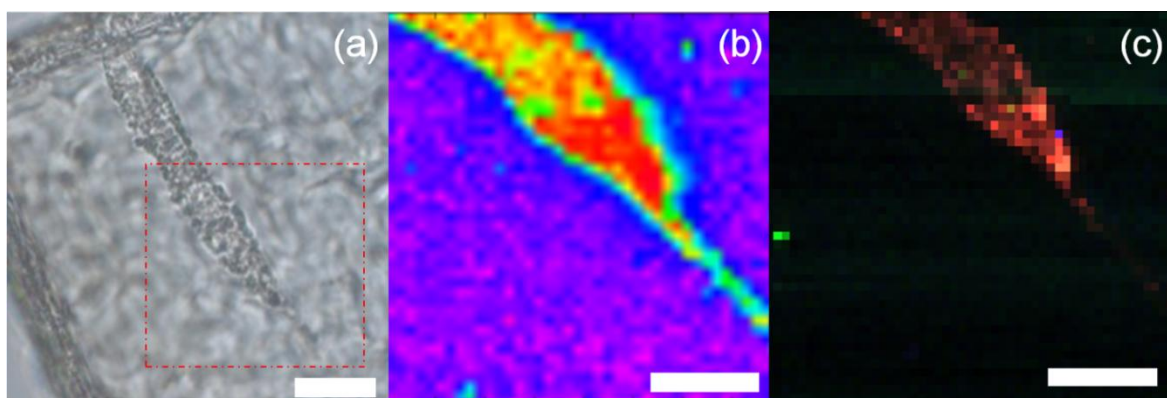
FIG 5. 11: XRF was performed across the entire track area with a set of 250 x 250 μm maps. (a) Optical micrograph of track #134. (b) Fe Kα fluorescence map inverted with respect to the optical image in (a). 'Hotter' regions indicate a greater intensity of Fe Kα. (c) RGB intensity map as in (b); Red (Fe Kα) Green (Ni Kα) & Blue (Ca Kα). Note the two Fe-Ni regions mid track and the blue hotspot indicating presence of calcium. Scale bar is 100 μm.

Due to time constraints only two hotspots were analyzed by XAFS. Hotspots in the terminal area and at the mid track position were analysed in the XANES and EXAFS regions. Fe-XANES spectra generated at the mid section of the track most closely fit the magnetite (Fe_3O_4) standard. This is different to the Fe-hotspots from track #41 track fitted their edges closer to hematite. The terminal hotspot of track #134, however, has a close fit to the pyrrhotite Fe(1-x)S standard. The midtrack and terminal hotspots show their respective XANES spectra in Fig 5.12. A comparison between the terminal hotspot spectra and the various Fe-sulphide standards (pyrrhotite and troilite FeS) is provided in Fig 5.13a. Other Fe-sulphide standards such as pyrite FeS_2 and pentlandite $(FeNi)_9S_8$ were not

available for this study. The old supposedly pentlandite standard prepared by FIB extraction for XAFS in section 3.10 was heavily oxidised and only contained Ni, enabling only Ni-XANES. A range of Fe-sulphide mineral standards have been measured by Fe-XANES at UC Berkeley's Advanced Light Source (Westphal et al., 2009). Fig 5.12b shows a comparison between their standards. Direct matching of external standards to the XANES measured in this study is complicated by the energy offset in the monochromators and different applied energy steps. However, the shape and period of oscillations can be compared for qualitative and semi-quantitative analysis.
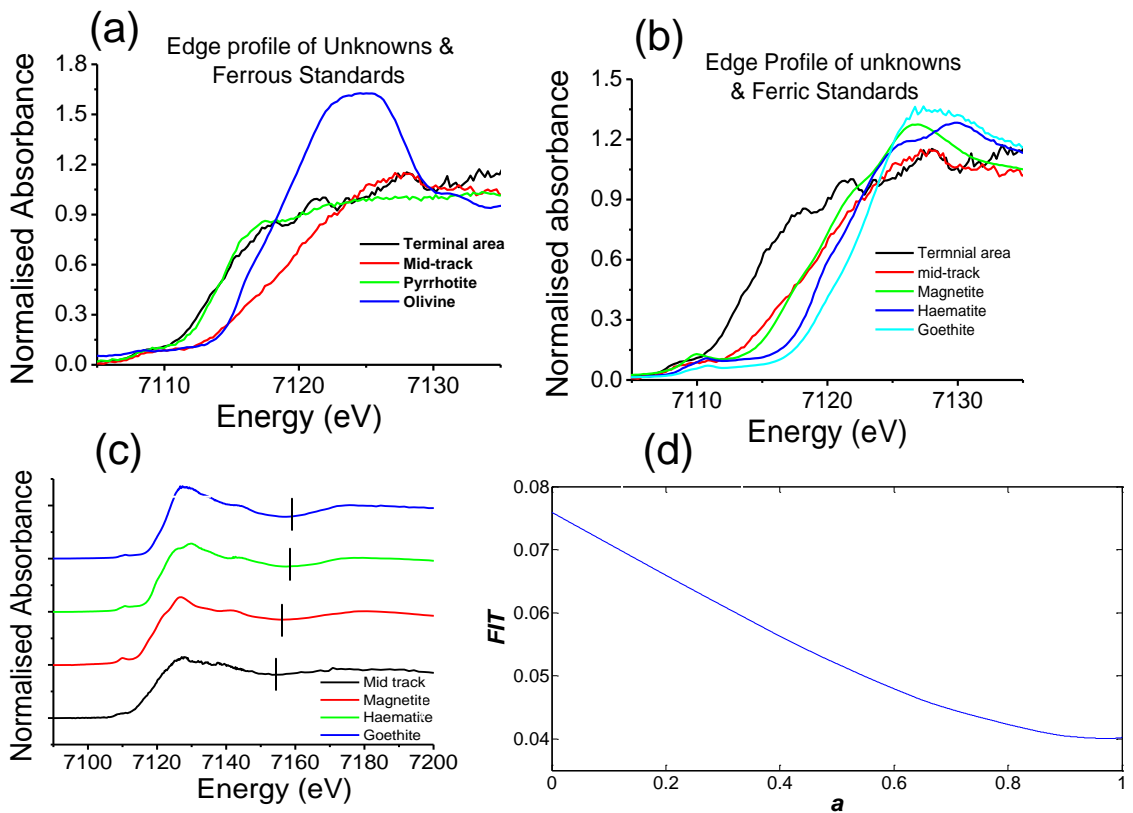
FIG 5.12: XANES and EXAFS of track #134. (a) The terminal and mid-track XANES compared with ferric standards. (b) Comparison with ferrous standards. The terminal area EXAFS is a very close fit to pyrrhotite. The mid–track spectra has its edge shifted towards the magnetite but is not an exact fit. (c) An oxide feature found at ~7140 eV could possibly be identified though not to an exact degree of certainty (vertical line). (d) The hematite-magnetite shows that the mid-track edge profile of this hotspot is almost all magnetite with a minimum found at 95% magnetite 5% hematite. *a* is the proportion factor of magnetite and hematite.
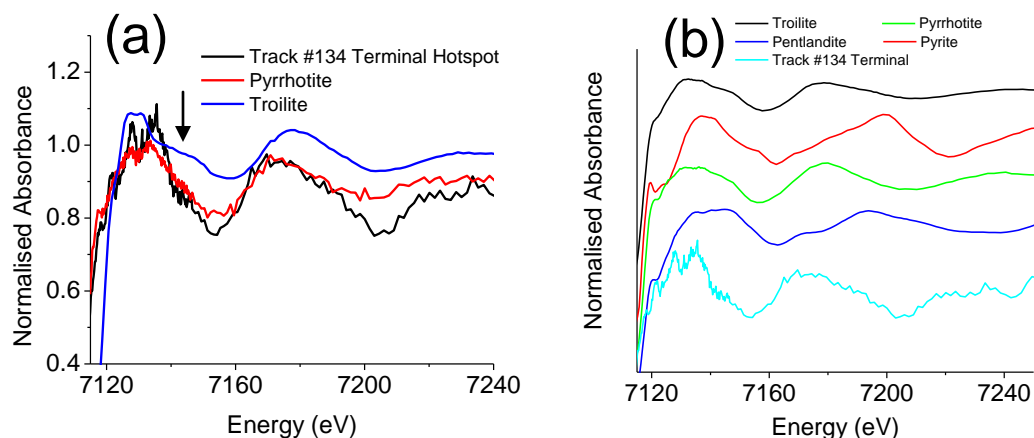
FIG 5.13: Comparison between terminal hotspot from track #134 and Fe-sulphide standards by Fe-XANES. (a) NHM pyrrhotite and track #134 hotspot measured at I-18. (b) Comparison of track #134 terminal hotspot with Fe-sulphide standards from the Berkeley ALS database. Note that experimental conditions differ between the unknown and standard spectra but relative shapes of the spectra are similar. Slower oscillations for pyrite and pentlandite (larger ΔE from peak to peak) do not correspond to the terminal hotspot spectra. Qualitatively, the first three oscillations are consistent with the pyrrhotite standard.

The UC Berkeley Fe-XANES of pyrrhotite and troilite, and to a lesser extent our NHM troilite standard are very similar to one another. Fig 5.13b shows the first oscillations of troilite (black) to mimic those in pyrrhotite (green). A noticeable difference could be the second oscillation (~7230 eV) that is weaker for troilite. A noticeable 'bump' at approximately 7150 eV is also found in troilite, that also overlaps with the distinguishing oxygen bonding absorbance feature in the pure Fe-oxides and silicates. The edge positions for all of these sulphides in the Berkeley database are indistinguishable from one another due to their equal charge states. Our NHM troilite, however, has a distinctive positive edge position compared to the pyrrhotite standard and has a prominent bump at the oxide region (~7150 eV) of the spectrum (arrowed in 5.13a). The troilite standard was extracted from an ordinary chondrite (Parnallee LL3) at the NHM. It is unclear under what conditions it was preserved under, but it seems to have a natural terrestrial oxidation overprint, similar to the heavily oxidised old pentlandite FIB standard from the Dept. of Geology, UoL (Section 3.4.2). This assumed terrestrial oxidation overprint is, however, similar to the oxidised Fe hotspots found in the *Stardust* samples by lacking the dramatic change in absorbance just past the edge, i.e. a prominent white line, and maintaining the flat spectrum more typical of the Fe-sulphides.

5.3.4 XRF and XANES of track #162

The Fe Kα and Ni Kα raw intensity fluorescence maps are shown in Fig 5.14. Each pixel represents a step size of 3 μm with a beam spot size of approximately 4 x 4 μm. Bright red hotspots would represent detectable peaks above background (e.g. Fig 5.15). At the immediate entrance of the track, the iron is concentrated at the margins of the track. Approximately 100 μm in from the track entrance, small hotspots are distributed across the track. These hotspots have been analysed by XANES and EXAFS.
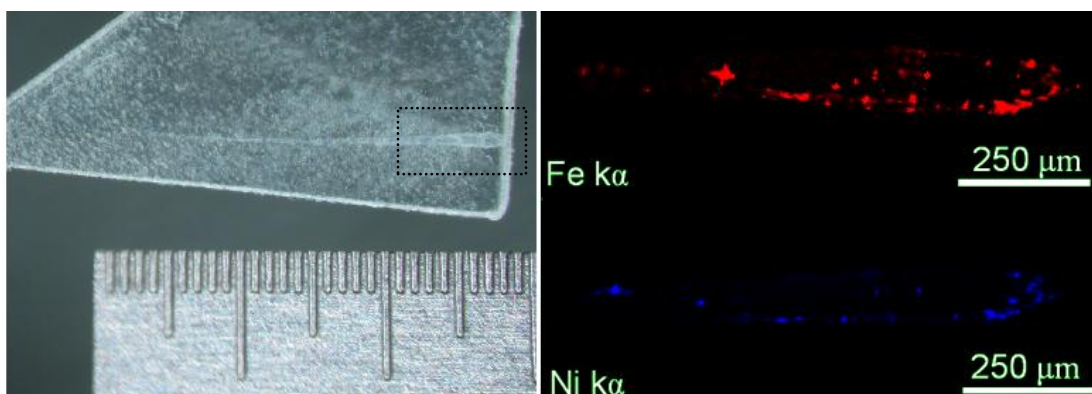
FIG 5.14: Fe and Ni Kα XRF map of the C2062,2,162,0,0 sample. The Intensities are measures of raw counts measured within regions of interest for the Kα lines.
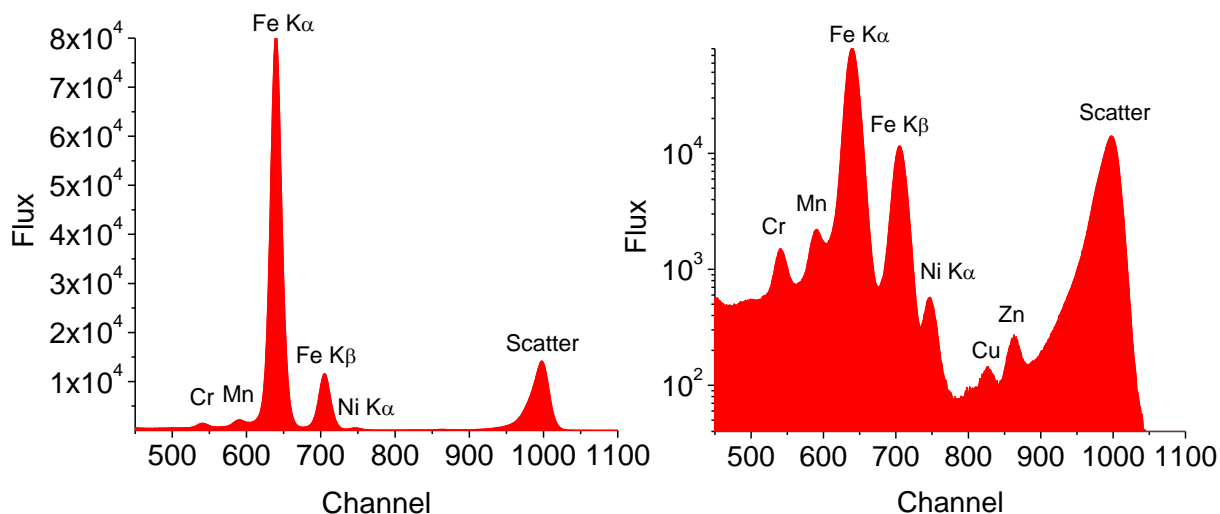
FIG 5.15: (a) 100 s point XRF spectra of large hotspot furthest left of the Fe Kα XRF map. Peaks of Cr and Mn are also associated with this hotspot. Ni is also shown in the same region as also indicated with the Ni Kα map. (b) Logarithmic scale of spectra showing the other elemental signatures more clearly, with also the addition of Cu and Zn Kα which are thought to be contamination (Zolensky et al. 2008).

The Fe-XANES in (Fig 5.16) shows Hotspot 4 to match closer to our olivine standard whilst the others are reminiscent of iron oxides with their distinctive edge positions, indicating the presence of ferric iron. This signature has been found on all of the hotspots we have studied with exception to Hotspot 4. Table 1 summarises their edge positions in comparison to the NHM standards.
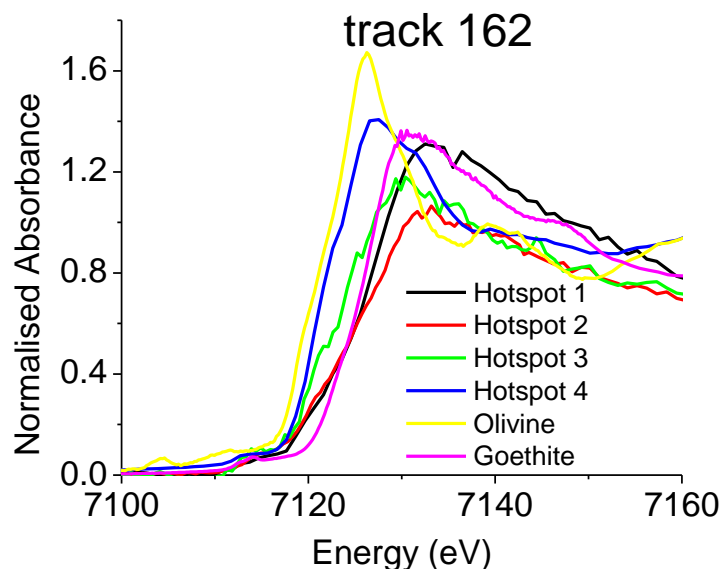
FIG 5.16: Fe-XANES region of four hotspots from track #162, that also have EXAFS spectra obtained for them (section 5.3.5). Three have similar edge positions and white lines that overlap with the Fe-oxide standards. The hotspot with closest fit to olivine XANES was also measured in the EXAFS region. Their respective spectra are plotted against our ferrous silicate standard (olivine) and ferric oxide (goethite). The edge positions of hotspots 1 and 2 are anomalously up to 0.4 eV beyond the pure ferric edge of goethite, The Berkely ALS XANES spectra of Geothite and Hematite have the same edge positions. This small error still shows the hotspots' edges to be in the ferric oxide edge positions (see Table.5.1 in the following section).

5.3.5 EXAFS of tracks #41, #134 and #162

Edge structures of selected hotspots were also obtained in their EXAFS regions. Peaks corresponding to the first shells of the structures were generally obtainable and their bond lengths were fitted using *DL_EXCURV*. Large noise levels have resulted in poorly defined amplitudes of the EXAFS oscillations. Thus, co-ordination sites from the background were difficult to fit to, ultimately leaving fits to only the first shells. The

spectra after background subtraction in *k*-space were also quite noisy for large values of *k*, and thus truncation of spectra of *k* as low as 7 Å^{-1} was necessary, increasing the error in calculated bond lengths after the FTs. Representative EXAFS spectra are found in the following section and summarized in Table 5.1. APPENDIX B provides the EXAFS spectra of the standards that are compared to the hotspots in Table 5.1.

Track #41

Representative EXAFS spectra of a hotspot from track #41 is provided in Fig 5.17. The FT of the EXAFS oscillations are in the *k* range from 2.5 – 7 Å^{-1} that resulted in a best fit to the single main peak corresponding to the Fe-O shell. The edge position fits closest to hematite as shown in Table 5.1 (Hotspot 1). The Fe-O distance when compared directly to the EXAFS of the NHM oxide standards (APPENDIX B) is consistent with hematite (1.99 Å)/goethite (2.01 Å). Thus, the Fe-O bond lengths of the EXAFS spectra are consistent with the bond lengths of our ferric oxide standards.
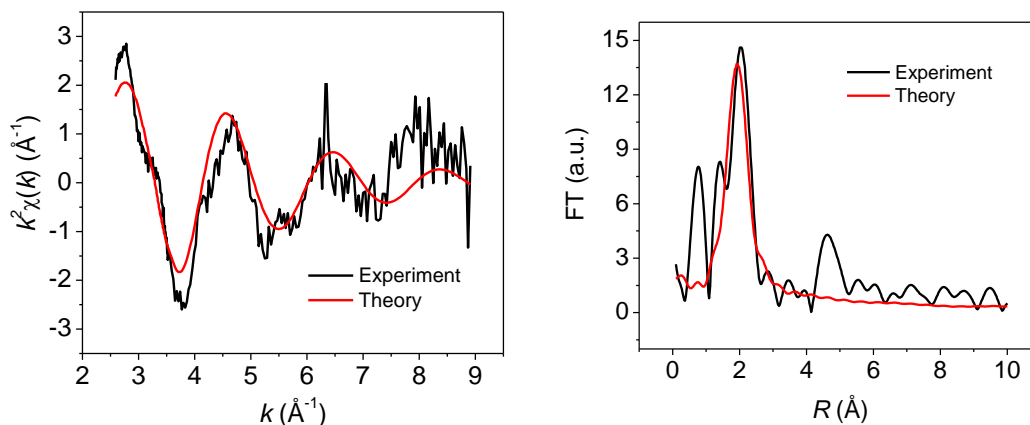
FIG 5.17: Representative Fe-EXAFS of the hotspots found in track #41. k^2 – weighted EXAFS Fe-O distance of 2.00 Å ± 0.03Å. This Fe-O bond length corresponds to a hematite/goethite Fe-O distance from the NHM standards (see Section 5.4.2, Table. 5.1 & APPENDIX BII. for standards). Note that only the Fe-O first shell has been fitted to and so any other large peaks produce errors between theory and experiment. These are most likely to be noise from the weak EXAFS signal. The distances of the Fe-O shell is however consistent with the average Fe-O distances of Fe-oxides (see APPENDIX BII as well).

Track #134

Two EXAFS spectra were obtained in track #134 – one mid track spectra and the other from the terminal hotspot. Again, the first shells we only fitted to using *DL_EXCURV*. EXAFS of the terminal hotspot from track #134 shows a best fit to an Fe-S structure, with 4 nearest neighboring S atoms at a distance of 2.29 ± 0.05 Å. From the mid-track EXAFS, a Fe-O shell was fitted with an Fe-O distance of 1.96 ± 0.03 Å.
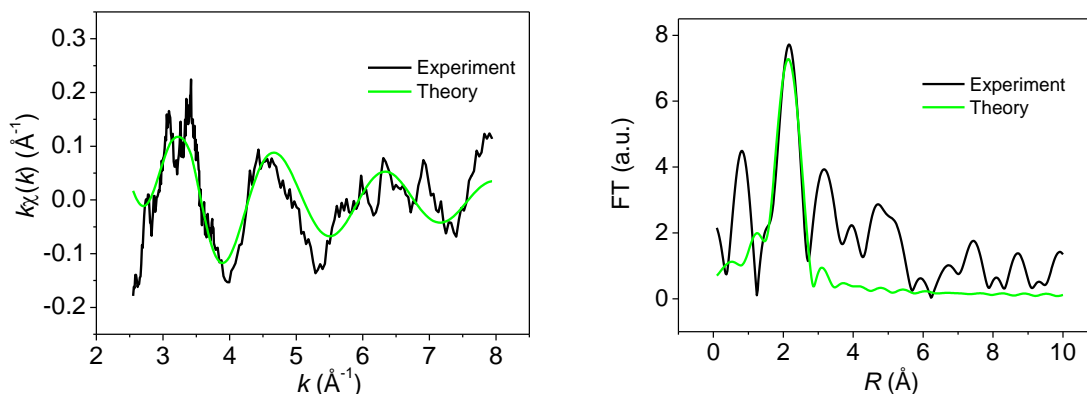
FIG 5.18: EXAFS of terminal hotspot. k-weighted EXAFS and FT of terminal grain respectively. The best fit to the terminal area was obtained with an FeS structure, with 4 nearest neighbouring S atoms at a distance of 2.29 +/-0.05 Å.
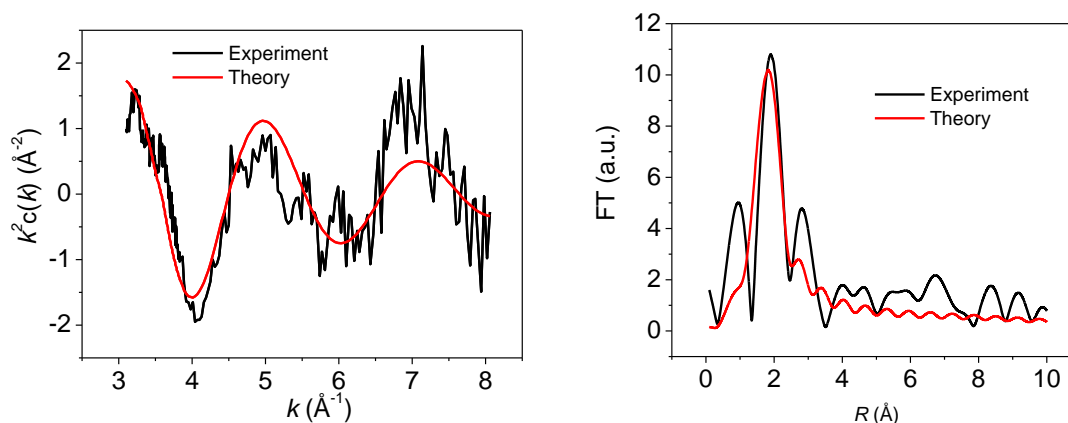
FIG 5.19: EXAFS of a mid-track hotspot from track #134. k^2-weighted EXAFS and FT of terminal grain respectively. The best fit to the terminal area was obtained with an Fe-O structure and an Fe-O distance of 1.96 ± 0.03 Å.

Track #162

Four hotspots, including the large hotspot at the end (XRF spectra in Fig 5.15) in Section 5.3.4 had EXAFS spectra obtained for them. The XANES region of their spectra are plotted in Fig 5.16. Three have edge positions and white lines that fit closest to ferric oxide. The hotspot fitting closest to the olivine XANES was also measured in the EXAFS region. Their respective spectra in *k* and *R* space are given in Fig 5.20. Hotspot 4, that has a distinctive edge position closest to the olivine standard (blue XANES in Fig 5.16) also measures an increased Fe-O bond length compared to the other Fe-oxides' EXAFS spectra (Fe-O 2.07 Å ± 0.03 Å). The other spectra have lower Fe-O distances consistent with the ferric oxide standards and also the positive edge positions.

TABLE 5.1: *XAFS of Stardust Hotspots in tracks #41, #134 and #162*

		1st Shell Distance (Fe-O)Å	1/2 Edge position (XANES) eV	Closest XANES Edge Position	Closest EXAFS (Fe-O)
TRACK #162	Hotspot 1	2.01	7124.59	Goethite	Goethite
	Hotspot 2	2.01	7124.24	Goethite	Goethite
	Hotspot 3	1.99	7122.13	Hematite	Hematite
	Hotspot 4	2.07	7120.63	Olivine	Olivine (forsterite)
TRACK #41	Hotspot 1	2.01	7122.39	Hematite	Goethite
	Hotspot 2	2.00	7122.61	Hematite	Hematite/Goethite
TRACK #134	Midtrack	1.96	7121.39	Magnetite	Hematite
	Terminal	2.31(Fe-S)	7117.85	Pyrrhotite	Fe-S
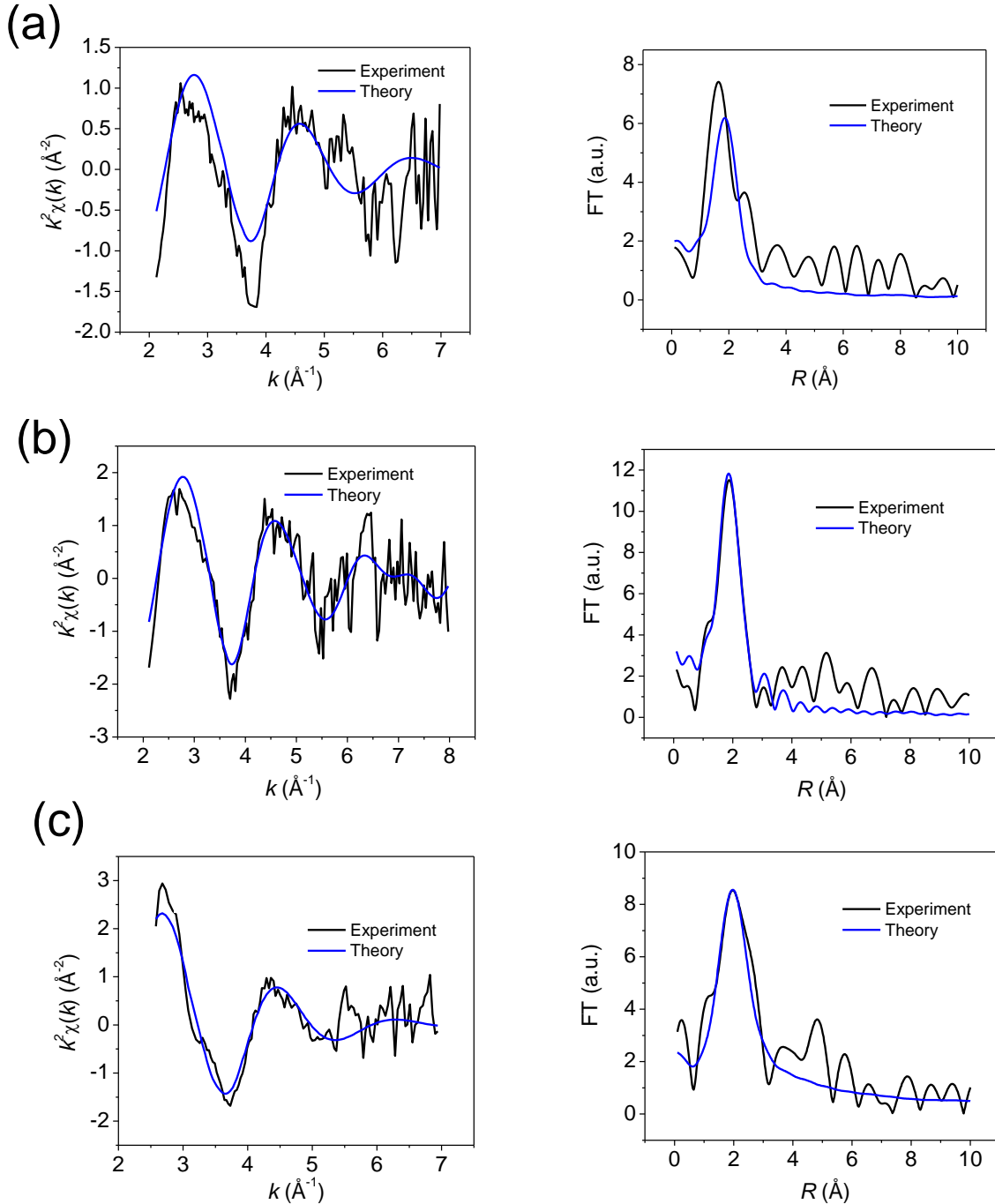
FIG 5.20: Representative EXAFS of Hotspots from track #162. (a) Hotspot 1 from Fig 5.16. Fe-O distance is 2.01 Å ± 0.03 Å. (b) Hotspot 3 from Fig 5.16. This hotspot corresponds to the large hotspot located towards the end of the track entrance (Fig 5.15). Fe-O distance is fitted to be 1.99 Å ± 0.03 Å, also consistent with the ferric oxide standards (Table. 1). (c) Hotspot 4 shown in Fig 5.15. Fe-O distance was fitted as 2.07 Å ± 0.03 Å, more consistent with the extended Fe-O coordination in a magnesium rich silicate molecule (see APPENDIX BIII) and our forsteritic San Carlos olivine EXAFS standard than Fe-oxide.
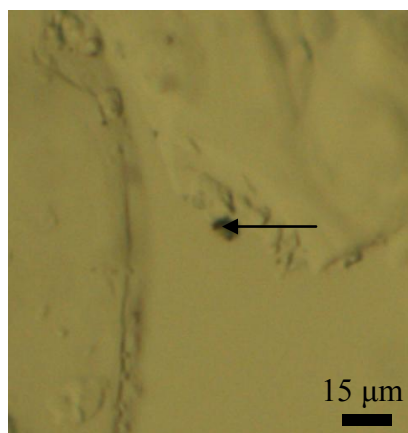
FIG 5.21: Reflected light image of selected region of C2044,0,41 (transverse slice from track 41, see Fig 5.7b. (Bridges et al. 2010). Shown arrowed is a grain captured in the aerogel on the wall of the track cavity (the bottom right quadrant of the figure is the track cavity, the other three quadrants are part of the extracted aerogel slice).

5.4 Discussion

The results have demonstrated a variety of iron-bearing oxides that have varying oxidation states. In this section we discuss the potential origin of the different iron oxides. We also consider the EXAFS results and assess the chemical coordination environments of these oxides in order to help us to understand possible changes in charge states and identify different mineral species.

5.4.1. How did the Iron Oxides Form?

Irradiation of the comet's surface, the extreme thermal processing of the cometary dust during capture, some heating during analysis and terrestrial contamination during manufacture of the aerogel or in laboratories, could all potentially explain the iron oxides found in the *Stardust* samples.

5.4.1.1. Space Weathering

Bridges et al. (2010) have suggested the submicron amorphous oxidised iron found in track #121 might have been a possible consequence of space weathering. If this space weathered material is present, mixed in below the comet's surface and was carried by the

jets from inside the comet into the coma then some of the nm-sized Fe-bearing particles e.g. in #121,1,0 might have originated as space weathered material on Comet Wild 2. However, the O-bearing nature of the Fe-rich phases studied here requires that if space-weathered material was present it has undergone subsequent oxidation. Grain sizes can also be microns in size which is uncharacteristic of nanophase space weathered phases (Figs. 5.5a, 5.21). The observed amorphous structure of the extracted grain is not consistent with this explanation either, unless amorphisation was due to melting of the grain during capture followed by rapid cooling.

5.4.1.2. Capture Heating

During capture at 6.1 kms^{-1}, the cometary grains experienced substantial heating. After the first demonstration of capture of mineral grains at high speed in aerogel (Tsou et al., 1988), several studies of the effect of capture on mineral grains, including melting at grain surfaces, quickly followed (e.g. Bunch et al., 1991, Barrett et al., 1992) and these are summarised in Burchell et al. (2006). More recent studies include Noguchi et al. (2007), Hörz et al. (2008) and Burchell et al. (2008). It is clear from the abundant melted, rounded Fe sulphide and metal grains found along the tracks that some melting and sulphur remobilisation has occurred. This can be seen for example, in the work of Leroux et al. 2008, who examined grains from track #41 as well, along with grains from track #35 (a Type B, bulbous track), and track #44 (a large feature where the incident particle hit both aerogel and the container wall) and some grains of unknown track type. Recrystallised sulphide-metal assemblages frequently occur as metal (usually kamacite) cores and sulphide (pyrrhotite) rims in grains that range in size from nm to <100 nm diameter. Taenite also occurs. Temperatures associated with capture of the cometary grains and metal-sulphide recrystallisation must have exceeded that of the Fe-Ni-S eutectic. This eutectic temperature increases with pressure but is at least 950-1000°C and gives a minimum temperature during capture.

There have been conflicting arguments as to whether capture heating in aerogel causes oxidation or reduction. Rietmeijer et al. (2008) described Fe silicides near the entrance of track #44: they suggested these resulted from the reduction of melted Fe-Ni sulphide grains. Nanometer sized grains that melted and comingled with impure silica melt have

been suggested to contain numerous FeNiS, silicates and 'dust-rich areas' by Rietmeijer (2009). Marcus et al. (2008) also reported light gas gun experiments where ferric iron had been reduced to ferrous compounds and considered that this was associated with capture heating in the presence of carbon within the aerogel. In contrast, Grossemy et al. (2008) used Fe-XANES to show that ferric iron-rich particles identified near the track mouth of Allende meteorite particle tracks in aerogel (shot with a light gas gun) were the result of the oxidation of olivine. The relatively high abundance of magnetite within the Allende meteorite means that some of the magnetite in the Grossemy et al. (2008) experiments (and thus by analogy within our samples) might have been derived from the meteorite (or in our case Comet Wild2) rather than being due to capture-related oxidation of other minerals. This still does not, however, explain the concentration of ferric iron at the track entrance of the Allende experiments. The large abundance of ferric iron oxides at the entrances of tracks #41 and #162 suggest that some oxidation has occurred during capture heating, at least within 1 mm of the track entrances and possibly further towards the track ends. The possible mechanisms for the formation of ferric Fe-oxides in our *Stardust* samples by capture heating will be discussed.

5.4.1.2.1 Mechanisms for Capture Related Oxidation by Silicate Alteration

XANES and EXAFS of one of the hotpots from the entrance of track #162 (Table 1) have identified one of the hotspots to be most consistent with a magnesium silicate signature. We briefly explore the formation of iron oxides by the capture of cometary silicates. The stability of silicon dioxide means that reducing SiO_2 for subsequent oxidation of cometary material is very unlikely. This raises the issue as to where the oxygen has come from for oxidation. Temperatures $>1000^{\circ}C$ upon flash heating would have been large enough for the melting of silica and have been reported in previous studies of capture heating effects from the *Stardust* mission (e.g. Spencer and Zare, 2007). Silicates would melt around the same temperatures as aerogel, liberating the Fe^{2+} cations to subsequently oxidise to Fe_3O_4 and Fe_2O_3 at higher oxygen fugacities. Stability of Si-O bond in liquid silica has been shown at much larger temperatures (e.g. Hicks et al. 2006), where a bonded silica liquid can be stable at 10^4 K. Thus, oxygen liberation from SiO_2 in

the aerogel and a pre-exisiting silicate seems unlikely. Pre-exisiting cometary oxides could indeed react with silicates.

5.4.1.2.2 Mechanisms for Capture Related Oxides by sulphide alteration

Our consistent identification of iron oxides at the entrances of tracks #41 and #162 suggests that evolution in the iron valency between the hotspots in track #134 from the mid track and terminal positions could be due to oxidation of cometary iron sulphides upon capture. Shells of magnetite have been identified around IDPs caused by atmospheric capture heating (Bradley et al., 1999). An analogous capture heating process may account for the mid track Fe-oxide in track #134. A shell of magnetite assumed to have formed at the track entrance around the pyrrhotite could have been ablated and re-distributed mid track to leave the original cometary material in the terminal area. However, we are still left with the enigma associated with free oxygen ions needed to react with Fe. There is also no record of the abundance of iron oxides across the entire track to compare with this study of samples close to the track entrances.

5.4.1.2.2 Mechanisms for Capture Related Oxidation of Fe, Ni metal

Assuming that an oxygen donor had arrived upon capture, Fe or Fe-Ni metal could oxidise to explain our results. Terminal grains of Fe-Ni metal were identified in track #41 (Oligiore et al., 2009) and are discussed further in Section 5.4.3.1.

5.4.1.3 Oxidation of Samples During their Terrestrial Residence

Oxidation of Fe-Ni metal after the samples were returned to Earth by interaction with the atmosphere is also a possibility which cannot be ruled out. This could have contributed, for example, to the limited oxidation identified in our Fe-XANES analyses of the Fe-Ni grains in track #41. The large interaction volume of the X-ray beam over the Fe-Ni hotspot must also be considered when associating this oxidation feature exclusively with the Fe-Ni metal. The same could apply to the grains in terminal areas of track #121 that may have been amorphous lumps of iron metal that subsequently partially oxidised on Earth, or were very weakly crystalline ferric oxide grains (e.g. ferrihydrite) that lacked detectable crystallinity shown by electron diffraction. Submicron grains would be the most

susceptible to oxidation with the much larger surface area to volume ratios. Our results do however, show the prevalence of micron sized Fe-oxide grains within our samples (e.g. Fig 56a, 5.20).

5.4.1.4 Heating During Analysis

The Fe-XANES and Raman spectra obtained from grains in tracks #41 and #121 show evidence for mixtures of hematite and magnetite at scales less than the $3 - 5$ μm spot size of the illumination laser in the Raman spectrometer and the synchrotron spot size (Bridges et al., 2010; Foster et al., 2008). As discussed above, tests on the laboratory analogues showed that both hematite and magnetite remained distinct after capture in aerogel at speeds of ~6 kms^{-1}, but that prolonged exposure to strong laser illumination of magnetite grains in aerogel could produce hematite (Bridges et al., 2010). This may have been relevant to just one of the grains which underwent a long duration analysis (Fig 13) in the track #41 sample, but not to the extracted terminal grains from track #121 – both the magnetite-hematite mixtures and amorphous Fe oxide. It is, therefore, suggested that, in most cases, the micron-scale magnetite grains are primordial *Stardust* grains and are not artefacts of analysis (See also the following Section 5.4.2). It is also noted that our XRF and Fe-XANES analyses identified magnetite-hematite in spots that had not been analysed at all by microRaman, so it is not believed that the Raman analyses caused the formation of the observed predominantly hematite and magnetite mixtures by these techniques.

5.4.2 Origin of the Different Fe Oxides: Capture Related or Cometary?

We suggest the Fe-Cr-V-Ti oxide in track #41 (Fig 5.9) are likely to be cometary in origin by the presence of vanadium. The Fe-Ti hotpot co-existing with this phase suggests it to be also a primordial cometary grain. Although these features are considered to be cometary in origin, the Fe oxide potentially has a more complex origin. Zn-bearing grains such as ones identified in track #162 are a sign that there is some contamination from the manufacture of the aerogel (Bridges et al., 2010). As described above the Raman analyses seems not to have formed the magnetite or amorphous Fe oxide but it is possible that some of the hematite signature which partially replaces magnetite in a large grain in track #41 (Fig 5.11) will be an analytical artefact. The Fe-XANES analyses suggest that capture

heating in the aerogel has partially oxidised the outer parts of the FeNi metal grains. The intermixing of grains such as Fe-Ti oxide spinels around the track #41 slice with magnetite-hematite is also consistent with more recent studies of track# 80 Stodolna et al., (2010). The magnetite in their track #80 samples comprised of 10% crystalline material with magnetite grains up to 1.5 μm in size. These grains were suggested to be evidence for low temperature alteration. However, there is no unambiguous proof for the cometary origin of the hematite-magnetite initially identified in our track #41 and #121 samples (Bridges et al., 2010) and further investigation is required. The presence of Fe-oxides that have been subsequently found at the entrance of track #162 affirms our ubiquitous identification of these phases in *Stardust* samples.

The amorphous Fe oxide in sample 121,1,0 from track #121 could have originated through melting and rapid cooling, followed by partial oxidation during capture of metallic iron. The origin of this amorphous phase is also uncertain and there is no firm evidence that it is not terrestrial oxidation or a contaminant from aerogel manufacture, like the Zn-Fe compound in track #41 and along the margins of the entrance of track #162. However, the 121,2,0 sample, studied by Raman does have a crystalline magnetite-hematite structure.

It is possible that most of the identified hotspots at the tracks entrances with the 2-4 μm size spot size may have been the result of submicron Fe-oxide phases produced by capture heating oxidation mechanism that is yet to be fully resolved. The resultant size distribution of iron oxides by such mechanisms is also unknown. However, large grains of iron oxides identified optically (e.g. Fig 5.21) eliminate the potential ambiguities raised from relative large probe sizes over the Fe-oxides. The mineralogies and morphologies of the incident cometary grains into aerogel that produced these track are still to be determined. It is possible that such large grains of Fe-oxide are indigenous to Wild2, possibly products from ablation of the incident poly-mineralogical particles. Conversely, the same may also apply to smaller sub-micron iron oxides that experienced more severe heating and ablation effects upon capture. Cometary Fe-oxides in our *Stardust* samples are discussed further in section 5.4.4.

Thus, the Fe oxides in these tracks have a variety of origins mainly related to the Comet Wild 2 parent body and capture heating-oxidation with relatively minor effects from MicroRaman analyses and possible terrestrial contamination of Fe-metal.

5.4.3 EXAFS of Fe Hotspots from *Stardust*

Bond length information of the first coordination shells from hotspots have been determined in all of our track samples. Due to the spot size of the beamline and the submicron nature of *Stardust*, a key assumption made when interpreting these results is that the calculated bond distances has been derived from a dominant phase in each hotspot that has contributed mostly to the EXAFS signal. Quantitative EXAFS have been performed by (e.g. Manceau et al. 2000) but the weak EXAFS signal and potentially heavily modified phases at the track entrances have resulted in the quality of the data enabling calculation of only Fe-O bond lengths. The EXAFS spectra have, however, shown to complement the XANES analyses very well for distinguishing between oxides, sulphides and silicates. This is clearly seen in Table.1 that summarises XANES identification with EXAFS.

5.4.3.1 Other XAFS Studies of *Stardust*

Initial synchrotron based studies of *Stardust* material were performed by Flynn et al. (2008) to determined the elemental composition of Comet Wild2 (see next Section 5.4.4). Since then, XANES analyses have been applied to a variety of *Stardust* samples for organic based (e.g. Matrajt et al. 2008), mineralogical and redox studies of Comet Wild2. The most recent work by Westphal et al. (2009) and Olgiore et al. (2010) used XANES for determining sulphide, F^0 and Fe-oxide (silicate, Fe^{2+}, Fe^{3+}) abundances in *Stardust* tracks. This was achieved by the selection of random hotspots for Fe-XANES and Monte Carlo simulations to eliminate statistical coincidences. The motivation of their XANES studies were to determine the Fe-oxidation state of Comet Wild2 and IDPs to compare with chondrite groups. Their selection of track entrances as well as grains with 'preserved redox state' in terminal areas was also accounted for by prerequisite work of Marcus et al. (2008). Marcus et al. suggested that FeO was reduced upon capture by the presence of carbon contaminant in aerogel that led to the formation of Fe carbides; termed as a smelting process. This reducing effect has been reflected in Westphal and Oligiore et al.'s evaluation of the oxidation state of Comet Wild2. Our results clearly seem to demonstrate the presence of oxidation at the track entrances of all of our samples. As described in section 5.4.2, our results also seem to be most consistent with the results of Grossemy et al 2008. Oligiore et al (2008) studied one of the terminal particles from track #41 that was

found to be a large grain of Fe-Ni metal – a mixture of kamacite and taenite named 'Simeio.' Based on a process of oxidation upon capture, this is consistent with our observations of the ferric oxides and suggested oxidised Fe-Ni metal in our track #41 entrance slice (Bridges et al 2010).

5.4.4 Comparisons of Iron Oxides to Chondrites and IDPs

Iron oxide is found in IDPs (Rietmeijer, 1998) intergrown with phyllosilicates and is interpreted as having resulted from low temperature hydrothermal alteration on a cometary CI-like parent body (Keller et al. 1992) or other carbonaceous parent body. Rietmeijer (1998) and Bradley et al. (1996) suggested that some magnetite found as overgrowths on silicate and sulphide minerals was the result of the heating and oxidation of silicates during atmospheric entry. Bradley (1994a) reported an Fe-Ni grain with a magnetite rim in an IDP. This was interpreted as having resulted from energetic particle bombardment during its passage in space. However, subsequent descriptions of space weathering effects have shown that this process is more likely associated with reduction e.g. Noble et al. (2007). Zolensky and Lindstrom (1992) described magnetite in 12 chondritic IDPs. They suggested that magnetite around the outer margins of IDPs was formed by oxidation of the IDPs during atmospheric entry, but that magnetite within the centres of IDPs was primary.

Magnetite is present in CI, CV, oxidised CO, CM and CR chondrites. Keller et al. (1992), Brearley and Jones, (1998) made the comparison between IDPs and CI chondrites because magnetite is one of the common signs of asteroidal alteration in this type of chondrite. Magnetite is the second most abundant phase in CI chondrites and has been described by Madsen et al. (1986); Morlok et al. (2006); Choi et al. (2003) and earlier work summarised in Brearley and Jones (1998). It occurs in a range of textures, but most commonly as 10-30 µm size subspherical aggregates. Fe_2O_3 as maghemite or hematite can also be present, although this could in turn be the product of magnetite oxidation (Haggerty and Baker, 1967). CI magnetite is intergrown with phyllosilicates, particularly serpentine. If the magnetite now present in our Comet Wild 2 samples originated through such alteration, it might be expected to be associated with phyllosilicates such as serpentine minerals. The lack of detected phyllosilicates might be due to dehydration and recrystallisation during capture, although it remains an anomalous absence in the Wild 2

analyses to date. Zolensky et al. (2008) have demonstrated the survival of serpentine minerals upon capture in aerogel. Thus, the evidence suggests that the lack of these coexisting low temperature phases from chondrites and IDPs and the track positions of the iron oxide grains suggest that capture heating related mechanisms seem favourable for these iron oxides.

The asteroidal alteration in chondrites is believed to have occurred between 2-15 Myr after the formation of CAIs, but there does not appear to be any narrow set of oxygen fugacities or fluid composition associated with it (Zolensky et al. 2008). Morlok et al. (2006) concluded that low temperature alteration, including magnetite, in CIs formed in a closed system, where mineralogical differences in the lithologies reflected heterogeneities in the starting material. Although asteroidal alteration is one possible origin for magnetite the origin for the Wild 2 grains remains uncertain.

Flynn (2008) used the result of 20 synchrotron analyses of tracks and fragments of tracks to suggest that the more volatile element abundances, e.g. Zn, Cu, showed an affinity to anhydrous porous IDPs but the more refractory elements, e.g. Ca to Fe, were closer to CI abundances. Our increased presence of Zn with also the evidence of Cu at the track entrance seems consistent with these observations. Although the volatile Zn is concentrated at the entrance, we also have to take caution in Zn and Cu abundances at the entrance due to suspected Zn and Cu contamination at the track entrance. Thus, as also suggested by Flynn, there may be no easy, exclusive correlation between Comet Wild 2 and either IDPs or CI chondrites. The results reported in this thesis and of the UK consortium analyses show an unequilibrated mixture of reduced (e.g. FeNi metal) and oxidised phases in close proximity within the tracks. These phases can be present in both types of planetary material – chondrite and IDP. However, Ishii et al. (2008) noted that amorphous silicates with embedded metal and sulphide (known as GEMS) were a major constituent of anhydrous porous IDPs, but that the initial reports of these in Comet Wild 2 samples were compatible with impact capture processing of the aerogel, rather than cometary GEMS of which there are currently no firm identifications in Wild 2. Furthermore, they noted that refractory minerals, CAIs, chondrules, and chondrule fragments are normally absent from, or exceedingly rare, in chondritic porous IDPs, but are found in almost all chondritic meteorites. Thus Ishii et al. suggested that Comet Wild-2 was most similar to chondritic

material originating within the inner Solar System. The studies of a terminal grain from track #154 (Chapter 6) re-enforces this link between the current *Stardust* inventory and chondrites.

5.5 Summary and Conclusions

Iron oxides have been identified in a slice taken ~0.8 mm along track #41, part of the length (750 μm) of track #162 from the entrance, track #134 and some terminal samples from track #121. V-rich chromite (Fe-Cr-V-Ti-Mn oxide), Fe-Ti oxide (ilmenite?), and partially oxidised Fe-Ni metal are present in track #41. The V-rich phase coexisting with the suggested Fe-Ti spinel and Fe-Ni metal are believed to be cometary. The terminal samples from track #121 also contain traces of sulphide and Mg-rich silicate. The Fe-oxide grains are shown to be ferric oxides with mixtures of magnetite, hematite and goethite by fitting of XANES edge positions. Others are amorphous (track #121). Ferric oxide is widespread throughout the samples from near the track entrances.

XANES of the terminal area in track #134 shows it to be an Fe-sulphide phase. Comparison to Fe-sulphides standards shows it to closely match to pyrrhotite. XANES spectra from a mid-track hotspot shows the presence of ferric oxide again that fits closest to 95% magnetite.

Fe-XANES and TEM suggests that capture heating in the aerogel has led to partial oxidation of some phases, notably the FeNi metal. This may also be the case in track #134 where metal from iron sulphide could have also have been oxidised. Magnetite - hematite mixtures shown by XANES analyses are abundant in the slice of track #41 and #162. These observations are also consistent with Raman spectroscopy performed by other collaborators of the UK *Stardust* consortium who have studied tracks #41, and #121. It is suggested that the large hematite/magnetite grains in track #41 are cometary.

EXAFS has also confirmed the identification of ferric oxides and has discriminated between the identified sulphides and silicates by matching Fe-O and Fe-S average nearest neighbouring bond lengths. This adds to the current fine structure methods used for analysing the mineralogy of *Stardust* grains, with a direct empirical approach in mineral identification that complements mineralogical 'fingerprinting' achieved with XANES.

There have been no reported EXAFS studies of *Stardust* material, most likely due to the beamline conditions at the selected synchrotons around the world use to analyse *Stardust* samples and due to the analytical challenge of analysing smaller phases than typical spot sizes and the potentially heavily altered material aerogel. Our results have shown that EXAFS at I-18 has reinforced our qualitative mineralogical identifications obtained by XANES with a component of direct structural information about these phases. Thus, EXAFS may be important for helping to explain XANES analyses but also determining molecular information of *Stardust* samples, especially monominerals.

Amorphous Fe oxide might either be a product of the capture-related or terrestrial atmospheric oxidation of metallic iron. Terrestrial contamination within the aerogel is also possible and is probably shown by the presence of a limited amount of Zn and Cu at the track entrances. Further work is required to determine the oxidation state of Fe along individual *Stardust* tracks to investigate this potential terrestrial oxidation overprint that cannot yet be entirely ruled out.

The oxides co-exist with reduced, metallic phases (partially oxidised due to capture or terrestrial alteration) providing further evidence that this comet consists of a diverse mixture of unequilibrated mineral assemblages. Further work is required to assess the similarities with IDP or chondrite samples and to calculate accurate abundances.

Chapter 6
A Unique Refractory Terminal Particle from *Stardust*: Comparison with Refractory Components from Chondrites and IDPs

6.1 Introduction

Currently, Comet Wild2 has been shown to be rich in crystalline high temperature silicates and with no unambiguous evidence of hydration (Brownlee, 2006; Zolensky et al., 2008). Along with the *Stardust* assemblage of crystalline silicates, refractory spinels and oxides have also been identified (Simon et al. 2007; Chi et al 2009). Refractory components presumably from the inner Solar System are recorded in a wide range of planetary materials. They can be found as inclusions (e.g. CAIs) in chondrites (MacPherson, 2003) or as Al-rich chondrules (e.g. Krot et al., 2001). They usually contain refractory elements such as Ca, Al and Ti, (hence CAIs) and are depleted in siderophile elements (Hutchison, 2004). They contain long lived and short lived radioisotopes (e.g. ^{207}Pb-^{206}Pb, - Chen and Wasserburg (1981) and ^{26}Al-^{26}Mg – Hevey and Sanders (2006) respectively) that have been measured to show that they predate the formation of chondrules. Absolute Pb – Pb ages of the oldest CAIs are 4.559 $\pm$ 0.015G.a. - approximately 2 M.a. before chondrule formation (Amelin et al., 2002). They are therefore the oldest objects to have crystallised in the Solar System (Brearley and Jones, 1998). They have been shown to have formed by a range of processes such as melting, evaporation and condensation processes in the Solar nebula (Brearley and Jones, 1998; MacPherson 2003; Beckett et al., 2006). Refractory minerals have also been found in IDPs (e.g. Tomeoka, 1983; Greshake, 1996) but less frequently. There are three commonly described types of refractory objects found in planetary materials. They are Calcium-Aluminium Inclusions (CAIs), Al-rich Chondrules (ARCs) and Amoeboid Olivine Aggregates (AOAs). A brief description of these refractory objects is provided:

6.1.1 Calcium Aluminium Rich Inclusions (CAIs)

CAIs contain some of the most refractory objects found in chondrites and are believed to be amongst the first solids to have formed in the protosolar disk (Amelin et al., 2002). They usually contain minerals such as corundum Al_2O_3, hibonite $(Ca,Ce)(Al,Ti,Mg)_{12}O_{19}$, Grossite $CaAl_4O_7$, perovskite $CaTiO_3$, melilite $(Ca,Na)_2[(Al,Mg,Fe)(Al,Si)SiO_7]$, spinel, Al–Ti-diopside $(Ca,Mg,Al,Ti)(Si,Al)O_3$, anorthite $CaAl_2Si_2O_8$, and forsterite Mg_2SiO_4 (Brearley and Jones, 1998). CAIs are most abundant in CV chondrites, the most famous being the Allende meteorite (Marvin et al., 1970), where they have been divided into type A (melilite–spinel-rich), type B (composed of pyroxene, melilite, spinel, plagioclase), forsterite-bearing type B, and type C (melilite-poor, pyroxene–plagioclase-rich), and fine-grained spinel-rich (Scott and Krot, 2007). They are also found in ordinary chondrites and enstatite chondrites but in far lower abundance compared to C chondrites (Bischoff anf Keil, 1984).

6.1.2 Amoeboid Olivine Aggregates (AOAs)

AOAs are the dominant type of refractory inclusions in most carbonaceous chondrite groups, including the least altered chondrites, CO3.0, CR2, CH, CB chondrites, Adelaide, and Acfer 094 (Scott and Krot, 2007). They are less refractory than CAIs, generally containing minerals such as forsterite (Fo_{98}), Fe, Ni-metal and Al-diopside, spinel, anorthite, and very rare melilite. They are characterised by having irregular morphologies, and their refractory constituents can vary in size from 1-500 μm (Webber and Bishoff 1997). Iron sulphides such as troilite can also be found within them. They are also unique by containing $\delta^{17}O$ and $\delta^{18}O$ ratios that consistently lie in the same position on the CCAM mixing line, unlike CAIs (Scott and Krot, 2007).

6.1.3 Aluminium Rich Chondrules (ARCs)

ARCs differ from the other types of refractory inclusions in that they are chondrules, having igneous textures but containing Al-enrichments e.g. >10 wt% Al_2O_3 (Bishoff and Keil, 1984). Again they are most frequently found in carbonaceous chondrites but also exist in ordinary chondrites. Some of them are plagioclase-rich or spinel-bearing

chondrules (Krot and Keil, 2002). They are intermediate in composition between ferromagnesian chondrules and some CAIs (Tronche et al., 2007).

The following chapter describes the mineralogy and morphology of a terminal particle from track #154 of the *Stardust* collector tray - Section C2063-1-154-1-0. The terminal particle contains refractory material that has affinities to the minerals found in refractory objects from early Solar System planetary materials. This unique particle from the *Stardust* mission emphasises the wide range of mineral compositions and temperatures in grains from Comet Wild2.

6.2 Samples and Methods

6.2.1 C2063-1-154-1-0, Terminal Particle. 2

The keystone of track #154 was extracted from Tile C2063. OM shows it to be a 922 μm length bulbous track containing 6 distinctive grains in terminal positions (Fig. 6.1). Preparation of the samples was done by NASA – JSC. Section C2063-1-154-1-0 was extracted from the keystone followed by the dissection of Terminal Particle 2 (T.2) (Fig 6.1). The aerogel wafer containing T.2 from track #154 was embedded in *Embed812* epoxy, and then cured under vacuum conditions for 48 hours. A potted butt was produced of T.2 with the terminal particle completely surrounded by aerogel.
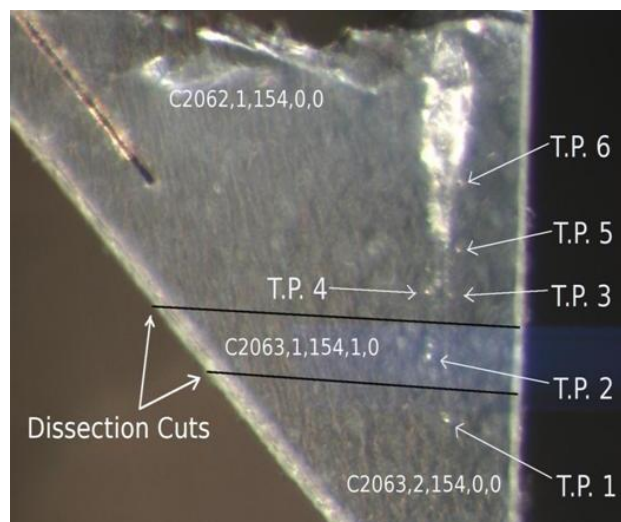
FIG 6.1: Optical micrograph of track #154. The segment containing terminal particle T.2 (sample C2063,1,153,1,0 was dissected from keystone 2062,1,1,154,0,0. *Image from NASA-JSC*.

6.2.2 Ultramicrotomed Sections of C2063-1-154-1-0 T.2.

The potted butt of Terminal particle T.2 embedded in epoxy was sliced into ultra thin sections by ultramicrotome onto an amorphous C/Cu grid using conventional microtome methods described by Barrat and Zolensky (1991). Updated methods for sample preparation may have also have been used as described by Matrajt and Brownlee (2006) but with epoxy rather than acrylic. Four separate C/Cu grid sections were provided for this study: C2063-1-154-1-14, C2063-1-154-1-15 and C2063-1-154-1-17. Microtomes of T.2 were sliced into varying thicknesses at JSC. C2063-1-154-1-14 was microtomed into 70 nm and 90 nm sections (Fig 6.2); C2063-1-154-1-15 into two 70 nm sections; C2063-1-154-1-17 into two 70 nm sections.
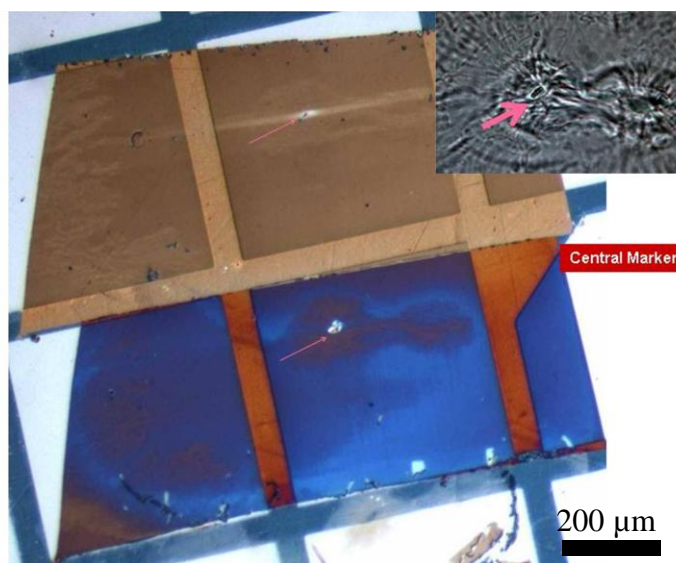
FIG 6.2: Optical micrograph of C2063-1-154-1-15 showing the two 70 nm microtomed samples on the amorphous C film Cu TEM grid. Inset shows T.2 embedded in epoxy prior to ultra-microtome. Note the surrounding aerogel around the terminal particle. The adjacent particle like feature next to T.2 is the alteration induced by terminal particle T.1 further down the track.

6.2.3 Transmission Electron Microscopy of T.2. Samples

TEM was performed with the UoL AMC's Jeol 2100. Its LaB_6 thermionic source was operated at 200 kV and 106-111 μA emission currents. Conventional TEM techniques described in Chapter. 2 were employed. BF imaging, DF, SAED, Nanobeam diffraction, HRTEM and STEM BF, DF and HAADF imaging were performed on the microtomed sections of T.2 track #154. TEM imaging was performed by condensing the beam with the

2nd condenser aperture (50 nm). However, search and alignment processes were performed under reduced electron dosage conditions with the 3rd condenser aperture.

EDX analyses were performed with the *PGT-Gamma tech* spectrometer. Initial TEM spot analyses of the first sections were performed under conventional operating conditions, i.e. maximum convergence angle α 5 and condenser lens C2. There were no records or experiments on the effects of conventional TEM analyses on the *Stardust* samples and thus conventional analytical conditions were initially employed to assess sample damage during analysis. Variable spot sizes were used depending on the size of particular features and ranged from 25 nm, 15 nm and 10 nm. Initial spot analyses on large regions were performed with 25 nm spot sizes. Initial spot analyses on C2063,1,154,1,14 were performed with the C2 aperture. With severe alteration of sample after some analyses, the C3 aperture was employed for reduced dosage. On particularly thin regions, count rates were too low (<80 cps). For higher count rates, the C2 aperture was used again, but C3 was acceptable for thicker regions yielding high count rates. EDX spectra were typically obtained from 100-200 s acquisitions depending on the sensitivity of the sample to damage and spot size.

AEM analyses were performed on the range of silicates that were identified. *K*-factors were used that were calibrated based on the method described in Section 2.10, principally based on Cliff Lorimer *K*-factors. The measurement of excess silica was a common problem faced upon AEM analyses. Variable amounts of Si were measured on regions of the same qualitative composition (see results). Variation in Si peaks and other peaks such as F were found at different areas of microtomed epoxy in an around the sample (see Section 6.3.5). Thus, it did not seem feasible to use a constant type of correction for an aerogel/acrylic overprint that has been used in other *Stardust* analyses (e.g. Zolensky et al. 2008). Out of the total set of AEM analyses, the quantitative results from silicate (pyroxene) analyses were grouped into ones that provided stoichiometric mineral compositions and those that did not. The most likely silicate types were also identified for some of the non stoichiometric analyses (see results Section 6.3.5.1). Imperfect stoichiometric analyses were used that had a deficit between the total cations and tetrahedral (Si,Al) of less than 5 at% from the ideal stoichiometry. This means 15 –20% total deficient cations or 20-25% in excess Si at%.

6.2.4 Ultra High Resolution FEG-SEM of T.2 samples

Following TEM analyses, the T.2 track #154 terminal samples were imaged with an FEI Sirion Field Emission Gun SEM (FEG-SEM). The FEG-SEM was operated at low kV (3.6 – 4 kV) in order to maximise the electron beam interaction volume with the ultra thin sections. Images were generated using the TDL detector under Ultra High resolution mode. The sample was too thin and too small to enable any reliable EDX data. Thus, chemical analyses were constrained to TEM-EDX.

FEG-SEM imaging has not been reported on these types of *Stardust* thin sections but is a useful tool for obtaining morphological information and correlating with TEM imaging and EDX.

SEM imaging, however, was performed after any TEM analyses due to the high dosage of electrons under SEM and lower accelerating voltage compared to TEM that may have undesirable sample damage such as carbon deposition and heating up of aerogel.

6.3 Results

6.3.1 Morphology of T2 track #154 microtomed sections

The 3 microtomed samples of the T2 from track #154 contained 2 thin sections on each grid. One slice contains the bulk grain whist the other has shards of the particle located around the particle rim (Fig 6.3). It is likely that the missing inner core in every section of the samples was an effect of sample preparation as these samples are brittle and fragile.

The three bulk slices of the grain are shown to be roughly oval or teardrop-shaped. The grains bulge towards the centre and are unevenly thinner at both ends (see next section for specific sizes). The fragmenting due to the effect of microtome is clearly visible. The topography of the thin sections can be seen in the FEG-SEM images of the samples as shown in Fig 6.3. Shards can be clearly seen that are not lying flat on the grid and that are frequently overlapping one another (e.g. Fig 6.3b). Contrasting due to edge effects on the shards would pose complexities for distinguishing between different grains and minerals within the sample (e.g. Fig 6.3b). Dynamical effects of the electron beam due to the interaction with crystalline material were visible by BF imaging. Moiré and thickness fringes were most likely the result of shards and flakes of ultra thin material at different

orientations and overlapping one another. Compressed aerogel seems to surround the rims of the slices (e.g. Fig 6.3).

6.3.2 C2063,1,154,1,14

BF imaging of sections 1 and 2 show that many of the shards produced contrast effects such as Moiré and thickness fringes indicating the presence of crystalline material (Fig. 6.4a). TEM-EDX surveys of most of these shards and contrasting regions within them suggest the presence of an Mg-Ca-Al-Ti silicate with consistently trace amounts of Fe, Co (silicate assumed by dominant Si and O Kα peaks. Its stoichiometry is consistent with a pyroxene composition (see Section 6.3.5). A clinopyroxene structure is indicated by SAED performed on one of the shards of section 2 on the grid (Fig. 6.4b). On the margins of this section, small grains of iron sulphide were identified <10 nm in size.

The only other phase identified in section 1 is a region of pure Mg-silicate identified by EDX – forsterite Mg_2SiO_4 (Fig. 6.5). BF imaging shows it to be intergrown with one of the shards of clinopyroxene located towards the rim of the particle. A mottling effect is also identified along the boundary between the pyroxene and forsterite (Fig. 6.5a). Its AEM composition is found in Table 6.1. TEM-EDX of the forsterite grain and the adjacent pyroxene grain are shown in Figs 6.5b and c respectively.

A region of section 2 also adjacent to the aerogel rim contains a range of silicates coexisting in an area of approximately 300×300 nm (Fig 6.6). TEM-EDX shows a forsterite grain along a boundary with another Mg rich silicate. AEM shows that to be Al-pigeonite (Table 6.2). Narrow flakes of this pigeonite were also found on the right edge of this region (Fig 6.6). AEM compositions of the two forsterite grains and pigeonite grains can be found in Table 6.1.
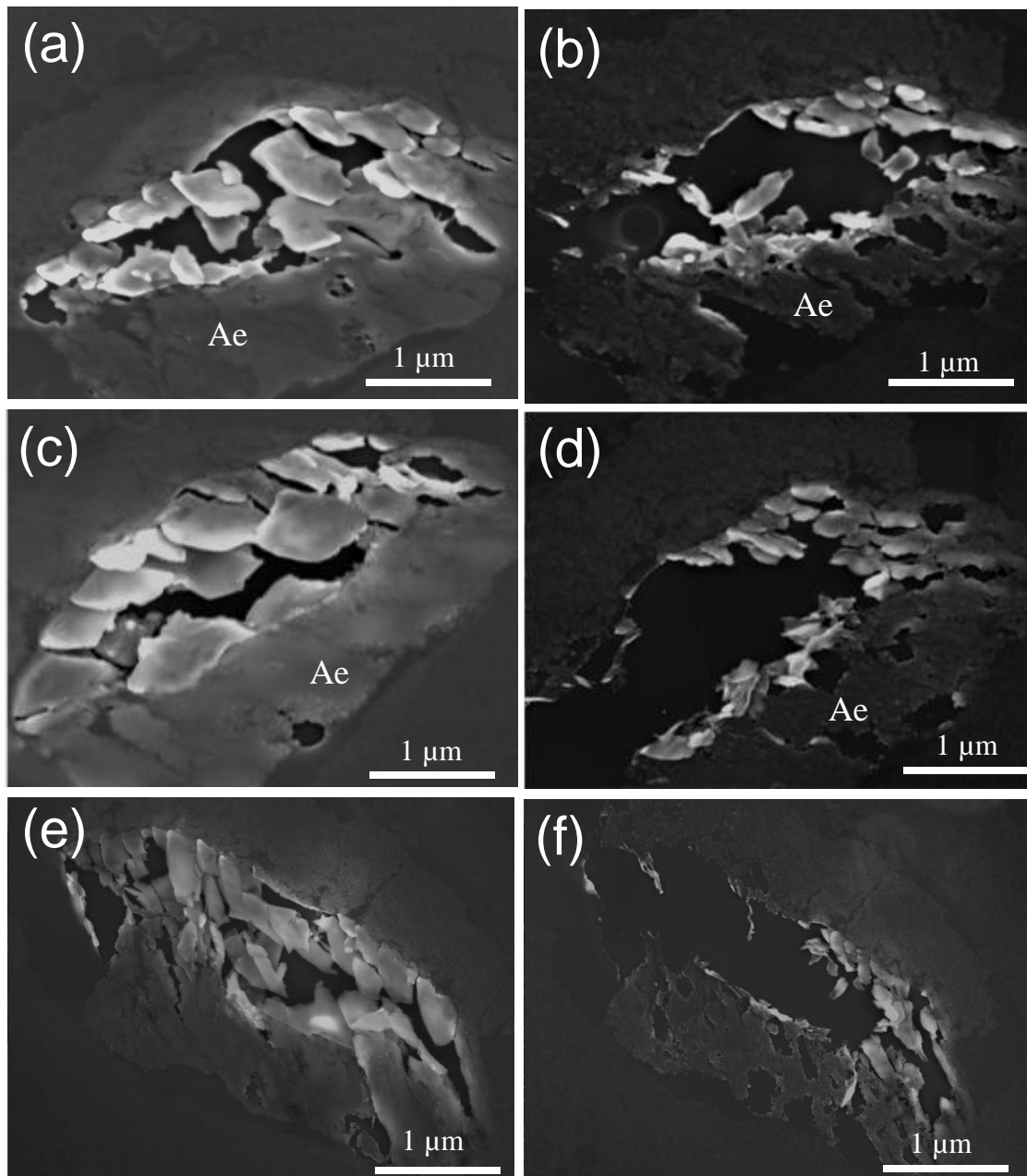
FIG 6.3: FEG-SEM images of the 6 sections particle#2 from track #154. Contrast is predominantly due to the edge effects of overlapping and differently orientated shards of material. (a) - (b) Section 1 and 2 of C2063-1-154-1-14. (c) - (d) Sections 1 and 2 of C2063-1-154-1-15 respectively. (e) - (f) C2063-1-154-1-17 Sections 1 and 2.
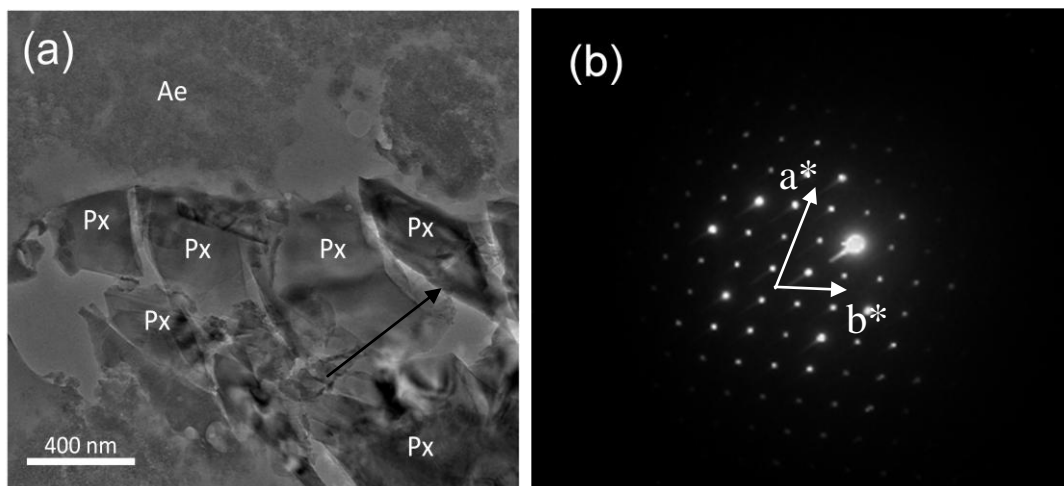
FIG 6.4: (a) Low magnification BF image of the end of C2063,1,154,1,14. Thickness fringes (bottom shard) indicate crystalline material. Bright Fresnel fringes (arrowed) indicate the over focussing conditions that may have been encouraged by the inclination of the shards to the electron beam making imaging difficult under focussed condition at 0° tilt. (b) SAED of a shard from section 2 indicating [0 -1 0] Zone axis of a monoclinic structure via simulation withWebEmaps software.
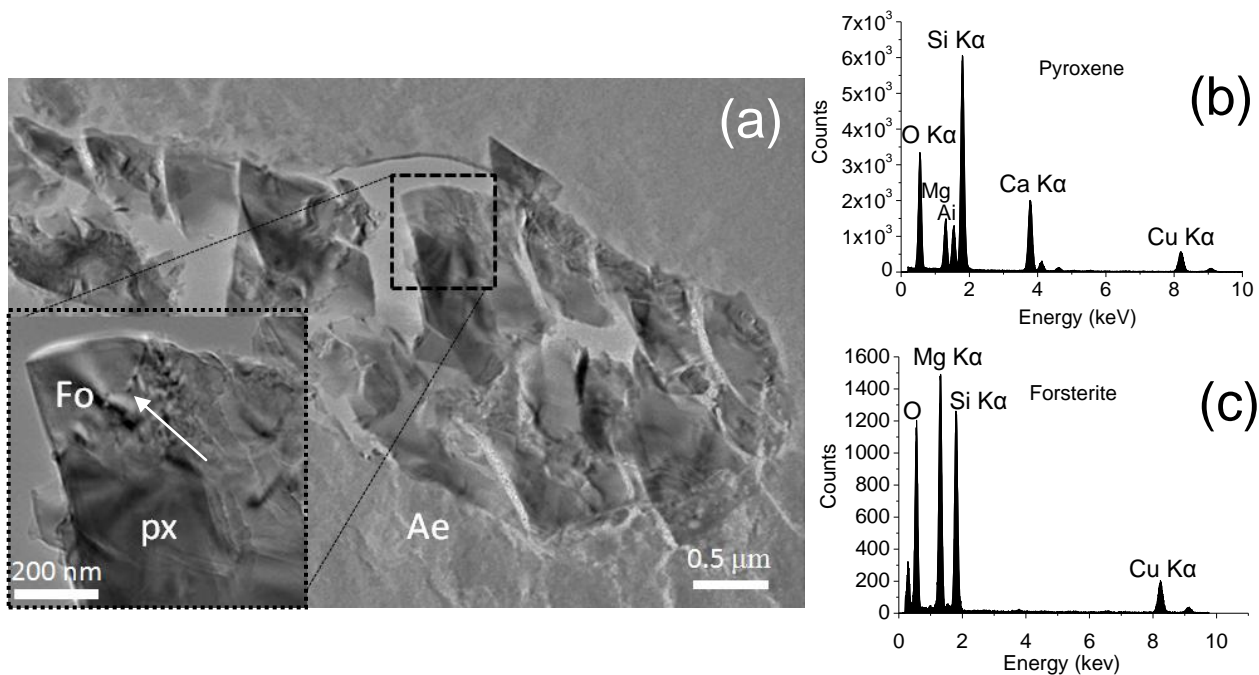
FIG 6.5: (a) Bright field TEM of section 1 of C2063,1,154,1,14. This bulk grain is Al-Ca pyroxene with trace forsterite. The inset shows the forsterite grain (Fo$_{99}$) with a type of 'mottling' at the grain boundary (arrow). Ae aerogel (b) TEM-EDX spectra of the Mg-Ca-Al pyroxene. (c) TEM-EDX of the forsterite grain.
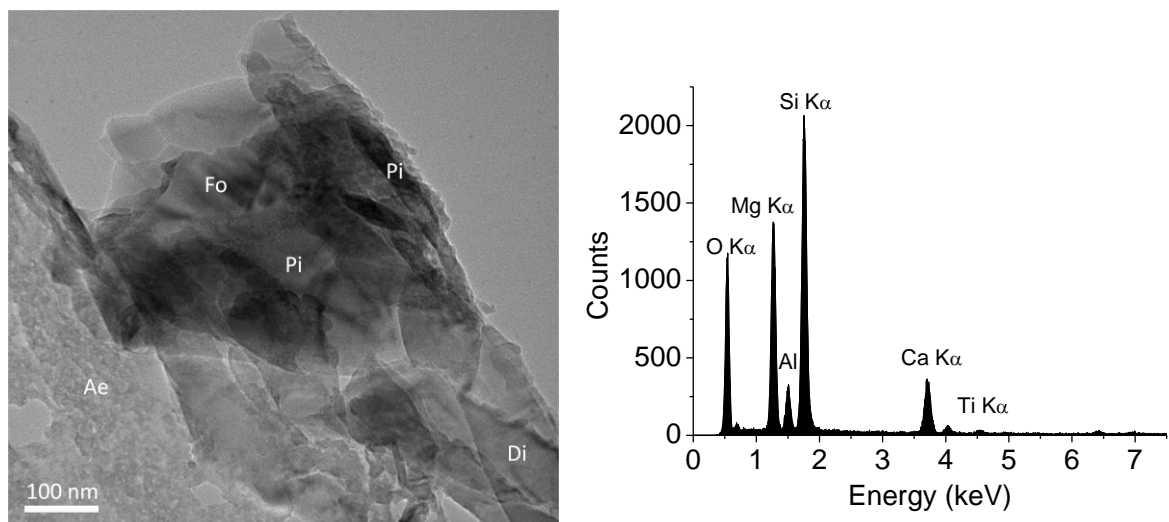
FIG 6.6: Section 2 of C2063,1,154,1,14. (a) BF image of a location close to the rim of the section. Different chemical signatures were identified, suggesting the presence of forsterite (Fo$_{98}$) on a boundary with pigeonite (Pi). Narrow flakes of material have also produced this pigeonite signature. See Table 6.1 for AEM analyses. (b) Representative TEM-EDX spectra of pigeonite. Fo$_{98}$ EDX is similar to that of 6.5c, with the Mg Kα peak larger than Si Kα peak. Pigeonite AEM in Table 6.2.

6.3.3 C2063,1,154,1,15

A low magnification BF and HAADF STEM image of C2063,1,154,1,15 is given in Fig 6.7. Crystalline material is again evident from the dynamical effects of the electron beam similar to those found in Fig 6.4a. Chemical EDX surveys of the shards also show the Ca-Al-Mg rich pyroxene signature across the entire slice. However, another intergrowth of Mg-silicate was found at the rims of the grain (Fig 6.8). EDX analyses of this grain are ambiguous. Its composition by AEM suggests an enstatite mineral in the corner of this region. However, EDX on the edge of the grain showed a dominant Mg peak indicative of forsterite. Re-analysis in the same location resulted in a lower Si peak relative to Mg. It is possible that aerogel had an effect on the initial EDX, producing a higher Si Kα peak. However, its stoichiometry after AEM analyses suggests it being enstatite rather than forsterite or an aerogel mixture (initial survey reported by Bridges and Changela, 2010). EDX on the edge of the grain obtained spectra with higher Mg Kα with respect to Si Kα. Constrained 10 nm EDX analyses across this region after these initial analyses included signatures closest to enstatite. Fig 6.8 shows the different spectra obtained at different

regions of this phase. Thus, it is suggested that this phase is enstatite with areas of forsterite as well. This region is clearly distinct from the dominant Ca-Mg-Al silicate, but seems to be petrologically linked. The Al_2O_3 contents of this silicate (Table 6.1 for Fo and Table 6.2 En) is 1.2 wt%.

An aerogel overprint complicates analyses by seeming to contribute to the amorphisation of grains after electron irradiation. It is plausible that an overlap with aerogel at this type of location in close proximity to the rim could have resulted in spectra with excess silica rather than depleted Si counts somehow erroneously giving an enstatite signature. However, the presence of a stoichiometric composition suggests the presence of enstatite.
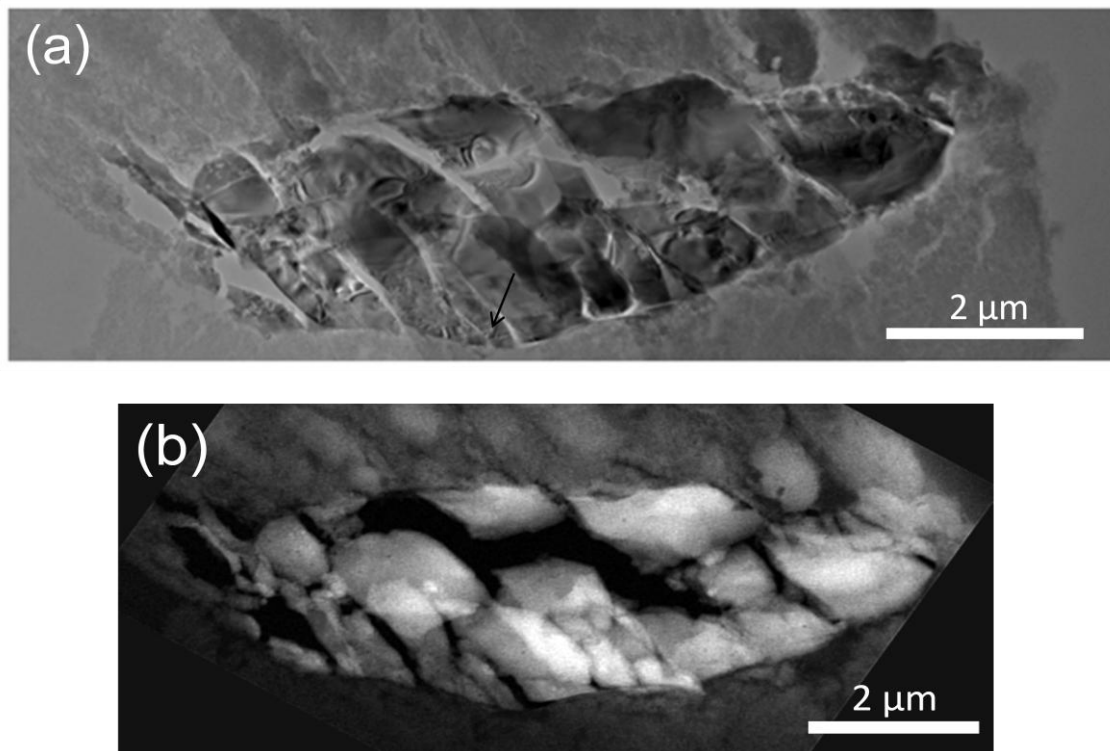
FIG 6.7: (a) Low magnification BF montage of C2063,1,154,1,15. Arrow indicates the suggested forsterite grain. All other shards chemically indicate Ca-Al pyroxene. (b) Low magnification STEM DF image of C2063,1,154,1,15.
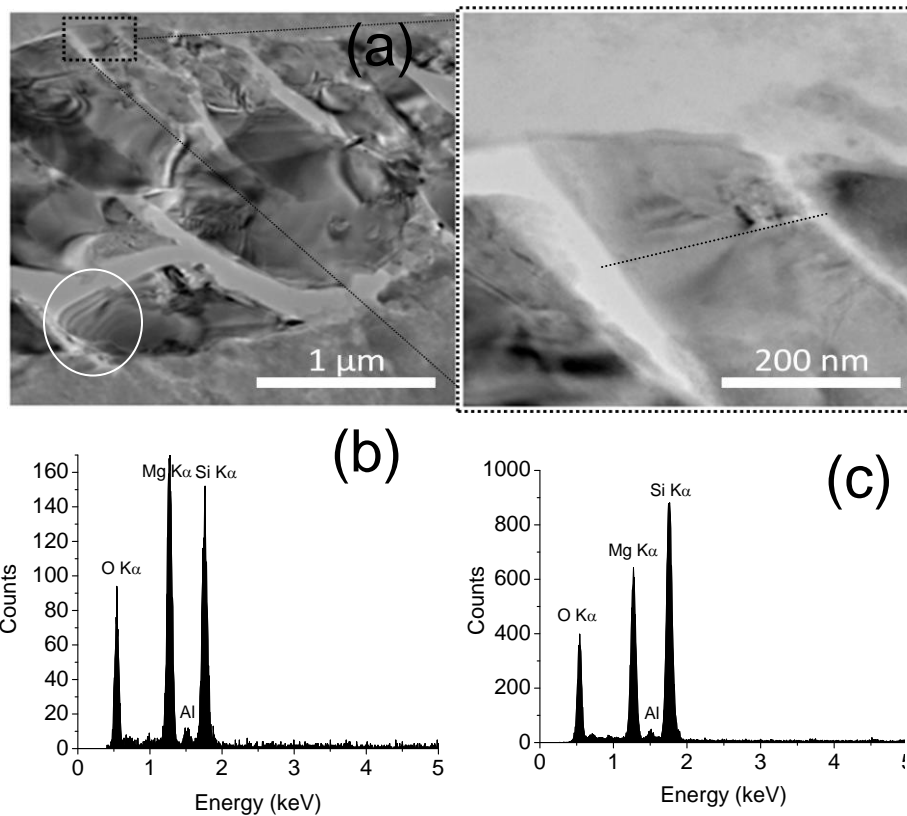
FIG 6.8: BF image of Mg-silicate at the rim of Section 1 C2063,1,154,1,15. The dashed line on the enlargement indicates the approximate transition zone from Mg-silicate (with trace Al) to Ca-Mg-Al pyroxene. Mottling is also seen at the rim of the grain. Thickness contours circles around the pyroxene can be seen on shards of surrounding material. (b) TEM-EDX at the rim of the grain suggesting the tentative forsterite signature. (c) TEM-EDX in the body of the grain Al_2O_3 contents is 1.2 wt%.
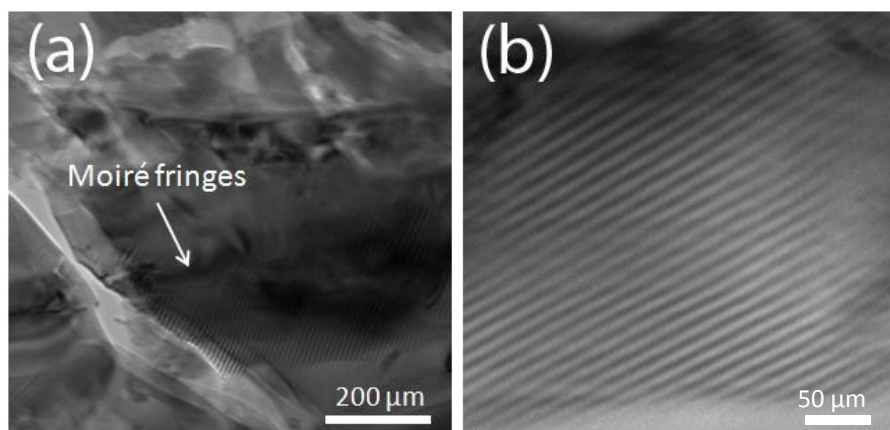
FIG 6.9: Overlapping of Ca-Al crystalline silicate grains again demonstrated by strong Moiré fringes. (a) Low magnification BF image of region of overlapping crystalline shards of material. (b) BF of the right hand part of the overlapping crystals region. (b) High resolution image of Moiré fringes. Regular fringes are 5.9 nm apart.

Section 2 of C2063,1,154,15 like the other section 2's has its inner core lacking. A HAADF image is given in Fig 6.10. The constrasting bright shards and regions indicate scattering of the beam by a combination of overlapping and tilting. All of the shards are again consistent with the pyroxene signature (i.e. Fig 6.5b) identified in the other sections (see Section 6.3.5 for chemical analysis). Small grains of Fe-Ni sulphide were also found at the rim of the grain (Fig 6.11). Qualitative 10 nm EDX spot analysis shows an equal relative intensity of the Fe Kα and S Kα peaks, with minor Ni. Ten nm spot size nano beam diffraction was performed on the larger iron sulphide grain.

1 µm
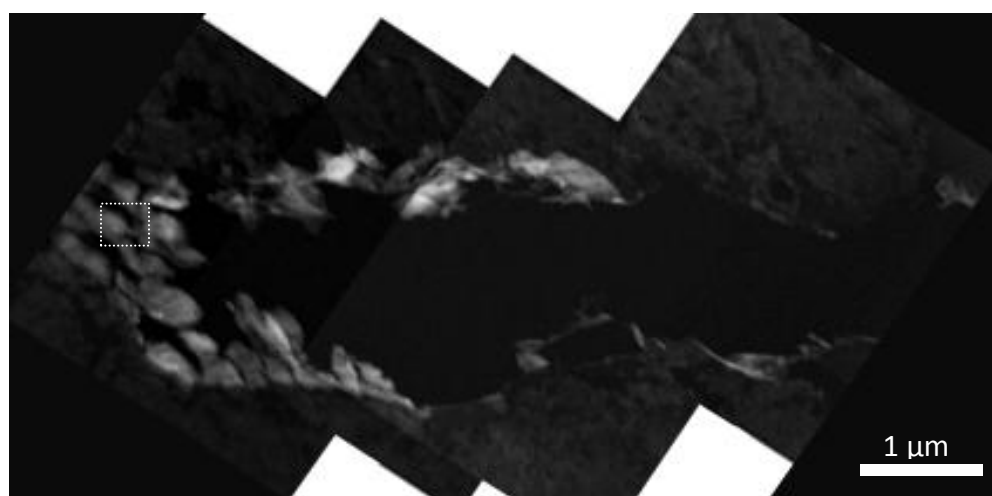
FIG 6.10: Low magnification HAADF image of section 2 from C2063,1,154,1,15. Contrasting shards of material are all Ca-Mg-Al silicate. Marginal Fe-sulphides can also found (e.g. region indiocated by square) - See next figure.
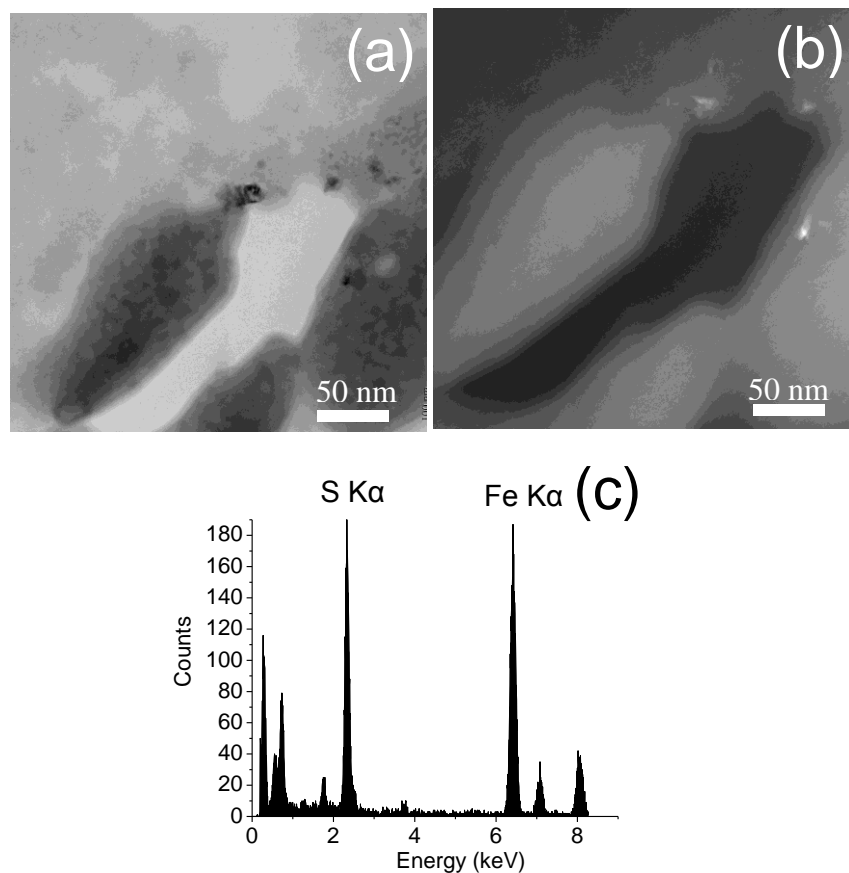
FIG 6.11: (a)-(b) TEM BF (a) and DF images of iron sulphides along the rim of section 2 of C2063,1,1,154,1,15. (c) TEM-EDX of Fe-S grain in centre of field of view.

6.3.4 C2063,1,154,1,17

A BF montage of Section 1 from C2063,1,1,154,1,17 is provided in Fig 6.12. This section is more slender than the other samples of the terminal grain but consists of the same EDX signature representing the Al-rich clinopyroxene for nearly all of the shards.

The only other mineral phase identified again was a small grain of forsterite in approximately the same position as the suspected forsteritic signature found in C2063,1,1,154,1,15 section 1 (Fig 6.13). Again in this region, initial spectra showed an olivine-type composition but Si content was typically higher for stoichiometric olivine (Mg_2SiO_4) after successive analyses in spot localities of the same region (see Table 6.1).
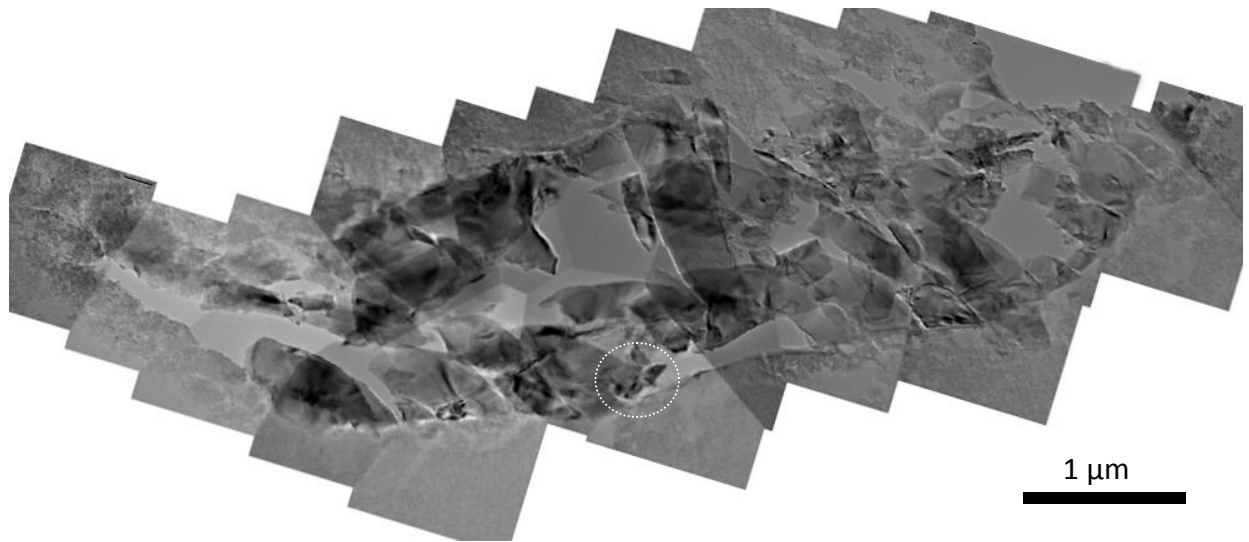
FIG 6.12: Low magnification BF image of section 1 of C2063,1,154,1,17. Except for marginal Fe-S grains, the only other composition apart from the pyroxene signature is the forsterite grain (circled). Note the locality with respect to the suspected forsterite phase in C2063,1,154,1,17 Section 1.
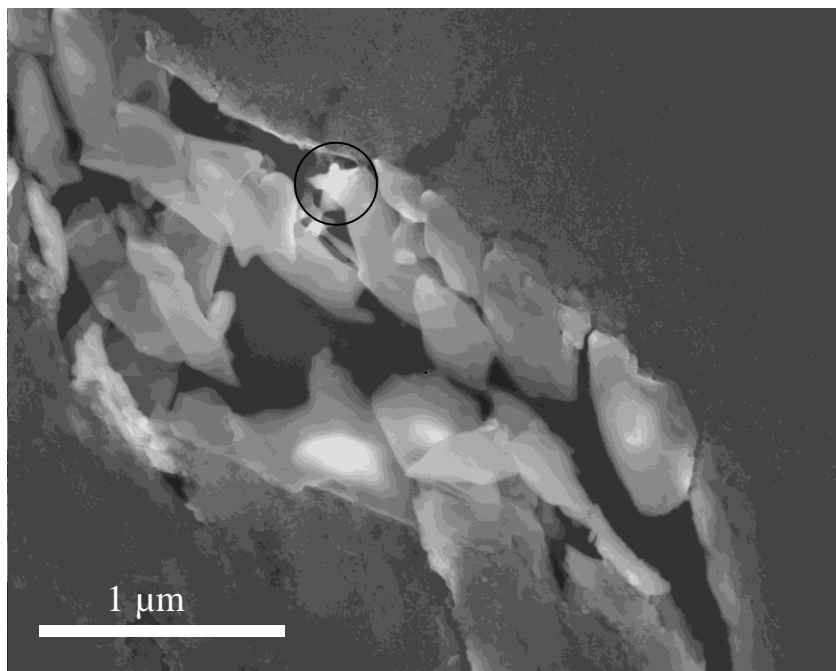
FIG 6.13: UHR FEG-Image of central part of section 1 C2063,1,154,1,17. Circled region shows the location of suggested forsterite grain. Note the similar location of this phase with respect to the Section 1 of C2063,1,154,1,15 suggesting that it is part of the same forsterite grain.
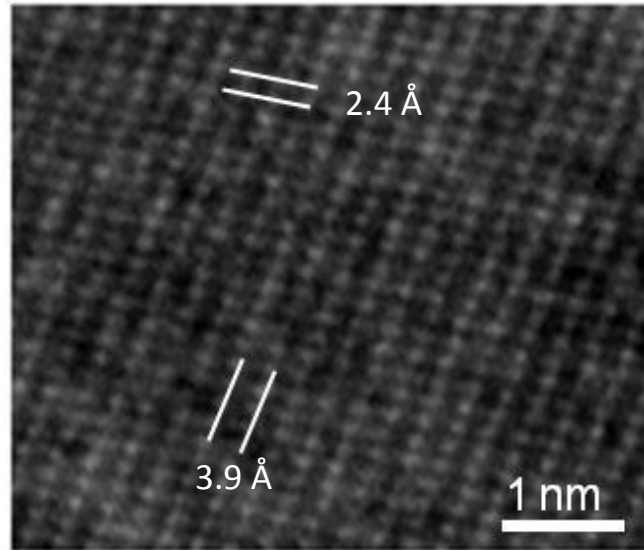
FIG 6.14: HRTEM of a thin shard from of Al-diopside from section 2 of C2063,1,154,1,17.

Fig 6.14 shows an HRTEM image of the Al-diopside from one of the small shards from section 2 C2063,1,154,1,17 (Fig 6.3f). Chemical EDX of this region is similar to that shown in Fig 6.15c. The following section shows how EDX signatures were determined from crystalline pyroxene that generally contained large excesses in Si relative to the cations.

6.3.5 Pyroxene Chemical Composition

TEM-EDX of the grain has complicated overprints of aerogel and/or acrylic with the microtomed grain. The overlapping of shards of material and the variable inclinations of those shards that are not completely flat on the copper grid are also a hindrance to TEM-EDX and AEM of individual phases. Thirty five separate EDX analyses have been performed on different shards from the thin sections with acquisition parameters described in Section 6.2.3. The spectra suggest a Ca-Mg-Al-(Ti) silicate with trace amounts of Fe and Co. Trace peaks of V and Cr were also recognised on some of the spectra but the trace Fe and Co were most consistently found. Representative spectra are shown in Fig 6.15.
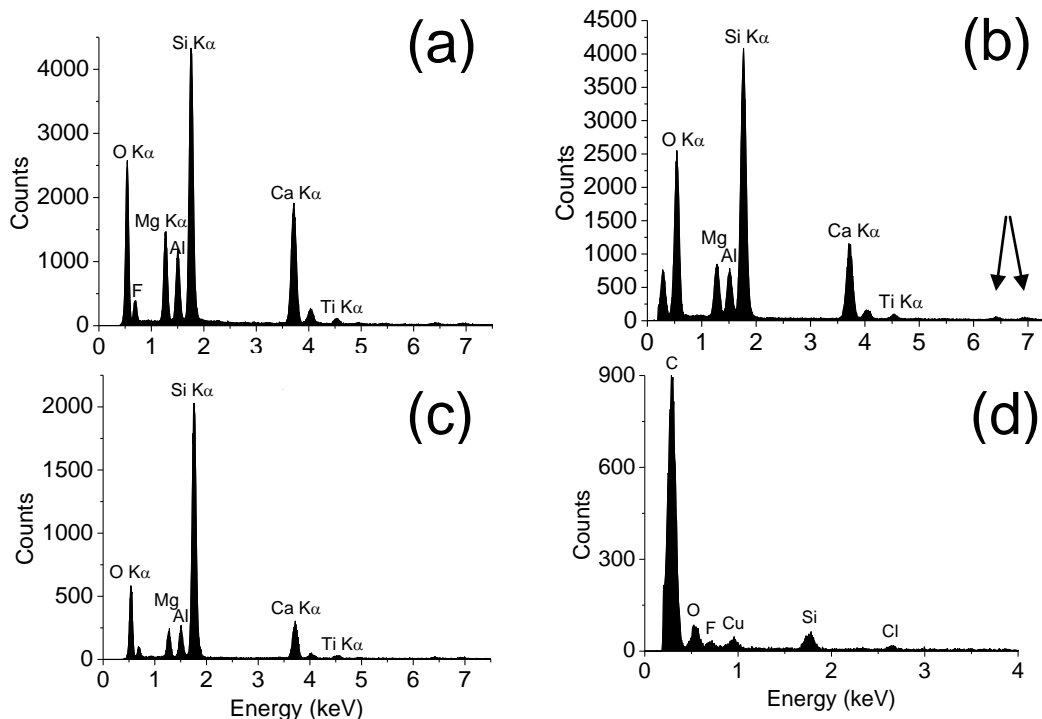
FIG 6.15: (a) Representative TEM-EDX of a shard from Section 2 of C2063-1-154-1-14. (b) Representative TEM-EDX of a shard from Section 1 of C2063-1-154-1-15. (c) Representative TEM-EDX of a shard from C2063-1-154-1-17. AEM analyses of (a)-(c) are shown in Table 6.3. Arrows show trace peaks of Fe and Co. (d) TEM-EDX of void space in Section 1 of C2063-1-154-1-15. Note the presence of F and Cl most likely associated with the epoxy and/or Si and O from overprinting aerogel. These peak intensities can vary at different regions of the slices away from the sample itself.

Table 6.3 shows the Cliff Lorimer based AEM results of the three silicate spectra shown in Fig 6.15 (a)-(c). Most spectra from the total EDX analyses indicate an excess in Si and are more representative of the spectra shown in Fig. 6.15c. 6.15a has the stoichiometry of a Al-diopside mineral, whereas 6.15b and c show a cation deficiency and Si excess compared to stoichiometric diopside $[(XY)(Si,Al)O_3]$ – where X and Y sites are usually filled by Ca, Mg, Al, Na, Fe and the transition elements]. Pyroxenes have an O/Si ratio of 3:1 (with the inclusion of Al in the Si sites). The composition from stoichiometric analyses is consistent with an Al-diopside (see next section). It is notable from the non stoichiometric spectra such as Fig 6.15c that the size of the Al Kα peak relative to the Mg Kα is higher. Perhaps the low energy Mg Kα photons were absorbed due to the suggested aerogel overprint/overlapping and inclinated shards in these analyses.

Although most analyses are not of perfect stoichiometric composition, the ratio of Mg/Ca content for all spectra with excess Si are, however, broadly consistent for all AEM analyses. Reitmeijer (1999) reported the presence of non-stoichiometric diopsides and Mg-wollastonites in an IDP, but the suggested aerogel overprint renders it difficult to infer the presence of similar phases. Magneium, Ca (and other cations) based silica rich glass has also been reported in *Stardust* sections. However, the dynamical effects of many shards in the form of Miore and thickness fringes of many of the shards that produced these silica-rich measurements and whichdeteriorate under the electron beam means that no definite sign of amorphous glass has been found. The consistent signature of trace amounts of Fe and Co (e.g. Fig 6.16) from different shards suggests a single pyroxene grain rather than distinct phases.
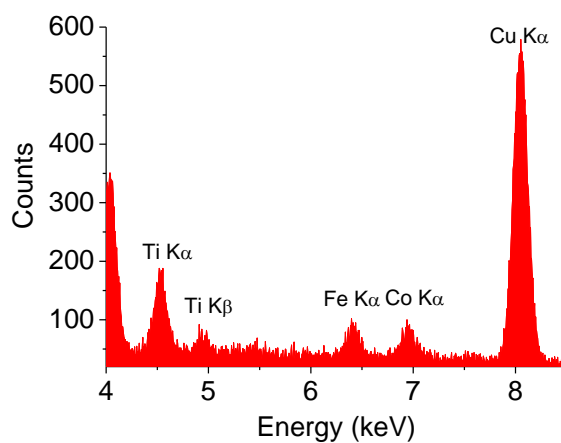
FIG 6.16: (a) 600 long integration spectrum of Al-diopside shard from C2063-1-154-1-15. The spectrum is truncated from 4 – 8 eV, showing the trace peaks recognisably above background for Fe Kα and Co Kα that has been consistently observed in spectra of the shards representing the Al-diopside signature.

The trace Co peak was also found in most of the Al-diopside spectra. The trace Co peak was always accompied with the trace Fe peak. They were also found within the forsterite and pigeonite phases found in the linked forsterite-pigeonite assemblage from section 2 of C2063-1-154-1-14 (Fig 6.6).

6.3.5.1 AEM

The AEM analyses of the Al-diopside and other identified pyroxene compositions i.e. pigeonite and tentative enstatite in T.2 track #154 are plotted on the pyroxene quadrilateral (Fig 6.17). The AEM compositions of the other phases discussed previously in the results are provided in Table 6.2 (forsteritic compositions) and Table 6.3 (pigeonite and enstatite compositions).

In the pyroxene quadrilateral of Fig 6.17, a separate plot is included for the non-stoichiometric, probable diopside analyses for the reasons mentioned in the previous section. Imperfect stoichiometric analyses were chosen that had a deficit between the total cations (i.e. Ca+Mg+Al+Ti+Fe+Co) and tetrahedral ions (Si,Al) of less than 5% from the ideal stoichiometry in at.%. This means 15 –20% total deficient cations or 20-25% in excess Si at%. The other analyses were discarded (i.e. those with similar spectra to 6.15c) to maintain a degree of consistency, although the spectra also generally have the Ca Kα peaks in consistent relative proportions to Mg Kα.

The AEM analyses of stoichiometric pyroxenes are shown in Table 3. The average composition of different shards of the Al-diopside from T.2 track #154 is $En_{50}Wo_{50}$ $(Mg_{0.88},Ca_{0.88},Al_{0.20},Ti_{0.02})(Si_{1.78},Al_{0.22})O_6$ with trace Fe and Co and occasional V. The Al-pigeonite composition is $En_{85}Wo_{15}$ $(Mg_{1.7},Ca_{0.3},Ti_{0.01})(Si_{1.8},Al_{0.2})O_6$ (TiO_2 and Al_2O_3 contents of 0.5 and 5.2 wt% respectively). The errors in the major element concentrations for Mg and Ca are approximately $\pm5\%$ based on AEM testing in Chapter 2. TiO_2 is always present in trace/minor quantities ($\sim$ 1 wt% oxide). Although experimental K-factors for Ti have not been determined, it is suggested that its calibrated value would not alter the measured TiO_2 by a large enough amount to provide larger average TiO_2 contents than ~1.5 wt% due to the marginal changes in the Ca and Fe K - factors (see Chapter 2). Counting statistics for these analyses may have induced higher errors in these stoichiometric analyses where lower counts rates were sometimes obtained for some thin shards of material. Such errors would account for some analyses crossing the diopside field and into the wollastonite field.

TABLE 6.1: *Representative olivine Analyses of T.2 track #154*

	(a)	(b)	(c)	(d)
MgO	55.4	54.9	51.9	52.0
SiO$_2$	44.1	43.4	46.9	46.4
Al$_2$O$_3$	0.5	0.6	1.2	0.8
FeO	-	0.7	-	0.9
CoO	-	0.4	-	-
Total	100	100	100	100
At%				
Mg	27.6	27.5	25.9	26.0
Si	14.8	14.6	15.7	15.6
Al	0.2	0.2	0.5	0.3
Fe	-	0.2	-	0.2
Co	-	0.1	-	-
O	57.4	57.4	58.0	57.9
Total	100	100	100	100
Mg/Si	1.9	1.9	1.7	1.7
O/Si	3.9	3.9	3.7	3.7
Fo	99	98	98	98

(b) From Fig. 6.5. (b) From Fig. 6.6 .(c) From Fig. 6.7. (d) From Fig 6.12.

TABLE 6.2: *Pigeonite and enstatite analyses of T.2 track #154*

	(a)	(b)	(c)
MgO	34.0	32.1	36.2
CaO	7.2	8.1	-
TiO$_2$	0.5	0.5	-
FeO	0.5	0.5	1.0
CoO	0.3	0.3	-
Al$_2$O$_3$	4.6	5.8	1.2
SiO$_2$	52.9	52.7	61.6
Total	100	100	100
At%			
Mg	17.4	16.5	18.1
Ca	2.6	3.0	-
Ti	0.1	0.1	-
Fe	0.2	0.1	0.3
Co	0.1	0.1	-
Al	1.9	2.3	0.5
Si	18.2	18.1	20.7
O	59.6	59.7	60.5
Total	100	100	100
O/(Si,Al)	3	3	2.9
Cation$_{TOT}$	20.4	20.6	18.9

(a) Pigeonite From Fig. 6.6. (b) Pigeonite From Fig. 6.6 .(c) Enstatite From Fig. 6.7.

TABLE 6.3: *AEM analyses of spectra in Fig 6.14(a)-(c). Representative AEM analyses of stoichiometric and non stoichiometric pyroxene in T.2 track #154.*

	(a)	(b)	(c)
MgO	16.4	11.16	6.65
CaO	23.2	14.48	9.35
TiO_2	0.6	1	0.82
FeO	–	0.48	0.35
CoO	–	0.47	0.32
Al_2O_3	10.8	9.16	7.16
SiO_2	48.9	63.25	75.34
Total	100	100	100
At%			
Mg	8.8	5.8	3.4
Ca	8.9	5.5	3.5
Ti	0.2	0.3	0.2
Fe	–	0.1	0.1
Co	–	0.1	0.1
Al	4.6	3.8	2.9
Si	17.6	22.2	26.0
O	60.0	62.2	63.8
Total	100	100	100
Cation$_{TOT}$	20.3	15.6	10.2
O/Si	3.0	2.8	2.5

(a) Spectra from 6.15a – Stoichiometric Al-diopside
(b) Spectra from 6.15b – Imperfect analyses
(c) Soectra from 6.15c – discarded non stoichiometric analyses
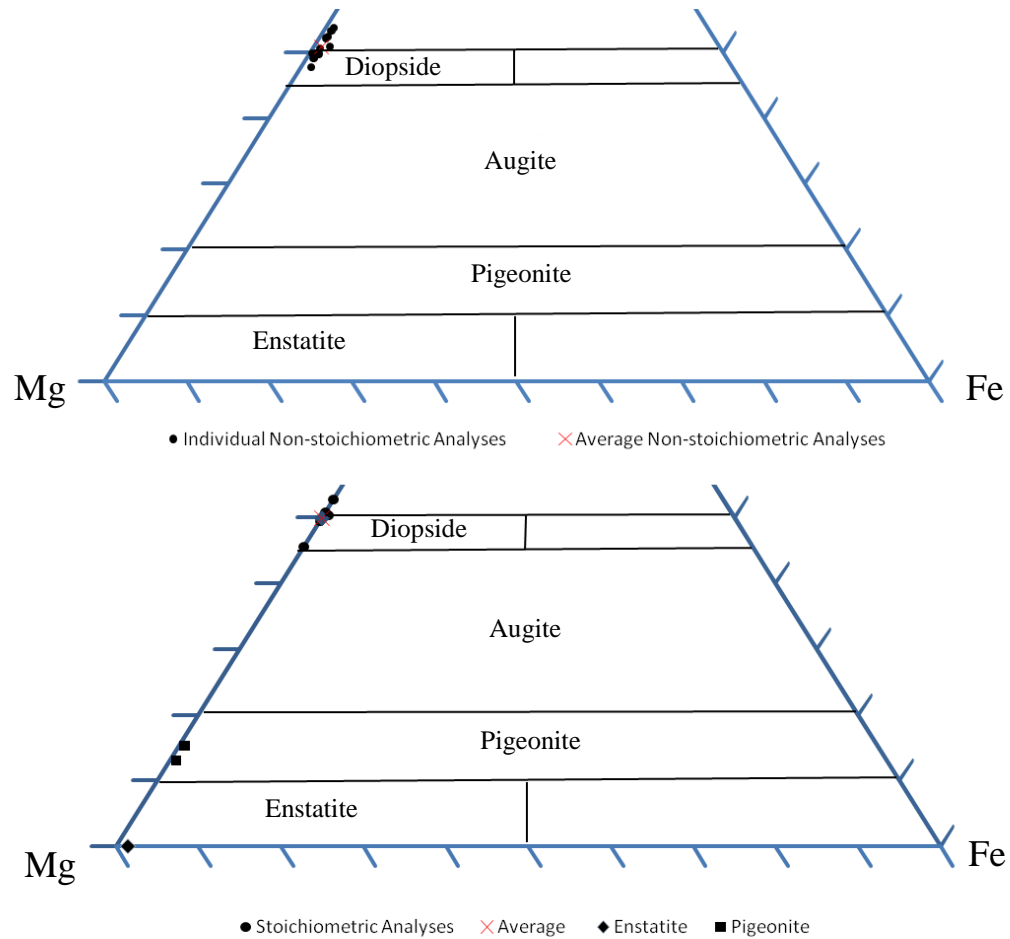
FIG 6.17: AEM analysis of different shard from all section of T.2 track #154. (a) Stoichiometric compositions from various EDX analyses. Some analyses are in the wollastonite field but the average composition sits in the diopside field. Errors from chapter 2 are approximately 5%, although some analyses were performed for shorter counting times. The other suggested pyroxenes identified in T.2. track #154 (i.e. pigeonite and enstatite) are also plotted in the quadrilateral. (b) Non stoichiometric analyses. The average composition on the pyroxene quadrilateral sits on the top of the diopside field.

TABLE 6.4:*AEM analyses of T.2. track #154 that produced stoichiometric diopside compositions*

	Stoichiometric Analyses of T.2 track #154							Average	STD
MgO	16.5	16.4	19.8	17.2	16.6	14.7	13.8	16.4	1.9
CaO	23.6	23.2	23.0	23.5	23.7	21.1	21.5	22.8	1.1
TiO_2	1.1	0.6	0.4	–	1.1	1.1	1.0	0.8	0.4
V	–	–	–	–	0.4	–	–	0.1	0.2
FeO	0.4	–	–	–	–	0.4	0.1	0.3	0.1
CoO	0.3	–	–	–	0.3	0.3	0.0	0.2	0.1
Al_2O_3	9.9	10.8	8.9	10.4	9.9	10.6	9.4	10.0	0.7
SiO_2	48.1	48.9	48.0	48.9	48.2	51.8	54.0	49.7	2.3
Total	100	100	100	100	100	100	100	100	–

								Average
Si	1.74	1.76	1.73	1.76	1.74	1.84	1.91	1.78
Al	0.26	0.25	0.27	0.24	0.26	0.16	0.09	0.22
Sum	2.0	2.0	2.0	2.0	2.0	2.0	2.0	2.0
Mg	0.89	0.88	1.06	0.92	0.89	0.78	0.73	0.88
Ca	0.92	0.89	0.89	0.90	0.92	0.80	0.81	0.88
Ti	0.03	0.02	0.01	–	0.03	0.03	0.03	0.02
Al	0.16	0.21	0.11	0.20	0.16	0.28	0.30	0.20
Sum	2.0	2.0	2.1	2.0	2.0	1.9	1.9	2.0
En%	49.3	49.6	54.5	50.5	49.3	49.2	47.3	50.0
Wo%	50.7	50.4	45.5	49.5	50.7	50.8	52.7	50.0

6.3.6 Summary of Mineralogy of T.2. track #154

TEM and FEG-SEM of T.2 track #154 shows this terminal grain to be dominated by clinopyroxene (Al-diopside) with trace/minor amounts of other phases - forsterite, pigeonite and probably enstatite. The average Al-diopside composition is $(Mg_{0.88},Ca_{0.88},Al_{0.20},Ti_{0.02})(Si_{1.78},Al_{0.22})O_6$ with a standard deviation of 1.9 and 2.2 wt% in MgO and CaO concentrations respectively. The composition of the trace phase of Al-pigeonite is $(Mg_{1.7},Ca_{0.3},Ti_{0.01})(Si_{1.8},Al_{0.2})O_6$. The trace forsterite and enstatite phases (Tables 6.1 and 6.2) are Fo_{98-99} and En_{98} respectively with also trace/minor amounts of Al (0.5 wt% Al_2O_3 in Fo_{99} and 1.2 wt% Al_2O_3 in En_{98}). The minor/trace phases seem to be along the rim of the grain. The forsterite-pigeonite assemblage is further away from the rim, although most materials in this section contained shards only found in the rim. Fine

grained assemblages of Fe-S and Fe,Ni-S can be found further along the rims of the particle and in aerogel. By area fractions of the microtomed section, track #154, T.2 has is ~97% Al-diopside coexisting with minor abundances of forsterite, pigeonite and tentative enstatite.

6.4 Discussion

6.4.1 Comparison of T.2 track #154 T.2 with the *Stardust* Inventory

Diopside has been identified in other *Stardust* track samples - Track #25, #58, #77 and #80. Terminal particle 'Inti' from track #25 has been shown to contain shards of diopside coexisting with other minerals that are typically found in CAIs. Its composition has been shown to very between pure diopside and Al, Ti-rich faissite (Simon et al., 2008). High Ti contents with up to 14.5 wt% TiO_2 (Chi et al., 2009) show that these fassaites are are unlike the pyroxene with low Ti abundances in T.2 track #154 discussed in this chapter. However, minor phases (100s nm across shards) of similar composition were also reported by Simon et al. (2008). Terminal particle 'Puki-B' from track #77 contains diopside or kosmochlore-diopside – a Na and Al-bearing pyroxene. It is a 200 nm grain embedded in Al-silicate glass (Joswiak et al., 2008). Joswiak et al. (2010) also described a terminal grain approximately 4 μm across containing Ca-Al-Ti augite with trace to minor amounts of Cr in an assemblage with forsterite and anorthite in track #130 in roughly equal proportions. This grain was suggested to represent fragments of Al-rich chondrules rather than AOAs. Leroux et al. (2008) have shown exsolution textures of diopside and pigeonite from enstatite and constrained the cooling temperature for this assemblage from 1200°C - 1400°C. Schmitz and Brenker (2008) showed the presence of high temperature orthorhombic protoenstatite (PEN) enstatite that has a minimum formation temperature of approximately 1000 $^{\circ}$C. Thus the mineral assemblage of T.2. track #154 is unique within the current *Stardust* inventory in being a grain composed mainly of Al-diopside with trace forsterite and pigeonite with some probable enstatite. Based on other reported analyses of *Stardust* grains, their total diopside area is very small compared to the area of T.2. track #154.

6.4.2 Geothermometry of T.2 track #154's Igneous Assemblage

Diopside is a silicate with formation temperatures at low pressures (10^{-5} bar) ranging from ~900 ^{o}C - ~1600 ^{o}C (Hutchison, 2004). The mineralogy of T.2. track #154 is an igneous assemblage. However, the bulk mineralogy of track #154 is not known as the entire, original mineral assemblage may not be present in the sections studied. Thiscomplicates any constraints on temperatures and cooling rates. For example, no feldspars have been identified that may have been indicative of a forsterite-diopside-anorthite system (Deer et al, 1966). Unknown pressures also complicate matters but low pressures are assumed consistent with origin on a planetesimal. A brief description of the thermometry related to the mineral assemblage is proposed. The minor/trace phases (pigeonite, forsterite, enstatite) associated with the Al-diopside in T.2 track #154 seem to be along the rim of the grain, the trace forsterite identified is clearly seen to be joined to the diopside (Fig. 6.13) and is thus suggested to be petrologically related to the diopside grain. Pigeonite also seems to be directly associated with a forsterite-diopside assemblage and in trace amounts with respect to the total 6 studied sections. Carlson (1988) experimentally determined phase equilibrium conditions under isobaric conditions for the enstatite-diopside system. A forsterite-saturated liquid is shown to have its forsterite + liquid isotherm meet the diopside eutectic between 1300 – 1400°C at atmospheric pressure. Pigeonite crystallises in the same temperature range but at a lower diopside composition of the liquid (diopside # ~0.2) (Carlson, 1983).

6.4.3 Comparison of T.2 track #154 with chondrites and IDPs

T.2. track #154 contains minerals that have been found in different chondrite classes. Its composition will be compared with similar mineral compositions found in other extraterrestrial materials. Diopside is a minor phase found in chondrules compared to CAIs where it can be found as a primary component (Hutchison, 2004). Chondrules or inclusions containing $\geq$10 wt% oxide Al_2O_3 were considered to be a threshold for Al-rich components (e.g. Al-rich chondrules or Al-rich pyroxene) by Bischoff and Keil (1984). Aluminium and Ti contents within Ca-Mg rich pyroxenes are used to compare T.2. track #154's Al-diopside composition with chondrites, IDPs and CAIs/AOA pyroxenes found in

chondrites. Other compositional relationships such as Ti, Fe and Co content will also be discussed.

6.4.3.1 Ordinary Chondrites

Type 3 and type 4 ordinary chondrites can contain Calcium-Aluminium rich objects although they are rare in ordinary chondrites compared to carbonaceous chondrites. They have been generally found in those of type 3-4 ordinary chondrites (Bischoff and Keil, 1983). Bischoff and Keil's study compared Ca-Al rich chondrules and CAIs in a variety of H-L-LL3-4 chondrites to show the widespread distribution of these phases across ordinary and carbonaceous chondrites. They describe Ca-Al-Ti rich pyroxenes (fassaites) in Allan Hills A78084 (H4 chondrite) having Al_2O_3 (8-12 wt%) and CaO (21.4 – 24.6 wt%) contents that are similar to the Al-diopside in T.2 track #154 but having significantly higher TiO_2 contents up to 3 times higher (from 1 to 3 wt%).

6.4.3.2 Carbonaceous Chondrites

The refractory objects described in section 1.1 are most common in carbonaceous chondrites. Some examples of similar minerals in these objects to that of T.2 track #154 are provided. Al-diopside can frequently be seen towards the rims of spherical CAI inclusions in carbonaceous chondrites (e.g. Krot et al. 2007). Spinel-rich CAIs frequently contain spinel cores that are rimmed by Al-diopside as shown by a CAI in the unique carbonaceous chondrite Acfer 094I that has affinities with CM and CO groups (Krot el al., 2004).

Amongst the various CAIs containing pyroxene, minor or trace phases such as enstatite and pigeonite can be found in different chondrite classes such as CH and CV chondrites (e.g. Zhang et al. 2009; Krot et al. 2007). The same may also apply to other chondrite groups containing refractory objects within them. Krot et al.'s (2001) analyses of pyroxenes in Al-rich chondrules also showed the presence of enstatite. Pigeonite, forsterite and enstatite minerals have been noted as characteristic of Al-rich chondrules by Brearley and Jones (1998). Plagioclase-Olivine Inclusions (POIs) can also be found that have some similar characteristics to Al-rich chondrules. They have mineral assemblages that are dominated by plagioclase and olivine with distinctive FeO poor pyroxenes that range from

Al-rich enstatite, pigeonite and diopside (Brearley and Jones, 1998). Thus the complete mineralogy of T.2 track #154 is similar to refractory formations found in chondrules but vitally lacking any feldspathic material or spinel, and inconsistent overall mineral assemblages.

Mineralogical assemblages that have some limited similarities to that of T.2 track #154 are Wark Lovering Rims (Wark and Lovering, 1977). They contain layer/ bands or ribbons at the rims of some CAIs and were first discovered in Allende (CV3). They described 5 - 10 μm wide layers of Al-diopside, progressively decreasing in Al and Ti and with a corresponding increase in Mg and Si (Wark and Lovering, 1977). However, they generally have higher amounts of FeO (e.g. 2.6 wt% oxide) compared to T.2 track #154. Forsterite rims can be found surrounding different types of CAIs (types A and B) and especially in the Allende CV group. In reduced CV chondrites, they contain coarse-grained (20–40 mm), anhedral forsterite ($Fa_{1–8}$ versus $Fa_{5–50}$ in the more oxidized Allende meteorite), Fe,Ni-metal nodules, and fine-grained refractory components composed of aluminum-diopside, anorthite, spinel, and in some cases, forsterite (Scott and Krot, 2007).

6.4.3.3 IDPs

Ca-Al rich inclusions in IDPs are typically found less frequently than in carbonaceous chondrites. There are, however, several studies of IDPs containing Al-diopside and faissite. Tomeoka and Buseck (1984) described an IDP with carbonaceous chondrite affinities. *Skywalker* IDP contained refractory pyroxene associated with phyllosilicate. This hydrated IDP contained a diopside grain with a TiO_2 content of 0.6 wt% and Al_2O_3 14.5 wt%. Zolensky et al's (1994) study of a suite of chondritic IDPs identified diopside in 40% of hydrous IDPs (27 IDPs analysed in this study). A single grain of diopside was found in the anhydrous type. They suggested that the presence of diopside indicated slower cooling mechanisms that were probably associated with formation on a parent body rather than nebula condensation. His study, however, dealing with the pure diopside composition contains no record of Al and Ti contents. Non-stoichiometric Mg-wollastonite was studied in a rare IDP by Reitmeijer (1999). The non stoichiometric pyroxenes contained excess Si and were thought to represent metastable Ca-

rich pyroxenes that were possibly altered by space weathering. The Al-rich pyroxenes had high Ti contents (~ 3-4 wt% TiO_2) compared with T.2 track #154.

Ca-Al rich Chondrules/Inclusions in Ordinary Chondrites

CAI in CV3, CR3, CO3 Chondrites

(a)

SiO₂ — CaO+Al₂O₃ — MgO ternary diagram legend:

- T.2 track #154
- CH/CR CAI
- CH CAI
- Allende CAI
- Inti
- Skywalker IDP
- Average T.2 track #154
- CH/CR Al-Chondrule
- CH Chondrule
- CR AOA
- Bulk Al-Diopside Chondrules CH/CR
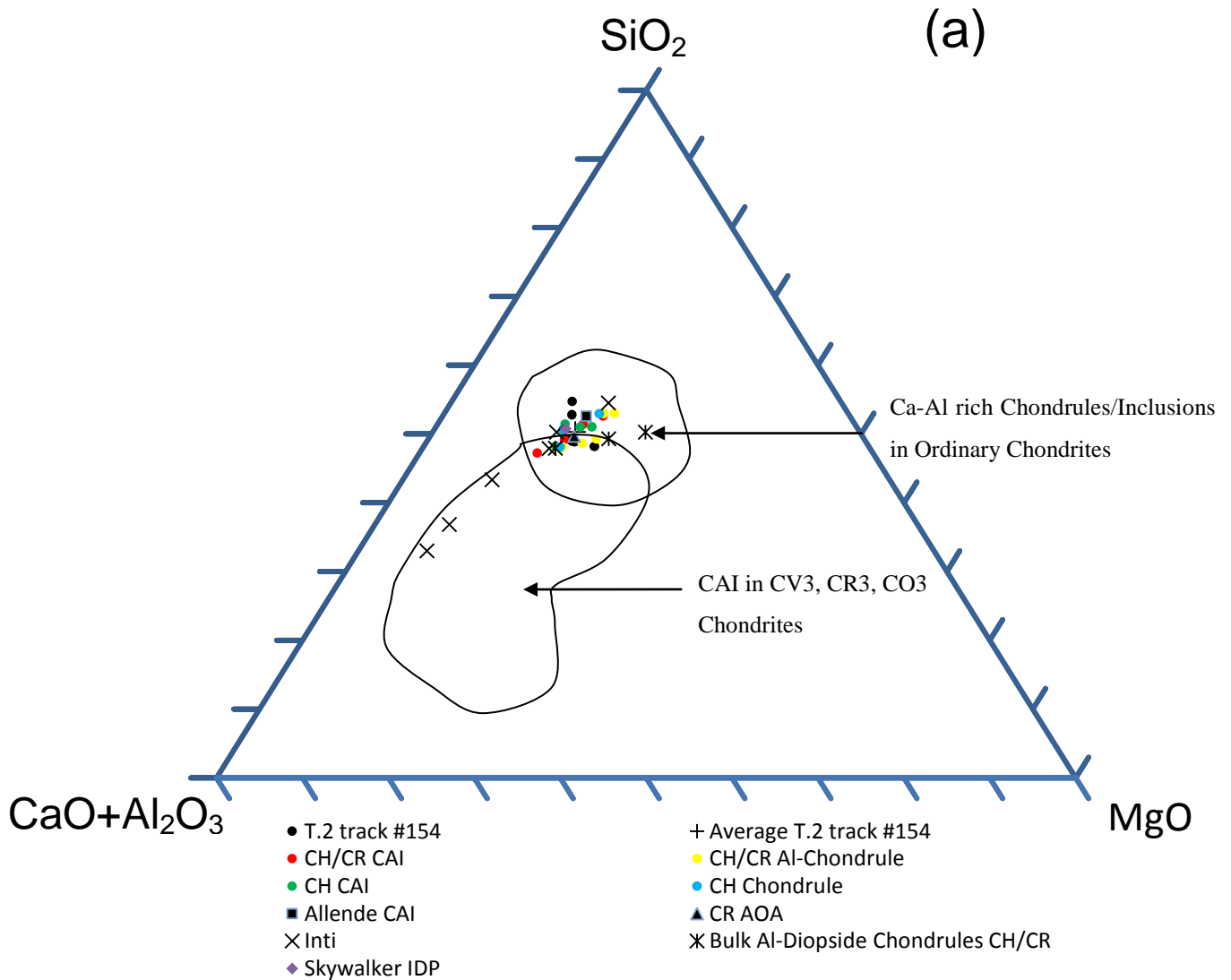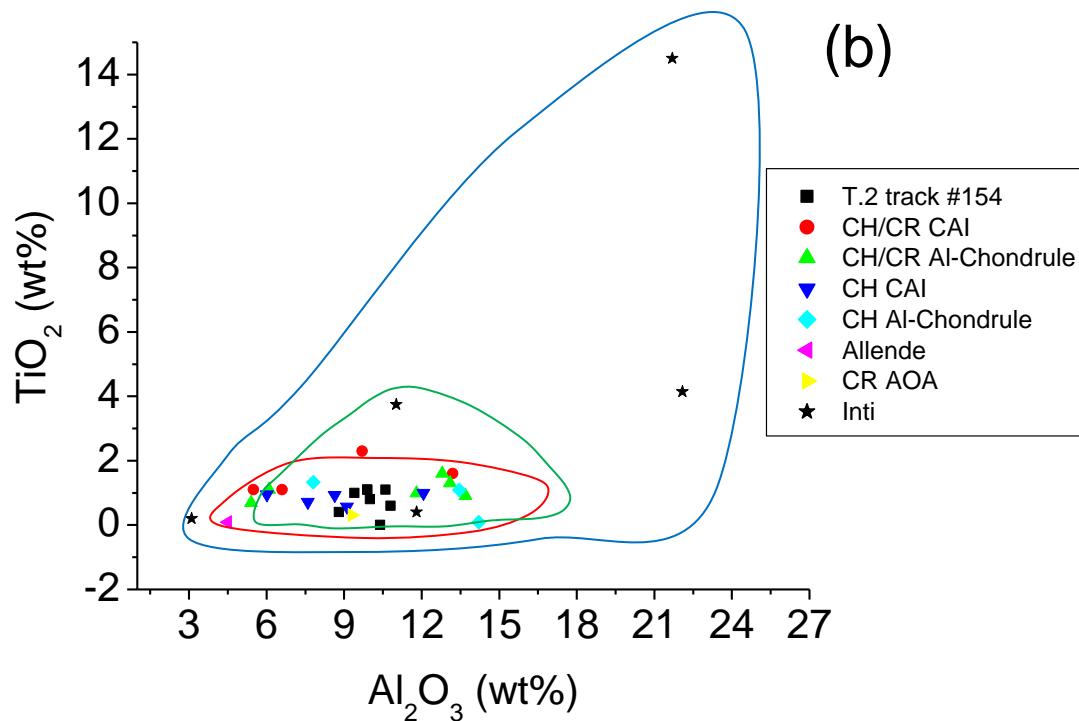
FIG 6.18: (a) Bulk composition fields of CAIs in C3 chondrites and Ca-Al rich chondrules and inclusions from ordinary chondrites from Bischoff and Keil (1983). Representative Ca-Al rich pyroxenes from various chondrites and IDPs are included in both fields, with the AEM analyses of Al-diopside in T.2 track #154. Its composition lies in both fields but at high end SiO_2 for CAIs in C3 carbonaceous chondrites. Representative pyroxenes from refractory chondrules and CAIs are given. Pyroxenes chosen had ~1 wt% TiO_2 and trace FeO. (b) Al_2O_3 contents against TiO_2 of T2 track #154 compared to representative pyroxenes from Fig 6.15a. Roughly equal TiO_2 contents at ~1 wt% have variable Al_2O_3 contents from approximately 4 – 14 wt%. Composition fields for pyroxenes in Al-chondrules and CAIs are from Krot et al. (2001) RED field = Al-diopside rich chondrules, BLUE field = Pyroxene-spinel assemblage pyroxene, GREEN field = Hibonite rich CAI. CH/CR CAI and CH/CR Al-Chondrules from Krot et al. (2001); CH CAI and CH Al-Chondrules from Zhang et al. (2009); Allende from Krot et al. (2007); CR AOA from Krot et al. (2004); Inti from Simon et al. (2008) and Chi et al. (2009); Bulk Al-Diopside Chondrules CH/CR from Krot et al. (2001); Skywalker IDP from Tomeoka and Buseck (1985).

We see from Fig 6.18a that Ca-Al rich pyroxenes from many different types of chondrites contain similar compositions when plotted in the ternary diagram Al+Ca – MgO – SiO_2. They cross both fields for the bulk compositions of CAIs and Al-rich inclusions from both ordinary and carbonaceous chondrites. Fig 6.18b shows the TiO_2 contents against Al_2O_3 for those pyroxenes plotted in 6.18a. Low abundances of TiO_2 correlate with variable

Al_2O_3 contents from 8-14 wt% oxide. Thus, the T.2 track #154 Al-diopside is similar to pyroxenes found in refractory objects from different chondrite classes. Some pyroxene analyses of from *Inti* are consistent with T.2 track #154 but most are more Ti and Al rich and Si poor, that is most consistently found in Al-diopside and faissites in CAIs.

6.4.3.4 Trace elements in T.2 track #154 Clinopyroxene

We see that the Al-diopside in T.2 track #154 (Table 6.4) contains trace amounts of Fe, Co and occasionally V. Pyroxene analyses from the literature used in Fig 6.15 ahow that low FeO abundances can be found in proxenes from different refractory objects. Titanium-bearing pyroxenes have been found to also contain trace/minor amount of V (e.g. Simon et al., 2007). However, the identified presence of trace Co in the Al-diopside T.2 track #154 is however very anomalous. Mafic rocks on Earth can contain up to 10s of p.p.m concentration of Co (e.g. Carr and Turekian, 1961). There is no record of Co recorded in extraterrestrial silicates in abundances to that found in this study. Note that Co was also found in some of the other trace minerals in the grain. More specifically, trace amounts of Fe and Co are only found within the forsterite and pigeonite phases in the linked forsterite-pigeonite assemblage (Fig 6.6). The abundance of Co in of any extraterrestrial pyroxene material is so rare that some type of unexplained detector analytical artefact should not be currently entirely ruled out.

6.4.5 Implications for the origins of T.2 track #154 and Comet Wild2/81P

Previous studies of *Stardust* grains from Comet Wild2 have identified refractory minerals assemblages similar to those found in chondrites and IDPs, demonstrating a mineralogical relationship with Comet Wild2. T.2 track #154 reinforces this claim. But how did T.2 track #154 and its bulk terminal grain form? Due to its mineralogical link with refractory objects from inner Solar System materials, the cometary grain consisting of T.2 track #154 could be fragments from inner solar system materials that contain these minerals. This puzzle is highlighted by the fact that chronological information is still lacking from most *Stardust* samples to compare with chondritic materials. However, terminal particle 'Coki' has be shown to contain an [26]Al abundance that is heavily depleted or even lacking compared to the oldest CAIs, indicating that this anorthite grain is not as

'pristine' or old as the earliest refractory objects (Matzel et al. 2010). If other Al-rich phases have a similar chronology, then they might be associated with crystallisation ages around the formation time of chondrules, suggesting a genetic link with chondritic materials after CAI formation. However, the Al-Mg ratio of the T2 sample from track #154 is too low for such analyses, which are normally performed on anorthite.

We have seen from Section 6.4.3 that the major element composition of the Al-diopside in T.2 #154 crosses the projections of both CAI bulk compositions in C3 chondrites and that of Ca-Al rich inclusions from ordinary chondrites. Pyroxenes from Ca-Al rich chondrules in carbonaceous chondrite are also at the SiO_2 rich end of the C3 projection. Representative Al-diopsides and Ca-Al rich pyroxenes from different classes of carbonaceous chondrites are consistent with the composition of T.2 #154 and lie in the bulk composition fields for CAIs and Al-rich chondrules for both carbonaceous and ordinary chondrites. Currently, it is not clear which type of refractory objects and chondrites have the highest abundance of Al-diopside having the same composition as the T.2 track #154 diopside. A quantitative mineralogical study has not been performed, but based on a statistical assumption; it is likely that this Al-diopside composition would be most widely recognised in CV chondrites where 50% of all CAIs have been found (Hutchison, 2004). In general, however, T.2 track #154 has a low Ti and Al content compared with aluminium diopside in CAIs, a composition field that is more constrained for Al-rich chondrules. Fig 6.15b shows that CAIs can contain approximately up to 10 wt% TiO_2 higher amounts of Ti compared to T.2 track #154 (Bridges and Changela, 2010).

The other trace phases that are petrologically linked to the Al-diopside could be explained by cooling at the rims of the grains from a liquid or possibly melting upon some type of shock event (Desch and Connolly, 2002). If shock could have played a role, further evidence for this could be found in the form of microstructural deformation at the rim of the diopside grain such as twin lamellae and slip planes (e.g. Ashworth, 1980). What seems to be a mottling at the joins of the Al-diopside and forsterite (e.g. Figs 6.5a and 6.8a) could be evidence of mosaicism (Leroux, 2001) although there is no conclusive evidence for this.

Track #154 contains 5 other terminal particles. Thus, the bulk composition of this entire fragment that was released from near the surface of Comet Wild2 has not yet been

determined. It is not clear whether T.2 track #154 was a larger grain that fragmented to make the other terminal particles or if some unknown 'binding' mechanisms held individual *Stardust* terminal particles together before producing a track in aerogel. These questions need to be addressed in order to determine any genetic links between refractory objects in chondrites, IDPs and Comet Wild2 *Stardust* particles. Mineralogically, T.2 track #154 most closely resembles the mineralogy of Al-rich chondrules but lacks any anorthite or spinel to fully constrain this mineralogical link to them, unless it is found in one of the other terminal particles. T.2 track #154's igneous petrology is not typical of the spinel-feldspar-pyroxene assemblages found in CAIs, AOAs and Stardust refractories such as 'Inti' from track #35. The formation of Al-diopside would have required high crystallisation temperatures that might have formed at much shorter heliocentric distances from a proto-Sun compared to the Kuiper Belt (Shu et al., 2001). Minerals with formation temperatures between the crystallisation temperatures of CAI-like assemblages (e.g. 'Inti' from Simon et al., 2007; Chi et al., 2009) and ferromagnesian chondrule-like igneous textures (e.g. 'Tajiaro' from Nakamura et al., 2008) would, most probably, have been required for the formation of T.2. track #154. Different chondrite groups have mineralogical affinities to T.2 track #154. For example, we see that CH, CV, and CR chondrites contain these mineralogical affinities. T.2 track #154's composition, however, may be unique to all other diopside components from *Stardust* and similar planetary mateirialsin potentially containing trace amounts of Co in its minerals.

6.4.4 Conclusions

A study of 6 microtomed sections of T.2 track #154 shows it to represent an approximately 7 x 3 μm grain that is almost completely dominated by an Al diopside $(Ca,Mg,Al,Ti)(Si,Al)SiO_3$, with trace Fe and occasional V. Unusually, Co may also be present but this remains to be firmly established. T2, track #154 is also an unusually large terminal grain from the current *Stardust* inventory.

T.2 track #154 is a refractory grain that has a similar mineralogy to pyroxene components of refractory inclusions and Al-rich chondrules in carbonaceous chondrites. It most closely resembles the mineralogy seen in Al-rich chondrules but lacks the characteristic feldspathic or spinel phases.

This study indicates that as well as other refractory minerals identified from previous studies, the coma of Comet Wild2 also contains large refractory pyroxene grains. This demonstrates the range of high temperature minerals that are associated with Comet Wild2. The Al-rich pyroxene probably formed at temperatures in between those of CAIs and ferromagnesian chondrules.

Chapter 7
Final Discussion & Conclusions

Here the key results of this thesis are discussed with suggestions for future work.

7.1 Advances in FIB-TEM and X-ray Spectroscopy of Planetary Materials

The results from Chapters 4 and 5 demonstrate how the FIB-SEM to TEM technique applied to different planetary materials can enhance the capabilities of *in situ* micron to submicron characterisation. A method has been derived for extracting soft silicate gels, phyllosilicates and other low temperature phases enclosed within harder framework silicates. The use of the FIB technique on soft materials requires the adaption of pre-existing methods employed with FIB extraction. We have distinguished between phases in the nakhlite veins through both chemical (EDX, WDS) and by structural information. For instance, phyllosilicates of the same chemical composition as the gel that co-exist with the gel along vein margins in Lafayette as crystalline but the gel is clearly not. However, one cannot know with complete certainty whether the extracted 'gel' was initially completely amorphous or not, and experimentation involving measured irradiation of gallium ions on similar phases could address this question. Another way could be the use of microtomed sections, if methods were found to select regions of the gel *in situ* for such methods.

A 200 nm grain of partially oxidised iron around a *Stardust* terminal grain that was extracted and analysed by TEM (Chapter 5) was also found to be amorphous. This study has shown that the FIB technique can be applied to *Stardust* samples, but a sample was chosen for extraction with no loss of other materials during FIB extraction. The use of this method in track #121 was ultimately justified by the existence of grains on the gold foil substrate away from the bulk terminal grain

The FIB-SEM technique has also been developed to extract parts of individual grains from powder standards for synchrotron-based microfocus spectroscopy and standards analyses. This approach may be useful for samples limited in size that cannot be

used by conventional sampling methods or which require particular micron-sized regions from larger domains for study. Problems encountered with conventional samples such as diluted powders may be overcome by eliminating grain size and thickness heterogeneities, but more testing is required under beamlines with appropriate standards, such as the NHM standards used for diluted boron nitride pellets. As well as the important capability of *in situ* synchrotron analysis, the same samples could also be transferred to other instruments such as the SEM and TEM for further characterisation.

In Chapter 2, a method was described that determined the experimental *K*-factors for the Jeol 2100 for AEM. Although this calibration method was proved to be successful on the Barwell and Frontier Mountain secondary standards, no secondary standard containing Al as a major element was available for testing to. Also, the dedicated standards that were used for calibration were selected in this study and not typical calibration standards, although proved to be effective for Fe, Mg and Ca. It is suggested that pure end member silicates, such as pure forsterite/enstatite, fayalite/ferrisilite, wollastonite etc and if available in synthetic or natural form may be more ideal for the experimental *K*-factor determination when performing AEM on silicates. This will allow individual elements to be calibrated one by one and then tested using similar standards and procedures that were used here. Also no calibration was made for Ti measurements described in Chapter 6. However, it is suggested that the very minor abundance of Ti in relation to relative errors would not have had an effect on the interpretation of the results obtained in Chapter 6, and thus the default *K*-factors sufficed. The calibration and testing methods used in this research, however, may provide a useful tool for experimental *K*-factor determination without a universal chemical ultra thin standard.

The elemental distribution of *Stardust* particles in the entrances of track numbers 41, 134 and 162 has been obtained. At *Diamond's* Beamline I18 XRF mapping has provided elemental distributions and identified hotspots for fingerprinting the mineralogy of these regions by XANES. The comparative use of XANES against standards has also been extended with EXAFS on the same *Stardust* tracks. These are the first reported EXAFS experiments performed on *Stardust* samples (and potentially any extraterrestrial materials) and have provided a quantitative approach for the identification of different mineral types. The mixing of phases within a large beam size of several microns in

Stardust samples can complicate mineral identification and the ability to establish chemical co-ordination environments. Pure mineral phases in terminal regions would be ideal for this.

7.2 Secondary Assemblages in the Nakhlites

This comprehensive micron-submicron mineralogical, compositional and morphological study has led to important new findings. What has been described as 'iddingsite', the fracture-based secondary assemblages common to all of the nakhlites has been more fully characterised. The core of every vein is an amorphous hydrated Fe-silicate - a 'gel.' The composition of this gel fractionates, being higher in Mg/Mg+Fe going down the depth profile of the nakhlites. This study has shown that the loose term 'iddingsite' used by some previous workers is in fact a mixture of the gel, phyllosilicate, salts/carbonates and iron oxides, most abundant and clearly seen in the Lafayette meteorite. Texturally, TEM and SEM images show that previously identified Fe-carbonate formed at the margins of the veins and have been replaced by phyllosilicate. This in turn leads to a complex intermix of fine grained silicates and iron oxides terminated by the amorphous gel at the cores of the veins. Zones of other alteration phases can be distinguished, such as Partially Broken Down Olivine PBO (in Yamato000593/749), Siderite (Nakhla and GV) and Siderite-Phyllosilicate (Lafayette). The gel is the ubiquitous alteration phase that is found in each of the olivine-bearing nakhlites.

Based on the compositional fractionation trend of the gel and the suggested ordering of the phases based on textures, a hypothesis has been made to describe the formation conditions of these assemblages on Mars. It is suggested that an impact heating event generated sawtooth fractures and a hydrothermal fluid flowed through the fractures from the lowest depths to the shallowest ones, progressively fractionating in Mg#. However, the trends that have been identified in this study need to be compared to the three other nakhlites not analysed in this study. Chemical analyses of the gel could be extended to more samples of veins and more thin sections the see if this compositional distinction in the gel holds true for them within the same samples.

Although terrestrial analogues of the nakhlite petrologies have been studied by others (e.g. Theo's flow Canada), there are none reported for the nakhlites' secondary

alteration assemblages. Localities on Earth with evidence of localised hydrothermal deposits in shock induced fractures should be investigated to establish an accurate analogue.

7.3 Capture Heating and the Composition of Comet Wild2

Synchrotron-based microfocus X-ray spectroscopy (XRF, XANES and EXAFS) have shown that Comet Wild2 contains a diverse range of Fe oxides – ranging from mixtures of ferric oxides (possibly magnetite, hematite and goethite mixtures), V-rich chromite (Fe-Cr-V-Ti-Mn oxide), Fe-Ti oxide, suggested partially oxidised Fe-Ni metal and Fe-silicate. The ubiquitous identification of ferric oxides in the *Stardust* samples is striking and atypical of the majority of analyses hat have been performed on terminal particles. The identification of these phases close to track entrances suggests that capture heating in the aerogel has led to oxidation of some phases. It is, however, still not clear where the oxygen would have originated for this oxidation, unless ferric iron was in fact generally concentrated at the track entrances and/or terrestrial oxidation has occurred on the *Stardust* particles. Regardless of these ideas, current models trying to understand the Fe oxidation state of Comet Wild2 need to take these results into account. If terminal particles alone are chosen to determine the Fe-oxidation state of Comet Wild2, this could lead to misleading conclusions if ferric cometary components are found predominantly at track entrances. Conversely, if a complete track is used to determine the Fe oxidation state of Comet Wild2 then corrections for oxidation along the tracks should be made. Bulk track Fe-oxidation state information should be determined for the analysis of complete tracks by these methods, e.g. pixel by pixel XANES mapping as well as XRF mapping. This study concentrated on selected hotspots from tracks. Analogues could also be considered i.e. light gas gun studies of individual ferran minerals or synthesised polyminerals fired into flight class aerogel to test these observations for any subsequent melting and oxidation to form Fe-oxides.

A detailed TEM study of a terminal particle has provided detailed mineralogical and morphological characterisation of a grain from the coma of Comet Wild2. T.2 track #154 is a $\sim$ 7 x 3 µm grain of Al diopside, average composition $(Ca_{0.88},Mg_{0.88},Al,Ti)(Si,Al)SiO_3$, with trace Fe and Co. It coexists with trace/minor amounts of Fo_{98-99} and pigeonite and

probably also enstatite with trace Al in and around the margins of the grain. This refractory grain is an unusually large grain of Al-diopside compared to other diopside phases that have been found and characterised before. Its observable trace Co content is also unique to all known silicates in *Stardust* as well as all planetary material silicates. It has a similar mineralogy to pyroxene components found in refractory objects in chondrites. Considering the thermometry of a Al-diopside assemblage with Al-pigeonite and forsterite, this study indicates that as well as other refractory minerals identified from previous studies, the coma of Comet Wild2 also consists of an 'intermediate' refractory that individually would have formed at temperatures less than those found in 'inti' (CAI-like) and greater than the other ferromagnesian chondrite assemblages. A study of other refractory mineral phases in other track #154 grains might help understand the origin of T.2 in track #154.

This study has reinforced the claim that Comet Wild2 contains a very diverse range of unequilibrated assemblages. The theory that comets are preserved remnants of the earliest record of the Solar System history holds true, but in unexpected ways. Rather than being 'primitive' with the composition of the Sun (CI-like for non gaseous elements), or abundant in the phases that were brought in to the solar nebula by the ISM, and containing evidence of aqueous alteration, typically found in primitive materials, Comet Wild2, instead, seems to consist of a mineralogy genetically linked with the inner Solar System, containing minerals that were amongst the first to crystallise prior to chondrule formation and also chondrule-like assemblages as well.

The main question that needs to be addressed is how these minerals that are also found in chondrites as inclusions predating chondrules and refractory chondrules themselves are found in comet-forming regions? Brownlee et al's (2003) paper about the *Stardust* Mission prior to the return of cometary samples addressed the key scientific questions about comets that were to be adddressed. Amongst them was the question regarding CAIs and chondrules, "Were any of fragments of them found? Any pryroxene aggregates found?" (Brownlee et al., 2003). T.2 track #154 is a pyroxene-rich assemblage. Its Al-diopside with trace/minor Al-pigeonite-forsterite assemblage most closely resembles components of Al-rich chondrules but lacking any feldspar or spinel. Several studies of *Stardust* samples have have found aggregates similar to chondrules e.g. 'Tojario' - Nakamura et al. (2008) and 'Iris' - Butterworth et al. (2010). Terminal particle 'Inti' has

mineralogical affinities to CAIs. Both studies of 'Inti' and 'Iris' show that Comet Wild2 contains micro equivalents of type II chondrites and CAIs. Thus, Comet Wild2 seems to have a diverse range of chondritic components and T.2 track #154 could add to this in the form of Al-rich chondrule components. These observations tie towards a violent mixing and transport process of dust from the inner solar system, where chondrites formed, to distances orders of magnitude further away from the primordial Sun in comet forming regions such as the Kuiper belt which is where Comet Wild2 is thought to have originated. However, there remain uncertainties that still lie around the above claim that chondritic fragments were exclusively the direct source of the dust aggregates found in Comet Wild2. Could *Stardust* grains such as T.2 track #154 represent the dust components that accreted to melt and form chondrules themselves? If, in future studies, they are found more often in *Stardust*, should we consider that they may have played a more important role in chondrule formation and early solar system evolution?

Oxygen isotopes by ion probe studies could be measured to further constrain any affinities T.2 track #154 has to particular refractory objects and/or chondrite groups. Further TEM-based microstructural studies could be aimed towards investigating capture related and/or nebula based shock events in the inner solar system.

In analytical terms, many lessons have been learnt that can be applied to other samples of the same grain that have yet to be analysed. First is the analytical challenge of *Stardust* particles. Pre-existing authors reporting TEM analyses of *Stardust* samples have described various methods for reducing sample damage. However, detailed descriptions of operating conditions for minimal sample damage on *Stardust* samples are lacking. Low dosage TEM seems vital for *Stardust* analyses, due to the substantial alteration of material. Ideally unaltered material is desirable to obtain chemical and crystallographical information. Low dosage TEMs used for biological samples could help towards this, i.e. stage controls that automatically 'search' under low dosage conditions, and move away from the sample after acquiring images, although this can be performed manually in conventional TEMs. Detailed guidelines describing optimal analytical conditions for the different TEMs that are used by the *Stardust* team, ideally tried and investigated on flight aerogel based analogue samples, should be published.

APPENDIX A: TEM and AEM CALIBRATION

TABLE 2.1: *Camera constants for evaporated Al_2O_3 at different camera lengths in the Jeol 2100 TEM.*

Camera Length	Diffraction order	d-spacing	Lλ
(cm)	N	(nm)	(nm pix)
10	3	0.234	26.196
10	4	0.202	26.622
10	8	0.143	28.876
Average Lλ			27.749
15	3	0.234	38.333
15	4	0.202	38.373
15	8	0.143	38.482
Average Lλ			38.396
20	3	0.234	50.365
20	4	0.202	50.144
20	8	0.143	50.178
Average Lλ			50.229

TABLE 2.2: *AEM composition of San Carlos Olivine*

Wt%	Representative	Average (N = 5)
MgO	47.6	49.1
FeO	9.2	9.1
SiO_2	41.9	40.9
Cl	0.5	0.3
NiO	0.8	0.6
Total	100	100
At%		
Mg	24.9	25.6
Fe	2.7	2.7
Si	14.7	14.3
Cl	0.1	0.2
Ni	0.5	0.3
O	57.1	57
Total	100	100
Mg#	**90**	**91**

TABLE 2.3: *Average SEM-EDX and TEM-EDX composition of Frontier Mountain Enstatite*

Wt%	SEM-EDX		AEM	
	Representative	Average (N = 6)	Representative	Average (N = 4)
MgO	30.2	30.4	30.5	30.1
FeO	12.1	12	12.7	13
SiO$_2$	56.1	56	56.2	56.3
MnO	0.5	-	0.3	0.3
Cr2O3	-	-	0.2	0.2
Total	98.7	98.4	100	100
At %				
Mg	16.2	16.3	16.1	15.9
Fe	3.6	3.6	3.8	3.9
Si	20.1	20.1	20	20
O	60.1	60.1	60	60
Mn	0.2	-	0.1	0.1
Cr	-	-	0.1	0.1
Total	100	100	100	100
O/Si	**3**	**3**	**3**	**3**
(Mg+Fe)/Si	**1**	**1**	**1**	**1**
En	**82**	**82**	**81**	**80**

TABLE. 2.4: *Diopside composition by SEM-EDX and TEM-EDX composition prior to and after Ca k-factor calibration.*

	SEM-EDX	**TEM-EDX**	**AEM**
	Average	Before	After
Wt%	(N = 3)	(N = 1)	(N = 1)
MgO	17.5	17.3	17.2
FeO	3.2	3.5	3.5
SiO_2	54.3	55.9	55.5
CaO	21.8	21.3	22.2
Al_2O_3	1.0	1.2	1.0
Cr_2O_3	0.7	0.7	0.7
Total	98.4	100.0	100.0
At %			
Mg	9.6	9.4	9.3
Fe	1.0	1.1	2.7
Si	20.0	20.3	20.2
Ca	8.6	8.3	8.6
Cr	0.2	0.2	0.2
Al	0.4	0.5	0.4
O	60.2	60.3	60.2
Total	100.0	100.0	100.0
O/Si	3.01	2.98	2.99
Wo #	44.00	44.00	44.00

TABLE. 2.5: *Kyanite composition by SEM-EDX and TEM-EDX composition prior to and after Al K-factor calibration.*

Wt%	SEM - EDX		TEM - EDX		AEM	
	Representative	Average (N = 4)	Representative	Average (N = 3)	Representative	Average (N = 3)
Al$_2$O$_3$	63.4	63.7	68.2	68.4	63.2	63.3
SiO$_2$	32.3	36.8	31.8	31.6	36.8	36.7
Total	95.7	100.5	100.0	100	100	100
At %						
Al	25.3	25.2	27.2	27.2	25.1	25.2
Si	12.3	12.4	10.7	10.7	12.4	12.4
O	62.3	62.5	62.1	62.1	62.5	62.5
Total	99.9	100.1	100.0	100.0	100.0	100.1
O/Si	5.1	5.0	5.8	5.8	5.0	5.0
Al/Si	2.1	2.0	2.5	2.5	2.0	2.0

TABLE. 2.6: AEM and WDS compositions of secondary standard - Barwell ordinary chondrite pyroxene

Wt%	WDS Representative	Average (N = 7)	AEM Representative	Average (N = 7)
MgO	16.9	16.7	15.7	15.7
FeO	4.7	4.9	4.8	4.9
SiO_2	53.4	53.2	55.5	55.8
CaO	21.9	22.1	22.0	21.7
Al_2O_3	0.8	0.5	0.3	0.2
Cr_2O_3	0.8	0.8	0.9	0.9
TiO_2	0.8	0.7	0.7	0.6
MnO	0.2	0.2	0.1	0.2
Na_2O	0.6	0.6	–	–
Total	100.1	99.7	100.0	100.0
At %				
Mg	9.2	9.1	8.6	8.6
Fe	1.4	1.6	1.5	1.5
Si	19.5	19.5	20.4	20.4
Ca	8.6	8.7	8.7	8.5
Al	0.2	0.2	0.1	0.1
Cr	0.2	0.3	0.3	0.3
Ti	0.2	0.2	0.2	0.2
Mn	0.1	0.1	0.0	–
Na	0.4	0.4	–	–
O	59.9	59.9	60.4	60.4
Total	100.0	100.0	100.0	100.0
En	47.9	47.1	45.7	46.2
Wo	44.7	44.8	46.3	45.7
Fs	7.4	8.1	8	8.1

APPENDIX B: Standards for EM and XAFS

I. Primary Mineral Standards for Electron Microscopy

Barwell Olivine

Description: Equilibrated olivine from the Barwell L6 ordinary chondrite.

Sample: Polished thin section on glass slide. FIB-TEM wafer

Composition: $(Mg_{0.75}Fe_{0.25})_2SiO_4$

Purpose: Fe and Mg *K*-factor calibration (Chapter 2).

Natural Diopside

Description: Mineral Standard provided by Dept. Geology UoL.

Sample: Polished resin block. FIB-TEM wafer

Composition: $(Mg_{0.5}Ca_{0.45}Fe_{0.05})SiO_3$ (Table. 5 APPENDX A)

Purpose: Ca *K*-factor calibration (Chapter 2).

Kyanite

Description: Mineral Standard provided by Dept. Geology UoL.

Sample: Polished resin block. FIB-TEM wafer

Composition: Al_2SiO_5 (Table. 6 APPENDX A)

Purpose: Al *K*-factor calibration (Chapter 2).

Nontronite

Description: Nontronite clay standard (Urgeirica Beira Alta, Portugal-MB 1972, 142) provided by NHM.

Sample: Chips of sample flaked on a carbon sticky mounted on Al stub. FIB-TEM wafer.

Composition: Unknown

Purpose: Lattice fringe spacing control for 2:1 phyllosilicate (Chapter 4).

II. Secondary Mineral Standards & Controls for Electron Microscopy

San Carlos Olivine

Description: Terrestrial olivine standard from New Mexico.

Sample: Chips that have been mounted and polished in a resin block. FIB-TEM wafer.

Composition: $(Mg_{0.91}Fe_{0.09}Ni_{0.003})_2SiO_4$ (Kohlstedt and Mackwell, 1987)

Purpose : Testing of Mg and Fe *K*-factors (Chapter 2)

Frontier Mountain Enstatite

Description: Enstatite found in L4-5 Frontier Mountain ordinary chondrite.

Sample: Polished thin section on glass slide. FIB-TEM wafer.

Composition: $(Mg_{0.82}Fe_{0.18})SiO_3$ (Table.3 APPENDIX A)

Purpose: Testing of Mg and Fe *K*-factors (Chapter 2)

Barwell Pyroxene

Description: Ca- rich equilibrated pyroxene found in L6 Barwell ordinary chondrite

Sample: Polished thin section on glass slide. FIB-TEM wafer.

Composition: $(Mg_{0.47}Ca_{0.45},Fe_{0.08})SiO_3$ (Table 6 APPENDIX A)

Purpose: Testing of Mg, Fe, Ca *K*-factors (Chapter 2)

Yamato000593 Symplectites

Description: Exsolution found in olivine grains of the nakhlites

Sample: Polished thin section on glass slide of Y000593. FIB-TEM wafer.

Composition: Magnetite lamella in augite (Noguchi et al., 2003).

Purpose: Testing of magnetite extraction to assess the FIB extraction process of iron oxides in *Stardust* (Chapter 5).

III. XAFS Standards at Diamond Beamline I-18

Samples prepared as diluted powdered pellets, ground with mortar and pestle for 10 minutes. Diluted with boron nitrides with concentrations 5 mg sample to 95 mg boron nitride. Pellets fastened on *Kapton* tape and measured under transmission for XAFS.

Admire Olivine - Forsterite

Composition: $(Mg_{0.88}Fe_{0.12})_2SiO_4$

Magnetite

Formula: Fe_3O_4

Hematite

Formula: Fe_2O_3

Goethite

Formula: $FeO(OH)$

Pyrrhotite

Formela: $Fe_{(1-x)}S$
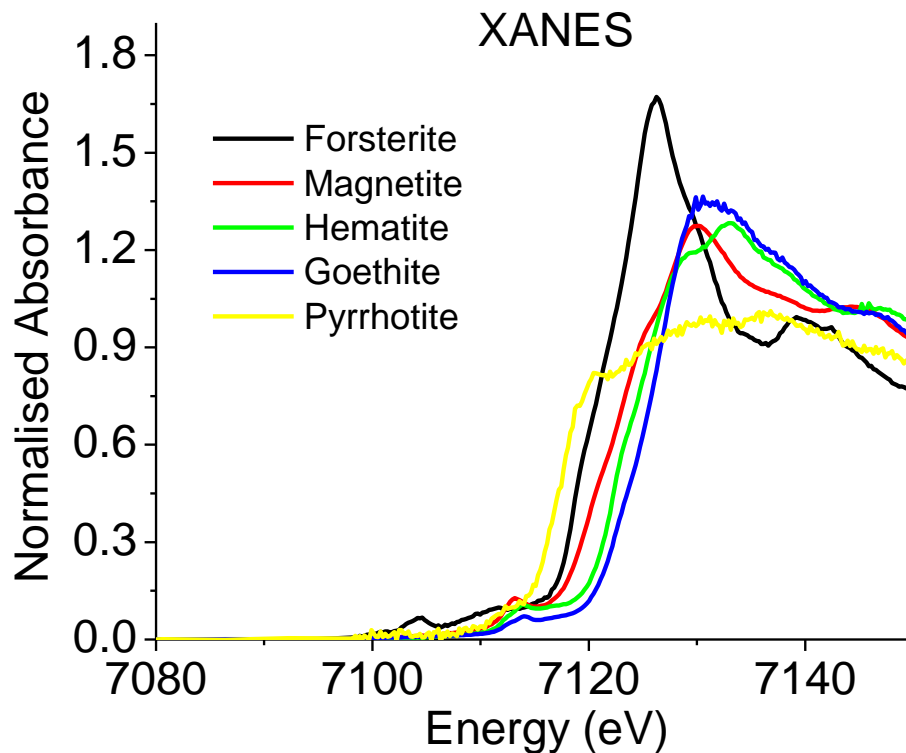
▲ NHM mineral standards by Fe-XANES.

EXAFS
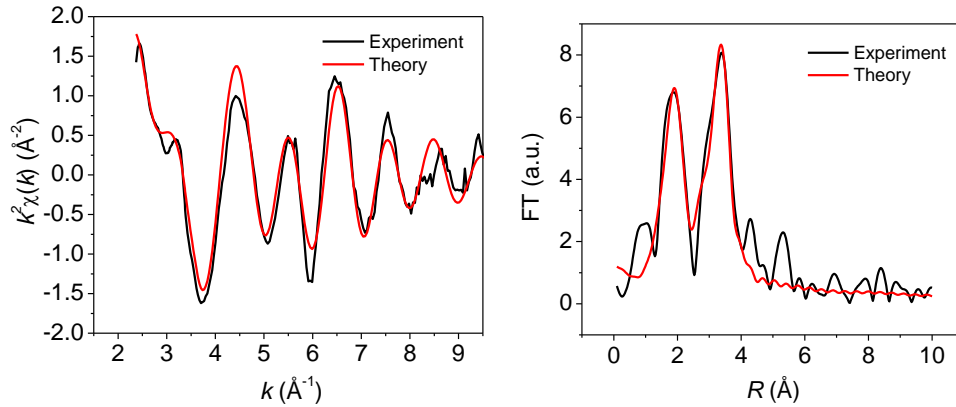
▲ Magnetite EXAFS. Fe-O = 2.03 Å $\pm$ 0.01 Å. Fe-Fe distances of 3.04 Å $\pm$ 0.01 Å and 3.49 Å $\pm$ 0.01 Å
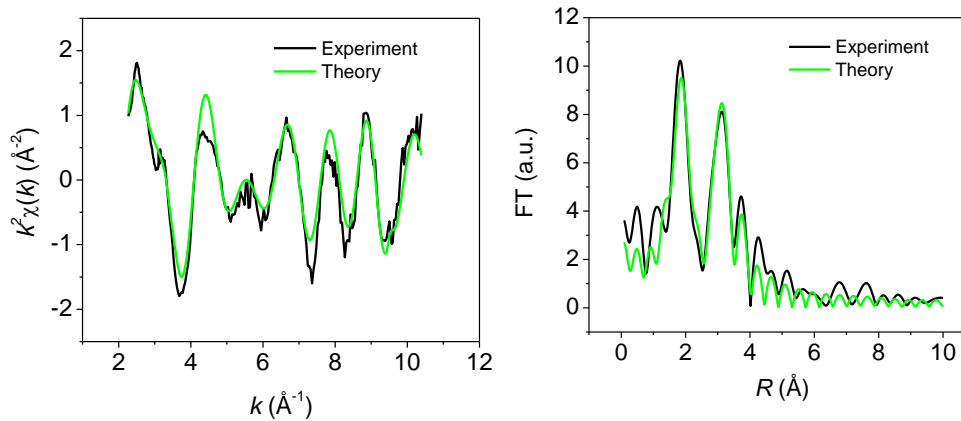
▲ Hematite EXAFS. Fe-O = 2.03 Å $\pm$ 0.02 Å. Fe-Fe distances of 3.00 Å $\pm$ 0.02 Å and 3.34 Å $\pm$ 0.01 Å
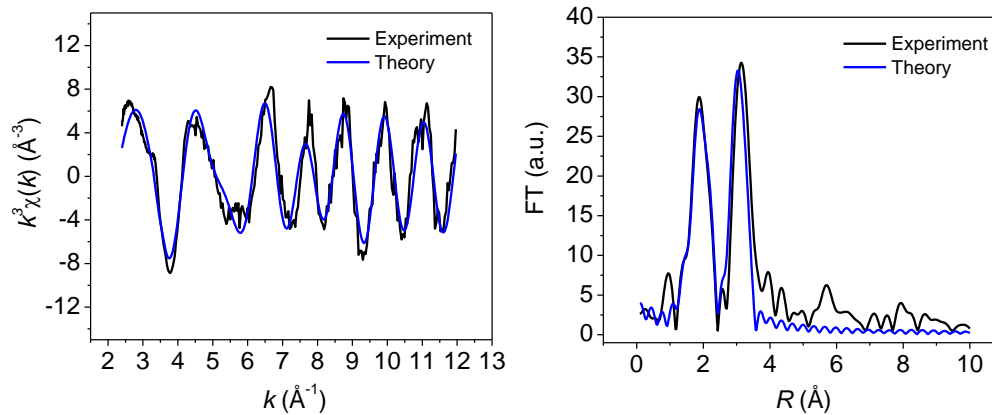
▲ Goethite EXAFS. Fe-O = 2.01 Å $\pm$ 0.01 Å. Fe-Fe = 3.03 Å $\pm$ 0.02 Å
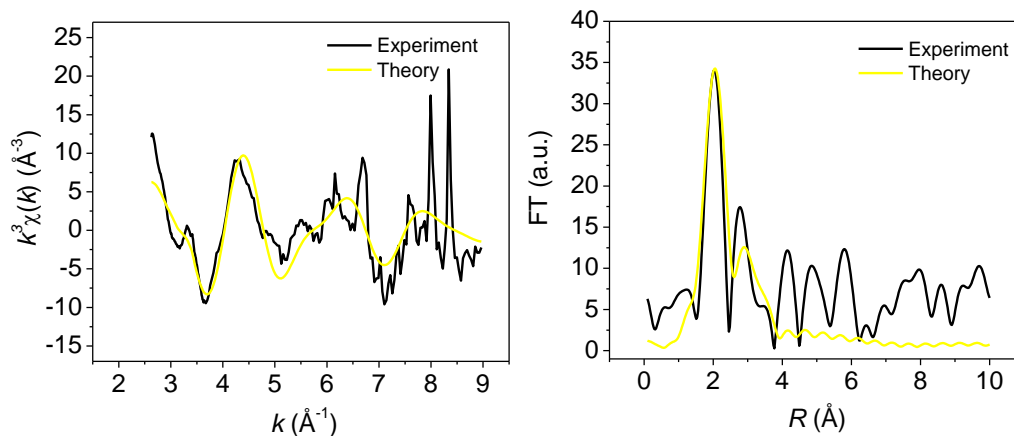
▲ Forsterite EXAFS. Fe-O = 2.09 Å $\pm$ 0.02 Å. Fe-Si = 3.24 Å $\pm$ 0.02 Å

Table 3.1: *Summary of bond distances calculated by EXAFS and compared with values from the Chemical Crystal Database (Fletcher et al., 1996).*

Mineral	1/2 Edge position (XANES) [eV]	1st Shell Distance (Fe-O) [Å]	CDS Database (ave Fe-O) [Å]	2nd Shell Distance(s) (Fe-Fe,Si,S) [Å]*	CDS Database (Fe-Fe,Si) [Å]
Magnetite	7121.31	2.03	2.03♠	(Fe-Fe) 3.04/3.49	2.96(14)/3.48(12)
Hematite	7122.60	1.98	2.03♣	(Fe-Fe) 2.99/3.34	2.96(3)/3.36(3)
Goethite	7124.11	2.02	2.04♥	(Fe-Fe) 3.04	
Olivine	7119.17	2.07	2.11♦	(Fe-Si) 3.27†	2.75(4)/3.26(4)
Pyrrhotite	7117.66	N.O.	N.O	N.O -	-

♠ Magnetite bond lengths from Bosi et al. (2009). Average Fe-O distance for a spit shell at 1.88 Å (4) and 2.06 Å (12).

♣ Hematite bond lengths from Paihe et al. (2008). Average Fe-O distance 1.94 Å (3) and 2.12 Å (3).

♥ Goethite bond lengths from Kaur et al. (2009). Average Fe-O distance 1.94 Å (3) and 2.12 Å (3).

♦ Olivine bond lengths from Yu et al. (1997). Mixed Fe-O shell from 2.07 – 2.21 Å, averaging 2.11 Å.

  * Fe – Fe shell best fits obtained with two shells, matching to two most dominant Fe – Fe co-ordinations from CDS database.

† Single Fe-Si shell for forsterite fitted averaging in the EXAFS for the split shell.

N.O. Pyrrhotite EXAFS was not obtainable.

APPENDIX C: SAD and HRTEM Measurements of the Nakhlites' Phyllosilicates

TABLE 4.1: *Lafayette Phyllosilicate d-spacings from polycrystalline diffraction*

Textural Setting	1st ring (Å)	2nd ring (Å)	3rd ring (Å)
Phyl. in olivine	2.60	1.55	1.31
Phyl. in mesostasis	2.47	1.57	1.36
Nontronite[*]	2.62	1.62	1.40

[*]Nontronite standard BM 1972, 142. Errors in diffraction measurements are ≤5 %

TABLE 4.2: *d-Spacing measurements of phyllosilicate basal fringes in Lafayette*

Textural Setting	d-Spacing (Å)[*]			
Veins in Olivine	0.79(10),	0.72(7),	0.91 (5)	
Rosettes	0.85(9),	0.85(9),	0.89(9),	0.9(6),
	0.93(7),	0.93(5),	1.06(6),	1.1(6)
Mesostasis	0.68(7),	0.67(7),	0.68(5),	1.1(4)

[*]d-spacings calculated from average no. of fringes, number in brackets.
Errors in diffraction measurements are ≤5% .

APPENDIX D: XANES Residual Fitting

I. MATLAB code for binary XANES fit (Hematite + Magnetite)

```
disp('-----------------------------------------------------');
clear all ;
data2 ;
mag = table(:,1) ;
goe = table(:,2) ;
hem = table(:,3) ;
plot(1:length(mag),mag) ;
plot(1:length(goe),goe) ;
plot(1:length(hem),hem) ;
%data = table(:,4) ;
data = table(:,5) ;
N = length(hem)
aa = linspace(0,1,101) ;
L = length(aa)
comparison = zeros(L,N) ;
for j = 1:L
   a = aa(j) ;
   for i = 1:N
     comparison(i,j) = (1-a)*hem(i) + a*mag(i) ;
   end
end
%x = comparison(:,1) - hem
average = zeros(L,1) ;
for j = 1:L
%difference = 0;
total = 0;
   for i = 1:N
      difference = abs(  ((data(i)) - comparison(i,j)));
      total = total + difference;
   end
average(j) = total/N;
end
figure(1) ;
clf ;
hold on ;
%plot(1:N,hem,'g') ;
%plot(1:N,mag,'y') ;
%plot(1:N,goe,'k') ;
%plot(1:N,data,'r') ;
%figure ;
plot(aa,average) ;
xlabel('a=mag') ;
hold off ;
figure(20) ;
clf ;
n = length(table) ;
plot(1:n,table) ;
legend('1-mag','2-geo','3-hem','4','5');
```

II. MATLAB Code for ternary fit (Hematite + Magnetite + Goethite)

```
disp('----------------------------------------------------') ;
clear all ;
figure(3) ;
data2 ;
mag = table(:,1) ;
goe = table(:,2) ;
hem = table(:,3) ;
data = table(:,4) ;
N = length(hem) ;
L = 101 ;
%amin = 0 ; amax =  1 ;
amin = 0.04 ; amax =  0.08 ;
%bmin = 0 ; bmax =  1 ;
bmin = 0.4 ; bmax =  0.8 ;
aa = linspace(amin,amax,L) ;
bb = linspace(bmin,bmax,L) ;
%comparison = zeros(L,N) ;
average = zeros(L,L) ;
smallest = 100 ;
for idx1 = 1:L
 a = aa(idx1) ;
 for idx2 = 1:L
  b = bb(idx2)*(1-a) ;
  %if a+b <= 1
   %c = 1-a-b ;
   c = (1-b)*(1-a) ;
   total = 0 ;
   for i = 1:N
    mix = a*hem(i) + b*mag(i) + c*goe(i) ;
    %total = total + abs(data(i) - mix) ;
    total = total + (abs(data(i) - mix))^2 ; %%%%%% LEAST SQUARES %%%%%
   end
   ave  = total / N ;
   average(idx2,idx1) = ave ; %%%%% r=2,c=1 %%%%%
   if ave < smallest
    smallest = ave ;
    fprintf('%f : %d %d : a=%f b=%f c=%f\n',smallest,idx1,idx2,a,b,c) ;
    ra = a ; rb = b ; rc = c ;
    raa = aa(idx1) ; rbb = bb(idx2) ;
   end
  %end
 end
end
clf ;
hold on ;
grid on ;
%plot(1:N,hem,'g') ;
%plot(1:N,mag,'y') ;
%plot(1:N,goe,'k') ;
%plot(1:N,data,'r') ;
%figure ;
[ga,gb] = meshgrid(aa,bb) ;
surf(ga,gb,average) ;
xlabel('a') ;
ylabel('b') ;
zlabel('MEAN SQUARED ERROR') ;
zmin = 0 ; zmax = 1.6e-3
%zlim([0 smallest]) ; %%%%%%%%%%%%%%%%%%%%%%%%%%%%%%%%%%
```

```
h =linspace(zmin,smallest,100) ;
for i = 1:length(h)
 plot3(raa,rbb,h(i),'ro') ;
end
%plot3(ra,rb,smallest,'ro') ;
%plot3(ra,rb,0,'ro') ;
hold off ;
```

APPENIDIX E: *Stardust* Samples

Stardust Samples Analysed – Chapters 5 and 6

C2005,2,121,1,0

Descrption: Terminal partice from track #121 pressed in Au foil.

C2005,2,121,2,0

Descrption: Terminal Partice from track #121 pressed in Au foil.

C2044, 10, 41, 0, 0

Descrption: Tranverse aerogel slice from entrance of track #41.

C2012,10,134,0,0

Descrption: Keystone containing complete track #134 on a silicon fork.

C2062,2,162,0,0

Descrption: Longitudinal section of the first 750 μm of track #162 .

C2063,1,154,1,14

Descrption: 90 nm microtromed terminal partice from track #154 in amorphous C/Cu grid.

C2063,1,154,1,15

Descrption: 90 nm microtromed terminal partice from track #154 in amorphous C/Cu grid.

C2063,1,154,1,17

Descrption: 90 nm microtromed terminal partice from track #154 in amorphous C/Cu grid.

References

Abramov O. and Kring D. A. (2005) Impact-induced hydrothermal activity on early Mars. *Journal of Geophysical Research* 110:E12S09.

Alwmark C., and Schmitz B. (2006) Extraterrestrial chromite in the resurge deposits of the early Late Ordovician Lockne crater, Central Sweden. *Earth and Planetary Science Letters* 253:291-303.

Amelin Y., Krot A. N., Hutcheon I. D., and Ulyanov A. A. (2002) Lead isotopic ages of chondrules and calcium– aluminum-rich inclusions. *Science* 297: 1678–1683.

Anders E. and Grevesse N. (1988) Abundances of the elements: Meteoritic and solar. *Geochimica et Cosmochimica Acta* 53:197-214.

Ashworth J. R., and Hutchison R. (1975) Water in non-carbonaceous stony meteorites. *Nature* 256:714-715.

Ashworth J. R. (1980) Deformation mechanisms in mildly shocked chondritic diopside. *Meteoritics* 15(2):105-115.

Attwood D. (1999) Soft X-rays and Extreme Ultraviolet Radiation: Principles and Applications. Cambridge: Cambridge University Press.

Baker L. L., Agenbroad D. J., and Wood S. A. (2000) Experimental hydrothermal alteration of a martian analogue basalt implications for martian meteorites. *Meteoritics & Planetary Science* 35:31-38.

Baker V. K. (2001) Water and the martian landscape. *Nature* 412:228-236.

Balsiger H. Altwegg K., Bühler F., Geiss J., Ghielmetti A. G., Goldstein B. E., Goldstein R., Huntress W. T., Ip W. H., Lazarus A. J., Meier A., Neugebauer M., Rettenmund U., Rosenbauer H., Schwenn R., Sharp R. D., Shelley E. G., Ungstrup E.,

and Young D. T. (1986) Ion composition and dynamics at Comet Halley. *Nature* 321:330-334

Banfield J. F., Veblen D. R., and Jones B. F. 1990. Transmission Electron Microscopy of subsolidus oxidation and weathering of olivine. *Contributions to Mineralogy and Petrology* 106: 110-113.

Barrett R. A. and Zolensky M. E. (1991) Analytical studies of impact experiments simulating capture of cosmic dust in silica aerogel (abstract). 22nd Lunar and Planetary Science Conference. 53–54.

Barrett R.A., Zolensky M.E., Hörz F., Lindstrom D.J., and Gibson E.K. (1992) Suitability of Silica Aerogel as a Capture Medium for Interplanetary Dust. *Proc. Of Lunar and Planetary Science* 22:203-212.

Beckett J. R., Connolly H. C., Ebel D. S. (2006) Chemical Processes in Igneous Calcium-Aluminum-rich Inclusions: a Mostly CMAS View of Melting and Crystallization. In Meteorites and the Early Solar System II., edited by Lauretta D. S., and McSween H. Y. The University of Arizona Press: 399-429.

Bence A. E., and Albee A. L. (1968) Empirical correction factors for the electron microanalysis of silicates and oxides. *Journal of Geology* 76(4):382-403.

Bibring J-P., Langevin Y., Gendrin A., Gondet B., Poulet F., Berthé M., Soufflot A., Arvidson R., Mangold N., Mustard J., and Drossart P. (2005) Mars Surface Diversity as revealed by the OMEGA/Mars Express Observations. *Science* 307(5715):1576-1581.

Bischoff A., and Keil K. (1983) Ca-Al-rich chondrules and inclusions in ordinary chondrites. *Nature* 303:588-592.

Bogard D.D., Nyquist L.E., and Johnson P. (1984) Noble gas contents of shergottites and implications for the Martian origin of SNC meteorites. *Geochimica et Cosmochimica Acta* 48(9):1723-1739.

References

Bosi F., Halenius U., and Skogby H. (2009) Crystal chemistry of the magnetite-ulvoespinel series. *American Mineralogist* 94:181-189.

Bradley J. P. (1994a) Nanometre scale mineralogy and petrography of fine-grained aggregates in anhydrous interplanetary dust particles. *Geochimica et Cosmochimica Acta* 58:2123-2#134.

Bradley J. P. (1994b) Chemically Anomalous, Preaccretionally Irradiated Grains in Interplanetary Dust from Comets. *Science* 265:925-929.

Bradley J. P., and Dai Z. R. (2004) Mechanism of formation of glass with embedded metal and sulfides. *The Astrophysical Journal* 617:650–655.

Bradley J. P., Keller L. P., Brownlee D. E., and Thomas K. L. (1996) Reflectance spectroscopy of interplanetary dust particles. *Meteoritics and Planetary Science* 31: 394-402.

Bragg W. H., and Bragg W. L. (1913) The reflection of X-rays by crystals. *Proceedings of the Royal Society of London. Series A* 88(605):428-438.

Brearley A. J., and Jones R. H. (1998) Chondritic Meteorites in Planetary Materials. (ed. J.J. Papike) in Reviews in Mineralogy, 36.

Bridges J. C., Burchell M. J., Changela H. G., Foster N. J., Creighton J. A., Busemann H., and Franchi I. A. (2010) Iron oxides in Comet 81P/Wild-2. *Meteoritics and Planetary Science* 45(1):55–72.

Bridges J. C., Franchi I. A., Hutchison R., Sexton A. S., and Pillinger C. T. (1998) Correlated mineralogy, chemical compositions, oxygen isotopic compositions and size of chondrules. *Earth and Planetary Science Letters* 155:183-196.

Bridges J.C., Franchi I.A., and Green S.F. (2007) *Stardust* microcrater residue compositional groups (abstract #2180). 38th Lunar and Planetary Science Conference. CD-ROM.

Bridges J. C., and Grady M. M. (2000) Evaporite mineral assemblages in the nakhlite (Martian) meteorites. *Earth and Planetary Science Letters* 176:267-279.

Bridges J. C., and P. H. Warren. (2006) The SNC meteorites: basaltic igneous processes on Mars. *Journal of the Geological Society, London* 163:229-251.

Bridges J. C., Catling D. C., Saxton J. M., Swindle, T. D., Lyon I. C., and Grady M. M. (2001) Alteration assemblages in the martian meteorites: implications for near-surface processes. In Chronology and Evoltuion of Mars., edited by Kallenbach R., Geiss J. and Hartmann W.K. Kluwer: Dordrecht. 365-392.

Bridges J. C., and Changela H. G. (2010) Refractory chondrule fragments with carbonaceous chondrite affinities in Comet Wild2/81P. (Abstract #2058). 41st Lunar and Planetary Science Conference. *CD-Rom.*

Bridges J. C., and Warren. P. H. (2006) The SNC meteorites: basaltic igneous processes on Mars. *Journal of the Geological Society, London* 163:229-251.

Brigatti M. F. (1983) Relationships between composition and structure in Fe-rich smectites. *Clay Minerals* 18:177-186.

Brigatti M. F., Lugli C., Poppi L., and Venturelli G. (1999) Iron-rich saponite: dissolution reactions and Cr uptake. *Clay Minerals* 34:637-645.

Broglie M. De (1913) *Comptes Rendus* 157:924-926.

Brownlee D., Burnett D., Clark B. C., Hanner M. S., Hörz F., Kissel J., Newburn S., Sandford S. A., Sekanina Z., Tsou P., and Zolensky M. (1996) STARDUST: Comet and interstellar dust sample return mission. *Physics, Chemistry, and Dynamics of Interplanetary Dust ASP Conference Series* 104:223-226

Brownlee D., Hörz F., Newburn R. L., Zolensky M., Duxbury T. C., Sandford S. A., Sekanina Z., Tsou P., Hanner M. S., Clark B. C., Green S. F., and Kissel J. (2004)

References

Surface of Young Jupiter Family Comet 81P/Wild 2: View from the Stardust Spacecraft. *Science* 304(5678):1764-1769.

Brownlee D., Tsou P., Aléon J., Alexander C. M. O'D., Araki T., Bajt S., Baratta G. A., Bastien R., Bland P., Bleuet P., Borg J., Bradley J. P., Brearley A., Brenker F., Brennan S., Bridges J. C., Browning N. D., Brucato J. R., Bullock E., Burchell M. J., Busemann H., Butterworth A., Chaussidon M., Cheuvront A., Chi M., Cintala M. J., Clark B. C., Clemett S. J., Cody G., Colangeli L., Cooper G., Cordier P., Daghlian C., Dai Z., d'Hendecourt L., Djouadi Z., Dominguez G., Duxbury T., Dworkin J. P., Ebel D. S., Economou T. E., Fakra S., Fairey S. A. J., Fallon S., Ferrini G., Ferroir T., Fleckenstein H., Floss C., Flynn G., Franchi I. A., Fries M., Gainsforth Z., Gallien J.-P., Genge M., Gilles M. K., Gillet Ph., Gilmour J., Glavin D. P., Gounelle M., Grady M. M., Graham G. A., Grant P. G., Green S. F., Grossemy F., Grossman L., Grossman J. N., Guan Y., Hagiya K., Harvey R., Heck P., Herzog G. F., Hoppe P., Hörz F., Huth J., Hutcheon I. D., Ignatyev K., Ishii H., Ito M., Jacob D., Jacobsen C., Jacobsen S., Jones S., Joswiak D., Jurewicz A., Kearsley A. T., Keller L. P., Khodja H., Kilcoyne A. L. D., Kissel J., Krot A., Langenhorst F., Lanzirotti A., Le L., Leshin L. A., Leitner J., Lemelle L., Leroux H., Liu M.-C., Luening K., Lyon I., MacPherson G., Marcus M. A., Marhas K., Marty B., Matrajt G., McKeegan K., Meibom A., Mennella V., Messenger K., Messenger S., Mikouchi T., Mostefaoui S., Nakamura T., Nakano T., Newville M., Nittler L. R., Ohnishi I., Ohsumi K., Okudaira K., Papanastassiou D. A., Palma R., Palumbo M. E., Pepin R. O., Perkins D., Perronnet M., Pianetta P., Rao W., Rietmeijer F. J. M., Robert F., Rost D., Rotundi A., Ryan R., Sandford S. A., Schwandt C. S., Schlutter D., Sheffield-Parker J., Simionovici A., Simon S., Sitnitsky I., Snead C. J., Spencer M. K., Stadermann F. J., Steele A., Stephan T., Stroud R., Susini J., Sutton S. R., Suzuki Y., Taheri M., Taylor S., Teslich N. ,Tomeoka K., Tomioka N., Toppani A., Trigo-Rodríguez J. M., Troadec D., Tsuchiyama A., Tuzzolino A. J., Tyliszczak T., Uesugi K., Velbel M., Vellenga J., Vicenzi E., Vincze L., Warren J., Weber I., Weisberg M., Westphal A. J., Wirick S., Wooden D., Wopenka B., Wozniakiewicz P., Wright I., Yabuta H., Yano H., Young E. D., Zare R. N. Zega T., Ziegler K., Zimmermann L., Zinner E., and Zolensky M. (2006) Comet 81P/Wild 2 under a microscope. *Science* 314:1711–1716.

Brownlee D. E., Tsou P., Anderson J. D., Hanner M. S., Newburn R. L., Sekanina Z.,

Clark B. C., Horz F., Zolensky M. E., Kissel J., McDonnell J. A. M., Sandford S. A., and Tuzzolino A. J. (2003) Stardust: Comet and interstellar dust sample return mission. *Journal of Geophysical Research* 108 E10 8111.

Burns R. G., and Martinez S. L. (1991) Mossbauer spectra of olivine rich achondrites: Evidence of preterrestrial redox reactions. *Proceedings of Lunar and Planetary Science.* 21:331-340.

Carlson W. D. (1988) Subsolidus phase equilibria on the forsterite-saturated join $Mg_2Si_2O_6$-$CaMgSi_2O_6$ at atmospheric pressure. *American Mineralogist* 73:232-241.

Carr M. (1996) *Water on Mars* p25 New York: Oxford University Press.

Carr M. H., and Turekian K. K. (1961) The geochemistry of Co. *Geochimica et Cosmochimica Acta* 23:9-60.

Carter D. B., and Williams C. B. (1996) Transmission Electron Microscopy. New York: Springer.

Castaing R. (1951) Thesis, University of Paris, ONERA Publication, #55.

Champness P. E. (2001) Electron Diffraction in the Transmission Electron Microscope. Oxford: BIOS Scientific.

Changela H.G., and Bridges J.C. (2009) TEM Study of Alteration Assemblages in the Nakhlites: Variation with Burial Depth on Mars (abstract #2302). 40th Lunar and Planetary Science Conference. CD-ROM.

Changela H. G. (2008) Focused ion beam techniques in TEM sample preparation of planetary materials -application to *Stardust* & SNC Meteorites. *UK Planetary Forum 2008.*

Chen J. H., and Wasserburg G. J. (1981) The isotopic composition of uranium and lead in Allende inclusions and meteoritic phosphates. *Earth and Planetary Science Letters* 52:1-5.

References

Chevrier V., Poulet F., and Bibring J. P. (2007) Early geochemical environment of Mars as determined from thermodynamics of phyllosilicates. *Nature* 448:60-63.

Chi M., Ishii H. A., Simon S. B., Bradley J. P.,Dai Z., Joswiak D., Browning N. D., Matrajt G. (2009) The origin of refractory minerals in comet 81P/Wild 2. *Geochimica et Cosmochimica Acta* 73:7150–7161.

Choi B.-G., and Wasson J. T. (2003) Microscale oxygen isotopic exchange and formation of magnetite in the Ningqiang anomalous carbonaceous chondrite. *Geochimica et Cosmochimica Acta* 67:4655-4660.

Clark B. C., Mason L. W., and Kissel J. (1987) Systematics of the "CHON" and other light-element particle populations in comet P/Halley. *Astronomy and Astrophysics* 187:779-784

Clark III B. C., Arvidson R. E., Gellert R., Morris R. V., Ming D. W., Richter L., Ruff S. W., Michalski J. R., Farrand W. H., Yen A., Herkenhoff K. E., Li R., Squyres S. W., Schroder C., Klingelhofer G., and Bell III J. F. (2007) Evidence for montmorillonite or its compositional equivalent in Columbia Hills, Mars. *Journal of Geophysical Research* 112:E06S01.

Cliff G., and Lorimer G. W. (1975) The quantitative analysis of thin specimens. *Journal of. Microscop.* 103:203-207.

Daubar I. J., and Kring, D. A. (2001) Impact-induced hydrothermal systems: heat sources and lifetimes (abstract #1727). 32nd Lunar and Planetary Science Conference. CD-ROM.

Deer W. A., Howie R. A. and Zussman J. (1966) *An Introduction to the Rock Forming Minerals*. Longmans, London. 528pp.

de Faria D.L.A., Venâncio Silva S., and de Oliveira M.T. (1997) Raman microspectroscopy of some iron oxides and oxyhydroxides. *Journal of Raman Spectroscopy* 28:873 – 878.

References

Demidov N. E., and Gilichinsky D. A. (2009) Terrestrial Permafrost Models and Analogues of Martian Habitats and Inhabitants. *Soil Biology* 16:323-341.

Desch S. J., and Connolly H. C. Jr. (2002) A model of the termal processing of particles in solar nebula shocks: application to the cooling rates of chondrules. *Meteoritics & Planetary Science* 37:183-207.

Ehlmann B. L., Mustard J. F., Murchie S. L., Poulet F., Bishop J. L. Brown A. J., Calvin W. M., Clark R. N., Des Marais D. J., Milliken R. E., Roach L. H., Roush T. L., Swayze G. A., Wray J. J. (2008) Orbital Identification of Carbonate-Bearing Rocks on Mars. *Science* 322:1828-1832.

Einstein A. (1905) Concerning an Heuristic Point of View Toward the Emission and Transformation of Light. *Ann. Phys.* 17:132.

Farnham T. L., and Schleicher D. G. (2005) Physical and compositional studies of Comet 81P/ Wild 2 at multiple apparitions. *Icarus* 173:533-558.

Fiore S., Huertas F. J., Huertas F., and Linares J. (1995) Morphology of kaolinite crystals synthesized under hydrothermal conditions. *Clays and Clay Minerals* 43(3):353-360.

Flynn G. J. (2008) Physical, Chemical, and Mineralogical Properties of Comet 81P/Wild 2 Particles Collected by *Stardust*. *Earth Moon Planet* 102:447–459.

Flynn G. J., Bleuet P., Borg J., Bradley J. P., Brenker F. E., Brennan S., Bridges J., Brownlee D. E., Bullock E. S., Burghammer M., Clark B. C., Dai Z. R., Daghlian C. P., Djouadi Z., Fakra S., Ferroir T., Floss C., Franchi I. A., Gainsforth Z., Gallien J.-P., Gillet Ph., Grant P. G., Graham G. A., Green S. F., Grossemy F., Heck P. R., Herzog G. F., Hoppe P., Hörz F., Huth J., Ignatyev K., Ishii H. A., Janssens K., Joswiak D., Kearsley A. T., Khodja H., Lanzirotti A., Leitner J., Lemelle L., Leroux H., Luening K., MacPherson G. J., Marhas K. K., Marcus M. A., Matrajt G., Nakamura T., Nakamura-Messenger K., Nakano T., Newville M., Papanastassiou D. A., Pianetta P., Rao W.,

Riekel C., Rietmeijer F. J. M., Rost D., Schwandt C. S., Sheffield-Parker J., Simionovici A., Sitnitsky I., Snead C. J., Stadermann F. J., Stephan T., Stroud R. M., Susini J., Suzuki Y., Sutton S. R., Taylor S., Teslich N., Troadec D., Tsou P., Tsuchiyama A., Uesugi K., Vekemans B., Vicenzi E. P., Vincze L., Westphal A. J., Wozniakiewicz P., Zinner E., and Zolensky M. E. (2006) Elemental compositions of comet 81P/Wild 2 samples collected by *Stardust*. *Science* 314:1731–1735.

Fraser G. W. (1989) X-ray detectors in astronomy. Cambridge: Cambridge University Press.

Fritz J., Artemieva N., and Greshake A. (2005) Ejection of martian meteorites. *Meteoritics & Planetary Science* 40:1393–1411.

Gates W. P., Slade P. G., Manceau A. and Lanson B. (2002) Site Occupancies By Iron In Nontronites. *Clay and Clay Minerals* 50: 223-239.

Gellert R., Rieder R., Anderson R. C., Brückner J., Clark B. C., Dreibus G., Economou T., Klingelhöfer G., Lugmair G. W., Ming D. W., Squyres S. W., d'Uston C., Wänke H., Yen A. and Zipfel1 J. (2004) Chemistry of Rocks and Soils in Gusev Crater from the Alpha Particle X-ray Spectrometer. *Science* 305(5685):829-832.

Giannuzzi L. A., and Stevie F. A. (2005) The Focused Ion Beam Instrument. New York: Springer.

Gibson E.K Jr., McKay D.S., Thomas-Keprta K.L., Wentworth S.J., Westall F., Steele A., Romanek C.S., Bell M.S., and Toporski J. (2001) Life on Mars: evaluation of the evidence within Martian meteorites ALH84001, Nakhla, and Shergotty *Precambrian Research* 106:15–34.

Gibson E.K Jr., McKay D.S., Clemett S.J., Thomas-Keprta K.L., Pillinger C.T., Verchovsky A.B., and Spencer L. (2010) (Abstract #5009) Nature of carbon in martian meteorites. *Meteoritics and Planetary Science 45, Supplement*.

Gillet P., Barrat J. A.,. Deloule E., Wadhwa M., Jambon A., Sautter V., Devouard B., Neuville D., Benzerara K., and Lesourd M. (2002) Aqueous alteration in the Northwest Africa 817 (NWA 817) Martian meteorite. *Earth and Planetary Science Letters* 203:431-444.

Golden D.C., Ming D.W., Schwandt C.S., Morris R.V., Yang S.V., and Lofgren G.E. (2000) An experimental study on kinetically-driven precipitation of calcium, magnesium, and iron carbonates from solution: Implications for the low-temperature formation of carbonates in martian meteorite Allan Hills 84001. *Meteoritics & Planetary Science* 35:457–465.

Goldstein J., and Newbury D. E. (2003) Scanning Electron Microscopy and X-Ray Microanalysis: A Text for Biologists, Materials Scientists, and Geologists. New York: Springer.

Gooding J. L. (1986) Clay-mineraloid weathering products in Antarctic meteorites. *Geochimica et Cosmochimica Acta* 50:2215-2223.

Gooding J. L (1992) Soil mineralogy and Chemistry on Mars: Possible clues from salts and Clays in SNC Meteorites. *Icarus* 99:28-41.

Gooding J. L., Wentworth S. J., and Zolensky M. E. (1988) Calcium carbonate and sulfate of possible extraterrestrial origin in the EETA 79001 meteorite. *Geochimica et Cosmochimica Acta* 52:909-915.

Gooding J. L., Wentworth S. J., and Zolensky M. E. (1991) Aqueous alteration of the Nakhla meteorite. *Meteoritics* 326:135-143.

Golden D.C., Ming D.W., Schwandt C.S., Morris R.V., Yang S.V., and Lofgren G.E. (2000) An experimental study on kinetically-driven precipitation of calcium, magnesium, and iron carbonates from solution: Implications for the low-temperature formation of carbonates in martian meteorite Allan Hills 84001. *Meteoritics & Planetary Science* 35:457–465.

Graham G. A., Teslich N. E., Kearsley A. T., Stadermann F. J., Stroud R. M., Dai Z., Ishii, H. A., Hutcheon I. D., Bajt S., Snead C. J., Weber P. K., Bradley J. P. (2008) Applied focused ion beam techniques for sample preparation of astromaterials for integrated nanoanalysis. *Meteoritics and Planetary Science* 43(3):561-569.

Grauby O., Petit S., Decarreau A., and Baronnet A. (1994) The nontronite-saponite series : An experimental approach. *European Journal of Mineralogy* 6:99-112.

Grossemy F., Borg J., Djouadi Z., Simionovici A., Lemelle L., Eichert D., Deboffle D., Westphal A. J., and Snead C. (2008) In-situ Fe XANES of extraterrestrial grains trapped in aerogel collectors: An analytical test for the interpretation of *Stardust* samples analyses. *Planetary and Space Science* 55:966-973.

Gurman S. J. (1984) A rapid curved-wave theory of EXAFS. *Journal of Physics C: Solid State Physics* 17:143-151.

Hagerty J. J., and Newsom H. E. (2003) Hydrothermal alteration at the Lonar Lake. impact structure, India: Implications for impact cratering on Mars. *Meteoritics & Planetary Science* 38:365-381.

Hanner M. S. (1999) The silicate material in comets. *Space Science Reviews* 90:99–108.

Harker D. E., Woodward C. E., and Wooden D. H. (2005) The dust grains from 9P/Tempel 1 before and after the encounter with Deep Impact. *Science* 310:278-280.

Hartmann W. K., and Neukum G. (2001) Cratering chronology and the cvolution of Mars., edited by Kallenbach R., Geiss J. and Hartmann W.K. Kluwer: Dordrecht. 365-392.

Harvey R. P. (2010) Carbonates and martian climate. *Science* 329:400-403.

Hevey P. J., and Sanders I. S. (2006) A model for planetesimal meltdown by Al-26 and its implications for meteorite parent bodies. *Meteoritics & Planetary Science* 41:95-106.

References

Hicks D. G., Boehly T. R., Eggert J. H., Miller J. E., Celliers P. M., and Collins G.W. (2006) Dissociation of Liquid Silica at High Pressures and Temperatures. *Physical Review Letters* 97(025502):1-4.

Hillier J., and Baker R. F. (1994) Microanalysis by Means of Electrons. *Journal of Applied. Physics* 15:663.

Hirsch P. B., Howie A., Nicholson R. B., Pashley D. W., and Whelan M. J. (1965) *Electron Microscopy of Thin Crystals.* London: Butterworth & Co. 549pp.

Hoffman N. (2000) White Mars: A new Model for Mars' surface and atmosphere based on CO_2. *Icarus* 146: 326–342.

Horita Z. (1998) Quantitative X-ray microanalysis in analytical Electron Microscopy. *Materials Transactions JIM* 39(9):947-958.

Horner J. N., Evans W., Bailey M. E., and Asher D. J. (2003) The populations of comet-like bodies in the Solar system. *Monthly Notices of the Royal Astronomical Society* 343(4):1057-1066.

Hörz F., Bastien R., Borg J., Bradley J. P., Bridges J. C., Brownlee D. E., Burchell M. J., Chi M., Cintala M. J., Dai Z. R., Djouadi Z., Dominguez G., Economou T. E., Fairey S. A. J., Floss C., Franchi I. A., Graham G. A., Green S. F., Heck P., Hoppe P., Huth J., Ishii H., Kearsley A. T., Kissel J., Leitner J., Leroux H., Marhas K., Messenger K., Schwandt C. S., Snead C., Stadermann F. J., Stephan T., Stroud R., Teslich N., Trigo-Rodríguez J. M., Tuzzolino A. J., Troadec D., Tsou P., Warren J., Westphal A., Wozniakiewicz P., Wright I., and Zinner E. (2006) Impact features on *Stardust*: Implications for Comet 81P/Wild 2 dust. *Science* 314:1716–1719.

Hörz F. ,Cintala M. J., See T.H., and Nakamura-Messenger K. (2008) Impact Experiments with Al_2O_3 Projectiles into Aerogel (abstract #1391). 39th Lunar and Planetary Science Conference. CD-ROM.

Hutchison R. Attwood D. (1999) Meteorites: A petrologic, chemical and osotopic synthesis.. Cambridge: Cambridge University Press.

Ishii H. A., Bradley J. P., Dai Z. R., Chi M. F., Kearsley A. T., Burchell M. J., Browning N. D., and Molster F. (2008) Comparison of comet 81P/Wild 2 dust with interplanetary dust from comets. *Science* 319:447-450.

Imae N., and Ikeda Y. (2007) Petrology of the Miller Range 03346 nakhlite in comparison with the Yamato-000593 nakhlite. *Meteoritics & Planetary Science* 42(2): 171–184.

Jeol Applications Manual. Titled: *Theory of the Scanning Electron Microscope.*

Jessberger E. K., Christoforidis A., and Kissel J. (1988) Aspects of the major element composition of Halley's dust. *Nature* 332:691-695.

Jones J. H. (1986) A discussion of isotopic systematics and mineral zoning in the shergottites: Evidence for a 180 M.y. igneous crystallization age. *Geochimica et Cosmochimica Acta* 50(6):969-977.

Joswiak D. J., Brownlee D. E., and Matrajt G. (2008) Surprisingly High Abundance of Na and Cr-rich Calcic Pyroxenes in *Stardust* Tracks (abstract #2177). 39th Lunar and Planetary Science Conference. CD-ROM.

Joswiak D. J., Brownlee D. E., Matrajt G., Westphal A. J., Snead C. J. (2009) Kosmochloric Ca-rich pyroxenes and FeO-rich olivines (Kool grains) and associated phases in Stardust tracks and chondritic porous interplanetary dust particles: Possible precursors to FeO-rich type II chondrules in ordinary chondrites. *Meteoritics and Planetary Science* 44(10):1561-1588.

Joswiak D. J., Brownlee D. E., Matrajt G., and Messenger K. N. (2010) Stardust track 130 terminal partice: possible Al-rich condrule fragment or Altered Amoeboid Olivine Aggragte (abstract #2119). 41st Lunar and Planetary Science Conference. CD-ROM.

Kaur N., Singh B., Kennedy B.J., Graefe M. (2009) The preparation and characterization of vanadium-substituted goethite: the importance of temperature. *Geochimica et Cosmochimica Acta* 73:582-593.

Kearsley A.T., Borg J., Graham G. A., Burchell M. J., Cole M. J., Leroux H., Bridges J. C., Hörz F., Wozniakiewicz P. J., Bland P. A., Bradley J. P., Dai Z. R., Teslich N., Westphal A., See T., Hoppe P., Heck P. R., Huth J., Stadermann F. J., Floss C., Marhas K., Zinner E., Stroud R., Stephan T., and Leitner J. (2008) Dust from comet Wild 2: interpreting particle size, shape, structure and composition from impact features on the *Stardust* aluminium foils. *Meteoritics and Planetary Science* 43:41 – 74.

Keller L. P., Thomas K. L., and McKay D. S. (1992) An interplanetary dust particle with links to CI chondrites. *Geochimica et Cosmochimica Acta* 56:1409-1412.

Kirkpatrick P. and Baez A. V. (1948) Formation of Optical Images by X-Rays. *Journal Optical. Society. America*. 38:766-773.

Klimentidis R., and Mackinnon I. D. R 1986. High resolution imaging of ordered mixed layer clays. *Clay and clay minerals* 34:155-164.

Klingelhöfer G., Morris R. V., Bernhardt B., Schröder C., Rodionov D. S.,de Souza, Jr. P. A., Yen A., Gellert R.,Evlanov E. N., Zubkov B., Foh J., Bonnes U., Kankeleit E., Gütlich P., Ming D. W., Renz F., Wdowiak T., Squyres S. W, and Arvidson R. E. (2004) Jarosite and Hematite at Meridiani Planum from Opportunity's Mössbauer Spectrometer. *Science* 306:1740-1745.

Kodama H., de Kimpe I. C. R., and Dejou J. (1998) Ferrian saponite in a gabbro saprolite at Mont Mégantic, Quebec. *Clays and Clay Minerals* 36(2):102-110.

Kohlstedt D. L., and Mackwell S. J. (1987) High-temperature stability of San Carlos olivine. *Contributions to Mineralogy and Petrology* 95(2):226-230.

Kohyama N., and Sudo T. (1975) Hisingerite occurring as a weathering product of iron-rich saponite. *Clays and Clay Minerals* 23:215-218.

Komadel P., Madejova J., Laird D. A., Xia Y., and Stucki J. W. (2000) Reduction of Fe(III) in griffithite. *Clay Minerals* 35:625–634.

Kondoh S., Kitamura M., and Morimoto N. (1985) Synthetic laihunite (ClassXFe-2/$^{2+}$)-3XFe-2X($^{3+}$)SiO$_4$), an oxidation-product of olivine. *American Mineralogist* 70:737-746.

Koningsberger D. C. and Prins R. (1988) X-ray Absorption: Principles, Applications, Techniques of EXAFS, SEXAFS, and XANES, in Chemical Analysis New York: John Wiley & Sons.

Köster H. M., Ehrlicher U., Gilgh A., Jordan R., Murad E., and Onnich K. (1999) Mineralogical and chemical characteristics of five nontronites and Fe-rich smectites. *Clay Minerals* 34:579-599.

Kronig R. L. de (1931) *Z. Physics* 70: 317-323.

Krot A. N., Fagan T. J., Keil K., McKeegan K. D., Sahijpal S., Hutcheon I. D., Petraev M. I., and Yurimoto H. (2004) Ca, Al-rich inclusions, amnoeboid olivine aggregates and Al-rich chondrules from the unique carbonaceous chodrite Acfer 094: I. Mineralogy and petrology. *Geochimica et Cosmochimica Acta* 68(9):2167-2184.f

Krot A. N. and Keil K. (2002) Anorthite-rich chondrules in CR and CH carbonaceous chondrites: genetic link between Ca, Al-rich inclusions and ferromagnesian chondrules. *Meteoritics and Planetary Science* 37:91–111.

Krot A. N., Mckeegan K. D. Yurimoto H., Hutcheon I. D., Chaussidon M., MACPherson G. J., and Paque J. (2007) Remelting of refractory inclusions in the chondrule-forming regions: Evidence from the chondrule-bearing Type C calcium-aluminum-rich inclusions from Allende. *Meteoritics and Planetary Science* 42;1197-1219.

Krot A. N., Petaev M. I., Russell S. S., Itoch S., Fagan T. J., Yurimoto H., Chizmadia L., Weisberg M. K., Komatsu M. Ulyanov A. A., and Keil K. (2004) Amoeboid olivine aggregates and realated objects in carbonaceous chondrites: records of nebula and asteroid processes. *Chemie der Erde* 64:185-239.

Krot A. N., Yurimoto H., Hutcheon I. D., Chaussidon M., MᴀᴄPherson G. J., and Paque J. (2007) Remelting of refractory inclusions in the chondrule − forming regions: Evidence from chondrule − bearing type C calcium − aluminium − rich inclusions from Allende. *Meteoritics and Planetary Science* 42(7/8):1197-1219.

Kuebler K., Jolliff B. L., and Treiman A. (2004) A Survey of alteration products and other secondary minerals recovered from Martian meteorites in Antarctica (abstract # 2228). 35th Lunar and Planetary Science Conference. CD-ROM.

Kuiper G. P. (1974) On the origin of the solar system. *Celestial Mechanics* 9:321-348.

Kwong W. Y., and Zhang W. Y. (2005) Electron-beam assisted platinum deposition as a protective layer for FIB and TEM applications. *IEEE* 5:469-471.

Lange R. A., and Carmichael I. S. E. (1987) Densities of Na_2O-K_2O-CaO-MgO-FeO-Fe_2O_3-Al_2O_3-TiO_2-SiO_2 liquids - new measurements and derived partial molar properties. *Geochimica et Cosmochimica Acta* 51:2931-2946.

Lapen T. J., Righter M., Brandon A. D., Debaille V., Beard B. L., Shafer J. T., and Peslier A. H. (2010) A Younger Age for ALH84001 and Its Geochemical Link to Shergottite Sources in Mars. *Science* 328(5976):347-351.

Lawler M. E., and Brownlee D. E. (1992) CHON as a component of dust from comet Halley. *Nature* 359:810-812.

Lee M. R., Bland P. A., and Graham G. (2003) Preparation of TEM samples by focused ion beam (FIB) techniques: applications to the study of clays and phyllosilicates in meteorites. *Mineralogical Magazine* 67(3):581-592.

Lee M. R., Brown D. J., Smith C. I., Hodson M. E., Mackenzie M., and Hellmann R. (2007) Characterization of mineral surfaces using FIB and TEM: A case study of naturally weathered alkali feldspars. *American Mineralogist* 92:1383-1394.

Lee M. R., Brown D. J., Hodson M. E., Mackenzie M., Smith C. I. (2008) Weathering microenvironments on feldspar surfaces: implications for understanding fluid-mineral reactions in soils. *Mineralogical Magazine* 72(6):1319–1328.

Lee M. R. (2010) Transmission electron microscopy (TEM) of Earth and planetary materials: A review. *Mineralogical Magazine* 74(1): 1–27.

Lee P. A., and Pendry J. B. (1975) The theory of X-ray absorption fine structure. *Physics Review B* 11:2795-2811.

Lentz R. C. F., Taylor G. J., and Treiman A. H. (1999) Formation of a martian pyroxenite: a comparative study of the nakhlites and Theo's Flow. *Meteoritics & Planetary Science* 34:919-932.

Leroux H. (2001) Microstructural shock signatures of major minerals in meteorites. *European Journal of Mineralogy* 13:253-272.

Leroux H., Rietmeijer F. J. M., Velbel M. A., Brearley A. J., Jacob D., Langenhorst F., Bridges J. C., Zega T.J., Stroud R.M., Cordier P., Harvey R. P., Lee M., Gounelle M., and Zolensky M. E. (2008) A TEM study of thermally modified comet 81P/Wild 2 dust particles by interaction with the aerogel matrix during the *Stardust* capture process. *Meteoritics and Planetary Science* 43:97–120.

Leroux H., Jacob D., Stodolna J., Messenger K. N., and Zolensky M. E. (2009) Igneous Ca-rich pyroxene in comet 81P/Wild 2. *American Mineralogist* 93:1933–1936.

Lormier G. W. (1984) X-ray microanalysis in the transmission electron microscope. *Bullitens of Matteials Science* 6(3):503-512.

Lytle F. W. (1999) The EXAFS family tree: a personal history of the development of extended X-ray absorption fine structure. *Journal of Synchrotron Radiation* 6:123-134.

Madsen M. B., Mørup S., Costa T. V. V., Knudsen J. M., and Olsen M. (1986) Superparamagnetic component in the Orgueil meteorite and Mössbauer spectroscopy studies in applied magnetic fields. *Nature* 321:501-503.

Martin T. P., Merlin R., Huffman D.R., Cardona M. (1977) Resonant two magnon Raman scattering in α-Fe_2O_3. *Solid State Communications* 22:565-567.

Massey M. J., Baier U., Merlin R., Weber W. H. (1990) Effects of pressure and isotopic substitution on the Raman spectrum of α-Fe_2O_3: identification of two-magnon scattering. *Physical Review B* 41:7822-7827.

Manceau A., Lanson B., Schlegel M. L., Harge J. C., Musso M., Rard L. E., Hazemann J., Chateigner D., and Lamble G.M. (2000) Quantitative Zn speciation in smelter-contaminated soils by EXAFS spectroscopy. *American Journal of Science* 300:289–343.

Manceau A., Lanson B., Drits V. A., Chateigner D., Wu J., Huo D., Gates W.P., and Stucki J. W. (2000) Oxidation-reduction mechanism of iron in dioctahedral smectites:II. Crystal chemistry of reduced Garfield nontronite. *American Mineralogist* 85:153–172.

Manning C. V., McKay C. P., and Zahnle K. J. (2006) Thick and thin models of the evolution of carbon dioxide on Mars. Icarus 180:38-59.

Marcus M. A., Fakra S., Westphal A.J., Snead C. J., Keller L. P., Kearsley A., and Burchell M. J. (2008) Smelting of Fe-bearing glass during hypervelocity capture in aerogel. *Meteoritics and Planetary Science* 43:87-96.

Marvin U. B., Wood J. A., and Dickey Jr J. S. (1970) Ca-Al rich phases in the Allende meteorite. *Earth and Planetary Science Letters* 7:346-350.

Matrajt G., and Brownlee D. E. (2006) Acrylic embedding of Stardust particles encased in aerogel. *Meteoritics and Planetary Science* 41(11):1715-1720.

Matrajt G., Ito M., Wirick S., Messenger S., Brownlee D. E., Joswiak D., Flynn G., Sandford S., snead C., and Westphal A. (2008) Carbon investigation of two *Stardust* particles: A TEM, NanoSIMS, and XANES study. *Meteoritics and Planetary Science* 43:315-334.

McGee J. J., and Keil K. (2001) Application of Electron Probe Microanalysis to the study of geoplogical and planetary materials. *Microscopy and Microoanaysis* 7(2):200-210.

McKie D., and McKie C. (1974) Crystalline Solids. London: Nelson.

Messenger S., Keller L. P., Stadermann F. J., Walker R. M., Zinner E. (2004) Samples of Stars Beyond the Solar System: Silicate Grains in Interplanetary Dust. *Science* 300:105-108.

Meyer C. (2006) Mars Meteorite Compendium. Accessed July 2009. http://www-curator.jsc.nasa.gov/antmet/mmc/Chap%20I.pdf

Michel F. M., Ehm L., Antao S. M., Lee P. L., Chupas P. J., Liu G., Strongin D. R., Schoonen M. A. A., Phillips B. L., Parise J. B. 2007. The Structure of Ferrihydrite, a Nanocrystalline Material. Science 316: 1726–1729.

Michette A. G. (1986) Optical systems for soft x rays. New York and London: Plenum Press.

Mikouchi T., Koizumi E., Monkawa A., Ueda Y., and Miyamoto M. (2003) Mineralogy and petrology of Yamato 000593: Comparison with other Martian nakhlite meteorites. *Antarctic Meteorite Research (NIPR)* 16:34-57.

Mikouchi T., Koizuni E., Monkawa A., Ueda Y., and Miyamoto M. (2003) Mineralogical comparison of Y000593 with other nakhlites: implications for relative burial depths of nakhlites (abstract #1944). 34th Lunar and Planetary Science Conference. CD-ROM.

Mikouchi T., Miyamoto M., Koizumi E., Makishima J., and Mckay G. (2006) relative burial depths of nakhlites: an update (abstract #1865). 37th Lunar and Planetary Science Conference. CD-ROM.

Misawa K., Kojima K., Imae N., and Nakamura N. (2003) The Yamato nakhlite consortium. *Antarctic Meteorite Research (NIPR)* 16:1-12.

Morlok A., Bischoff A., Stephan T., Floss C., Zinner E., and Jessberger E. K. (2006) Brecciation and chemical heterogeneities of CI chondrites. *Geochimica et Cosmochimica Acta* 70:5371-5394.

Morris R.V., Ruff S. W., Gellert R., Ming D. W., Arvidson R. E., Clark B. C., Golden D. C., Siebach[4] K, Klingelhöfer G., Schröder C., Fleischer I., Yen A.S., and Squyres S.W. (2010) Identification of Carbonate-Rich Outcrops on Mars by the Spirit Rover. *Science* 329(5990):421-424.

Mosselmans J. F. W., Quinn P. D., Dent A. J., Cavill S. A., Moreno S. D., Peach A., Leicester P. J., Keylock S. J., Gregory S. R., Atkinson K. D., and Rosell J. R. (2009) I18 - the microfocus spectroscopy beamline at the *Diamond* Light Source. *Journal of Synchrotron Radiation* 16:818-824.

Mulvey T., and Wallington M. J. (1969) The focal properties and aberrations of magnetic electron lenses. *Journal of Physics E* 2(2):466-472.

Mustard J. F., Murchie S. L., Pelkey S. M., Ehlmann B. L., Milliken R. E., Grant J. A.,. Bibring J.-P., Poulet F., Bishop J., Noe Dobrea E., Roach L., Seelos F., Arvidson R. E., Wiseman S., Green R., Hash C., Humm D., Malaret E., McGovern J. A., Seelos K., Clancy T., Clark R., Des Marais D., Izenberg N., Knudson A., Langevin Y., Martin T., McGuire P., Morris R., Robinson M., Roush T., Smith M., Swayze G., Taylor H., Titus T., and Wolff M. (2008) Hydrated silicate minerals on Mars observed by the Mars Reconnaissance Orbiter CRISM instrument. *Nature* 454:305-309.

Nakamura T., Noguchi T., Tsuchiyama A., Ushikubo T., Kita N.T., Valley J.W., Zolensky M.E., Kakazu Y., Sakamoto K., Mashio E., Uesugi K., and Nakano T. (2008) Chondrule like Objects in Short-Period Comet 81P/Wild 2. *Science* 321:1664 − 1667.

Naumov M. V. (2005) Principal features of impact-generated hydrothermal circulation systems: mineralogical and geochemical evidence. *Geofluids* 5:165–184.

Neugebauer M. (1990) Spacecraft observations of the interaction of active comets with the solar wind. *Reviews of Geophysics* 28(2):231-252.

Newsom, H. E., Hagerty J. J., and Goff F. (1999) Mixed hydrothermal fluids and the origin of the Martian soil, *Journal of Geophysical Research* 104(E4):8717–8728.

Newville M. 2004. Fundamentals of XAFS. *Consortium for Advanced Radiation Sources*

Nier A. O. and Shlutter D. J. (1993) The Thermal History of Interplanetary Dust Particles Collected in the Earth's Stratosphere. *Meteoritics* 28:675.

Nimis P., Tesalina S. G., Omenetto P., Tartarotti P., and Lerouge C. (2004) Phyllosilicate minerals in the hydrothermal mafic–ultramafic-hosted massive-sulfide deposit of Ivanovka (southern Urals): comparison with modern ocean seafloor analogues. *Contributions to Mineralogy and Petrology* 147:363–383.

Noble S. K., Pieters C. M., and Keller L. P. (2007) An experimental approach to understanding the optical effects of space weathering. *Icarus* 192: 629-642.

Noguchi, T., Imae, N., Misawa, K., and Nakamura, T. (2003) Mineralogy of ''iddingsite'' and symplectite in Y000593 and 000749: implication for their post-crystallization and aqueous alteration. NIPR Symposium 2003.

Noguchi, T., T. Nakamura, K. Misawa, N. Imae, T. Aoki, and Toh S. (2009) Laihunite and jarosite in the Yamato 00 nakhlites: alteration products on Mars? *Journal of Geophysical Research 114:*E10004.

Noguchi T., Nakamura T., Okudaira K., Yano H., Sugita S., and Burchell M.J. (2007) Thermal alteration of hydrated minerals during hypervelocity capture to silica aerogel at the flyby speed of *STARDUST*. *Meteoritics and Planetary Science* 42:357-372.

Nyquist L.E., Bogard D.D., Shih C.-Y., Greshake A., Stöffler D., and Eugster O. (2001) Ages and geologic histories of martian meteorites. *Space Science Reviews* 96(1-4):105-164.

Ogliore R.C., Butterworth A.L., Fakra S.C., Gainsforth Z., Marcus M.A., and Westphal A.J. (2010) Comparison of the oxidation state of Fe in comet 81P/Wild 2 and chondritic-porous interplanetary dust particles. *Earth and Planetary Science Letters* 296(3-4):278-286.

Ogliore, R.C., Butterworth, A.L., Fakra, S., Frank, D., Gainsforth, Z., Marcus, M.A., Westphal, A.J., (2008) Chemical analysis of a large *Stardust* track associated with a presolar grain. (abstract #2363) 39th Lunar and Planetary Science Conference. CD-Rom.

Oort J. H (1950) The structure of the cloud of comets surrounding the Solar System, and a hypothesis concenring its origin. *Bulletin of the Astronomical Institutes of the Netherlands* 11(408):91-110.

Orloff J. Swanson L. Utlaut Mark. (2002) High Resolution Focused Ion Beams. Cambridge University Press: Cambridge.

Pailhe N.,Wattiaux A., Gaudon M., and Demourgues A. (2008) Impact of structural features on pigment properties of alpha - Fe_2O_3 haematite. *Journal of Solid State Chemistry* 181:2697-2704.

de Pater I., and Lissauer J. J. (2001) Planetary Scienes. Cambirdge: Cambridge University Press.

Park J., Garrison D. H., and Bogard D. D. (2009) ^{39}Ar – ^{40}Ar ages of the martian nakhlites. *Geochimica et Cosmochim Acta* 73(7):2177–2189.

Pieters C. M., Taylor L. A., Noble S. K., Keller L. P., Hapke B., Morris R. V., Allen C. A., McKay D. S., and Wentworth S. (2000) Space weathering on airless bodies: Resolving a mystery with lunar samples. *Meteoritics and Planetary Science* 35:1101-1107.

Pingitore N. E., Iglesias A., Bruce A., Lytle F., and Wellington G. M. (2002) Valences of iron and copper in coral skeleton: X-ray absorption spectroscopy analysis *Microchemical Journal* 71:205-210.

Poulet F., Bibring J.-P., Mustard J. F., Gendrin A., Mangold N., Langevin Y., Arvidson R. E., Gondet B., and Gomez C. (2005) Phyllosilicates on Mars and implications for early martian climate *Nature* 438:623-627.

Prietzel J., Thieme J., Eusterhues K. and Eichert D. (2007) Iron speciation in soils and soil aggregates by synchrotron-based X-ray microspectroscopy (XANES, mu-XANES). *European Journal of Soil Science* 58:1027-1041.

Reed S. J. B. (2005) Electron Microprobe Analysis and Scanning Electron Microscopy in Geology. Cambridge University Press.

Richardson O. W. (1901) On the negative radiation from hot platinum, *Proc. Camb. Phil. Soc.,* 11: 286–295.

Rietmeijer F. J. M. (1998) Interplanetary Dust Particles in Planetary Materials (ed. J.J. Papike) pp. 3-1 to 3-398. Reviews in Mineralogy 36 Mineralogical Society of America.

Rietmeijer F. J. M. (1999) Metastable non-stoichiometric diopside and Mg-wollastonite: An occurrence in an interplanetary dust particle. *American Mineralogist* 84:1883–1894.

Rietmeijer F.J.M. (2004) First report of taenite in an asteroidal interplanetary dust particle: Flash-heating simulates nebula dust evolution (abstract #1060). 35th Lunar and Planetary Science Conference. CD ROM

Rietmeijer F. J. M., Nakamura T., Tsuchiyama A., Uesugi K., and Nakano T. (2008) Origin and formation of iron-silicide phases in the aerogel of the *Stardust* mission. *Meteoritics and Planetary Science* 42:121-134.

References

Romero R., Robert M., Elsass F., and Garcia C. (1992) Evidence by transmission electron microscopy of weathering microsystems in soils developed from crystalline rocks. *Clay Minerals* 27:21-33.

Romanek C. S. et al. (1998) Oxygen isotopic record of silicate alteration in the Shergotty-Nakhla-Chassigny meteorite Lafayette. *Meteoritics and Planetary Science* 33:775-784.

Russell S. S., MacPherson G. J., Leshin L. A., and McKeegan K. D. (2000) ^{16}O enrichments in aluminium-rich chondrules from ordinary chondrites. *Earth and Planetary Science Letters* 184:57-74.

Sayers D. E., Stern E. A., and Lytle F. W. (1971) New technique for investigating Noncrystalline Structures: Fourier Analysis of the Extended X-ray Absorption Fine Structure. *Physical Review Letters* 27(18):1204-1207.

Saxton J. M., Lyon I. C., Chatzitheodoridis E., and Turner G. (2000) Oxygen isotopic composition of carbonate in the Nakhla meteorite: Implications for the hydrosphere and atmosphere of Mars. *Geochimica et Cosmochimica Acta* 64:1299–1309.

Scherzer O. (1936) Über einige Fehler von Elektronenlinsen. *Zeitschrift für Physik A Hadrons and Nuclei* 101:593-603.

Schmitz S., and Brenker F. E. (2008) Microstructural indications for protoenstatite precursor of cometary mgsio3 pyroxene:a further high-temperature component of Comet Wild-2. *The Astrophysical Journal* 681: L105–L108.

Schofield P. F., Knight K. S., Stretton I. C. (1996) Thermal expansion of gypsum investigated by neutron powder diffraction. *American Mineralogist* 81:847-851.

Schwenzer S. P. and Kring D. A. (2009) Impact-generated hydrothermal systems capable of forming phyllosilicates on Noachian Mars. *Geology* 37:1091-1094.

Scott E. R. D., and Krot A. N. (2007) Chondrites and their components. In *Meteorites, Comets and Planets* (ed. A. M. Davis) Chapter 1.07, *Treatise on Geochemistry.*

Sephton M. A. IP Wright, I. Gilmour, JW de Leeuw, MM Grady, and CT Pillinger, (2002) High molecular weight organic matter in martian meteorites. *Planetary and Space Science* 50:711-716.

Shebanova O.N., and Lazor P. (2003) Raman study of magnetite (Fe_3O_4): laser induced thermal effects and oxidation. *Jounal of Raman spectroscopy* 34:845 – 852.

Sheridan P. J. (1989) Determination of experimental and theoretical K_{Asi} factors for a 200-kV analytical electron microscope. *Journal of Electron Microscopy Technique* 11:41-61.

Sherman G. D., Ikawa H., Uehara G., and Okazaki E. (1962) Types of occurrence of nontronite and nontronite-like minerals in soils. *Pacific Science* 16:57-62.

Shu F. H., Shang H., Gounelle M., and Glassgold A. E. (2001) The origin of chondrules and refractory inclusions in chondritic meteorites. *Astrophysical Journal* 548:1029-1050.

Simon S. B., Joswiak D. J., Ishii H. A., Bradley J. P., Chi M., Grossman L., Aléon J., Brownlee D. E., Fallon S., . Hutcheon I. D., Matrajt G., Mckeegan K. D. (2008) A refractory inclusion returned by Stardust from comet 81P/Wild 2. *Meteoritics and Planetary Science* 43(11):1861-1877.

Simon S. B., Sutton S. R., Grossman L. (2007) Valence of titanium and vanadium in pyroxene in refractory inclusion interiors and rims. *Geochimica et Cosmochimica Acta* 71:3098–3118.

Soderblom L. A., Becker T. L., Bennett G., Boice D. C., Britt D. T., Brown R. H., Buratti B. J., Isbell C., Giese B., Hare T., Hicks M. D., Howington-Kraus E., Kirk R. L., Lee M., Nelson R. M., Oberst J., Owen T. C., Rayman M. D., Sandel B. R., Stern S. A., Thomas N., and Yelle R. V. (2002) Observations of Comet 19P/Borrelly by the Miniature Integrated Camera and Spectrometer Aboard Deep Space 1. *Science* 296(5570):1087-1091.

References

Soderblom L. A., Anderson R. C., Arvidson R. E., . Bell III J. F, Cabrol N. A., Calvin W., Christensen P. R., Clark B. C., Economou T., Ehlmann B. L., Farrand W. H., Fike D., Gellert R., . Glotch T. D.,Golombek M. P., Greeley R., Grotzinger J. P., Herkenhoff K. E, Jerolmack D. J., Johnson J. R., Jolliff B., Klingelhöfer G., Knoll A. H., Learner Z. A., Li R., Malin M. C., McLennan S. M., McSween H. Y., Ming D. W., Morris R. V., Rice, J. W. Jr., Richter L., Rieder R., Rodionov D., Schröder C., Seelos IV, F. P.Soderblom J. M., Squyres S. W., Sullivan R., Watters W. A., Weitz C. M., Wyatt M. B., Yen A., and Zipfel J. (2004) Soils of Eagle Crater and Meridiani Planum at the Opportunity Rover Landing Site. *Science* 306:1723-1726.

Spencer L. M., Mckay D. S., Gibson E. K., Thomas-Keprta K. L., Wentworth S. J., and Clemett S. J. 2008. Observation and analysis of martian meteorite Y000593: evidence for biosignatures (abstract #1680) 39th Lunar and Planetary Science Conference. CD-ROM.

Spencer M. K., and Zare R. N. (2007) Comment on Organics Captured from Comet 81P/Wild 2 by the *Stardust* Spacecraft. *Science* 317:1680.

Stern S. A. (2003) The evolution of comets in the Oort cloud and Kuiper belt. *Nature* 424:639-642.

Stokes D. J. (2008) Principles and Practise of Variable Pressure/Environmental Scanning Electron Microscopy (VP-ESEM). Sussex: Wiley & Sons.

Stodolna J., Jacob D., and Leroux H. (2010) Mineralogy of *Stardust* track 80: evidences for aqueous alteration and igneous process. (abstract #1657) 41st Lunar and Planetary Science Conference. CD-ROM.

Stroud, R.M., Alexander, C.M.O., and MacPherson, G.J. (2000) A precise new method of microsampling chondritic material for transmission electron microscope analysis: preliminary application to calcium-aluminium-rich inclusions and associated matrix material in the Vigarano CV3 meteorite. Meteoritics and *Planetary Sciences Supplement*, 35, A153.154.

Swindle T. D., Treiman A. H., Lindstrom D. J., Burkland M. K., Cohen B. A., Grier J., Li B., and Olson E. K. (2000) Noble gases in iddingsite from the Lafayette meteorite: Evidence of liquid water on Mars in the last few hundred million years. *Meteoritics & Planetary Science* 37:107-115.

Tenderholt A., Hedman B., and Hodgson K. O. (2007) PySpline: A Modern, Cross-Platform Program for the Processing of Raw Averaged XRF Edge and EXAFS Data: X-ray Absorption fine Structure – XAFS 13. (Eds B Hedman and P Paianetta) AIP Conference Proceedings 882: 105-107.

Tomeoka K. and Buseck P. R. (1985) Hydrated interplanetary dust particle linked with carbonaceous chondrites? *Nature*, 314, 338-340.

Tosca N. J., Milliken R. E., and Michel F.M. (2008) Smectite formation on early mars: experimental constraints (abstract #7030). *LPI Workshop on Martian Phyllosilicates: Recorders of Aqueous Processes.*

Trigo-Rodriguez J.M., Domínguez G., Burchell M.J., Hörz F., and Llorca J. (2008) Bulbous Tracks Arising From Hypervelocity Capture In Aerogel. *Meteoritics and Planetary Science* 43:75–86.

Tsou P., Brownlee D.E., Laurance M.E., Hrubesh L., and Albee A. (1988) Intact capture of hypervelocity micrometeoroid analogs. Proceedings, 19th Lunar and Planetary Science conference. pp. 1205 – 1206.

Treiman A. H. (2005) The nakhlite meteorites: Augite-rich igneous rocks from Mars. *Chemie der Erde* 65:203–270.

Treiman A. H., Barret R. A., and Gooding J. L. (1993) Preterrestrial aqueous alteration of the Lafayette (SNC) meteorite. *Meteoritics & Planetary Science* 28:86-97.

Treiman A., Gleason J. D.; Bogard D. D. (2000) The SNCs are meteorites from Mars. *Planetary and Space Science* 48:1213-1230.

Treiman A. H., and Goodrich C.A. (2002) Pre-terrestrial aqueous alteration of the Y-000593 and Y-000749 nakhlite meteorites. *NIPR Symposium Antarctic Meteorites* XXVII:166–167.

Treiman A. H., and Irving A. J. (2008) Petrology of the nakhlite (martian) meteorite Norwthwest Africa (NWA) 998. *Meteoritics & Planetary Science* 43:829-854.

Treiman A.H., and Lindstrom D. J. (1997) Trace element geochemistry of Martian iddingsite in the Lafayette meteorite. *Journal of Geophysical Research* 102(E4):9153-9163.

Tronche E. J., Hewins R. H., and MacPherson G. J. (2007) Formation conditions of aluminium-rich chondrules. *Geochimica et Cosmochimica Acta* 71:3361-3381.

Tsou P., Brownlee D., Sandford S. A., Hörz F., Zolensky M. (2003) Wild 2 and interstellar sample collection and Earth return. *Journal of Geophysical Research* 108(8113) 21pp.

Tsuno K. (1999) Optical design of electron microscope lenses and energy filters. *Journal of Electron Microscopy.* 48(6): 801-820.

Vicenzi E. P., and Heaney P. J. (2000) Multiple Martian Fluids: The alteration sequence in the Lafayette SNC Meteorite. *Meteoritics & Planetary Science* 35:A164-A165.

Vicenzi E. P., and Eiler J. (1998) Oxygen isotopic composition and high-resolution secondary ion mass spectrometer imaging of martian carbonate in Lafayette meteorite. *Meteoritics & Planetary Science* 33:A159-A160.

Vicenzi E. P., and Heaney P. J. (1999) Examining martian alteration products using *in situ* tem sectioning: a novel application of the Focused Ion Beam (FIB) for the study of extraterrestrial materials (abstract #2005). 30th Lunar and Planetary Science Conference.

References

Wark D. A., and Lovering J. F. (1977) Marker events in the early evolution of the Solar System: Evidence from rims of Ca-Al rich inclusions in carbonaceous chondrites. *8th Lunar and Planetary Science Conference*. 95-112.

Weber D. and Bischoff A. (1997) Refractory inclusions in the CR chondrite Acfer 059-El Djouf 001: petrology, chemical composition, and relationship to inclusion populations in other types of carbonaceous chondrites. *Chem. Erde* 57:1–24.
Weissman P. R. (1999) Diversity of comets: formation zones and dynamical paths. *Space Science Reviews* 90:301–311.

Weissman P.R., and Campins H. (1993) Short - Period Comets. In *Near Earth Resources* (ed. Lewis J. Matthews M.S., and. Guerreri M.L) 569-617. Univ. AZ Press, Tucson

Wentworth S. J., and Gooding J. L. 1994. Carbonates and sulfates in the Chassigny meteorite:further evidence of aqueous chemistry on the SNC parent planet. *Meteoritics* 29: 860-863.

Westphal A. J., Brownlee D. E., Butterworth A. L., Fakra S., Gainsforth Z., Joswiak D., Marcus M. A., Snead C. J., and Ogliore R. C. (2008) Oxidation state of Fe in the Jupiter-family Comet Wild 2 (abstract #2133). 39th Lunar and Planetary Science Conference. CD-ROM.

Westphal A. J., Fakra S. C., Gainsforth Z., Marcus M. A., Ogliore R. C., and Butterworth A. L. (2009) Mixing fraction of inner solar system material in Comet 81P/Wild2. *The Astrophysical Journal* 694:18–28.

Westphal A. J., Snead C., Borg J., Quirico E., Raynal P.I., Zolensky. M. E., Ferrini G., Colangeli. L., and Palumbo P. (2002) Small hypervelocity particles captured in aerogel collectors: Location, extraction, handling and storage. *Meteoritics and Planetary Science* 37:855-865.

Whipple F. L. (1950) A comet model. I. The acceleration of Comet Enke. *Astrophysical Journal* 111:375-395.

Wittry D. B., and Barbi N. C. (2002) X-ray crystal spectrometers and monochromators in microanalysis. *Microscopy and Microanalysis* 7(2):124 -141.

Wood C. A., and Ashwal L. D. (1981) SNC meteorites: Igneous Rocks From Mars? *Proceedings of. Lunar and Planetary Science* 12B:1359-1375.

Wooden D. H. (2002) Comet grains: their IR emission and their relation to ISM grains. *Earth, Moon and Planets* 89:247–287.

Yu S. C. (1997) Effects of pressure on the crystal structure of olivine in harzburgite xenolith of basalt. *Proceedings of National Science Council* 21:173-179.

Zega T. J., Nittler L. R., Busemann H., Hoppe P., and Stroud R. M. (2007) Coordinated isotopic and mineralogic analyses of planetary materials enabled by in situ lift-out with a focused ion beam scanning electron microscope. *Meteoritics and Planetary Science* 42:1373-1386.

Zhan Z. X., Wang K. Y., Yao H.T., and Cao Z.L. (2009) Fabrication and characterization of aspherical lens manipulated by an electrostatic field. *Applied Optics* 48(22):4375-4380.

Zhou B., and He D. (2008) Raman spectrum of vanadium pentoxide from density-functional perturbation theory. *Journal of Raman Spectroscopy* 39:1475–1481.

Ziebold T. O. and Ogilvie R. E. (1963) Quantitative Analysis with the Electron Microanalyzer. *Analytical Chemistry*, 35: 621-627.

Zinner E. (1996) Stardust in the laboratory. *Science* 271:5245, 41-42.

Zolensky M. E., and Barrett R. A. (1994) Compositional variations of olivines and pyroxenes in chondratic interplanetary dust particles. *Meteoritics* 29:616-620.

References

Zolensky M. E., Zega T. J., Yano H., Wirick S., Westphal A. J., Weisberg M. K., Weber I., Warren J. L., Velbel M. A., Tsuchiyama A., Tsou P., Toppani A. ,Tomioka N., Tomeoka K., Teslich N. Taheri M. Susini J. Stroud R. Stephan T. Stadermann F. J. Snead C. J. Simon S. B., Simionovici A, Rietmeijer F. J. M., Rao W., Perronnet M. C., Papanastassiou D. A., Okudaira K., Ohsumi K., Ohnishi I., Nakamura-Messenger K., Nakamura T., Mostefaoui S., Mikouchi T., Meibom A., Matrajt G., Marcus M. A., Leroux H. ,Lemelle L., Le L. Lanzirotti A., Langenhorst F., Krot A. N., Keller L. P., Kearsley A. T., Joswiak D., Jacob D., Ishii H., Harvey R., Hagiya K., Grossman L., Grossman J. N., Graham G. A., Gounelle M., Gillet Ph., Genge M. J., Flynn G., Ferroir T., Fallon S., Ebel D. S., Dai Z. R., Cordier P., Clark B., Chi M., Butterworth A. L., Brownlee D. E., Bridges J. C., Brennan S., Brearley A., Bradley J. P., Bleuet P., Bland P. A., and Bastien R. (2006) Mineralogy and petrology of comet 81P/Wild 2 nucleus samples. *Science* 314:1735–1739.

Zolensky M. E., Krot A. N., and Benedix G. (2008) Record of low-temperature alteration in asteroids. *Reviews of Mineralogy and Geochemistry* 68:429-462.

Zolensky M., Messenger K. N., Rietmeijer F, Leroux H., Mikouchi T., Ohsumi K., Simon S., Grossman L, Stephan T, Weisberg M, Velbel M., Zega T., Stroud R., Tomeoka K, Ohnishi I, Tomioka N, Nakamura T, Matrajt G, Joswiak D, Brownlee D., Langenhorst F, Krot A, Kearsley A, Ishii H, Graham G, Dai Z. R., Chi M., Bradley J, Hagiya K., Gounelle M., Keller L., and Bridges J. (2008)a Camparing Wild2 paricles to chondrites and IDPs. *Meteoritics and Planetary Science* 43(1-2):261-277.

Zhang A., and Hsu W. (2009) Refractory inclusions and aluminium-rich chondrules in Sayh al Uhaymir 290 CH chondrite; Petrography and mineralogy. *Meteoritics and Planetary Science* 44(6):787-804.

Zolensky M. E., and Lindstrom D. J. (1992) Proceedings of Lunar and Planetary Science, 22, 161-169.

Zuo J.M., and Mabon J.C. (2004) Web-based Electron Microscopy Application Software: Web-EMAPS *Microscpy Microanalysis 10 (Suppliment 2).* URL: http://emaps.mrl.uiuc.edu/